

Millimeter Interferometry

Proceedings from

IMISS2

“IRAM Millimeter Interferometry Summer School 2”

edited by A.Dutrey^{1,2}

¹ Institut de RadioAstronomie Millimétrique
300 rue de la piscine
F-38406 Saint Martin d'Hères Cedex, FRANCE

² Laboratoire d'Astrophysique de Grenoble
BP53
F-38041 Grenoble Cedex 9, France

In Memoriam

This book is dedicated to the memory of our esteemed colleagues

- Bernard AUBEUF
- Francis GILLET
- Henri GONTARD
- David LAZARO
- Roland PRAYER
- Patrick VIBERT

and of the other 19 persons who died on 1st of July, 1999, in the tragic accident of the cable car giving access to the IRAM interferometer site or on december 15th, 1999, in the crash of the helicopter ensuring transport between the Plateau de Bure and the valley.

Bernard AUBEUF and Patrick VIBERT had been with the IRAM interferometer since the very beginning of its construction. With the help of Henri GONTARD, they had assumed the difficult task of handling the cable car, the general maintenance of the Plateau de Bure buildings, as well as long days of snow clearing to allow the configuration changes in winter. Francis GILLET and Roland PRAYER had been regularly joining the IRAM staff for the summer maintenance, and for the construction of the antennas. David LAZARO was working in the workshop at IRAM headquarters as a precision mechanics.

15 employees of companies working as contractors for IRAM (either on the baseline extension, or on facilities like telephone equipment) also lost their lives in the first accident. 3 engineers working on the telepherique reconstruction and the pilot died in the helicopter crash.

These persons were not astronomers but without their efforts, millimeter astronomy would never have come to the Plateau de Bure site and you would not be reading this book. We wish to dedicate these proceedings to their memory.

Preface

This book contains the updated proceedings from the summer schools held at IRAM in Grenoble from September 14 to September 18, 1998 for IMISS1 and from June 12 to June 16, 2000 for IMISS2. Both schools were attended by more than 50 participants from abroad. Not all lectures have been put in written form: the schools also included a general introduction to millimeter astronomy by Dr. Clemens THUM (IRAM). IMISS2 also contained an introduction on interferometry from the point of view of the quantum mechanics by Dr. Dennis DOWNES (IRAM). A visit to the IRAM interferometer on Plateau de Bure was an essential part of the first school. In the second one, visits to the receiver and correlator laboratories were organized.

The schools would not have occurred without the dedication of Mrs Catherine BERJAUD, who kindly took care of all logistics problems before and during the schools. Dr. Stéphane GUILLOTEAU is also thanked for organizing IMISS1 and doing the edition of the first series of lectures.

During IMISS1, the visit to the interferometer would not have been possible without the contribution of the technical and operator staff of the telescope. Special thanks to the operators Sophie LEONARDON, Michel DAN and André RAMBAUD who also made the films which were presented as an introduction to the Plateau de Bure interferometer at IMISS2. We also acknowledge the receiver and correlator groups who managed the visits to the labs during IMISS2.

We also thank Alain PERRIGOUARD and Roger AHTCHOU for help with the video equipment which gave us a lot of fun during the “real time” sessions.

Finally, Anne DUTREY would like to thank Mrs Cathy BERJAUD for a careful reading of the manuscript, fighting against the last typo errors.

Participants to IMISS1 and IMISS2

This section contains the list and e-mail addresses of participants to IMISS1 and IMISS2 and two photos taken during IMISS2.

Table 1: IMISS1, list of participants

NAME	Email
ANDERSSON Andreas	andreas@astro.su.se
ANTERRIEU Eric	anterrieu@obs-mip.fr
BACMANN Aurore	abacmann@cea.fr
BAUDRY Alain	alain.baudry@observ.u-bordeaux.fr
BERGER Jean-Philippe	berger@obs.ujf-grenoble.fr
BONTEMPS Sylvain	bontemps@astro.su.se
BREMER Michael	bremer@iram.fr
BROOKS Kate	kbrooks@newt.phys.unsw.edu.au
BROWN David	dbrown@mrao.cam.ac.uk
CASTETS Alain	Alain.Castets@obs.ujf-grenoble.fr
CHARMANDARIS Vassilis	Vassilis.Charmandaris@obspm.fr
DOLE Hervé	dole@ias.fr
DUCHENE Gaspard	Gaspard.Duchene@obs.ujf-grenoble.fr
DUTREY Anne	dutrey@iram.fr
DUVERT Gilles	Gilles.Duvert@obs.ujf-grenoble.fr
EISLOFFEL Jochen	jochen@tls-tautenburg.de
GERMAIN Benoit	Benoit.Germain@obspm.fr
GREVE Albert	greve@iram.fr
GUELIN Michel	guelin@iram.fr
GUETH Frédéric	gueth@mpifr-bonn.mpg.de
GUILLOTEAU Stéphane	guillote@iram.fr
HARDER Stephan	Stephan.Harder@obs.ujf-grenoble.fr
HERPIN Fabrice	herpin@observ.u-bordeau.fr
ISAAC Kate	isaak@astro.umd.edu
KLEIN Randolf	rklein@otto.astro.uni-jena.de
KRAUSE Oliver	krause@mpia-hd.mpg.de
LAZAREFF Bernard	lazareff@iram.fr
LEFLOCH Bertrand	lefloch@astro.iem.csic.es
LOINARD Laurent	Laurent.Loinard@obs.ujf-grenoble.fr
LUCAS Robert	lucas@iram.fr
MALBET Fabien	Fabien.Malbet@obs.ujf-grenoble.fr
MAOLI Roberto	maoli@mesioa.obspm.fr
MINIER Vincent	vincent@oso.chalmers.se
MONIN Jean-Louis	monin@obs.ujf-grenoble.fr
MORENO Rafael	moreno@iram.fr
MOTTE Frédérique	Fmotte@cea.fr
NAVARRINI Alessandro	navarrin@iram.fr
NERI Roberto	neri@iram.fr
NICCOLINI Gilles	nicolin@obs-nice.fr
NIETEN Christoph	chnieten@mpifr-bonn.mpg.de
PANIS Jean-François	panis@biaa.sinica.edu.tw
PISANU Tonino	tpisanu@ira.bo.cnr.it
RAVERA Laurent	Laurent.Ravera@cesr.fr
ROBERT Didier	robert@iram.fr

Table 2: IMISS1, list of participants continued

NAME	Email
SANCHEZ CONTRERAS Carmen	sanchez@oan.es
SCHNEIDER Nicola	schneider@ph1.uni-koeln.de
TARCHI Andrea	atarchi@astro.uni-bonn.de
THUM Clemens	thum@iram.fr
TRIGILIO Corrado	trigilio@ira.oto.cnr.it
UMANA Grazia	umana@ira.oto.cnr.it
WIESEMEYER Helmut	wiesemey@iram.fr
WILD Wolfgang	wild@iram.es

Table 3: IMISS2, list of participants

NAME	Email
ARCE Hector	harce@cfa.harvard.edu
AUGEREAU Jean-Charles	Jean-Charles.Augereau@obs.ujf-grenoble.fr
BACMANN Aurore	bacmann@astro.uni-jena.de
BELLOCHE Arnaud	belloche@discovery.saclay cea.fr
BELTRAN Maria-Teresa	mbeltran@cfa.harvard.edu
BERGER Jean-Philippe	berger@enserg.fr
BIOLLUZ Gilles	gbiolluz@yahoo.com
BOONE Frederic	Frederic.Boone@obspm.fr
BREMER Michael	bremer@iram.fr
BRETHERTON Derek	deb@astro.livjm.ac.uk
CASTRO-CARRIZO Arancha	Carrizo@oan.es
CECARELLI Cecilia	Cecilia.Ceccarelli@obs.ujf-grenoble.fr
COLOM Pierre	colom@obspm.fr
COMITO Claudia	ccomito@mpifr-bonn.mpg.de
CONTINI Thierry	tcontini@eso.org
DAN Michel	dan@iram.fr
DANNERBAUER Helmut	dannerb@mpe.mpg.de
DARTOIS Emmanuel	dartois@iram.fr
DELGADO Guillermo	gdelgado@eso.org
DE VRIES Christopher	devries@astro.umass.edu
DOWNES Dennis	downes@iram.fr
DUTREY Anne	dutrey@iram.fr

Table 4: IMISS2, list of participants continued

NAME	Email
ELS Sebastian	sels@eso.org
FOSSE David	fosse@isis.iem.csic.es
GALLEGO CALVENTE Teresa	tgallego@iram.es
GREVE Albert	greve@iram.fr
GROSSO Nicolas	ngrosso@xray.mpe.mpg.de
GUETH Frédéric	gueth@iram.fr
GUILLOTEAU Stéphane	guillote@iram.fr
HAFOK Heiko	hafok@ph1.uni-koeln.de
HAGUENAUER Pierre	Pierre.Haguenauer@obs.ujf-grenoble.fr
HAIKALA Lauri	lhaikala@sc.eso.org
HENRY Florence	Florence.Henry@obspm.fr
HILY-BLANT Pierre	hilyblan@iram.es
KERVELLA Pierre	pkervell@eso.org
LAZAREFF Bernard	lazareff@iram.fr
LE FLOCH'H Emeric	elefloch@eso.org
LEONARDON Sophie	Leonardo@iram.fr
LOINARD Laurent	loinard@iram.fr
LUCAS Robert	lucas@iram.fr
MALBET Fabien	Fabien.Malbet@obs.ujf-grenoble.fr
MAO Ruiqing	rqmao@mpifr-bonn.mpg.de
MAUERSBERGER Rainer	mauers@iram.es
MEGE Pierre	Pierre.Mege@obs.ujf-grenoble.fr
MELCHIOR Anne-Laure	A.L.Melchior@obspm.fr
MORENO Raphael	moreno@iram.fr
MUELLER Sebastien	muller@iram.fr
NAKANISHI kouichiro	nakanisi@nro.nao.ac.jp
NERI Roberto	neri@iram.fr
NICCOLINI Gilles	nicolin@obs-nice.fr
NUERNBERGER Dieter	nurnberger@iram.fr
OTAROLA Angel	aotarola@eso.org
PARDO CARRION Juan Ramon	pardo@isis.iem.csic.es
PETY Jérôme	pety@Ira.ens.fr
PRIEUR Jean-Louis	jean-louis.prieur@ast.obs-mip.fr
RAMBAUD André	rambaud@iram.fr
SCHREYER Katharina	martin@astro.uni-jena.de
SEGRANSAN Damien	Damien.Segransan@obs.ujf-grenoble.fr
TEYSSIER David	teyssier@Ira.ens.fr
THI Wing-Fai	thi@strw.leidenuniv.nl
THOMAS Bertrand	thomas@iram.es
THUM Clemens	thum@iram.fr
VALLEJO Olivier	vallejo@observ.u-bordeaux.fr
VASTEL Charlotte	Charlotte.Vastel@cesr.fr
WIESEMEYER Helmut	wiesemey@iram.fr
WILGENBUS David	david.wilgenbus@obspm.fr
ZUCCONI Antonio	zucconi@arcetri.astro.it



Figure 1: Participants to IMISS2



Figure 2: Participants to IMISS2

Contents

In Memoriam	iii
Preface	v
Participants to IMISS1 and IMISS2	vii
1 Radio Antennas	1
1.1 Introduction	1
1.2 Basic Principles	2
1.3 The perfect Single-Dish antenna	3
1.4 The real Single-Dish Antenna	7
1.4.1 Systematic Deformations: Defocus, Coma, Astigmatism	7
1.4.2 Random Errors	10
1.5 Radiometric Relations	13
2 Millimetre Interferometers	15
2.1 Basic principle	15
2.2 The Heterodyne Interferometer	17
2.2.1 Source Size Effects	17
2.2.2 Finite Bandwidth	19
2.3 Delay Tracking and Frequency Conversion	20
2.4 Fringe Stopping and Complex Correlator	21
2.5 Fourier Transform and Related Approximations	21
2.6 Array Geometry & Baseline Measurements	23
3 Millimetre Very Long Baseline Interferometry	25
3.1 Introduction	25
3.2 mm-VLBI Arrays	26
3.2.1 The CMVA Array	26
3.2.2 The VLBA Array	29
3.3 Available Resolution	29
3.4 Polarization Observations	31
3.5 The Feasibility of mm-VLBI: Signal-to-Noise Ratio and Detections	31
3.6 From observations to correlations, step by step	32
3.6.1 Observing Techniques	32
3.6.2 Data Recording	36
3.6.3 Correlation Time	36
3.6.4 Phase Correction	36
3.6.5 Correlation	36
3.7 The observable sources with mm-VLBI	38
3.7.1 Which Kind of sources can we observe	38
3.7.2 The field of view	38
3.7.3 An example: mm-VLBI Observations of QSO 3C 273	40

4	Introduction to Optical/Near-Infrared Interferometry	43
4.1	Introduction	43
4.1.1	Brief history of optical interferometry	43
4.1.2	Current and future optical interferometers	44
4.2	Optical versus millimeter radio interferometry	45
4.2.1	Common issues	45
4.2.2	Main differences	45
4.3	Description of optical interferometers	46
4.3.1	Functional description	46
4.3.2	Specific applications	49
4.4	Formation of the interferometric fringes	51
4.4.1	Beam combination	51
4.4.2	Fringe coding and detection	53
4.5	Main challenges in interferometry	54
4.5.1	Atmosphere turbulence	54
4.5.2	Other atmosphere systematics	55
4.5.3	Fighting the atmosphere: complexity and accuracy	56
4.5.4	Noise sources - Sensitivity	57
4.6	Conclusion	59
5	Receivers : an overview for non-specialists	63
5.1	Introduction	63
5.2	Coupling optics	63
5.3	Why we need heterodyne receivers	66
5.4	Local oscillator system	67
5.5	Local oscillator injection	67
5.6	Photon-assisted tunneling	67
5.7	Mixer	69
5.8	Cryostat	70
5.9	Actual receivers	70
6	Cross Correlators	73
6.1	Introduction	73
6.2	Basic Theory	74
6.3	The Correlator in Practice	77
6.3.1	Digitization of the input signal and clipping correction	78
6.3.2	Time lag windows and spectral resolution	82
6.3.3	Main limitations	83
6.4	The correlator on Plateau de Bure	87
6.4.1	The third-generation correlator	87
6.5	Appendix	88
6.5.1	Summary of definitions	88
6.5.2	Clipping correction for 4-level quantization	89
7	LO System and Signal Transport	91
7.1	An Heterodyne Interferometer	91
7.1.1	The simple interferometer	91
7.1.2	The heterodyne interferometer	91
7.1.3	Frequency conversion	92
7.1.4	Signal phase	92
7.2	Delay lines requirements	94
7.2.1	Single sideband processing in a finite bandwidth	94
7.2.2	Double sideband system	95
7.3	sideband separation	95

7.3.1	Fringe rate method	95
7.3.2	Phase switching method	95
7.4	The PdB Signal and LO transport system	96
7.4.1	Signal path	96
7.4.2	LO generation	98
7.4.3	Further signal processing	98
7.4.4	Phase stability requirements	98
7.4.5	Cable electrical length control	99
7.5	Next generation instruments	99
8	The Plateau de Bure Interferometer	101
8.1	History	101
8.2	Description	101
8.3	Array operation	103
8.3.1	Array calibration	103
8.3.2	Array observations	106
8.4	Proposal submission and contact people	108
9	Bandpass and Phase Calibration	111
9.1	Definitions and formalism	111
9.1.1	Baseline based vs antenna based gains	112
9.1.2	Gain corrections	113
9.2	Bandpass calibration	113
9.2.1	Bandpass measurement	113
9.2.2	IF passband calibration	113
9.2.3	RF bandpass calibration	114
9.2.4	Sideband calibration	115
9.3	Phase calibration	115
9.3.1	Phase referencing by a nearby point source	116
9.3.2	Phase referencing by a point source in the primary beam	117
9.3.3	Phase referencing using another band or another frequency	117
10	Atmospheric Absorption	119
10.1	The physical and chemical structure of the Atmosphere	119
10.1.1	Constituents of the atmosphere	119
10.1.2	Thermodynamics of the air	120
10.1.3	Hydrostatic equilibrium	121
10.1.4	Water	122
10.2	Atmospheric radiative transfer in the mm/submm	122
10.2.1	Introduction	122
10.2.2	Unpolarized radiative transfer equation	122
10.2.3	Spectroscopic parameters	123
10.2.4	Line shapes	125
10.2.5	Non-resonant absorption	126
10.2.6	Radiative transfer through atmospheric hydrometeors	127
10.3	Fourier Transform Spectroscopy for site testing	128
10.3.1	FTS measurements at Mauna Kea	128
10.3.2	FTS measurements at Atacama (future ALMA site)	130
10.4	Atmospheric absorption evaluation	131
10.4.1	Correction for atmospheric absorption, T_A^*	131
10.5	Phase fluctuation evaluation	134
10.5.1	Cause of Phase Fluctuations	134
10.5.2	Simulations of phase fluctuations	134
10.5.3	Phase Correction Methods	134

10.5.4	Example of phase correction	135
11	Atmospheric Fluctuations	139
11.1	Introduction	139
11.2	Hydrodynamical basics of turbulent motion	141
11.3	Statistical properties of turbulence	143
11.4	Remote sounding techniques	145
11.5	Current phase correction at IRAM	146
11.6	Phase correction during off-line data reduction	149
11.7	Frequently asked questions	150
12	Amplitude and Flux Calibration	153
12.1	Definition and Formalism	153
12.2	Single-dish Calibration of the Amplitude	154
12.2.1	Low opacity approximation and implication for T_{cal}	155
12.2.2	Absolute errors on T_{cal} due to instrumental parameters	156
12.2.3	Relative errors or errors on T_{cal}^L/T_{cal}^U	156
12.2.4	Estimate of the thermal noise	159
12.3	Flux Calibration (visitor's nightmare)	159
12.3.1	Introduction	159
12.3.2	Calibration procedure at Bure	160
12.3.3	Determining the absolute flux scale on a project	161
12.3.4	Possible biases and remedies	162
12.3.5	The program FLUX	164
12.4	Interferometric Calibration of the Amplitude	164
12.4.1	Correction for the antenna gain $\Gamma_i(t)$	164
12.4.2	Estimate of the atmospheric decorrelation factor f	165
12.4.3	Fitting Splines: the last step	168
12.4.4	A few final checks	168
13	Calibration of data in Practice	171
13.1	Introduction	171
13.1.1	Contents of the account	171
13.1.2	Before starting the data reduction	172
13.1.3	Activating the CLIC environment	172
13.2	The "First Look" procedure	172
13.3	The "Standard Calibration (2-receivers)" procedure	173
13.3.1	Inputs	174
13.3.2	Actions or Outputs	174
13.3.3	Results of the calibration	175
14	UV Plane Analysis	177
14.1	uv tables	177
14.1.1	uv table contents	177
14.1.2	How to create a uv Table	178
14.2	uv data plots	179
14.3	Data editing	180
14.4	Position shift	181
14.5	Averaging	181
14.5.1	Data compression	181
14.5.2	Circular averaging	182
14.6	Model fitting	182
14.6.1	Position measurement	183
14.7	Continuum source subtraction	183
14.8	Self calibration by a point source	183

15 The Imaging Principles	187
15.1 Fourier Transform	188
15.1.1 Direct Fourier Transform	188
15.1.2 Fast Fourier Transform	188
15.1.3 Gridding Process	188
15.2 Sampling & Aliasing	189
15.3 Convolution and Aliasing	189
15.4 Error Analysis	191
15.5 Weighing and Tapering	191
15.6 The GILDAS implementation	193
15.7 Deconvolution	193
15.7.1 The CLEAN method	194
15.7.2 Interpretation of CLEAN	195
15.7.3 The CLEAN variants	195
15.7.4 The GILDAS implementation	196
16 Advanced Imaging Methods: WIPE	197
16.1 Introduction	197
16.2 Object space	198
16.3 Experimental data space	199
16.4 Image reconstruction process	200
16.4.1 Synthesized aperture	200
16.4.2 Synthetic beam	201
16.4.3 Regularization frequency list	201
16.4.4 Data space	202
16.4.5 Object representation space	202
16.4.6 Objective functional	202
16.4.7 Uniqueness and robustness	203
16.5 Implementation of WIPE at IRAM	205
17 Mosaicing	209
17.1 Introduction	209
17.2 Image formation in a mosaic	210
17.3 Mosaicing in practice	212
17.4 A CLEAN-based algorithm for mosaic deconvolution	214
17.5 Artifacts and instrumental effects	217
17.6 Concluding remarks	219
18 Imaging in Practice	221
18.1 Visualisation	221
18.2 Photometry	222
18.2.1 From Flux density to Brightness temperature	222
18.2.2 Accuracy of Flux density estimates	222
18.3 Short Spacings	224
18.3.1 UV_SINGLE	224
18.4 Dirty Tricks	225
18.4.1 MOMENTS	225
18.4.2 Continuum Subtraction	226
19 Low Signal-to-noise Analysis	227
19.1 Continuum Source	227
19.1.1 Flux measurement	227
19.1.2 Other parameters	228
19.2 Spectral Line Sources	230

20 Basic Principles of Radio Astrometry	233
20.1 Introduction and Basic Formalism	233
20.2 The Phase Equation	234
20.3 Determination of Source Coordinates and Errors	235
20.4 Accurate Position Measurements with the IRAM Interferometer	236
20.4.1 Absolute positions	237
20.4.2 Relative Positions and Self-calibration Techniques	238
20.5 Sources of Position Uncertainty	239
20.5.1 Known Limitations	239
20.5.2 Practical Details	240
21 Mm versus Optical Interferometry: a qualitative comparison	243
21.1 The basic equation of interferometry	243
21.1.1 Additive interferometry	244
21.1.2 Multiplicative interferometry	244
21.2 Getting the fringes	244
21.3 Atmospheric behaviour and noise properties	245

Chapter 1

Radio Antennas

Albert Greve

greve@iram.fr

IRAM, 300 rue de la Piscine, F-38406 Saint Martin d'Hères

1.1 Introduction

We can define a *radio antenna* as an instrument which *collects*, and *detects*, *electromagnetic radiation* from a certain *area* and *direction* of the sky, allowing to build up an image from individual observations. In radio astronomy we are interested in the detection and analysis of radiation emitted from celestial objects, i.e. solar system bodies, stars, interstellar gas, galaxies, and the universe. The electromagnetic radiation observed in radio astronomy covers the wavelength range from several meters, say 10 m (= 30 MHz), to a fraction of a millimeter, say 0.3 mm (≈ 1000 GHz). Since the antenna must be many wavelengths in diameter in order to collect a large amount of energy and to provide a reasonable directivity (angular resolution), it is evident that antennas for meter wavelengths may have dimensions of many 10 meters to several 100 meters, while antennas for millimeter wavelengths have dimensions of several meters to several 10 meters ($\approx 10\,000$ to $50\,000 \lambda$'s). The technique of mechanical construction is therefore different for meter and millimeter wavelength antennas: antennas for m-wavelengths can be constructed, for instance, as mesh-wire networks and plate arrays, mm-wavelength antennas are full-aperture solid surface parabolic reflector antennas. Typical examples are the obsolete Mills-Cross antenna, the Effelsberg and GBT 100-m antennas, and the IRAM 30-m (Pico Veleta) and 15-m (Plateau de Bure) antennas. However, despite the variety of mechanical constructions, all antennas can be understood from basic principles of electromagnetic radiation, optics, and diffraction.

Here we discuss full-aperture parabolic antennas, like the IRAM antennas, which are used for observations at $\sim 3 - 0.8$ mm wavelength (100 - 350 GHz). These antennas are very similar to optical reflector telescopes and use in particular the Cassegrain configuration of a parabolic main reflector and a hyperbolic subreflector (Figure 1.3), with an image formed at the secondary focus near the vertex of the main reflector where the receiver, or a receiver-array, is installed. These antennas are steerable and can observe in any direction of the visible hemisphere, with the facility of tracking, scanning, and mapping of a source.

The collected radiation is concentrated in the secondary focus and is (coherently) detected by a receiver at a certain frequency ν (or wavelength λ) and within a certain bandwidth $\Delta\nu$ (or $\Delta\lambda$). Heterodyne mm-wavelength receivers, which preserve the phase of the incident radiation, have small bandwidths of the order of $\Delta\nu = 0.5 - 2$ GHz so that $\Delta\nu/\nu = \Delta\lambda/\lambda \approx 0.5 \text{ GHz}/100 \text{ GHz} \approx 1/200$. From the point of view of antenna optics, these receivers detect “monochromatic” radiation, and the antenna characteristics can be calculated for a monochromatic wave (as will be done below). Bolometer receivers, on the other hand, detect power in a broad bandwidth of the order of $\Delta\nu \approx 50$ GHz so that $\Delta\nu = 50 \text{ GHz}/250 \text{ GHz} \approx 1/5$. These detectors are no longer monochromatic, and the chromatism of the antenna must be considered in their application.

The construction and operation of a radio antenna is based on exact physical theories, like Maxwell’s theory of electromagnetic radiation, the pointing theory of an astronomical instrument, the transformation (mixing, down-conversion, amplification) and detection of electromagnetic radiation, etc. The theory of a radio antenna presented here is, however, only the very tip of an iceberg (of several 100 000 published pages), but may provide sufficient information for the user astronomer to understand the basic principle of a telescope, either a perfect one, which nobody has but which can be described with high precision, or a real one, with small defects and aberrations, which can be described with sufficient detail to apply corrections.

The theory, construction, and use of radio antennas is contained in many textbooks and journals such as IEEE Transactions Antennas and Propagation, Radio Science, Applied Optics. A biased selection is mentioned here: [Born & Wolf 1975] [Reynolds et al. 1989] [Love 1978] [Lo and Lee] [Kraus 1982] [Goldsmith 1988]

1.2 Basic Principles

The properties of electromagnetic radiation propagation and of radio antennas can be deduced from a few basic physical principles, i.e.

1. the notion that Electromagnetic Radiation are Waves of a certain Wavelength (λ), or Frequency (ν), and Amplitude (\mathbf{A}) and Phase (φ);
2. from Huygens Principle which says that each element of a wavefront is the origin of a Secondary Spherical Wavelet;
3. the notion that the Optical Instrument (like a single-dish antenna, a telescope, etc.) combined with a receiver manipulates the incident wavefront through their respective phase and amplitude transfer functions.

Summarized in one sentence, and proven in the following, we may say that the radio antenna transforms the radiation incident on the aperture plane (\mathcal{A}) to an image in the image plane (\mathcal{I}), also called focal plane. Following Huygens Principle illustrated in Figure 1.1, the point $\mathbf{a}(x,y) \equiv \mathbf{a}(\vec{r})$ of the incident wavefront in the aperture plane \mathcal{A} is the origin of a spherical wavelet of which the field $\delta\mathbf{E}(\mathbf{a}')$ at the point $\mathbf{a}'(u,v) \equiv \mathbf{a}(\vec{u})$ in the image plane \mathcal{I} is

$$\delta\mathbf{E}(\vec{u}) = \mathbf{A}(\vec{r})\exp[i\mathbf{k}\mathbf{s}]/s \quad (1.1)$$

with $\mathbf{k} = 2\pi/\lambda$. The ensemble of spherical wavelets arriving from all points of \mathcal{A} at the point $\mathbf{a}'(\vec{u})$ of the image plane \mathcal{I} produces the field

$$\mathbf{E}(\vec{u}) = \int_{\mathcal{A}} \mathbf{A}(\vec{r})\Lambda(\beta)[\exp(i\mathbf{k}\mathbf{s})/s]dx dy \quad (1.2)$$

For the paraxial case, when the rays are not strongly inclined against the direction of wave propagation (i.e. the optical axis), the inclination factor Λ can be neglected since $\Lambda(\beta) \approx \cos(\beta) \approx 1$. Also, $s \approx s_0$ for paraxial rays, but $\exp[i\mathbf{k}\mathbf{s}] \neq \exp[i\mathbf{k}\mathbf{s}_0]$ since these are cosine and sine terms of s where a small change in

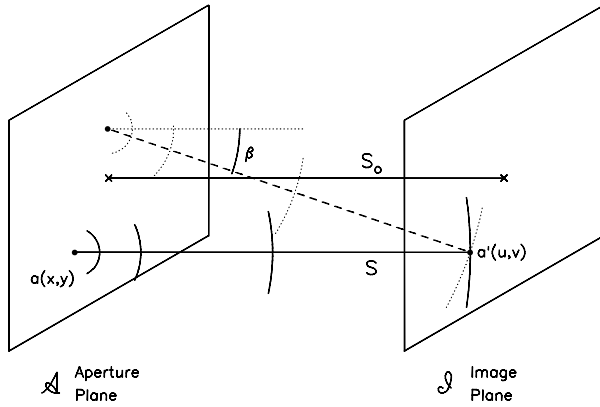


Figure 1.1: Illustration of Huygens Principle. The individual points of the plane wavefront in the aperture plane (\mathcal{A}) are the origin of secondary spherical wavelets, which propagate to the right, and superpose to form a plane wavefront in the image plane (\mathcal{I}). The optical instrument (telescope) is placed in between \mathcal{A} and \mathcal{I} .

s may produce a large change of the cosine or sine value. Thus, for the paraxial approximation we may write

$$s = [(x - u)^2 + (y - v)^2 + z^2]^{1/2} \approx R + g(x, y, R) - (xu + yv)/R \quad (1.3)$$

with

$$R = (x^2 + y^2 + z^2)^{1/2} \quad \text{and} \quad g(x, y, R) = (x^2 + y^2)/2R \quad (1.4)$$

When using these expressions in Eq.1.2, we obtain

$$E(u, v) = [\exp(ikR)/s_0] \int_{\mathcal{A}} A(x, y) \exp[ik(g(x, y, R) - (ux + vy)/R)] dx dy \quad (1.5)$$

This equation describes the paraxial propagation of a wavefront, for instance the wavefront arriving from a very far away star. In particular, this equation says, that without disturbances or manipulations in between \mathcal{A} and \mathcal{I} the plane wavefront continues to propagate in straight direction as a plane wavefront.

1.3 The perfect Single-Dish antenna

We now place an optical instrument (a mirror, lens, telescope etc.) in the beam between \mathcal{A} and \mathcal{I} with the intention, for instance, to form an image of a star. Optical instruments are invented and developed already since several centuries; however, the physical-optics (diffraction) understanding of the image formation started only a good 200 years ago. Thus, speaking in mathematical terms, the telescope (\mathcal{T}) manipulates the phases (not so much the amplitudes) between the points (\vec{r}) of the aperture plane (\mathcal{A}) and the points (\vec{u}) of the image plane (\mathcal{I}) by the phase transfer function $\Omega_{\mathcal{O}}(\vec{r}, \vec{u})$, so that the wavefront converges in the focal point. The receiver (\mathcal{R})/detector introduces an additional modulation of the amplitude $\Omega_{\mathcal{R}}(\vec{r}, \vec{u})$, as described below. Using this information, the field distribution in the focal plane (\mathcal{I}) of the telescope becomes

$$E(\vec{u}) = [\exp(ikR)/s_0] \int_{\mathcal{A}} A(\vec{r}) \Omega_{\mathcal{O}} \Omega_{\mathcal{R}} \exp[ik(g(x, y, R) - (ux + vy)/R)] dx dy \quad (1.6)$$

The phase modulation of the parabolic reflector used in a radio telescope is, fortunately,

$$\Omega_{\mathcal{O}} = \exp[-ik g(x, y, F)] \quad (1.7)$$

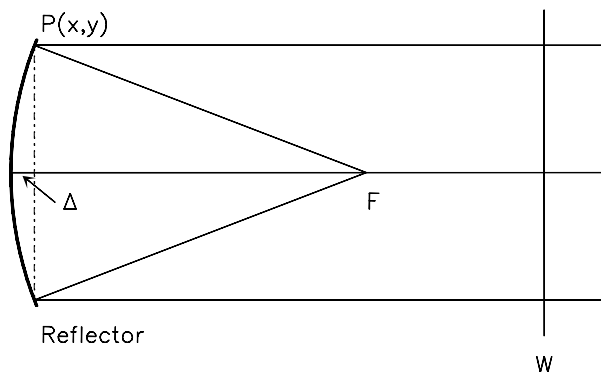


Figure 1.2: Phase modulation of a reflector. The plane wavefront (W) propagates to the left and the ray reflected at P(x,y) toward the focus F is shifted in phase by the amount Δ .

(where F is the focal length of the reflector), which inserted into Eq.1.6 eliminates this term in the exponent so that

$$E(\vec{u}) = [\exp(ikF)/F] \int_{\mathcal{A}} A(\vec{r}) \Omega_R \exp[-ik(ux + vy)/F] dx dy \equiv \mathcal{FT}[A(\vec{r}) \Omega_R(\vec{r})] \quad (1.8)$$

This equation says that the field distribution $E(\vec{u})$ in the focal plane of the telescope is the Fourier transform (\mathcal{FT}) of the receiver-weighted field distribution $A(\vec{r}) \Omega_R(\vec{r})$ in the aperture plane. Since $E(\vec{u}) E^*(\vec{u}) \neq \delta(\vec{u} - \vec{u}_o)$ for a realistic optical instrument/telescope with limited aperture size, we arrive at the well known empirical fact that the image of a point-like object is not point-like; or, with other words, the image of a star is always blurred by the beam width of the antenna $\Theta_b \propto \lambda/D$, with D the diameter of the reflector.

To close the argumentation, we need to show that the telescope manipulates the incident wave in the way given by Eq.1.7). To demonstrate this property in an easy way, we consider in Figure 1.2 the paraxial rays of a parabolic reflector of focal length F. From geometrical arguments we have

$$(F - \Delta)^2 + (x^2 + y^2) = F^2 \quad (1.9)$$

which for small Δ becomes

$$\Delta = -(x^2 + y^2)/F \equiv -g(x, y, F) \equiv \Omega_O(\vec{r}) \quad (1.10)$$

which is the instrumental phase modulation function Ω_O used above. The proof is given for a simple parabolic reflector; however, a combined telescope with main reflector and subreflector can be treated in a similar way, leading to the same result.

The fundamental Eq.1.8 can be used to show that an interferometer is *not* a single dish antenna, even though one tries with many individual telescopes and many telescope positions (baselines) to simulate as good as possible the aperture of a large reflector. If we assume for the single dish antennas that $A(\vec{r}) \equiv 1$ and $\Omega_R \equiv 1$, then the power pattern $P(\vec{u})$ (beam pattern) in the focal plane of the single antenna is

$$P(\vec{u}) = E(\vec{u}) E^*(\vec{u}) = \int_{\mathcal{A}} \int_{\mathcal{A}} \exp[-ik\vec{u}(\vec{x}_1 - \vec{x}_2)] (dx dy)_1 (dx dy)_2 \propto [J_1(\vec{u})/u]^2 \quad (1.11)$$

where J_1 is the Bessel function of first order (see [Born & Wolf 1975]). The function $[J_1(u)/u]^2$ is called Airy function, or Airy pattern. The interferometer does not simulate a continuous surface, but consists of individual aperture sections $\mathcal{A}_\infty, \mathcal{A}_\epsilon, \dots$ of the individual telescopes, so that its power pattern $P_\Sigma(\vec{u})$ (beam pattern) in the focal plane is

$$P_\Sigma(\vec{u}) = \sum_n \sum_m \int_{\mathcal{A}_n} \int_{\mathcal{A}_m} \exp[ik\vec{u}(\vec{x}_1 - \vec{x}_2)] (dx dy)_1 (dx dy)_2 \neq P(\vec{u}) \quad (1.12)$$

The important result of this equation is the fact that the image obtained with the interferometer is “incomplete”, though certainly not as blurred as seen with a single telescope ($\Theta_D \propto \lambda/D$), but having the superior

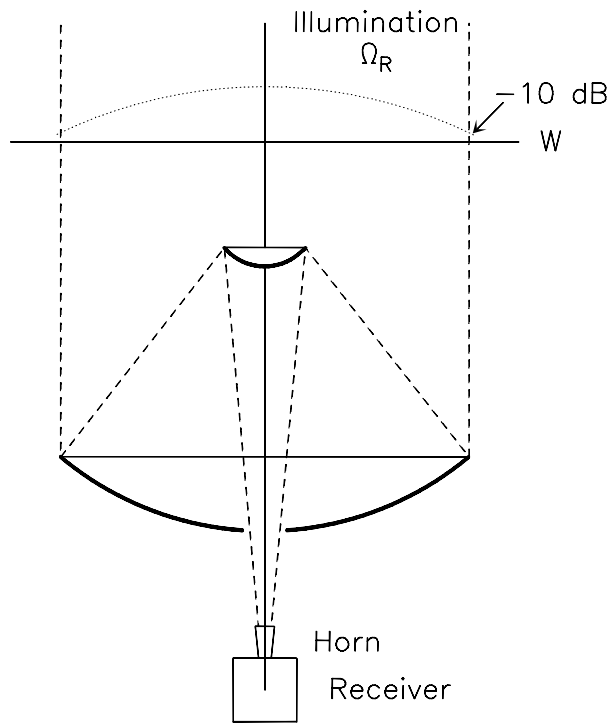


Figure 1.3: The figure shows a Cassegrain telescope and the illumination Ω_R of the incident plane wavefront W .

resolution of the spatial dimension (approximately the longest baseline \mathcal{B}) of the array ($\Theta_B \propto \lambda/\mathcal{B}$). For the Plateau de Bure interferometer $\mathcal{B}/D \approx 300\text{ m}/15\text{ m} \approx 20$ so that $\Theta_B \approx 1/20 \Theta_D$. The incompleteness sometimes requires (in particular for mm-VLBI observations which are very similar) additional information for a full image reconstruction, for instance that the object consists of several point-like sources, or a point-like source and a surrounding halo, etc. (see for instance the number of components in CLEAN).

The single telescope selects a part of the incident plane wavefront and 'bends' this plane into a spherical wave which converges toward the focus. This spherical wavefront enters the receiver where it is mixed, down-converted in frequency, amplified, detected, or correlated. The horn-lens combination of the receiver modifies the amplitude of the spherical wavefront in a way expressed by the function $\Omega_R(\vec{r})$. This function, called taper or illumination function of the horn-lens combination, weighs the wavefront across the aperture, usually in a radial symmetric way. Figure 1.3 shows, schematically, the effect of a parabolic taper as often applied on radio telescopes, and expressed as

$$\Omega_R(\rho) = K + [1 - \rho^2]^p \quad (1.13)$$

with ρ the normalized radius of the circular aperture, and K and p being constants. For $A(\vec{r}) \equiv 1$ (i.e. an incident wavefront without structure) the diffraction integral is

$$E_T(\vec{u}) = \int_{\mathcal{A}} \Omega_R(\vec{x}) \exp[-ik\vec{u}\vec{x}] dx dy \quad \text{and} \quad E(\vec{u})E^*(\vec{u}) \equiv A_T(\vec{u}) \quad (1.14)$$

E_T is the tapered field distribution in the focal plane, and A_T the tapered beam pattern.

Figure 1.4 shows as example a two-dimensional cut through the calculated beam pattern A_T of the IRAM 15-m telescope at $\lambda = 3\text{ mm}$, once without taper (i.e. for $\Omega_R(\vec{x}) \equiv 1$), and for a -10 dB edge taper, i.e. when the weighting of the wavefront at the edge of the aperture is $1/10$ of that at the center (see Figure 1.3). As seen from the figure, the taper preserves the global structure of the non-tapered beam pattern, i.e. the main beam and side lobes, but changes the width of the beam (BW: Θ_b), the position of the first null (Θ_{nb}), and the level of the side lobes. The effect of the taper depends on the steepness of the main reflector used in the telescope, as shown in Figure 1.5. The influence of several taper forms is given in Table 1.1 [Christiansen and Hogbom 1969].

The complete telescope, i.e. the optics combined with the receiver, has a beam pattern $A_T(\vec{u})$ (in optics called point-spread-function) with which we observe point-like or extended objects in the sky

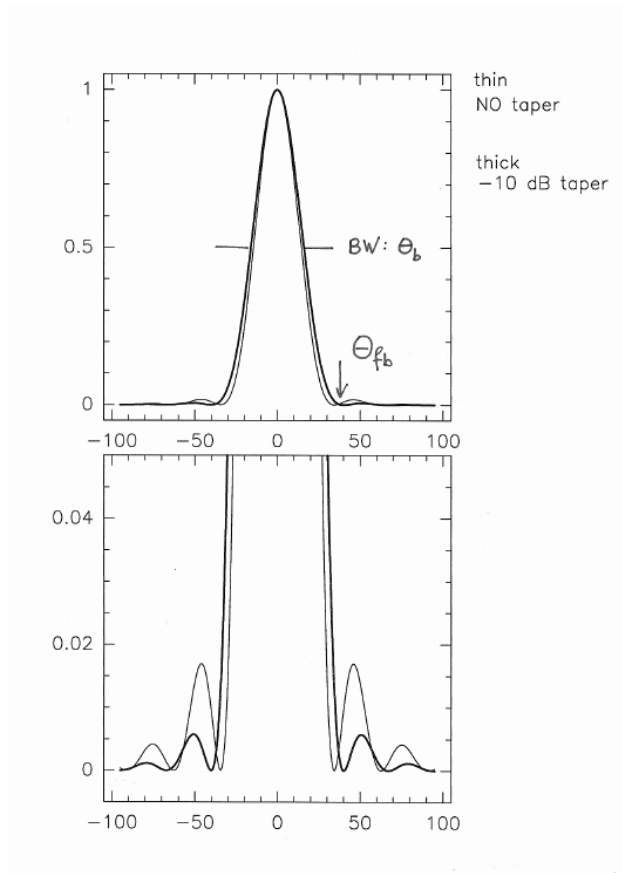


Figure 1.4: The figure shows the calculated beam pattern of the IRAM 15-m telescope at $\lambda = 3$ mm without taper, and for a -10dB edge taper. The horizontal scale is in arcseconds, the vertical scale is normalized power.

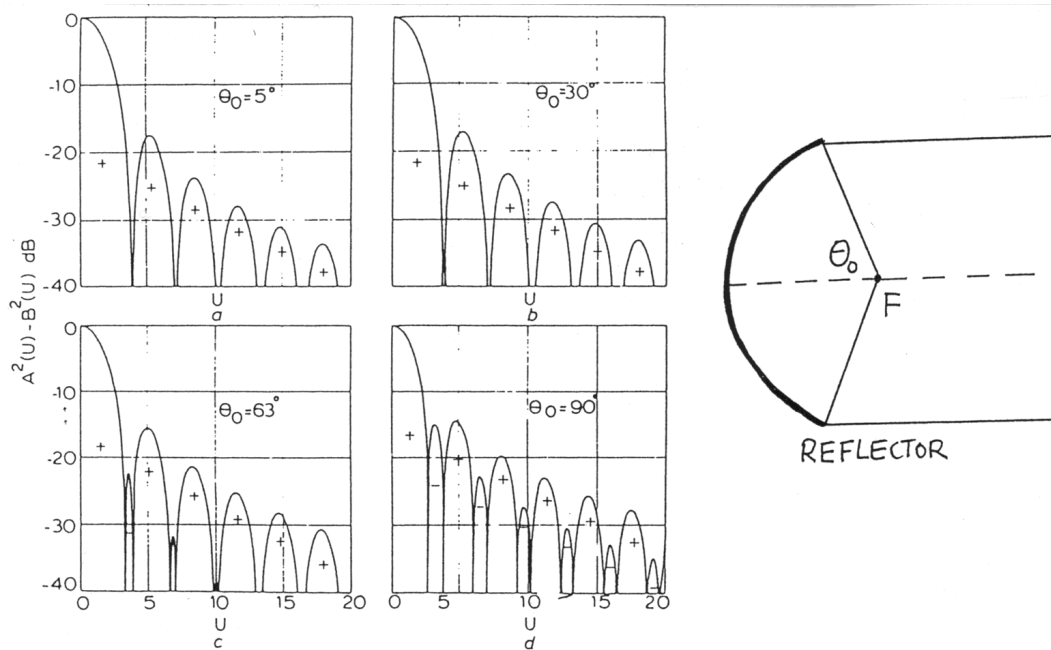


Figure 1.5: Illustration of the tapered beam pattern for telescopes using parabolic main reflectors of different steepness, expressed by the opening angle θ_o . IRAM 30-m and 15-m telescopes: $\theta_o \approx 63^\circ$, optical telescopes: $\theta_o \approx 5^\circ$. From [Minnet & Thomas 1968], Copyright: © 1968 IEE, with kind permission from IEE Publishing Department.

p	K	Θ_b (radian)	Θ_{fb} (radian)	First sidelobe (dB)	Aperture Efficiency
0	0	$1.02 \lambda/\mathcal{D}$	$1.22 \lambda/\mathcal{D}$	17.6	1.00
1	0	$1.27 \lambda/\mathcal{D}$	$1.62 \lambda/\mathcal{D}$	24.7	0.75
2	0	$1.47 \lambda/\mathcal{D}$	$2.03 \lambda/\mathcal{D}$	30.7	0.55
1	0.25	$1.17 \lambda/\mathcal{D}$	$1.49 \lambda/\mathcal{D}$	23.7	0.87
2	0.25	$1.23 \lambda/\mathcal{D}$	$1.68 \lambda/\mathcal{D}$	32.3	0.81
1	0.5	$1.13 \lambda/\mathcal{D}$	$1.33 \lambda/\mathcal{D}$	22.0	0.92
2	0.5	$1.16 \lambda/\mathcal{D}$	$1.51 \lambda/\mathcal{D}$	26.5	0.88

Table 1.1: Beamwidths, side lobe levels, and maximum aperture efficiency (ϵ_o) for various parameters of the tapering function. Adapted from [Christiansen and Hogbom 1969]

with the intention to know their position, structural detail, and brightness distribution B_S as function of wavelength. The telescope thus provides information of the form

$$I(\vec{u}) \propto \int_{\text{Source}} A_T(\vec{u} - \vec{u}') B_S(\vec{u}') d\vec{u}' \quad (1.15)$$

If the telescope is perfect, and we know A_T , we can use the information $I(\vec{u})$ to derive the calibrated brightness distribution B_S of the source distribution.

When we point the antenna toward the sky, in essence we point the beam in the direction of observation. If, for instance, we observe a point-like source it is evident that the peak of the main beam should point exactly on the source which requires that the pointing errors ($\Delta\Theta$) of the telescope should be small in comparison to the beam width. The loss in gain is small, and acceptable, if the mispointing $\Delta\Theta < 1/10 \Theta_b$. Since modern radio telescopes use an alt-azimuth mount, this criterion says the mispointing in azimuth ($\Delta\Theta_{az}$) and elevation ($\Delta\Theta_{el}$) direction should not exceed $1/\sqrt{2}$ this value. The pointing and focus (see below) of the IRAM antennas are regularly checked during an observation, and corrected if required. The corresponding protocol of an observing session at Plateau de Bure, using 5 antennas, is shown in Figure 1.6.

1.4 The real Single-Dish Antenna

A telescope, however, is never perfect since mechanical, thermal, and wind-induced deformations of the structure occur, and the optics may be misaligned and/or have production imperfections, for one or the other reason. The resulting effect on the beam pattern is negligible if the corresponding wavefront deformations introduced by these imperfections are small compared to the wavelength of observation, generally smaller than $\sim \lambda/15$; the effect is noticeable and disturbing when the wavefront deformations are large compared to the wavelength ($\sim 1/4\lambda$ and larger). The wavefront deformations due to such imperfections may be of systematic nature, or of random nature, or both.

1.4.1 Systematic Deformations: Defocus, Coma, Astigmatism

There are three basic systematic surface/wavefront deformations (occasionally associated with pointing errors) with which the observer may be confronted, i.e. defocus, coma, and astigmatism (a transient feature on the IRAM 30-m telescope).

1. The most important systematic wavefront/beam error is due to a **defocus** of the telescope. This error is easily detected, measured, and corrected from the observation of a strong source at a number of focus settings. Figure 1.7 shows, as example, the beam pattern measured on Jupiter with the telescope being gradually defocused. Evidently, the peak power in the main beam decreases, the power in the side lobes increases, until finally the beam pattern has completely collapsed. To be on

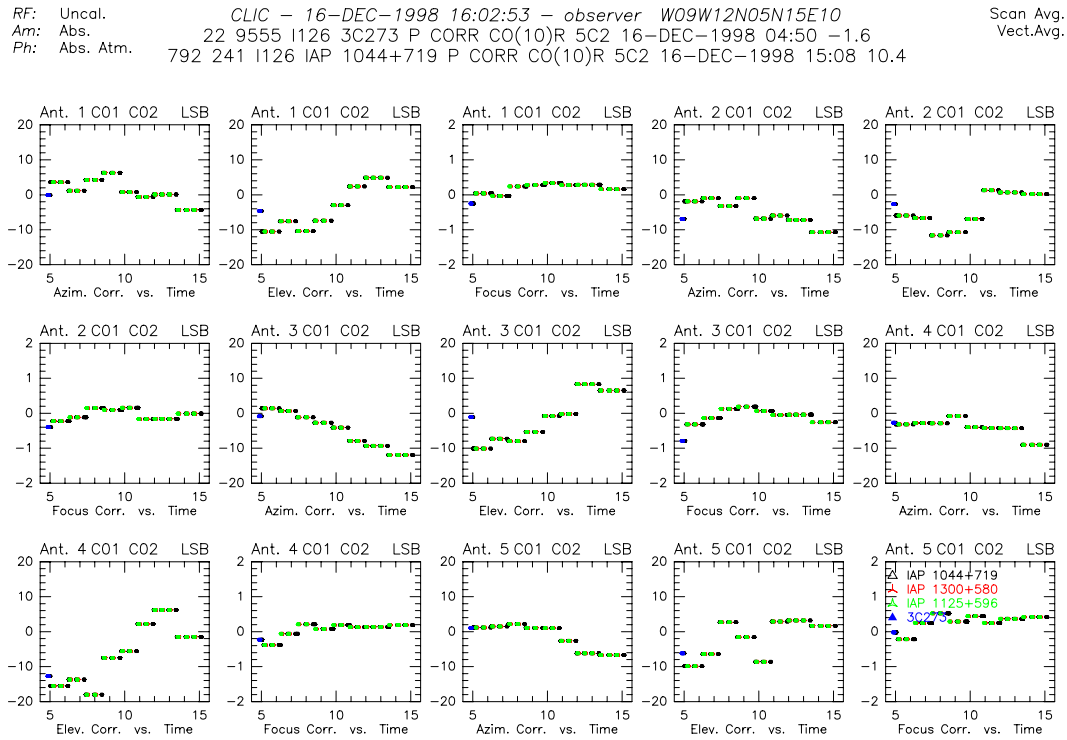


Figure 1.6: Protocol of pointing corrections applied in azimuth and elevation direction, and focus corrections; shown for 5 antennas during an observation which lasted 6 hours.

the safe side for observations, the defocus of the telescope should not exceed $\sim 1/10\lambda$. A defocus does *not* introduce a pointing error.

2. A telescope may have a **comatic** wavefront/beam error due to a misaligned subreflector, shifted perpendicular off the main reflector axis. Figure 8 shows, as example, a cross scan through a comatic beam of the IRAM 15-m telescope, especially produced by displacement of the subreflector. A comatic beam pattern introduces a pointing error. It may be useful for the observer to recognize this error, in particular if unexplained pointing errors occur in an observations. [The IRAM telescopes are regularly checked for misalignments, and correspondingly corrected.]
3. A telescope may have an **astigmatic** wavefront/beam error, usually introduced by complicated mechanical and/or thermal deformations (a transient feature on the IRAM 30-m telescope). While this beam deformation is easily recognized by the observer from the difference in beam widths measured from in-and-out-of-focus cross scans, the improvement of the telescope usually is difficult, and out of reach of the observer. A focused astigmatic beam does *not* introduce a pointing error. Figure 1.9 shows the focused beam pattern measured on a telescope which has a strong astigmatic main reflector (amplitude of the astigmatism ~ 0.5 mm).

The beam deformation of systematic wavefront deformations occurs close to the main beam, and the exact analysis should be based on diffraction calculations. A convenient description of systematic deformations uses Zernike polynomials of order (n,m) [Born & Wolf 1975]. Without going into details, the Zernike-type surface deformation $\delta_{n,m} = \alpha_{n,m} R_n(\rho) \cos(m\theta)$ [with (ρ, θ) normalized coordinates of the aperture, and R special polynomial functions] with amplitude $\alpha_{n,m}$ has a quasi rms-value $\sigma = \alpha_{n,m}/\sqrt{n+1}$ and introduces a loss in main beam intensity of

$$\epsilon_{\text{sys}}/\epsilon_o \approx \exp[-(4\pi\alpha/\lambda)^2/(n+1)] \quad (1.16)$$

For primary coma $n = 1$, for primary astigmatism $n = 2$. Although the beam deformation may be very noticeable and severe, the associated loss in main beam intensity may still be low because of the reduction

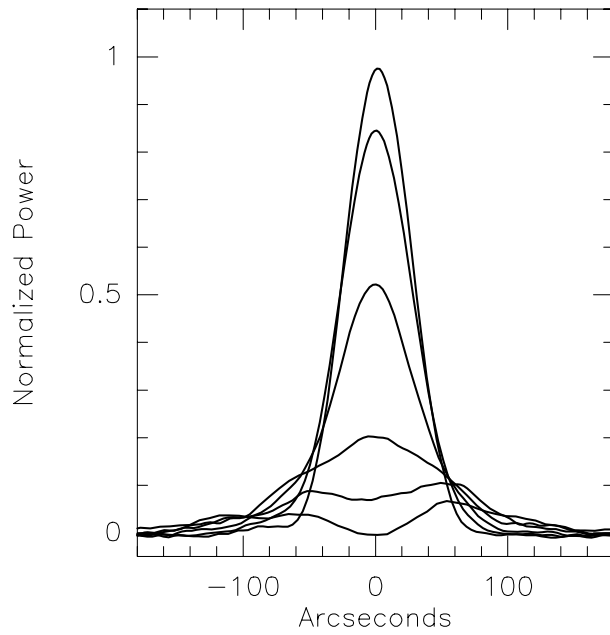


Figure 1.7: Effect on the beam pattern (scans across Jupiter) introduced by defocusing the IRAM 15-m telescope (shifts of the subreflector in steps of $\lambda/4$, $\lambda = 3$ mm).

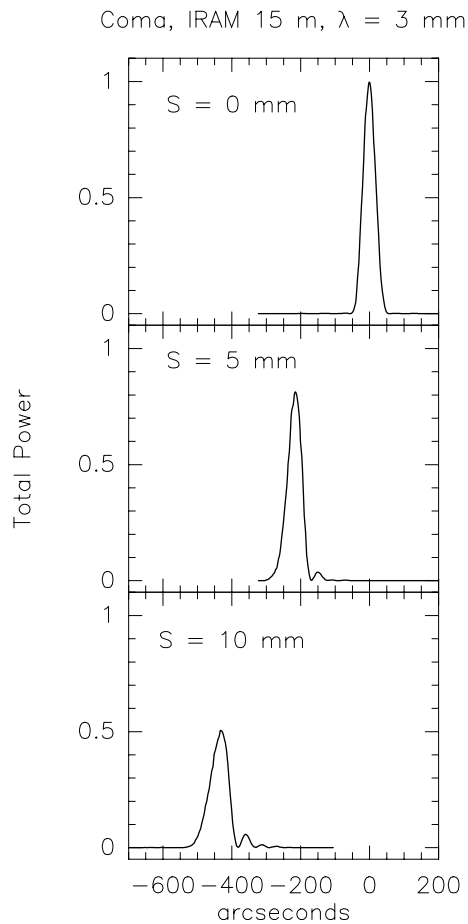


Figure 1.8: Illustration of a comatic beam (scanned in the direction of the coma) especially produced on the IRAM 15-m telescope. The shift of the subreflector is indicated by S . The beam pattern is perfect at $S = 0$. Note the shift of the beam (pointing error) when the subreflector is shifted.

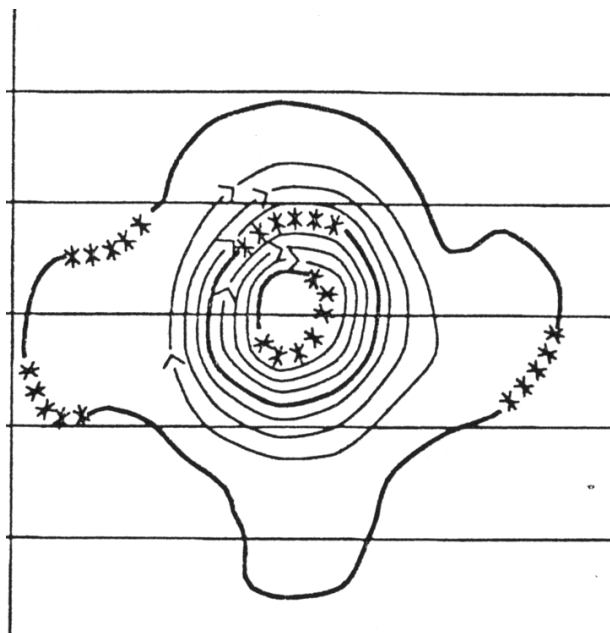


Figure 1.9: Illustration of an astigmatic beam pattern; well focused.

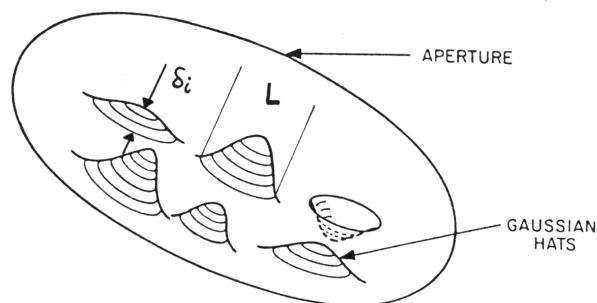


Figure 1.10: Explanation of random errors (δ) and their correlation length (L), for Gaussian hat-like deformations (example). From [Ruze 1966], Copyright: © 1966 IEEE, reprinted by permission of IEEE, Inc.

by the factor $(n+1)$.

1.4.2 Random Errors

Besides systematic surface/wavefront deformations explained above (mainly due to misalignment of the optics), there are often permanent random deformations on the optic surfaces like ripples, scratches, dents, twists, misaligned panels, etc., with spatial dimensions ranging from several wavelengths to significant areas of the aperture. These deformations introduce identical deformations of the wavefront, which cannot be expressed in mathematical form (as the Zernike polynomials used above). Nevertheless, the effect on the beam pattern of this type of deformations can be analyzed in a statistical way and from a simple expression, the RUZE equation. This equation is often used to estimate the quality of a telescope, in particular as function of wavelength. The values obtained from this equation are directly related to the aperture efficiency, and beam efficiency, of the telescope, and hence are important for radiometric measurements (see Sect.1.5).

As illustrated in Figure 1.10, there are two parameters which allow a physical-optics description of the influence of random errors, i.e. the rms-value (root mean square value) σ of the deformations, and their correlation length L .

Random errors occur primarily on the main reflector; the other optical components of the telescope (subreflector, Nasmyth mirror, lenses, polarizers) are relatively small and can be manufactured with good precision. In order to explain the rms-value σ , we assume that the reflector aperture is divided into *many* elements ($i = 1, 2, \dots, N$), and that for each element $[i]$ the deformation $\delta(i)$ of the reflector is known with

respect to a smooth mean surface. The rms-value of these random surface deformations is

$$\sigma = \sqrt{\sum_{i=1,N} \delta(i)^2 / N} \quad (1.17)$$

The surface deformations $\delta(i)$ introduce corresponding wavefront deformations $\varphi(i)$, approximately two times larger than the mechanical deformations δ in case we are dealing with reflective optics. The rms-value σ_φ of the corresponding phase deformations of the wavefront is

$$\sigma_\varphi = 2 k R \sigma \quad (1.18)$$

again with $k = 2\pi/\lambda$, and $R \approx 0.8$ a factor which takes into account the steepness of the parabolic main reflector [Greve & Hooghoudt 1981].

A description of the wavefront deformation by the rms-value σ_φ is incomplete since the value does not contain information on the structure of the deformations, for instance whether they consist of many dents at one part of the aperture, or many scratches at another part. A useful physical-optics description requires also a knowledge of the correlation length L of the deformations. L is a number ($L \leq \mathcal{D}$) which quantifies the extent over which the randomness of the deformations does not change. For example, the deformations of a main reflector constructed from many individual panels, which may be misaligned, often has a random error correlation length typical of the panel size, but also a correlation length of 1/3 to 1/5 of the panel size due to inaccuracies in the fabrication of the individual panels. A typical example is the 30-m telescope [Greve et al. 1998].

When knowing, by one or the other method, the rms-value σ_φ and the correlation length L , it is possible to express the resulting beam shape in an analytic form which describes well the real situation. The beam pattern $\mathcal{F}(\times)$ of a wavefront with random deformations (σ_φ, L) [the telescope may actually have several random error distributions] consists of the degraded diffraction beam $\mathcal{F}_c(\times)$ and the error beam $\mathcal{F}_e(\times)$ such that

$$\mathcal{F}(\Theta) = \mathcal{F}_c(\Theta) + \mathcal{F}_e(\Theta) \quad (1.19)$$

with

$$\mathcal{F}_c(\Theta) = \exp[-(\sigma_\varphi)^2] A_T(\Theta) \quad (1.20)$$

where $A_T(\Theta)$ is the tapered beam pattern (Eq.1.14), and

$$\mathcal{F}_e(\Theta) = a \exp[-(\pi\Theta L/\lambda)^2] \quad (1.21)$$

where

$$a = (L/\mathcal{D})^2 [1 - \exp(-\sigma_\varphi^2)] / \epsilon_o \quad (1.22)$$

In these equations, \mathcal{D} is the diameter of the telescope aperture, λ the wavelength of observation, Θ the angular distance from the beam axis, and ϵ_o the aperture efficiency of the perfect telescope. In the formalism used here the beam is circular symmetric. The error beam $\mathcal{F}_e(\times)$ has a Gaussian profile of width FWHP) $\Theta_e = 0.53\lambda/L$ [radians], i.e. the smaller the correlation length (the finer the irregular structure), the broader is the beam width Θ_e . The random errors of panel surface deformation and panel alignment errors may have large error beams (up to arcminutes in extent) which can pick up radiation from a large area outside the actual source. A knowledge of the structure and of the level of the error beam(s) is therefore important when mapping a source and making absolute power measurements. Figure 1.11 shows the diffraction beam and the combined error patterns measured on the 30-m telescope at various wavelengths. The smaller the wavelength of observation, the smaller is the power received in the main beam and the larger the power received in the error beam. Due to its particular mechanical construction, this telescope has three error beams [Greve et al. 1998].

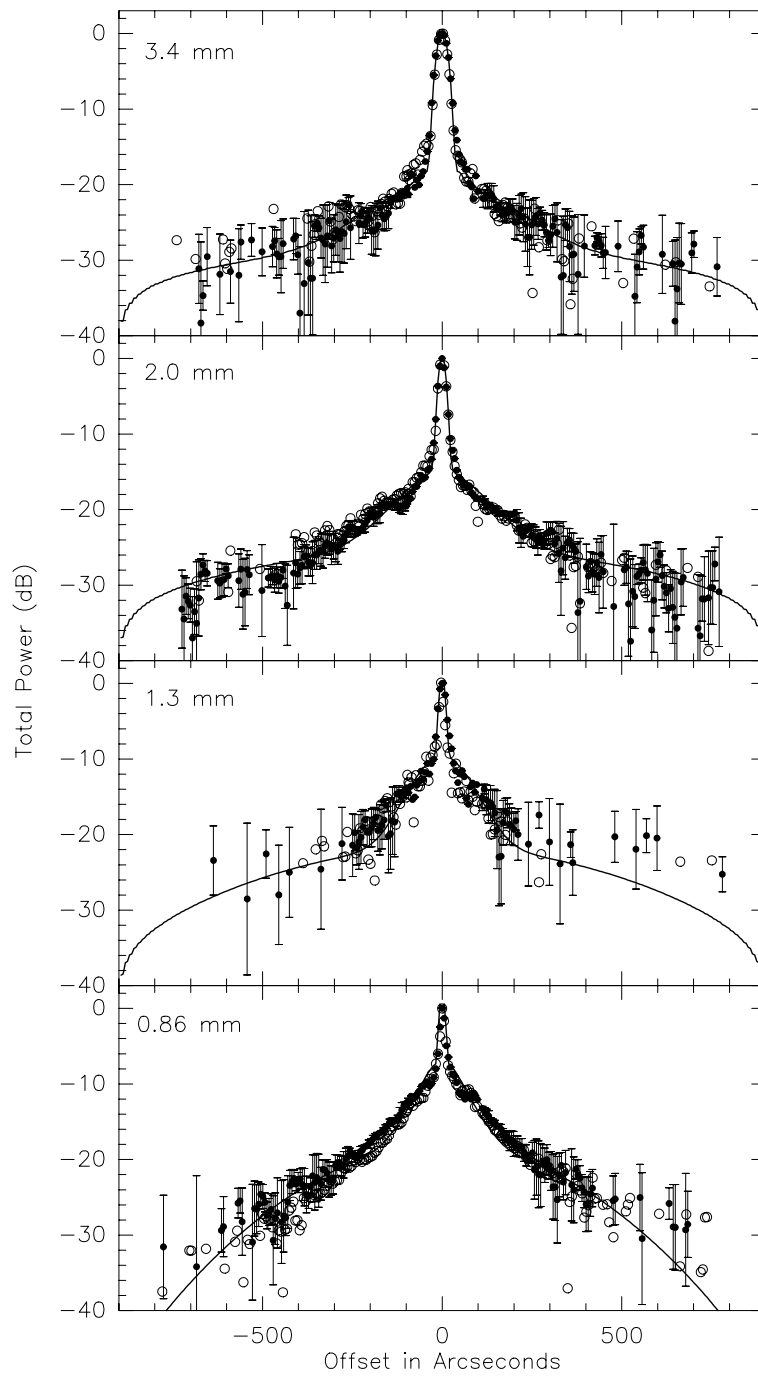


Figure 1.11: Beam pattern measured on the IRAM 30-m telescope. The beam consists of the diffraction beam (\approx main beam) and a combined, extended error beam (solid line).

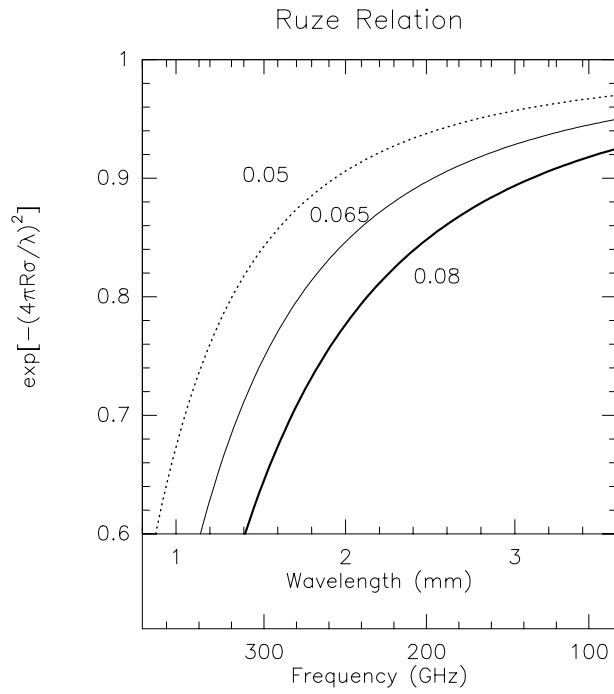


Figure 1.12: Illustration of the RUZE relation $\exp[-(4\pi R\sigma/\lambda)^2]$ as function of wavelength (frequency) and values $R\sigma$ as indicated (mm).

1.5 Radiometric Relations

The imperfections of a telescope, either due to systematic or random errors, produce beam deformations, a loss in gain, and focus and pointing errors. These effects must be taken into account when mapping and measuring a source. Information on the beam pattern obtained from a map (for instance holography map) of a strong point-like source; information on the sensitivity [Jy/K] and calibration of the telescope is obtained from absolute power measurements of, for instance, the planets, of which the brightness temperatures are quite well known. This information is usually collected by the observatory staff, and provided to the observer (30-m Telescope Manual; observation protocols of Plateau de Bure measurements).

We summarize the influence of random deformations, at least as far as the main beam is concerned, since for this case the RUZE equation provides sufficient precision for an understanding of the telescope behaviour; also for the astronomer observer without going into complicated radio optics detail. This relation appears in the expression of the diffraction beam \mathcal{F}_c (see Eq.1.20) and shows clearly the fact that the degradation of the telescope, in particular for power measurements, increases exponentially with wavelength.

Aperture Efficiency:

$$\epsilon_{\text{ap}} = \epsilon_o \exp[-\sigma_\varphi] = \epsilon_o \exp[-(4\pi R\sigma/\lambda)^2]$$

Antenna Gain:

$$S/T_A^* = 2(k/A)\eta_f/\epsilon_{\text{ap}} \approx 2(k/A) \exp[+(4\sigma R/\lambda)^2]/\epsilon_{\text{ap}} \quad [\text{Jy/K}]$$

Beam Efficiency:

$$\begin{aligned} \eta_b &= 0.8899 [\Theta_b/(\lambda/D)]^2/\epsilon_{\text{ap}} \\ \Theta_b &= \alpha\lambda/D, \quad 1 \leq \alpha \leq 1.2 \quad [\text{radians}] \\ \eta_b &\approx 1.2 \epsilon_o \exp[-(4\pi R\sigma/\lambda)^2] \end{aligned}$$

The quantities in these expressions are ϵ_o : aperture efficiency of the perfect telescope (usually of the order of $\sim 75 - 90\%$; see Table 1.1); ϵ_{ap} : effective aperture efficiency at the wavelength λ , including all wavefront / telescope deformations; σ : rms-value of the telescope optics deformations; $R \approx 0.8$: reduction factor for a steep main reflector ($N = F/D \approx 0.3$); S : flux density of a point source [Jy]; T_A^* : measured antenna temperature [K] (see also Chapter 10); A : geometric surface area of the telescope [m^2]; η_f : forward efficiency, measured at the telescope for instance from a sky dip; Θ_b : main beam width (FWHP).

Chapter 2

Millimetre Interferometers

Stéphane Guilloteau

guillote@iram.fr

IRAM, 300 rue de la Piscine, F-38406 Saint Martin d'Hères, France

This lecture presents the principle of the heterodyne interferometer. An heterodyne interferometer is composed of **antennas** (described in A.Greve lecture, Chapter 1), **receivers** (described in B.Lazareff lecture, Chapter 5), a **correlator** (described in H.Wiesemeyer lecture, Chapter 6) and an awful lot of cables and connections. This lecture only describes the basic principles; a more complete description, including subtleties due to multiple frequency conversions and digital delay lines, is given in R.Lucas lecture, Chapter 7.

2.1 Basic principle

The **antenna** produces a Voltage proportional to the linear superposition of the incident electric field pattern. For a simple monochromatic case:

$$U(t) = E \cos(2\pi\nu t + \Phi) \tag{2.1}$$

In the **receiver**, a **mixer** superimposes the field generated by a **local oscillator** to the antenna output.

$$U_{LO}(t) = Q \cos(2\pi\nu_{LO} t + \Phi_{LO}) \tag{2.2}$$

The mixer is a non-linear element (such as a diode) whose output is

$$I(t) = a_0 + a_1(U(t) + U_{LO}(t)) + a_2(U(t) + U_{LO}(t))^2 + a_3(U(t) + U_{LO}(t))^3 + \dots \tag{2.3}$$

The second order (quadratic) term of Eq.2.3 can be expressed as

$$\begin{aligned}
 I(t) = & \dots \\
 & + a_2 E^2 \cos^2(2\pi\nu t + \Phi) \\
 & + 2a_2 EQ \cos(2\pi\nu t + \Phi) \cos(2\pi\nu_{LO} t + \Phi_{LO}) \\
 & + a_2 Q^2 \cos^2(2\pi\nu_{LO} t + \Phi_{LO}) \\
 & + \dots
 \end{aligned} \tag{2.4}$$

Developping the product of the two cosine functions, we obtain

$$\begin{aligned}
 I(t) = & \dots \\
 & + a_2 EQ \cos(2\pi(\nu + \nu_{LO})t + \Phi + \Phi_{LO}) \\
 & + a_2 EQ \cos(2\pi(\nu - \nu_{LO})t + \Phi - \Phi_{LO}) \\
 & + \dots
 \end{aligned} \tag{2.5}$$

There are obviously other terms in $2\nu_{LO}$, 2ν , $3\nu_{LO} \pm \nu$, etc... in the above equation, as well as terms at very different frequencies like ν , 3ν , etc...

By inserting a filter at the output of the `mixer`, we can select only the term such that

$$\nu_{IF} - \Delta\nu/2 \leq |\nu - \nu_{LO}| \leq \nu_{IF} + \Delta\nu/2 \tag{2.6}$$

where ν_{IF} , the so-called *Intermediate Frequency*, is a frequency which is significantly different from than the original signal frequency ν (which is often called the *Radio Frequency* ν_{RF}).

Hence, after mixing and filtering, the output of the `receiver` is

$$I(t) \propto EQ \cos(2\pi(\nu - \nu_{LO})t + \Phi - \Phi_{LO}) \tag{2.7}$$

or

$$I(t) \propto EQ \cos(2\pi(\nu_{LO} - \nu)t - \Phi + \Phi_{LO}) \tag{2.8}$$

i.e.

- changed in frequency: $\nu \rightarrow \nu - \nu_{LO}$ or $\nu \rightarrow \nu_{LO} - \nu$
- proportional to the original electric field of the incident wave: $\propto E$
- with a phase relation with this electric field: $\Phi \rightarrow \Phi - \Phi_{LO}$ or $\Phi \rightarrow \Phi_{LO} - \Phi$
- proportional to the `local oscillator` voltage: $\propto Q$

The frequency change, usually towards a lower frequency, allows to select ν_{IF} such that amplifiers and transport elements are easily available for further processing. The mixer described above accepts simultaneously frequencies which are (see Fig.2.1)

- higher than the `local oscillator` frequency.
This is called Upper Side Band (USB) reception
- lower than the `local oscillator` frequency.
This is called Lower Side Band (LSB) reception

and cannot *a priori* distinguish between them. This is called Double Side Band (DSB) reception. Some receivers are actually insensitive to one of the frequency range, either because a filter has been placed at the receiver input, or because their response is very strongly frequency dependent. Such receivers are called Single Side Band (SSB) receivers.

An important property of the receiving system expressed by Eq.2.8 is that the sign of the phase is changed for LSB conversion. This property can be easily retrieved recognizing that the **Frequency** ν is the **time derivative of the Phase** Φ . Assume the phase varies linearly with time:

$$\begin{aligned}
 \Phi(t) &= 2\pi n t \\
 n &= \frac{1}{2\pi} \frac{d\Phi}{dt}
 \end{aligned} \tag{2.9}$$

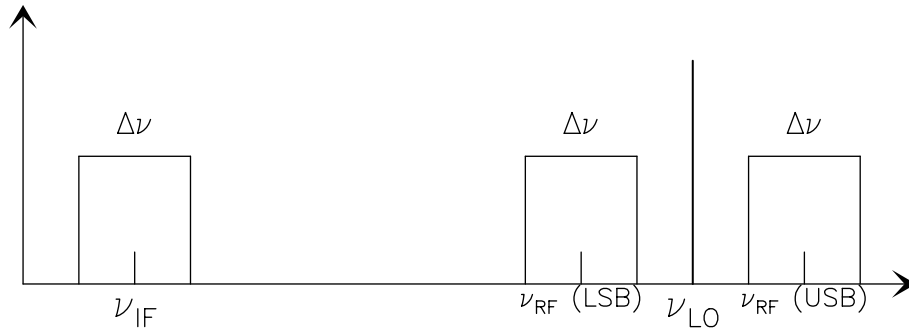


Figure 2.1: Relation between the IF, RF and local oscillator frequencies in an heterodyne system

In this case, the signal

$$\begin{aligned} I(t) &\propto \cos(2\pi\nu t + \Phi(t)) \\ &\propto \cos(2\pi(\nu + n)t) \end{aligned} \quad (2.10)$$

is just another monochromatic signal with slightly shifted frequency.

2.2 The Heterodyne Interferometer

Figure 2.2 is a schematic illustration of a 2-antenna heterodyne interferometer.

Let us forget the frequency conversion for some time, i.e. assume $\nu_{IF} = \nu_{RF} \dots$

The input (amplified) signals from 2 elements of the interferometer are processed by a **correlator**, which is just a voltage multiplier followed by a time integrator. With one incident plane wave, the output $r(t)$ is

$$r(t) = \langle v_1 \cos(2\pi\nu(t - \tau_g(t))) v_2 \cos(2\pi\nu t) \rangle = v_1 v_2 \cos(2\pi\nu\tau_g(t)) \quad (2.11)$$

where τ_g is obviously the geometrical delay,

$$\tau_g(t) = (\mathbf{b} \cdot \mathbf{s})/c \quad (2.12)$$

The derivation assumes that v_1, v_2 and $\tau_g(t)$ varies slowly compared to the averaging timescale, which should nevertheless be long enough compared to frequency ν .

As τ_g varies slowly because of Earth rotation, $r(t)$ oscillates as a cosine function, and is thus called the *fringe pattern*. As we had shown before that v_1 and v_2 were proportional to the electric field of the incident wave, the correlator output (fringe pattern) is thus proportional to the power (intensity) of the wave.

2.2.1 Source Size Effects

The signal power received from a sky area $d\Omega$ in direction \mathbf{s} is (see Fig.2.3 for notations) $A(\mathbf{s})I(\mathbf{s})d\Omega d\nu$ over bandwidth $d\nu$, where $A(\mathbf{s})$ is the antenna power pattern (assumed identical for both elements, more precisely $A(\mathbf{s}) = A_i(\mathbf{s})A_j(\mathbf{s})$ with A_i the voltage pattern of antenna i , and $I(\mathbf{s})$ is the sky brightness distribution

$$dr = A(\mathbf{s})I(\mathbf{s})d\Omega d\nu \cos(2\pi\nu\tau_g) \quad (2.13)$$

$$r = d\nu \int_{\text{Sky}} A(\mathbf{s})I(\mathbf{s}) \cos(2\pi\nu\mathbf{b} \cdot \mathbf{s}/c) d\Omega \quad (2.14)$$

Two implicit assumptions have been made in deriving Eq.2.14. We assumed incident plane waves, which implies that the source must be in the far field of the interferometer. We used a linear superposition of the

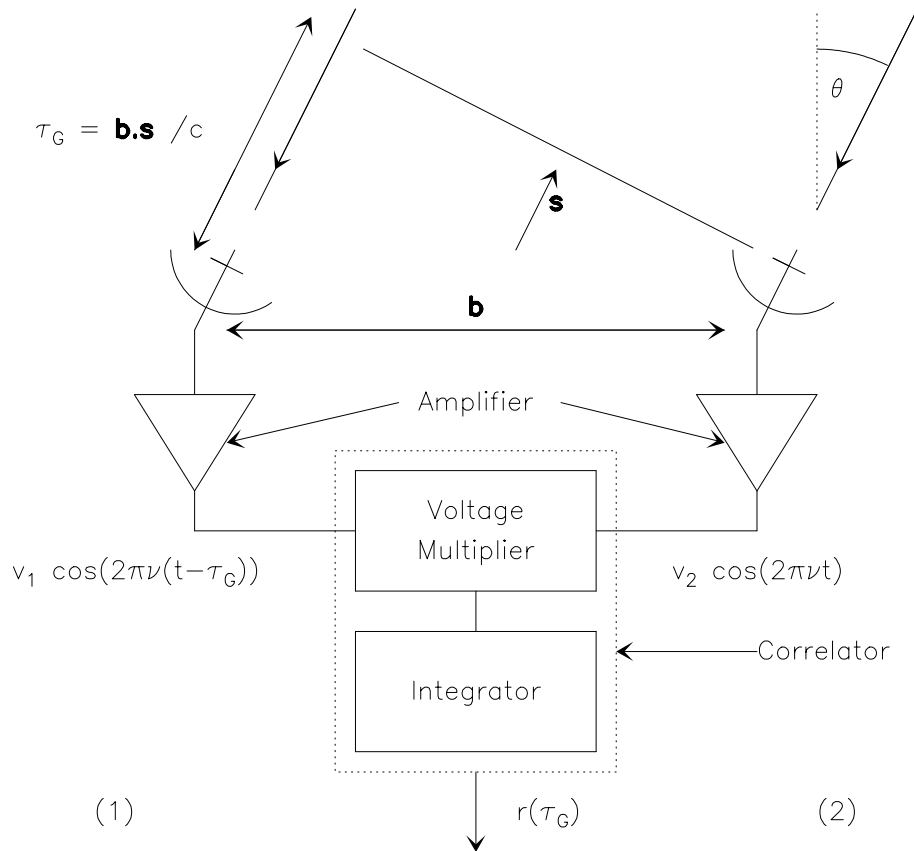
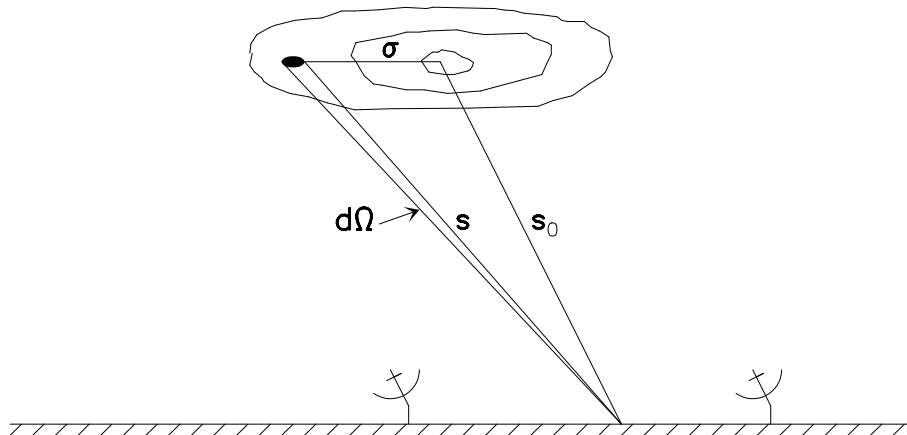


Figure 2.2: Schematic Diagram of a two-element interferometer

Figure 2.3: Position vectors used for the expression of the interferometer response to an extended source, schematically represented by the iso-contours of the sky brightness distribution. \mathbf{s}_0 is the tracking center of the interferometer, \mathbf{s} the source vector, and $d\Omega$ a solid angle around the source.

incident waves, which implies that the source must be spatially incoherent. These assumptions are quite valid for most astronomical sources, but may be violated under special circumstances. For example VLBI observations of solar system objects would violate the first assumption, while observations of celestial masers could violate the second one (if they were coherent as laboratory lasers, but observations have revealed astronomical masers are in fact incoherent).

When the interferometer is tracking a source in direction \mathbf{s}_o , with $\mathbf{s} = \mathbf{s}_o + \boldsymbol{\sigma}$

$$\begin{aligned} r &= d\nu \cos(2\pi\nu\mathbf{b}\cdot\mathbf{s}_o/c) \int_{S_{ky}} A(\boldsymbol{\sigma})I(\boldsymbol{\sigma}) \cos(2\pi\nu\mathbf{b}\cdot\boldsymbol{\sigma}/c)d\Omega \\ &- d\nu\sin(2\pi\nu\mathbf{b}\cdot\mathbf{s}_o/c) \int_{S_{ky}} A(\boldsymbol{\sigma})I(\boldsymbol{\sigma}) \sin(2\pi\nu\mathbf{b}\cdot\boldsymbol{\sigma}/c)d\Omega \end{aligned} \quad (2.15)$$

We define the *Complex Visibility*

$$V = |V|e^{i\Phi_V} = \int_{S_{ky}} A(\boldsymbol{\sigma})I(\boldsymbol{\sigma})e^{(-2i\pi\nu\mathbf{b}\cdot\boldsymbol{\sigma}/c)}d\Omega \quad (2.16)$$

which resembles a Fourier Transform...

We thus have

$$\begin{aligned} r &= d\nu (\cos(2\pi\nu\mathbf{b}\cdot\mathbf{s}_o/c)|V| \cos(\Phi_V) - \sin(2\pi\nu\mathbf{b}\cdot\mathbf{s}_o/c)|V| \sin(\Phi_V)) \\ &= d\nu|V| \cos(2\pi\nu\tau_G - \Phi_V) \end{aligned} \quad (2.17)$$

i.e. the correlator output is proportional to the amplitude of the visibility, and contains a phase relation with the visibility.

2.2.2 Finite Bandwidth

Integrating over $d\nu$,

$$R = \frac{1}{\Delta\nu} \int_{\nu_0-\Delta\nu/2}^{\nu_0+\Delta\nu/2} |V| \cos(2\pi\nu\tau_G - \Phi_V)d\nu \quad (2.18)$$

Using $\nu = \nu_0 + n$

$$R = \frac{1}{\Delta\nu} \int_{-\Delta\nu/2}^{\Delta\nu/2} |V| \cos(2\pi\nu_0\tau_G - \Phi_V + 2\pi n\tau_g)dn \quad (2.19)$$

$$\begin{aligned} &= \frac{1}{\Delta\nu} \left[\int_{-\Delta\nu/2}^{\Delta\nu/2} |V| \cos(2\pi\nu_0\tau_G - \Phi_V) \cos(2\pi n\tau_g)dn \right. \\ &\quad \left. - \int_{-\Delta\nu/2}^{\Delta\nu/2} |V| \sin(2\pi\nu_0\tau_G - \Phi_V) \sin(2\pi n\tau_g)dn \right] \end{aligned} \quad (2.20)$$

$$\begin{aligned} &= \frac{1}{\Delta\nu} |V| \cos(2\pi\nu_0\tau_G - \Phi_V) [\sin(2\pi n\tau_g)]_{-\Delta\nu/2}^{\Delta\nu/2} \frac{1}{2\pi\tau_g} \\ &\quad + \frac{1}{\Delta\nu} |V| \sin(2\pi\nu_0\tau_G - \Phi_V) [\cos(2\pi n\tau_g)]_{-\Delta\nu/2}^{\Delta\nu/2} \frac{1}{2\pi\tau_g} \end{aligned} \quad (2.21)$$

$$= |V| \cos(2\pi\nu_0\tau_G - \Phi_V) \frac{\sin(\pi\Delta\nu\tau_g)}{\pi\Delta\nu\tau_g} \quad (2.22)$$

The fringe visibility is attenuated by a $\sin(x)/x$ envelope, called the bandwidth pattern, which falls off rapidly. A 1% loss in visibility is obtained for $|\Delta\nu\tau_g| \simeq 0.078$, or with $\Delta\nu = 500\text{MHz}$ and a baseline length $b = 100\text{m}$, when the zenith angle θ (defined in Fig.2.3) is 2 arcmin only. Thus, the ability to track a source for a significant hour angle coverage requires proper compensation of the geometrical delay when a finite bandwidth is desired.

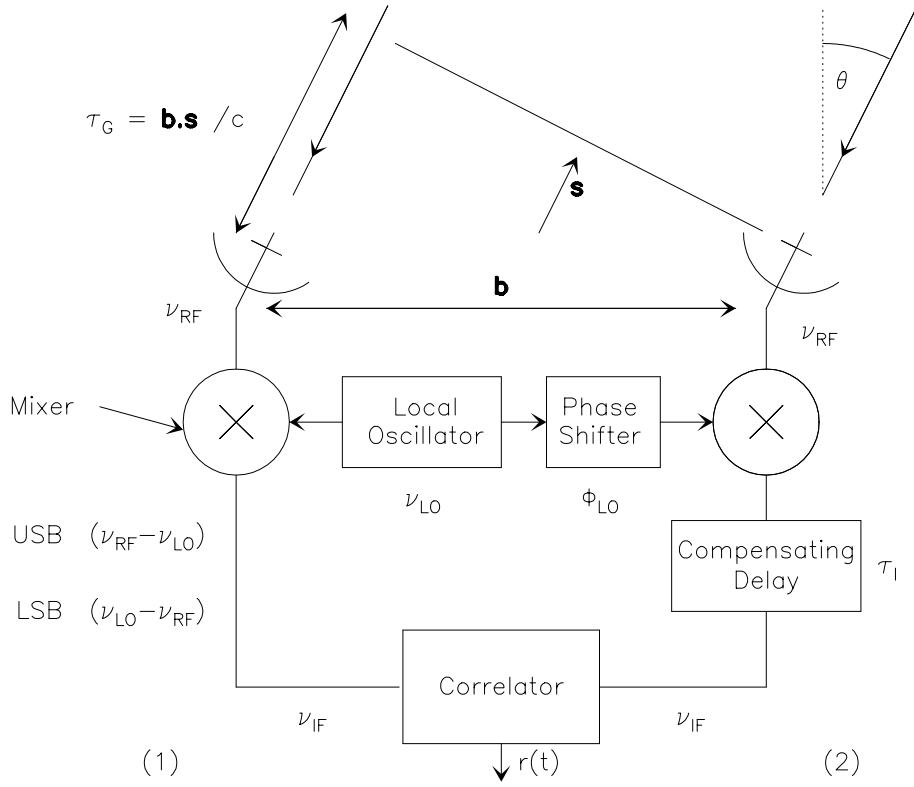


Figure 2.4: 2-element heterodyne interferometer with delay tracking after frequency conversion

2.3 Delay Tracking and Frequency Conversion

To compensate for the geometrical delay variations, delay lines with mirrors (as in optics...) would be completely impractical given the required size of the mirrors. The compensating delay is thus performed electronically after one (or several) frequency conversion(s), as illustrated in Fig.2.4. This can be implemented either by switching cables with different lengths, or in a more sophisticated way, by using shift memories after digital sampling of the signal in the correlator. Apart for a few details (see R.Lucas lecture, Chapter 7), the principle remains identical.

In the case presented in Fig.2.4, for USB conversion, the phase changes of the input signals from antenna 1 and 2 before reaching the correlator are respectively

$$\Phi_1 = 2\pi\nu\tau_G = 2\pi(\nu_{LO} + \nu_{IF})\tau_G \quad (2.23)$$

$$\Phi_2 = 2\pi\nu\tau_I + \Phi_{LO} \quad (2.24)$$

Introducing $\Delta\tau = \tau_g - \tau_I$ as the delay tracking error, the correlator output is

$$\begin{aligned} r &= A_o|V| \cos(\Phi_1 - \Phi_2 - \Phi_V) \\ USB \quad r &= A_o|V| \cos(2\pi(\nu_{LO}\tau_G + \nu_{IF}\Delta\tau) - \Phi_V - \Phi_{LO}) \\ LSB \quad r &= A_o|V| \cos(2\pi(\nu_{LO}\tau_G - \nu_{IF}\Delta\tau) - \Phi_V - \Phi_{LO}) \end{aligned} \quad (2.25)$$

When the two sidebands are superposed, we can just sum the USB and LSB outputs, which yields (after usual re-arrangement of the cosine expressions)

$$DSB \quad r = 2A_o|V| \cos(2\pi(\nu_{LO}\tau_G - \Phi_V - \Phi_{LO})) \cos(2\pi\nu_{IF}\Delta\tau) \quad (2.26)$$

This shows that the amplitude is modulated by the delay tracking error. The tolerance can be exceedingly small. For example, at Plateau de Bure, the IF frequency ν_{IF} is 3 GHz, and a 1 % loss is obtained as soon as the delay tracking error would be 7.5 picoseconds, i.e. a geometrical shift of 2.2 mm only. Due

to Earth rotation, the geometrical delay changes by such an amount in 0.1 s for a 300 m baseline. Hence, delay tracking would have to be done quite fast to avoid sensitivity losses. To avoid this problem, it is common to use sideband separation. The delay tracking error should then be kept small compared to the bandwidth of each spectral channel, $\Delta\tau_G \ll 1/\Delta\nu$, and the delay can then be adjusted much less frequently.

2.4 Fringe Stopping and Complex Correlator

With the Earth rotation, the cosine term of Eq.2.22 modulates the correlator output quasi-sinusoidally with a *natural fringe rate* of

$$\nu_{LO}d\tau_g/dt \simeq \Omega_{earth}b\nu_{LO}/c \quad (2.27)$$

which is of order of 10 Hz for $b=300$ m baselines and $\nu_{LO} = 100$ GHz. Note that the fringe rate only depends on the effective angular resolution ($b\nu_{LO}/c \simeq b/\lambda$ is the angular resolution, $2''$ in the above example).

The fringe rate is somewhat too high for simple digital sampling of the visibility. An exception is VLBI (because there is no other choice), although the resolutions are < 1 mas. The usual technique is to modulate the phase of the local oscillator Φ_{LO} such that $\Phi_{LO}(t) = 2\pi\nu_{LO}\tau_g(t)$ at any given time. Then Eq.2.25 is reduced to

$$r_r = A_o|V|\cos(\pm 2\pi\nu_{IF}\Delta\tau - \Phi_V) \quad (2.28)$$

(with the + sign for USB conversion, and the – sign for LSB conversion), is a slowly varying output, which would be constant for a point source at the reference position (or delay tracking center). This process is called *Fringe Stopping*, since it stops the *fringe pattern* modulation. After fringe stopping, we can no longer measure the amplitude $|V|$ and the phase Φ_V separately, since r_r is now a constant for a point source. A modulation of the delay tracking could be used to separate $|V|$ and Φ_V . Instead, it is more convenient and effective to use a second correlator, with one signal phase shifted by $\pi/2$. Its output is

$$r_i = A_o|V|\sin(\pm 2\pi\nu_{IF}\Delta\tau - \Phi_V) \quad (2.29)$$

With both correlators, we measure directly the real r_r and imaginary r_i parts of the complex visibility r . The device is thus called a “**complex**” correlator.

Note: From Eq.2.28, a delay tracking error $\Delta\tau$ appears as a phase slope as a function of frequency, with

$$\Phi(\nu_{IF}) = \pm 2\pi\nu_{IF}\Delta\tau \quad (2.30)$$

2.5 Fourier Transform and Related Approximations

The *Complex Visibility* is

$$V = |V|e^{i\Phi_V} = \int_{S_{ky}} A(\boldsymbol{\sigma})I(\boldsymbol{\sigma})e^{(-2i\pi\nu\mathbf{b}\cdot\boldsymbol{\sigma}/c)}d\Omega \quad (2.31)$$

Let (u, v, w) be the coordinate of the baseline vector, in units of the observing wavelength ν , in a frame of the delay tracking vector \mathbf{s}_0 , with w along \mathbf{s}_0 . (x, y, z) are the coordinates of the source vector \mathbf{s} in this frame. Then

$$\begin{aligned} \nu\mathbf{b}\cdot\mathbf{s}/c &= ux + vy + wz \\ \nu\mathbf{b}\cdot\mathbf{s}_0/c &= w \\ z &= \sqrt{1 - x^2 - y^2} \\ \text{and } d\Omega &= \frac{dxdy}{z} = \frac{dxdy}{\sqrt{1 - x^2 - y^2}} \end{aligned} \quad (2.32)$$

Thus,

$$V(u, v, w) = \int_{-\infty}^{+\infty} \int_{-\infty}^{+\infty} A(x, y) I(x, y) e^{-2i\pi(ux+vy+w(\sqrt{1-x^2-y^2}-1))} \frac{dxdy}{\sqrt{1-x^2-y^2}} \quad (2.33)$$

with $I(x, y) = 0$ when $x^2 + y^2 \geq 1$.

If (x, y) are sufficiently small, we can make the approximation

$$(\sqrt{1-x^2-y^2}-1)w \simeq \frac{1}{2}(x^2+y^2)w \simeq 0 \quad (2.34)$$

and Eq.2.33 becomes

$$V(u, v) = \iint A'(x, y) I(x, y) e^{-2i\pi(ux+vy)} e^{-i\pi(x^2+y^2)w} dxdy \quad (2.35)$$

$$\text{with } A'(x, y) = \frac{A(x, y)}{\sqrt{1-x^2-y^2}} \quad (2.36)$$

i.e. basically a 2-D Fourier Transform of AI , but with a phase error term $\pi(x^2 + y^2)w$. Hence, on limited field of views, the relationship between the sky brightness (multiplied by the antenna power pattern) and the visibility reduces to a simple 2-D Fourier transform.

There are other approximations related to field of view limitations. Let us quantify these approximations.

- **2-D Fourier Transform**

We can further neglect the phase error term in Eq.2.36, if the condition

$$|\pi(x^2 + y^2)w| \ll 1 \quad (2.37)$$

is fulfilled. Now, note that

$$w < w_{\max} \simeq \frac{b_{\max}}{\lambda} \simeq \frac{1}{\theta_s} \quad (2.38)$$

where θ_s is the synthesized beam width. Thus, if θ_r is the field of view to be synthesized, the maximum phase error, obtained at the field edges $\theta_r/2$, is

$$\Delta\phi = \frac{\pi\theta_r^2}{4\theta_s} \quad (2.39)$$

Using $\Delta\phi < 0.1$ radian (6°) as an upper limit (note that this is the maximum phase error, i.e. the mean phase error is much smaller) result in the condition (with all angles in radian...):

$$\theta_r < \frac{1}{3}\sqrt{\theta_s} \quad (2.40)$$

- **Bandwidth Smearing**

Assume u, v are computed for the center frequency ν_0 . At frequency ν_0 , we have

$$V(u, v) \rightleftharpoons AI(x, y) \quad (2.41)$$

The similarity theorem on Fourier pairs give

$$V\left(\frac{\nu_0}{\nu}u, \frac{\nu_0}{\nu}v\right) = \left(\frac{\nu}{\nu_0}\right)^2 I\left(\frac{\nu}{\nu_0}x, \frac{\nu}{\nu_0}y\right) \quad (2.42)$$

Averaging over the bandwidth $\Delta\nu$, there is a *radial smearing* equal to

$$\sim \frac{\Delta\nu}{\nu_0} \sqrt{x^2 + y^2} \quad (2.43)$$

Config.	Resolution	Frequency (GHz)	2-D Field	0.5 GHz Bandwidth	1 Min Time Averaging	Primary Beam
Compact	5''	80 GHz	5'	80''	2'	60''
Standard	2''	80 GHz	3.5'	30''	45''	60''
Standard	2''	220 GHz	3.5'	1.5'	45''	24''
High	0.5''	230 GHz	1.7'	22''	12''	24''

Table 2.1: Field of view limitations as function of angular resolution and observing frequency for the Plateau de Bure interferometer.

and hence the constraint

$$\sqrt{x^2 + y^2} \leq 0.1 \frac{\theta_s \nu_0}{\Delta \nu} \quad (2.44)$$

if we want that smearing to be less than 10% of the synthesized beam.

- **Time Averaging**

Assume for simplicity that the interferometer observes the Celestial Pole. The baselines cover a sector of angular width $\Omega_e \Delta t$, where Ω_e is the Earth rotation speed, and Δt the integration time. The smearing is *circumferential* and of magnitude $\Omega_e \Delta t \sqrt{x^2 + y^2}$, hence the constraint

$$\sqrt{x^2 + y^2} \leq 0.1 \frac{\theta_s}{\Omega_e \Delta t} \quad (2.45)$$

For other declinations, the smearing is no longer rotational, but of similar magnitude.

To better fix the importance of such approximations, the relevant values for the Plateau de Bure interferometer are given in Table 2.1. Note that these fields of view correspond to a maximum phase error of 6° only, or to a (one dimensional) distortion of a tenth of the synthesized beam, and thus are not strict limits. In particular, atmospheric errors often results in larger errors (which are independent of the field of view, however).

2.6 Array Geometry & Baseline Measurements

The uv coverage

Using a Cartesian coordinate system (X, Y, Z) with Z towards the pole, X towards the meridian, and Y towards East, the conversion matrix to u, v, w is

$$\begin{pmatrix} u \\ v \\ w \end{pmatrix} = \frac{1}{\lambda} \begin{pmatrix} \sin(h) & \cos(h) & 0 \\ -\sin(\delta) \cos(h) & \sin(\delta) \cos(h) & \cos(\delta) \\ \cos(\delta) \cos(h) & -\cos(\delta) \sin(h) & \sin(\delta) \end{pmatrix} \begin{pmatrix} X \\ Y \\ Z \end{pmatrix} \quad (2.46)$$

where h, δ are the hour angle and declination of the phase tracking center.

Eliminating h from Eq.2.46 gives the equation of an ellipse:

$$u^2 + \left(\frac{v - (Z/\lambda) \cos(\delta)}{\sin(\delta)} \right)^2 = \frac{X^2 + Y^2}{\lambda^2} \quad (2.47)$$

The uv coverage is an ensemble of such ellipses. The choice of antenna configurations is made to cover the uv plane as much as possible.

Baseline measurement

Assume there is a small baseline error, $(\Delta X, \Delta Y, \Delta Z)$. The phase error is

$$\Delta\phi = \frac{2\pi}{\lambda} \Delta\mathbf{b} \cdot \mathbf{s}_0 \quad (2.48)$$

$$= \cos(\delta) \cos(h) \Delta X - \cos(\delta) \sin(h) \Delta Y + \sin(\delta) \Delta Z \quad (2.49)$$

Hence, if we observe N sources, we have for each source

$$\phi_k = \phi_0 + \cos(\delta_k) \cos(h_k) \Delta X - \cos(\delta_k) \sin(h_k) \Delta Y + \sin(\delta_k) \Delta Z \quad (2.50)$$

i.e. a linear system in $(\Delta X, \Delta Y, \Delta Z)$, with N equations and 4 unknown (including the arbitrary phase ϕ_0). This can be used to determine the baselines from phases measured on a set of sources with known positions h_k, δ_k .

From the shape of Eq.2.49, one can see that the determination of $\Delta X, \Delta Y$ requires large variations in h , preferably at declination $\delta \sim 0$, while that of ΔZ requires large variations in δ . However, ϕ_k in Eq.2.50 is multi-valued (the 2π ambiguity...). Retaining the function in the $[-\pi, \pi[$ interval only, the system to solve is in fact

$$\text{mod}(\phi_0 + \cos(\delta_k) \cos(h_k) \Delta X - \cos(\delta_k) \sin(h_k) \Delta Y + \sin(\delta_k) \Delta Z - \phi_k + \pi, 2\pi) - \pi = 0 \quad (2.51)$$

which is a linear system of equations only if $\Delta X, \Delta Y, \Delta Z$ are small enough so that the shifted modulo function is the identity. Baseline determination usually proceeds through a ‘‘brute force’’ technique, by making a grid search (with π phase steps) around the most likely values for X, Y, Z .

Chapter 3

Millimetre Very Long Baseline Interferometry

Albert Greve

greve@iram.fr

IRAM, 300 rue de la Piscine, F-38406 Saint Martin d'Hères, France

Millimeter–Wavelength Very Long Baseline Interferometry is interferometry at millimeter wavelengths (3.5–1.3 mm: 86 GHz–230 GHz) with disconnected telescopes using the longest baselines on Earth (1 000–10 000 km) in order to achieve the highest angular resolution (0.01–0.00005'). The disconnected telescopes need special time/frequency references provided by the observatory–own Hydrogen–masers, synchronized to GPS time signals. The observations are recorded on tape for correlation at special correlator stations. The correlation gives visibility tables. mm–VLBI sees only sources which emit non–thermal radiation at brightness temperatures of $T_B \approx 10^9 - 10^{12}$ K. These sources represent the 'hot' and energetic component of the Universe, for instance masers and quasars.

3.1 Introduction

Throughout the universe, the common astronomical objects – stars, stellar clusters, molecular clouds, galaxies, AGNs, QSOs, clusters of galaxies – have typical linear dimensions, and only seldom span a factor of 10 to 100 in scale. The more distant the objects, the smaller therefore their apparent angular size, and hence a higher angular resolution and larger collecting area of a telescope is required to distinguish significant structural detail at a significant level of detection. According to a fundamental optics principle, the angular resolution Θ of a full aperture telescope (optical or radio) of diameter \mathcal{D} , or of an interferometer consisting of several connected or disconnected telescopes of longest baseline separation \mathcal{B} , observing at the wavelength λ , is

$$\Theta \propto \lambda/D \text{ or } \Theta \propto \lambda/B [\text{rad}] \quad (3.1)$$

If, therefore, the telescope or the baseline has a diameter/length of $\mathcal{D} = \mathcal{B} = n\lambda$, the resolution is

$$\Theta \propto \lambda/\mathcal{D} \propto \lambda/\mathcal{B} \propto 1/n \quad (3.2)$$

In words, the larger the number (n) of wavelengths spanned by the diameter/baseline the higher is the angular resolution. From these relations it is evident that a high angular resolution is obtained by using short wavelengths (for instance millimeters instead of centimeters), and/or large telescopes, and/or long baselines ([inter]continental distances instead of kilometers). In order to obtain a resolution of $\Theta = 1''$ [the seeing limit at optical wavelengths set by the turbulence of the Earth's atmosphere], the size of the telescope or interferometer baseline must be

$$\mathcal{D}[1''] = \mathcal{B}[1''] \approx 2 \times 10^5, \lambda \quad (3.3)$$

which is $\mathcal{D}[1''] = \mathcal{B}[1''] = 600 \text{ m}$ at $\lambda = 3 \text{ mm}$ (100 GHz). To be comparable in resolution with the HST of $\Theta \approx 10^{-2} \times 1'' = 0.01''$, a telescope/baseline of $\mathcal{D} = \mathcal{B} = 60 \text{ km}$ at $\lambda = 3 \text{ mm}$ is required. To obtain however a resolution of $\Theta = 10^{-2} \times 10^{-2} \times 1'' = 0.0001'' = 0.1 \text{ mas}$ at mm-wavelengths it is evident that the telescope must have Earth dimensions. Such a 'telescope' can only be an interferometer of some sort, of which the telescopes are disconnected and located across a continent, or on different continents, or on different continents and in Space.

The image quality of a mm-VLBI array depends on the available uv -coverage. However, mm-VLBI telescopes cannot be displaced, they are arranged in the given configuration of the observatory sites (see Fig. 3.1), and uv -coverage is only obtained by Earth rotation. The sensitivity of a mm-VLBI array depends on the collecting area and the precision (aperture efficiency) of the participating telescopes.

Very long baseline interferometry, on baseline dimensions of the Earth's diameter and satellite orbits, requires special techniques to record in-phase the different segments of a wavefront emitted by a source and being received by the individual telescopes of the array. This in-phase recording is achieved by locking the oscillators of the receiver and tape recorder unit to a very precise observatory time standard (Hydrogen-maser), which in turn is synchronized to an 'outside clock', available at all stations. This outside clock is provided by time signals of the Global Positioning System (GPS).

3.2 mm-VLBI Arrays

The wet atmosphere, even at high altitudes, has transmission windows at $\sim 3 \text{ mm}$ ($\sim 100 \text{ GHz}$), $\sim 2 \text{ mm}$ ($\sim 150 \text{ GHz}$), $\sim 1.3 \text{ mm}$ ($\sim 230 \text{ GHz}$), and at shorter wavelengths, through which radio signals can propagate to the surface of the Earth. The observing facilities of mm-VLBI, summarized in Table 3.1, make use of these atmospheric windows.

The remark 'Proposal' in Table 3.1 indicates that the array is available to observers on a competitive proposal basis. The 2-mm and 1.3-mm observations are in an experimental state. The mentioned 1.3-mm observations were experimental, and successful.

3.2.1 The CMVA Array

The CMVA (Coordinated Millimeter VLBI-)array contains the telescopes of 12 observatories which operate together in coordinated observations for approximately 15 days per year. The telescopes are located in North-America, Europe, and Chile. The performances of the telescopes at 86 GHz (3.5 mm) are given in Table 3.2, the location of the telescopes is shown in Figure 3.1. The European telescopes of the CMVA are located essentially in the direction North-South, the American telescopes are located essentially in the

Table 3.1: mm-VLBI Arrays and Experimental Observations

Frequency (Wavel.)	Array	Telescopes	Baseline	Observing
86 GHz (3.5 mm)	CMVA	Table 2	~ 8 000 km	Proposal
86 GHz (3.5 mm)	VLBA(*)	Table 3	~ 8 000 km	Proposal
150 GHz (2.0 mm)	—	PV-KP-SEST		experim.
230 GHz (1.3 mm)	—	OVRO-KP	~ 500 km	experim. (**)
	—	PV-PdBure	~ 1000 km	experim. (***)

PV: Pico Veleta (Spain), KP: Kitt Peak (USA), OVRO: Owens Valley Obs. (USA), SEST: La Silla (Chile).
 (*) sub-array of the VLBA array (Table 3.3); (**) [Padin et al. 1990]; (***) [Greve et al. 1995],
 [Krichbaum et al. 1998]

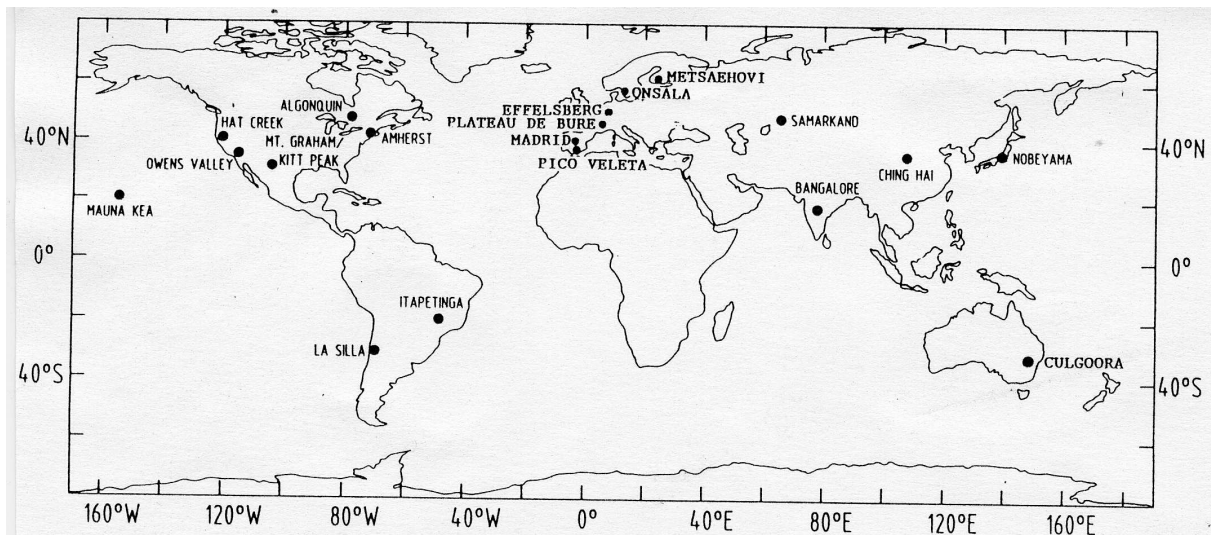


Figure 3.1: Observatories participating in cm and mm-wavelength VLBI. The mm-VLBI observatories of the CMVA (Table 3.2) are concentrated in Western Europe and North America. From [Felli & Spencer 1989], Schilizzi p404, with kind permission from Kluwer Academic Publishers.

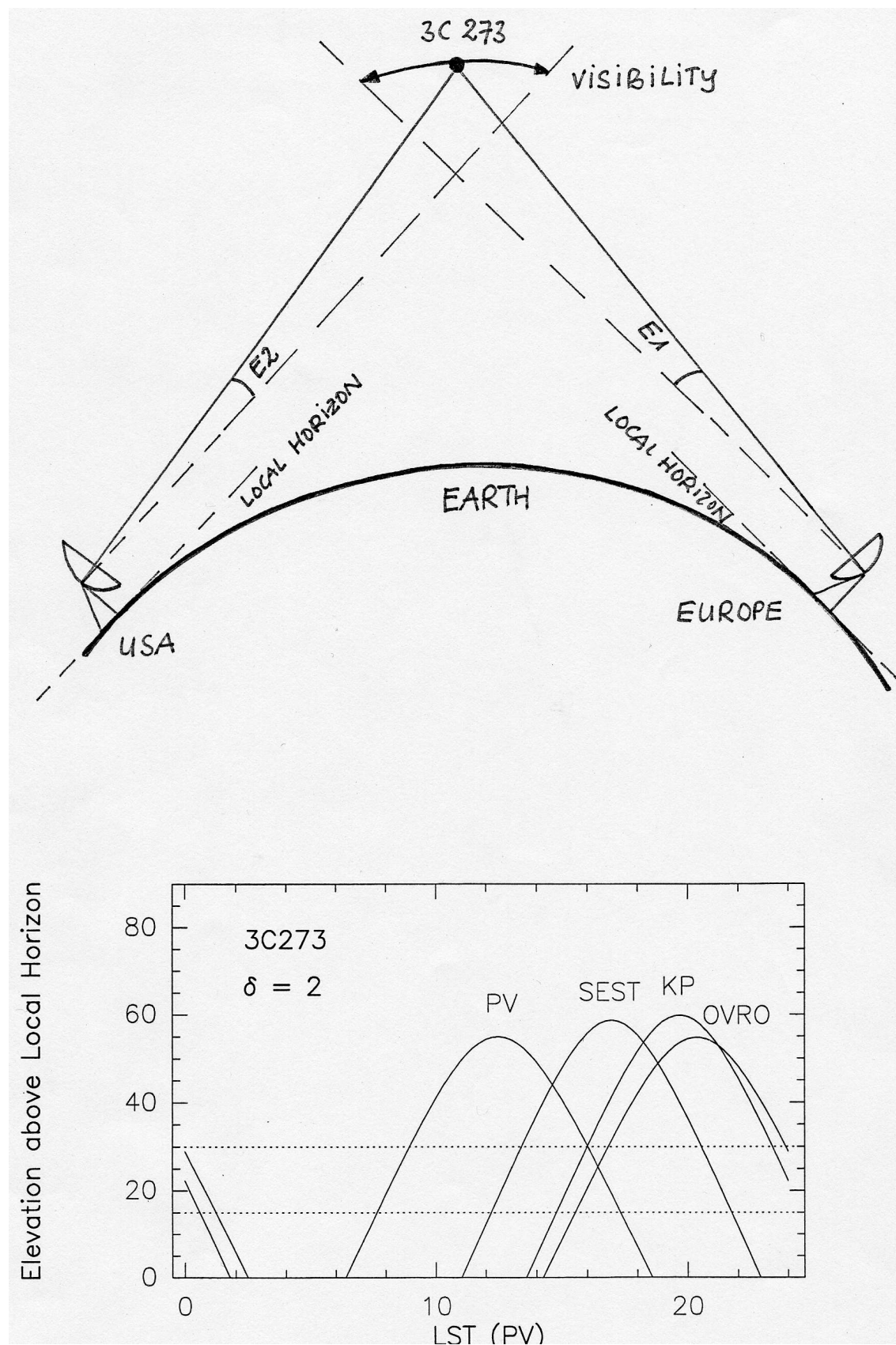


Figure 3.2: Illustration of the low elevation visibility (E_1 , E_2) of the QSO 3C 273 (RA: $12^{\text{h}} 29^{\text{m}}$, Dec: $2^{\circ} 3'$, 1950). The lower part of the figure shows the relative elevation of 3C 273 at Pico Veleta (Spain; LST: local sidereal time reference), SEST (Chile), Kitt Peak (USA), and Owens Valley (USA). The mutual visibility is given by the overlap areas of the individual curves.

Table 3.2: The Coordinated Millimeter VLBI Array = CMVA (86 GHz)

Telescope	Country	\mathcal{D} [m]	T_{sys} [K]	Gain [K/Jy]	η_A	Altitude [m]
CMVA						
Effelsberg	Germany	60	350	0.13	0.13	~ 0
Haystack	USA	37	200	0.058	0.15	~ 0
Pico Veleta	Spain	30	150	0.14	0.60	3000
Onsala	Sweden	20	250	0.056	0.49	~ 0
SEST	Chile	15	300	0.032	0.50	2500
Amherst	USA	14	300	0.024	0.43	~ 0
Metsähovi	Finland	14	300	0.017	0.30	~ 0
(Kitt Peak ^(*))	USA	12	150	0.023	0.56)	2000
Owens Valley	USA	4×10.4	300	0.067	0.55	1500
Hat Creek	USA	7×6.1	300	0.050	0.65	1000
Expected						
P. de Bure	France	6×15	150	0.045	0.7	2500
GBT	USA	[100]				~ 0
LMT	Mex(-USA)	50				4600
Yebes	Spain	40				500
ALMA	Chile	64×12	(70)	(0.03)	(0.8)	5000

(*) out of operation since July 2000.

direction East–West. As applied in other interferometers, the CMVA array uses Earth rotation to obtain uv–coverage. Some of the strong mm–VLBI sources (3C 273, 3C 279), which are regularly monitored (see Figure 3.9), are located at low declination ($\text{Dec} = 2^\circ, -5^\circ$) so that they can be simultaneously observed only at low local elevations, as illustrated in Figure 3.2 for 3C 273 and the stations Pico Veleta – SEST – Kitt Peak – Owens Valley. The low elevation usually implies a high line-of-sight system temperature (T_{sys}), thus a low signal-to-noise ratio, and thus a low detection sensitivity (Sect.3.5). The low elevation implies also that the uv–coverage may be incomplete, the synthesized beam asymmetric, and the final map distorted.

Table 3.2 contains also several telescopes expected to be available in future. These are telescopes with large collecting areas; the dedicated mm–wavelength telescopes (PdB, LMT, ALMA) are located at high altitudes.

3.2.2 The VLBA Array

The VLBA (Very Long Baseline–)array, which consists of 10 dedicated 25–m diameter telescopes (Table 3.3, Figure 3.3), is located on the North–American continent, including one antenna on Hawaii. This array observes routinely at 43 GHz. The array is being upgraded for observations at 86 GHz (3.5 mm); a sub–array (+) is available for 86 GHz VLBI observations. Some of these telescopes collaborate in CMVA observations.

3.3 Available Resolution

Table 3.4 gives an overview of the angular resolution available from the Plateau de Bure interferometer and the CMVA–VLBA mm–wavelength VLBI–arrays (USA + Europe). The table gives for comparison the parameters of the Pico Veleta 30–m telescope (Spain). The table gives also the linear scale corresponding to the angular resolution Θ for a source located at 50 Million pc distance.

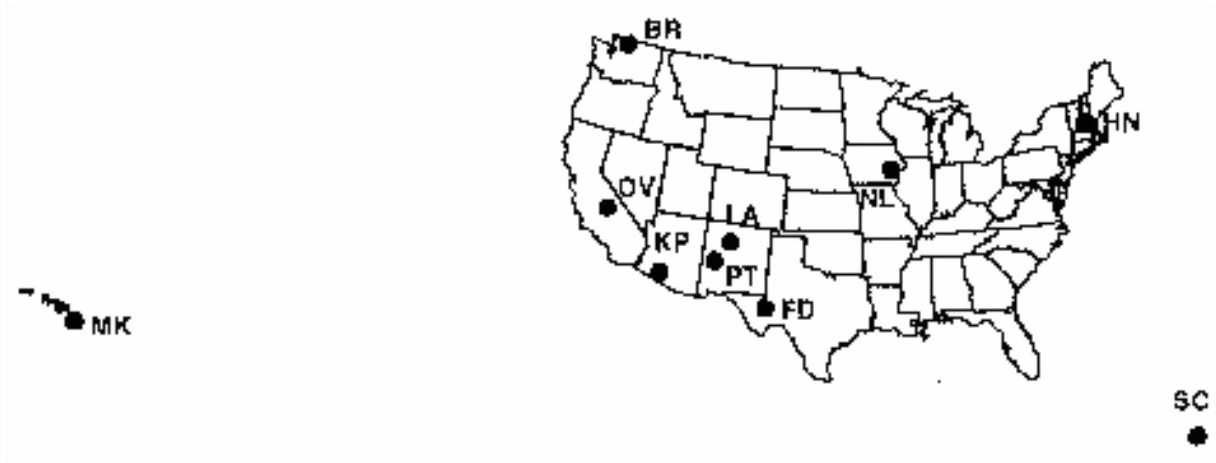


Figure 3.3: The VLBA array (Table 3.3) (from [Zensus et al. 1995]).

Table 3.3: The VLBA Array [10×25 m antennas] (partially operating at 86 GHz)

	Code	Location (USA)	Elevation (m)
	SC	St. Croix VI	16
	HN	Hancock NH	309
+	NL	N. Liberty IA	241
+	FD	Ford Davis TX	1616
+	LA	Los Alamos NM	1967
+	PT	Pie Town NM	2371
+	KP	Kitt Peak AZ	1916
+	OV	Owens Valley CA	1207
	BR	Brewster WA	255
+	MK	Mauna Kea HI	3720

Table 3.4: Diameter (\mathcal{D}), Baselines (\mathcal{B}), Resolution (Θ), Linear Scale

Diameter/ Baseline	Telescopes	$\lambda = 3.5 \text{ mm}$ \mathcal{B}/λ	$\lambda = 3.5 \text{ mm}$ Θ	Linear Scale at 50 Mpc
$\mathcal{D} = 0.03 \text{ km}$	30-m PV (Single Dish)	8×10^3	$24''$	6000 pc
$\mathcal{B} = 0.3 \text{ km}$	PdB (Interferom.)	8×10^4	$2.4''$	600 pc
$\mathcal{B} = 1\,500 \text{ km}$	PV - PdB (VLBI)	4×10^8	$0.0005''$	0.1 pc
$\mathcal{B} = 8\,000 \text{ km}$	CMVA/VLBA (VLBI)	2×10^9	$0.000\,09''$	0.02 pc

Table 3.5: Polarization Possibilities (LCP, RCP)

Telescope	Polarization (number of channels, 4 MHz)	Bandwidth
Effelsberg	14 LCP	122 MHz LCP
Onsala	14 LCP	122 MHz LCP
+ Pico Veleta	7 LCP / 7 RCP	56 MHz LCP / 56 MHz RCP
+ Haystack	7 LCP / 7 RCP	56 MHz LCP / 56 MHz RCP
Amherst	14 LCP	122 MHz LCP
+ Pietown	4 LCP / 4 RCP	28 MHz LCP / 28 MHz RCP
+ BIMA	7 LCP / 7 RCP	56 MHz LCP / 56 MHz RCP

3.4 Polarization Observations

The continuum radiation of Quasars (QSO) and the line radiation of SiO masers is polarized, in single dish and interferometer observations from a few percent to $\sim 10\%$ for QSO's, and up to $\sim 70 - 80\%$ for the individual components of SiO masers. VLBI observations are normally made at Left Hand–Circular Polarization (LCP = \mathcal{L}) in order to eliminate amplitude modulations of a polarized source due to hour angle variations. For polarization observations, measurements are made at LCP and RCP (right hand–circular, \mathcal{R}) polarization. The Stokes parameters I, Q, U, V, describing the polarization, and the complex correlations $\mathcal{R}\mathcal{R}$, $\mathcal{L}\mathcal{L}$, $\mathcal{R}\mathcal{L}$, $\mathcal{L}\mathcal{R}$ are related by $\mathcal{R}\mathcal{R} = I + V$; $\mathcal{L}\mathcal{L} = I - V$; $\mathcal{R}\mathcal{L} = Q + iU$; and $\mathcal{L}\mathcal{R} = Q - iU$ ([Kemball et al. 1995]).

Table 3.5 summarizes the possibility of VLBI polarization observations (status 2000) at 86 GHz. The BIMA (Hat Creek) interferometer can be phased and split into 3 antennas LCP and 3 antennas RCP; this will eventually also be possible with the PdB interferometer.

Polarization observations at 86 GHz of QSO's are so far without convincing success, mainly because of their low degree of polarization; VLBI polarization observations at 86 GHz of SiO masers are in progress.

3.5 The Feasibility of mm–VLBI: Signal–to–Noise Ratio and Detections

The operation and sensitivity, and the present situation and future wishes of mm–VLBI are easily explained from a discussion of the relation expressing the signal–to–noise ratio of an observation with a two–telescope VLBI interferometer. An unresolved source with a size comparable or smaller than the synthesized beamwidth (Θ), measured with both telescopes (1,2), is considered to be detected if the signal–to–noise ratio (SNR) of the observation is ~ 7 or higher, i.e. $7 \leq \text{SNR}$. The relation of the SNR is ([Rogers et al. 1984])

$$\text{SNR} = L \sqrt{\eta_1 A_1 \eta_2 A_2 / (T_{1,sys} T_{2,sys})} \times 2\tau \Delta\nu \times (F/2k) \quad (3.4)$$

$$\text{SNR} = L(\pi/4) D_1 D_2 \sqrt{(\eta_1 \eta_2 / (T_{1,sys} T_{2,sys}))} \times 2\tau \Delta\nu \times (F/2k) \quad (3.5)$$

with A the geometrical area = $\pi(D/2)^2$ and \mathcal{D} the diameter of the telescope (Tables 3.2 & 3.3); η the aperture efficiency (Table 3.2); ηA the effective collecting area; T_{sys} the system temperature (Table 3.2); $\Delta\nu$ the bandwidth (112 MHz for MkIII); τ the integration time; F the correlated flux density; k the Boltzmann constant; and L the correlator efficiency ($\approx 2/\pi$ for a 2–level quantization).

From this relation we note that:

- the incorporation of a large–diameter high–precision telescope significantly improves the performance of a mm–VLBI array. If an array of two telescopes of diameter $\mathcal{D}_1 = \mathcal{D}_2 = 15$ m and efficiency $\eta_1 = \eta_2 = 0.3$ performs at the signal–to–noise ratio $\text{SNR}(2 \times 15\text{m})$, the replacement of one telescope by, for instance, the

Table 3.6: SNR for 86 GHz (3.5 mm) Observations: Pico Veleta – Haystack (~ 6000 km)

Source	S(86 GHz) [Jy] (single dish)	SNR (VLBI)
3C 273	25	182–203
3C 279	20	163
3C 345	5.5	6–13
NRAO530	6.5	21–81
1749+096	3.0	21–43
1823+568	2.8	35–43
2145+067	4.5	5–19
3C 454.3	10	78–66

Results obtained at 215 GHz (1.3 mm) on the ~ 1000 km baseline Pico Veleta–PdB are given in Table 3.7 ([Krichbaum et al. 1998]).

IRAM 30-m telescope with $\mathcal{D}_2 = 2\mathcal{D}_1 = 30$ m and $\eta_2 = 2\eta_1 = 0.6$ improves the signal-to-noise ratio by $\text{SNR}(15\text{m} \ \& \ 30\text{m}) = 2 \times \text{SNR}(2 \times 15\text{m})$: the array has a 2 times higher sensitivity. It is evident that the future incorporation of the PdB interferometer, the LMT, and ALMA (Table 3.2) will greatly improve the sensitivity of mm-VLBI.

- for observations at mm-wavelengths the location of a telescope at 2000–3000 m altitude generally reduces T_{sys} because of the lower amount of atmospheric water vapour, i.e. $T_{sys}(\text{high site}) \approx (1/3) \times T_{sys}(\text{low site}) \approx (1/3) \times (300-500) \text{ K} \approx 150 \text{ K}$. The lower value of T_{sys} increases the SNR by a factor of 2, or more. Such a decrease of the line-of-sight T_{sys} is especially important for intercontinental/transatlantic baselines where the sources are usually observed at low local elevations (Figure 3.3). Table 3.2 shows that several telescopes of the CMVA array unfortunately are located at low altitudes. Again, the incorporation of PdB Interferometer (2500 m), the LMT (4600 m), and ALMA (5000 m) will greatly improve the sensitivity of mm-VLBI.
- for continuum observations, the foreseen increase in bandwidth of presently $\Delta\nu = 112$ MHz by a factor of two, or more (MkIV), will increase the sensitivity of mm-VLBI by a factor of 1.5, or more.
- the integration time τ is usually limited by the stability of the Hydrogen-maser to values $\tau(100 \text{ GHz}) \approx 1000$ s and $\tau(230 \text{ GHz}) \approx 100$ s (Sect.3.6). Often however, the integration time is shorter, $\tau(100 \text{ GHz}) \approx 100-200$ s and $\tau(230 \text{ GHz}) \approx 10-20$ s, because of phase disturbances introduced by atmospheric water vapour fluctuations. Segmented correlations and atmospheric phase corrections increase the sensitivity of mm-VLBI.
- the SNR is proportional to the *correlated* (unresolved) flux density (F) of the source. At mm-wavelengths it is found that the correlated flux density is often significantly smaller than the total flux density (S) measured with a single dish telescope. It is found, globally, that $F \approx (1/3-1/5) \times S$. As example, for 3C 273 it is observed that $S(86 \text{ GHz}) \approx 20$ Jy while $F(86 \text{ GHz}) \approx 4$ Jy, and $S(230 \text{ GHz}) \approx 10$ Jy while $F(230 \text{ GHz}) \approx 2$ Jy. The presently available CMVA array has sufficient sensitivity to detect sources of total flux density $S \leq 2-3$ Jy.

To illustrate the present situation and possibilities of mm-VLBI, Table 3.6 summarizes the SNR of detections at 86 GHz measured on the baseline Pico Veleta (Spain) – Haystack (USA) ([Krichbaum et al. 1994]; [Beasley et al. 1995]).

3.6 From observations to correlations, step by step

3.6.1 Observing Techniques

A 2-telescope disconnected mm-VLBI array and the (far away) correlator station are shown in Figure 3.4. mm-VLBI observations are made with telescopes separated by several hundreds or thousands of kilometers

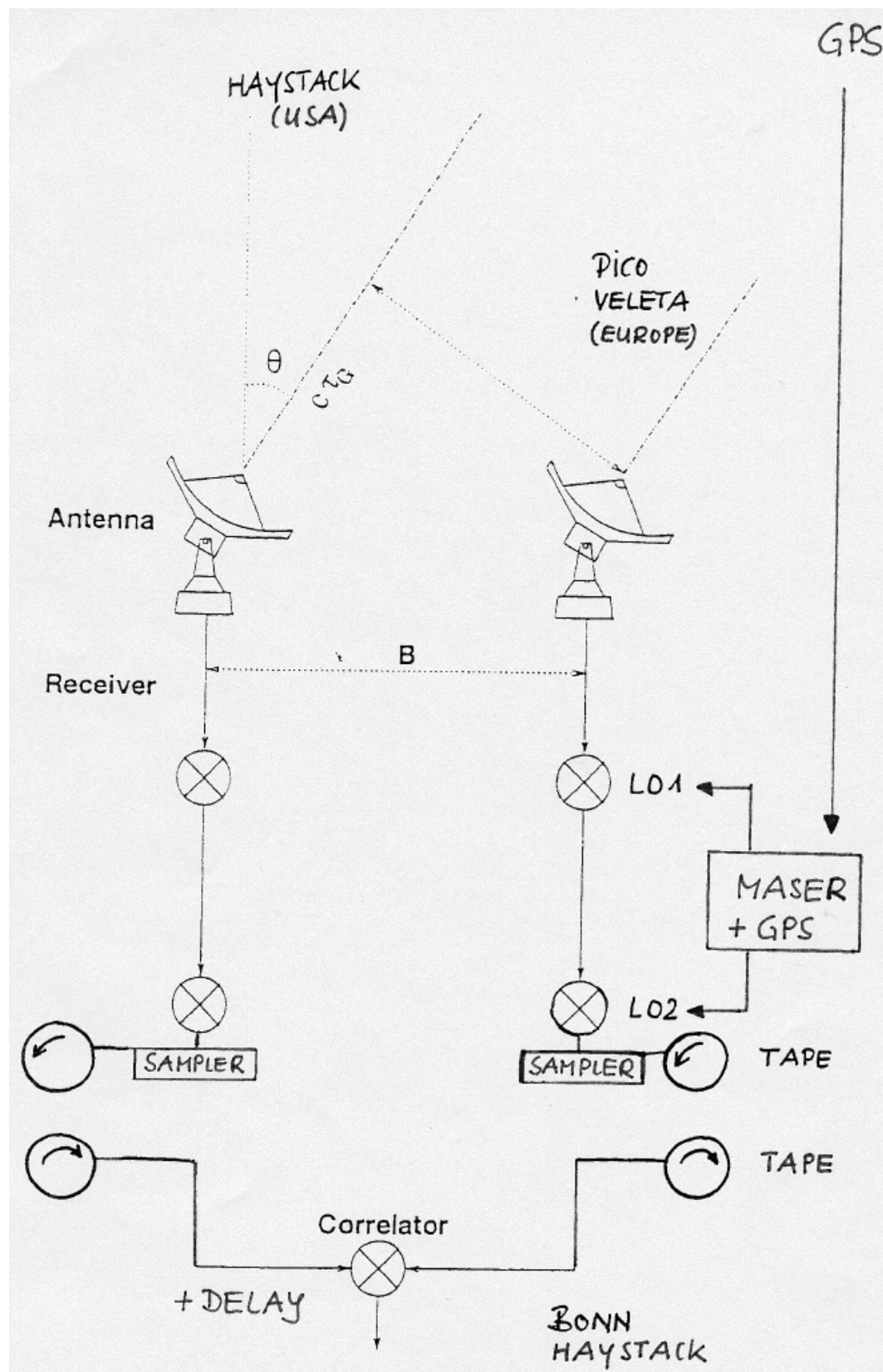


Figure 3.4: Disconnected two-telescope VLBI array; one telescope is located in Europe, the other one is located in the USA. At both observatories, the local oscillators (LO_1 , LO_2), the sampler, and the tape unit are locked to the observatory H-maser, synchronized to the satellite GPS time signal. The observations are correlated either at Haystack or Bonn; here the delays and Doppler shifts are introduced.

Table 3.7: SNR for 215 GHz (1.3 mm) Observations: Pico Veleta – Bure (~ 1000 km)

Source	z	S(215 GHz) [Jy] (single dish)	SNR (VLBI)	F(215 GHz) [Jy] (VLBI)
4C 39.25	0.69	3.5 ± 0.7	< 4	< 0.5
3C 273	0.16	9.2 ± 0.6	7	0.4–0.7
3C 279	0.54	11.0 ± 1.0	35	3–3.8
1334–127	0.54	3.1 ± 0.7	12	0.5–1.1
3C 345	0.59	3.0 ± 0.4	6	≤ 0.4
NRAO530		6.2 ± 0.5	11	0.5–0.8
Sgr A*		4.1 ± 0.5	6	0.5–0.9

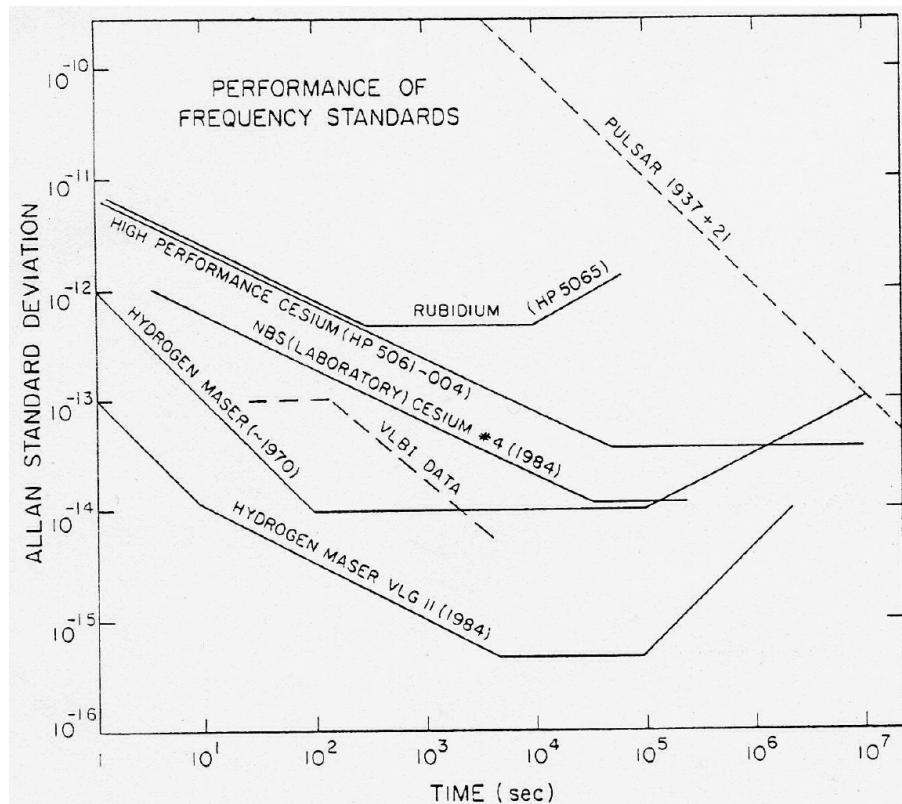


Figure 3.5: Allan standard deviation vs. integrated time for several frequency standards. The phase fluctuations of mm-VLBI are usually dominated by atmospheric phase fluctuations. From [Thompson et al. 1986]. Copyright: ©1986 Wiley-Interscience Publications. Reprinted by permission of John Wiley & Sons, Inc.

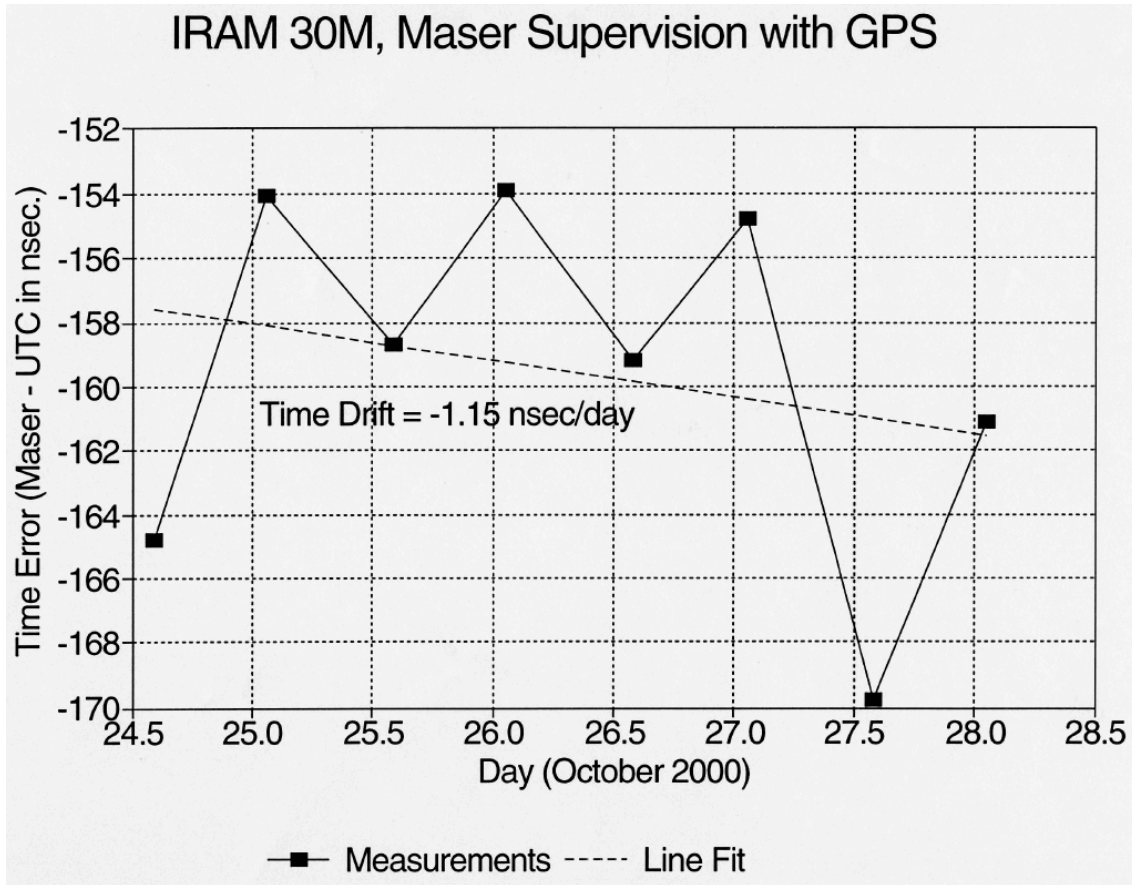


Figure 3.6: Typical H-maser drift measured at Pico Veleta (by courtesy of J. Penalver, IRAM).

not sharing a common time/frequency reference as used in connected interferometry. At each VLBI-telescope therefore the receivers, frequency down-up converters, tape recorders, phase-calibration systems etc. are locked to a Hydrogen-maser which has a typical short-term stability of $\sim 10^{-15}$ and a typical drift of a few 10 nano-seconds per day, or smaller, as shown in Figures 3.5 & 3.6. The VLBI time/frequency systems of the individual telescopes are locked to the GPS system which gives an absolute time reference at the participating telescopes of a few hundred nano-seconds, or better. This time difference must be retrieved a posteriori in the data correlation.

mm-VLBI observations are made at a fixed frequency, preferably at Single-Side-Band tuning in order to reduce noise from the non-used sideband. Fringe rotation and Doppler shifts are introduced a posteriori at the correlator.

3.6.2 Data Recording

In VLBI observations, the telescopes are disconnected and real-time correlation of the signals from the individual telescopes is not possible. At each telescope, the signals are recorded on tape synchronous with the time signal provided by the Hydrogen-maser. In MkIII mode observations, the data are available as 28 channels of 4 MHz bandwidth each; the bandwidth of the recording is $\Delta\nu = 28 \times 4 \text{ MHz} = 112 \text{ MHz}$. The 28 tracks are recorded simultaneously on magnetic tape. The required bitrate of the recording is

$$\text{bits/s} = 2n_c\Delta\nu \quad (3.6)$$

For $\Delta\nu = 112 \text{ MHz}$ and a sampling efficiency $n_c \approx 1 - 1.6$, the bitrate recorded on tape is $\sim 224 \text{ Megabites/s}$. mm-VLBI is being upgraded to 256 MHz bandwidth, and more (MkIV).

3.6.3 Correlation Time

The short-term frequency stability (up to a few 1000 s, see Figure 3.5) of a Hydrogen-maser is $\sim 10^{-15}$. There are long-term drifts which can be checked against GPS signals (see Figure 3.6) and adjusted so that they are below, say, ten nano-seconds per day. The maximum possible integration time (τ) of an observation is set by the requirement that the relative frequency drift $\Delta\nu$ must not exceed, say, $\Delta\nu \approx 0.2$ radians. The integration time then is ([Kellerman & Thompson 1985])

$$\Delta\nu/(2\pi\nu\tau) \approx 0.2/(2\pi\nu\tau) \approx 10^{-15} \quad (3.7)$$

This relation gives $\tau(86 \text{ GHz}) \approx 350 \text{ s} \approx 5 \text{ minutes}$ and $\tau(230 \text{ GHz}) \approx 150 \text{ s} \approx 2 \text{ minutes}$.

3.6.4 Phase Correction

Because of phase variations introduced by atmospheric water vapour fluctuations, the correlation time τ derived above can be significantly shorter, $\tau \approx 10 - 30 \text{ s}$, especially when observing at high frequencies. Because of the scarcity of strong mm-wavelength VLBI sources at sufficiently close distances in the sky, phase referencing as used in connected mm-wavelength interferometry (for instance used on PdB) has not yet generally been applied in mm-VLBI. Efforts are however undertaken to apply phase corrections from local line-of-sight water vapour measurements (sky emission measurements). As an example, the phase stability of a 86 GHz and 215 GHz measurement between Pico Veleta and Plateau de Bure is shown in Fig.3.7. A typical atmosphere-induced phase variation and phase correction applied to 86 GHz VLBI measurements made at Pico Veleta is shown in Figure 3.8.

3.6.5 Correlation

The recorded mm-wavelength VLBI data are correlated at Haystack (USA) or at Bonn (Germany). The end-product of the correlation are calibrated visibility values (uv-tables) which can be used in the same way as data, for instance, obtained with the PdB interferometer.

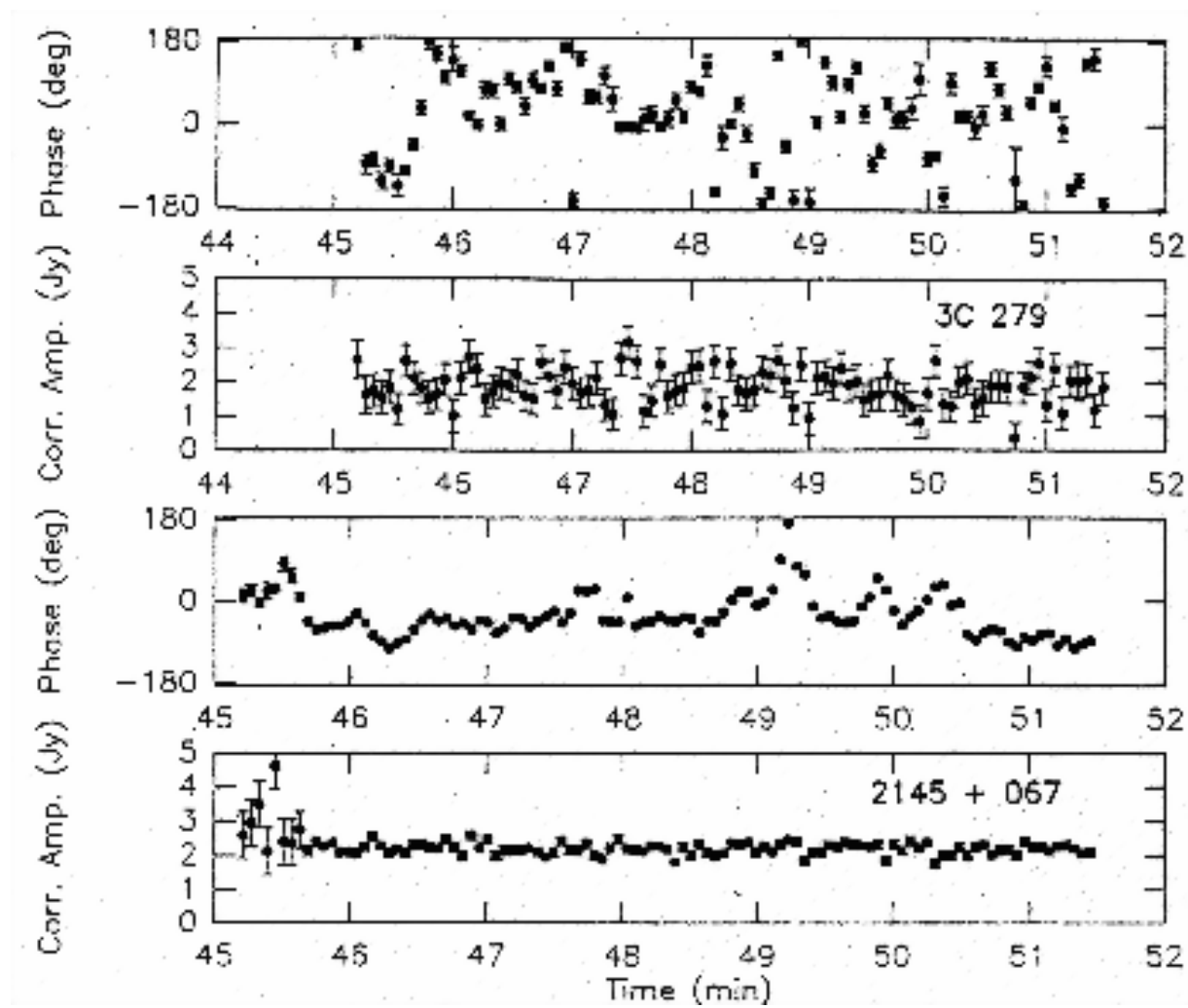


Figure 3.7: VLBI at 215 GHz and 86 GHz between Pico Veleta and Plateau de Bure (1994). The 6.5 minute records show amplitude and phase stability for 3C 279 at 215 GHz (upper panel) and 2145+067 at 86 GHz (lower panel).

3.7 The observable sources with mm–VLBI

3.7.1 Which Kind of sources can we observe

Mm–VLBI sees non–thermal sources emitting, for instance, maser or synchrotron radiation at a high brightness temperature (T_B). The associated astronomical sources are, for instance, masers (SiO) and AGNs and QSOs with jets. mm–VLBI is insensitive to the cold component of the Universe like molecular clouds and other thermal sources. The cold component is observed with interferometers like the Plateau de Bure instrument.

The correlated flux density F of a source with brightness temperature T_B , subtending the solid angle Ω in the sky, is

$$F = (2k/\lambda^2)T_B\Omega \quad (3.8)$$

The correlated flux density ΔF observable within the bandwidth $\Delta\nu$ and integration time τ is

$$\Delta F = (2k/A_{eff})T_{sys,eff}/\sqrt{2\tau\Delta\nu} \quad (3.9)$$

with $A_{eff} = \sqrt{\eta_1 A_1 \eta_2 A_2}$ the effective surface area of telescope 1 & 2 and $T_{sys,eff} = \sqrt{T_{1,sys} T_{2,sys}}$ the effective system temperature. To arrive at a numerical value of T_B let us assume that we want to detect the source with an accuracy of $\Delta F \approx \epsilon F$, where $0 < \epsilon < 1$. We assume furthermore that the source is unresolved and small and has a size comparable to the VLBI array resolution, hence $\Omega \approx (\lambda/B)^2$. Using these relations we obtain

$$T_B \approx T_{sys,eff} B^2 / (\epsilon A \sqrt{2\tau\Delta\nu}) \quad (3.10)$$

A mm–VLBI array of two telescopes of 15–m diameter, observing at a system temperature $T_{sys,eff} = 200$ K, a bandwidth of $\Delta\nu = 112$ MHz, and an integration time limited by the system and atmospheric phase stability to $\tau \approx 100$ s, can only detect sources which have brightness temperatures of $T_B \approx 10^9 - 10^{12}$ K.

3.7.2 The field of view

Evidently, a mm–VLBI array of 8000–10 000 km baseline has only a limited field of view (θ_{fov}). Since a disconnected mm–VLBI array does not directly track phase, an estimate of the field of view is obtained by noting that the delay τ between two antennas (see Figure 3.4) separated by the baseline B and observing in the direction θ

$$\tau = (B/c) \cos \theta \quad (3.11)$$

and that the delay difference $\Delta\tau$ for a small angular displacement $\Delta\theta$ from the main direction of observation is

$$\Delta\tau = -(B/c) \sin \theta \Delta\theta \quad (3.12)$$

with c the velocity of light. Since delay corrections are only made in the correlator, the field of view is restricted to directions in which delay smearing ($\Delta\tau$) does not exceed, approximately, $\Delta\tau \leq 1/(2\Delta\nu)$. Using this criterion, the field of view is

$$\theta_{fov} \approx \lambda/B(\nu/\Delta\nu) \quad (3.13)$$

For $\nu = 86$ GHz, $\Delta\nu = 112$ MHz (MkIII), and $B = 10\,000$ km we obtain $\theta_{fov} \approx 0.05 - 0.02'' \equiv 50 - 20$ mas.

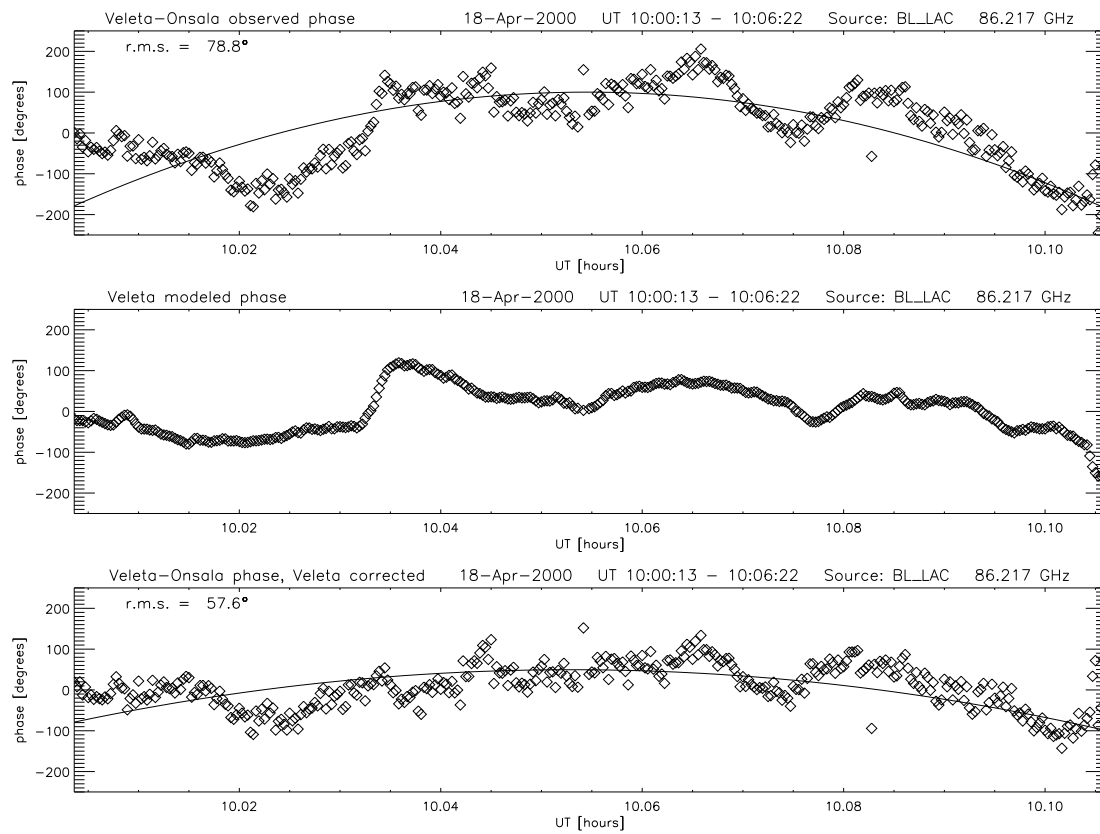


Figure 3.8: mm-VLBI phase correction at 86 GHz. The upper panel shows the phase variation measured on the baseline Pico Veleta – Onsala. The center panel shows the contribution of the phase variation predicted for Pico Veleta from atmospheric water vapour measurements (200 GHz line-of-sight sky emission). The lower panel shows the improvement in phase stability when the predicted phase fluctuations are taken into account (by courtesy of M. Bremer, IRAM, A. Roy and D. Graham, MPIfR).

3.7.3 An example: mm-VLBI Observations of QSO 3C 273

Fig.3.9 shows observations of the Quasar 3C 273 at 22 GHz (top), 43 GHz (center), and 86 GHz (bottom), performed nearly at the same epochs of 1995.15 (22 and 43 GHz) and 1995.18 (86 GHz). Contour levels in all maps are $(-0.5,)$ 0.5, 1, 2, 5, 10, 15, 30, 50, 70, and 90 % of the peak flux density of 3.0 Jy/beam (top), 5.4 Jy/ (center), and 4.7 Jy/beam (bottom). All maps are restored with the same beam of size of 0.4×0.15 mas, oriented at $pa = 0^\circ$. The maps are arbitrarily centered on the eastern component (the core); the dashed lines guide the eye and help to identify corresponding jet components in the three maps.

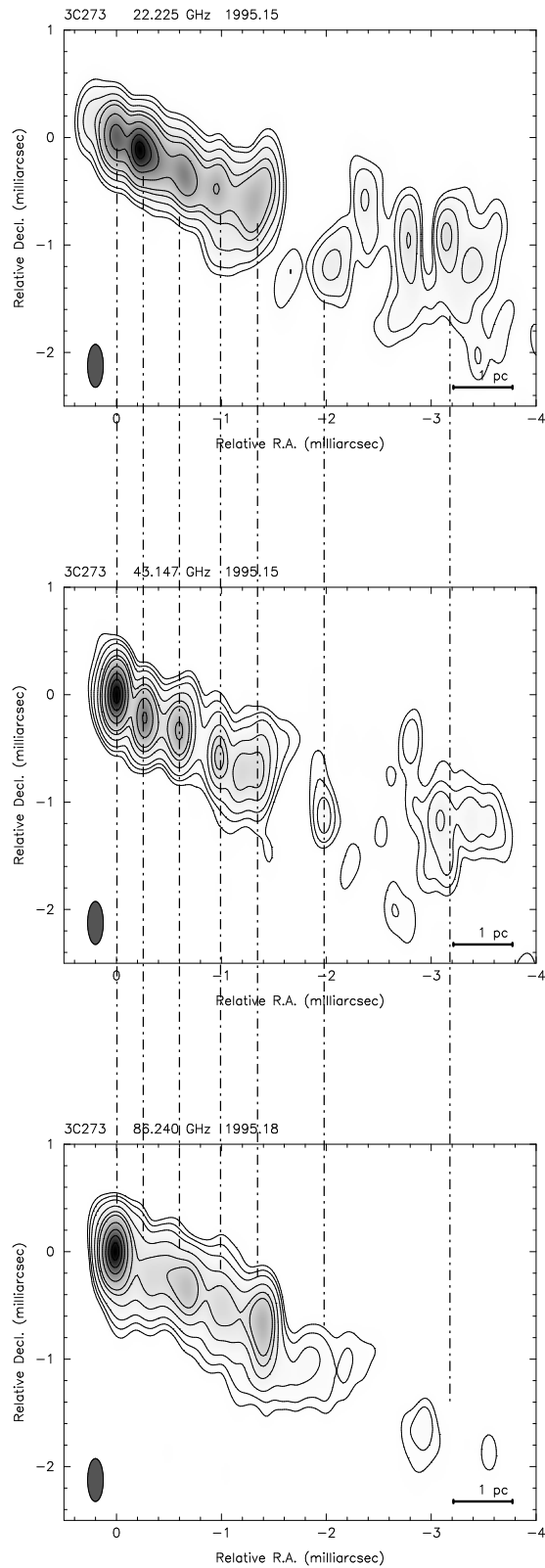


Figure 3.9: VLBI observations of QSO 3C 273 at 22 GHz (1.3 cm) [top], 43 GHz (7.0 mm) [center], and 86 GHz (3.5 mm) [bottom]. The 86 GHz map is obtained from observations with the CMVA array (by courtesy of T. Krichbaum, MPIfR).

Chapter 4

Introduction to Optical/Near-Infrared Interferometry

Fabien Malbet

Fabien.Malbet@obs.ujf-grenoble.fr

LAOG, BP 53, F-38041 Grenoble Cedex 09, France

4.1 Introduction

This chapter is focused on optical (i.e. visible and infrared) interferometry with in mind the comparison of this technique with radio interferometry developed in the other chapters of this book. The objective is to give some keys to understand how optical interferometers works. I present first a small history of optical interferometry followed by a census of interferometers in operation or in construction (Sect. 4.1). Section 4.2 discusses the common points and main differences between optical and radio interferometry at millimeter wavelengths. Then I describe how an optical interferometer works (Sect. 4.3) at the system level and at the signal detection level (Sect. 4.4). Finally I present in Sect. 4.5 the main limitations that optical interferometry faces like the atmospheric turbulence and other sources of noise in the measured signal.

4.1.1 Brief history of optical interferometry

Stellar interferometry has been first proposed by Fizeau in 1868. At that time, the phenomenon of light interference is already well studied and the physicists know that the contrast of the fringes depends on the geometry of the source. [Fizeau 1868] suggests to deduce the star diameter from the extinction of the fringe contrast with widely separated slits. [Stéphan.1873] installs a mask with two apertures on the 0.80-m telescope of the Marseille observatory to test Fizeau's method. He detects fringes but the contrast of fringes do not decrease with the aperture distance. He concludes that stars must be smaller than 0.158 arcsec.

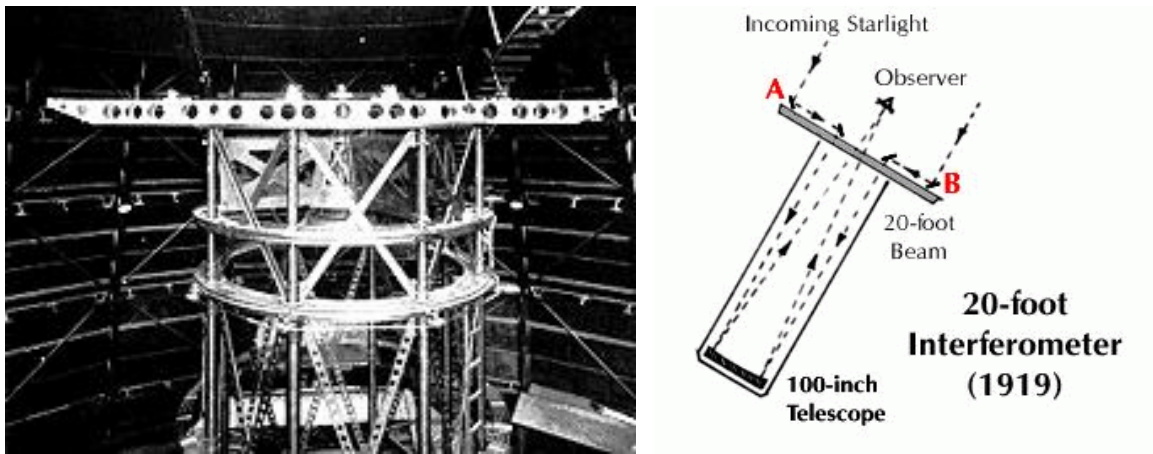


Figure 4.1: Michelson 20-foot interferometer installed on 100-in telescope at Mount Wilson.

Following his own work on the measurement of light speed, Michelson seems to have independently discovered optical interferometry in the 1890's. In order to span a large range of baselines, he and Pease install a 20-foot metal beam above the 100-in telescope of Mount Wilson. Two mirrors inclined by 45 degrees send the light to the middle of the telescope where two other mirrors inject the light in the telescope. The interferometric fringes are formed at the focus of the telescope (see Fig. 4.1). By translating the outside mirrors, the baseline changes and therefore also the contrast of the fringes. In the 1920's, [Michelson & Pease 1921] measure the first diameters of stars that required baselines longer than 3m. To extend these first results, Pease builds a stand-alone interferometer on a 50-foot metal beam, but fails in getting calibrated results because of the unexpected importance of mechanical flexures.

During almost 50 years, direct detection interferometry stalled. [Hanbury Brown & Twiss 1956] invented intensity interferometry which is limited to a small handset of bright sources. Interferometry had a new birth in the mid-1970's with the advent of new technology: detectors, actuators, servo-control, etc. [Labeyrie 1975] was the first to directly combine the light from two separated telescopes in the optical range. Since that time several interferometers with relatively small apertures have been built and operated. A list of current and future interferometers is given in Table 4.1 and commented in next section.

In 1988, the heterodyne techniques used in the radio domain was first implemented in an operating interferometer at $10 \mu\text{m}$ by the *Infrared Spatial Interferometer* (ISI, [Danchi et al. 1988]).

4.1.2 Current and future optical interferometers

Current interferometers (see list in Table 4.1) are composed of relatively small telescopes, with diameters ranging between 15 centimeters to 1.5 meters. The number of telescopes used to combine the light is usually two, but if two facilities work routinely with 3 or more apertures (COAST and NPOI). The maximum baseline length ranges between a few meters up to several hundreds of meters (e.g. SUSI). Almost each interferometer has its own beam combination scheme (see Sect. 4.4.1). They work either in the visible ($0.4 - 1 \mu\text{m}$) or the infrared ($1 - 10 \mu\text{m}$) domains.

Each interferometer has been designed with one main astrophysical objective: synthetic aperture imaging (COAST, UK), high resolution spectroscopy in the visible (GI2T, France), high accuracy measurement in the near-infrared (IOTA, USA), high resolution spectroscopy in the thermal infrared (ISI, USA), wide angle astrometry (NPOI, USA), narrow angle astrometry and phase reference (PTI, USA), stellar astrophysics in the visible (SUSI, Australia). CHARA (USA), which obtained its first fringes at the end of 1999, aims at binary observations and synthetic aperture imaging.

The new generation consists of interferometers with very large telescopes: the VLTI with $4 \times 8\text{-m}$

Table 4.1: List of ground-based optical interferometers in operation or in construction.

Name	Facility	# tel.	\mathcal{D} (m)	\mathcal{B} (m)
COAST	Cambridge Optical Aperture Synthesis Telescope	5	0.4	20
GI2T	Grand Interféromètre à 2 Télescopes	2	1.52	65
IOTA	Infrared & Optical Telescope Array	2*	0.4	38
ISI	Infrared Spatial Interferometer	2*	1.65	85*
NPOI	Naval Prototype Optical Interferometer	3*	0.12*	35*
PTI	Palomar Testbed Interferometer	3	0.4	110
SUSI	Sidney University Stellar Interferometer	2	0.14	640
CHARA	Center for High Angular Resolution Astrophysics	6	1	350
KI-main	Keck Interferometer main array	2	10	60
KI-outriggers	Keck Interferometer auxiliary array	4	1.8	140
VLTI/VIMA	Very Large Telescope Interferometer main array	4	8	130
VLTI/VISA	Very Large Telescope Interferometer sub-array	3	1.8	200
LBT	Large Binocular Telescope	2	8.4	23

* upgrade in progress

telescopes, the *Keck Interferometer* with 2×10 -m telescopes and the LBT with two 8-m telescopes. Their main objective is the gain in flux sensitivity which will allow for the first time the study of extra-galactic sources. Both the VLTI and the *Keck Interferometer* are supplemented by auxiliary 1.8-m telescopes, that are still larger than the largest apertures in the previous generation of interferometers.

4.2 Optical versus millimeter radio interferometry

Optical and millimeter radio interferometry are essentially the same technique used in two different wavelength domains. Although they share the same fundamentals and the same objectives (see Sect. 4.2.1), their implementations can exhibit some significative differences (see Sect. 4.2.2). More details are given in Chap. 21.

4.2.1 Common issues

Both optical and millimeter interferometers study the coherence of the electric field by the mean of separated apertures, called telescopes, siderostats or antennas. The principle of these two techniques is based on the Zernike-Van Cittert theorem, i.e. the degree of coherence of the light is directly related to the Fourier transform of the spatial distribution of the intensity of the observed object [Goodman 1985].

By using separated apertures, both techniques achieve high angular resolution observation, with a resolution tens to hundreds of time larger than single aperture in the same wavelength domain. They therefore face similar difficulties, since they both used diluted arrays and have to find the best array configurations to reach their respective objectives. Similarly to millimeter radio interferometry, optical interferometry has also to calibrate the measured complex visibilities.

When optical interferometry will become as mature as millimeter interferometry, one will probably use very similar algorithm to reconstruct images from the calibrated visibilities.

4.2.2 Main differences

The differences come mainly from the wavelength domains: the typical optical wavelength is $1 \mu\text{m}$, which corresponds to a frequency of 300 THz to be compared with the typical millimeter radio wavelength of 1 mm and the corresponding 300 GHz frequency.

The first consequence is the actual angular resolution that can be achieved, defined by the fringe spacing λ/\mathcal{B} . The typical resolution reached in the optical domain is about 1 milli-arcsecond whereas in the millimeter domain, the Plateau de Bure Interferometer (PdBI) reaches about 1 arcsecond. ALMA

with its extended baselines will be able to get 0.03 arcsecond but the information will still be 100 times less resolved than with optical interferometers.

A second difference comes from the type of detection and beam combination. In millimeter interferometry, the signal detection occurs at the antenna level thanks to the heterodyne technique. The signal is coupled with a reference signal of high coherence and therefore one records the amplitude and the phase of the coming electric field. The signals from each antenna are then digitized and the combination takes place in the correlator (see first chapters of this book). An electronic phase delay is applied to take into account the difference in path length between two arms. In the optical domain, the heterodyne technique has been successful at $10 \mu\text{m}$ [Gay & Journet 1973, Johnson et al. 1974]. This technique however happens to be not sensitive. That is why optical interferometry is usually achieved by direct detection of interferences. The light beams are propagated to a central lab, where the optical path is equalized and are combined to form interferences before being detected. Since the detection techniques measure only the power of the electric field, one has to code the fringes either temporally or spatially (see Sect. 4.4.2). Finally the two techniques give different types of interferences: respectively multiplicative and additive. The heterodyne technique directly gives access to the electric field ψ_k for each aperture and therefore the interference signal is multiplicative (see also Chapter 2 and 21).

The quadratic detection in the direct technique gives additive interferences:

$$I_{kl} = \langle (\psi_k + \psi_l)(\psi_k + \psi_l)^* \rangle = I_k + I_l + 2\sqrt{I_k I_l} v_{kl} \cos \phi_{kl}, \quad (4.1)$$

where $\langle \dots \rangle$ stands for a temporal average over a time long compared to the inverse frequency of the signal, I_k is the intensity of the k -th beam, and v_{kl} and ϕ_{kl} are respectively the amplitude and phase of the normalized visibility. One of the consequences is a different type of calibration process, another is that visibility unit is Jansky in the millimeter domain, whereas in the optical domain it is dimension-less, i.e. flux normalized.

A third and important difference is the influence of the atmosphere. In the optical domain the dominant effect is the corrugation of the wavefront. The spatial Fried's parameter, r_0 , which corresponds to the spatial scale of the turbulence is smaller than the telescope size. Typical numbers are $0.1 - 0.2 \text{ m}$ in the visible and $0.5 - 1 \text{ m}$ in the near infrared. That is a reason why many interferometers have aperture diameters below 1 m (see Table 4.1). In the millimeter, r_0 is larger than the antenna sizes. The temporal Fried's parameter, t_0 , which corresponds to the temporal scale of the turbulence is of the order of $10 - 100 \text{ ms}$ in the optical versus several minutes in the millimeter. That is why it is possible to use phase referencing (phase calibration on a source with known phase) with radio interferometers by off-pointing the interferometer, when it is almost impossible to calibrate the phase in the optical. The only way to retrieve the phase is to measure closure phases with more than 3 apertures or to use a dual-beam interferometer and an accurate metrology like for narrow-angle astrometry (see Sect. 4.3.2). The fact that the phase is almost impossible to get in the optical makes therefore a large difference in the way the data are processed to obtain images.

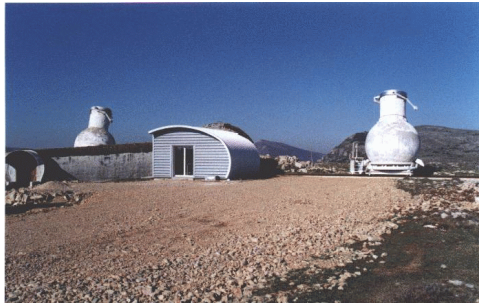
A last difference is the type of noise encountered. The main source of noise in millimeter interferometry is the thermal noise. In optical interferometry, the three type of noises are the photon noise, the read-out noise of the detectors and the background noise, coming either from thermal emission or from the sky brightness. In addition, noise from the atmosphere turbulence, either photometric fluctuations or speckles, must be taken into account.

4.3 Description of optical interferometers

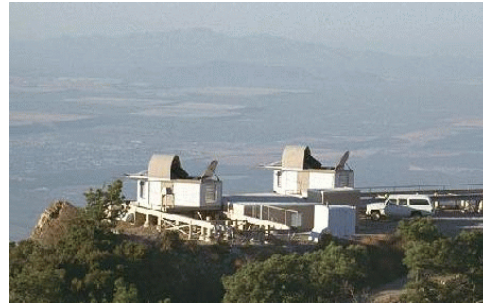
This section is dedicated to the overview of interferometric systems. We first go through the functional description of a typical optical interferometer, then describe the different types of interferometers with specific objectives.

4.3.1 Functional description

Optical interferometry aims at measuring the complex degree of coherence of the observed object. To achieve such a goal, optical interferometers require the following functionalities:



GI2T



IOTA



CHARA



VLTI

Figure 4.2: Four examples of optical interferometers. The array can be linear and continuous (GI2T), L-shaped with several stations (IOTA), Y-shaped with fixed telescopes (CHARA) or the filling of an equivalent 200-m aperture (VLTI).

- **Interferometric array.** Several types of array configurations have been designed in order to give access to the different spatial frequencies (see Fig. 4.2). The three criteria are the number of telescopes, but also the length and the orientation angle of their associated baselines. One can choose to have either fixed telescopes (PTI, KI, VLTI/VIMA) or movable telescopes (GI2T, IOTA, VLTI/VISA). Like in radio interferometry, Earth rotation allows to sample the uv tracks. If the object displays a wavelength-independent structure like a binary, the coverage of the uv plane can be performed with spatial frequencies at different wavelengths.
- **Apertures.** They ensure the light collection. Either siderostats (IOTA, PTI, SUSI) with diameter less than 50 cm or more or less traditional telescopes (GI2T, CHARA, KI, VLTI) for larger diameters can be used. In case of large siderostats, a fixed beam compressor is used to compress the beam diameter for propagation toward the central lab.
- **Beam transportation.** Once the object light has been captured by the apertures, one carries out the individual beams toward the combination laboratory. Usually the optical path is designed so that a complete symmetry of the mirrors in each arms minimizes the differential polarization effects. The optical train contains typically of the order of 20 mirrors. [Froehly 1981] suggested to use optical fibers to carry the light from the apertures to the lab. This technology has been tested by [Coudé Du Foresto, Mazé, & Ridgway 1993] and is the key of the coming O'HANA project which will gather the light from the 8-m class telescopes on the Maunaea Kea in Hawaii [Perrin et al. 2000]. Some interferometers use vacuum optics (PTI, IOTA, NPOI,...) to decrease the dispersion due to the propagation in the air of the delayed beam (see Sect. 4.5.2).
- **Wavefront correction.** The incoming light travels through the atmospheric turbulence (see Sect. 4.5.1). The wavefront is then corrugated and the images of the object move due the *seeing*. Almost

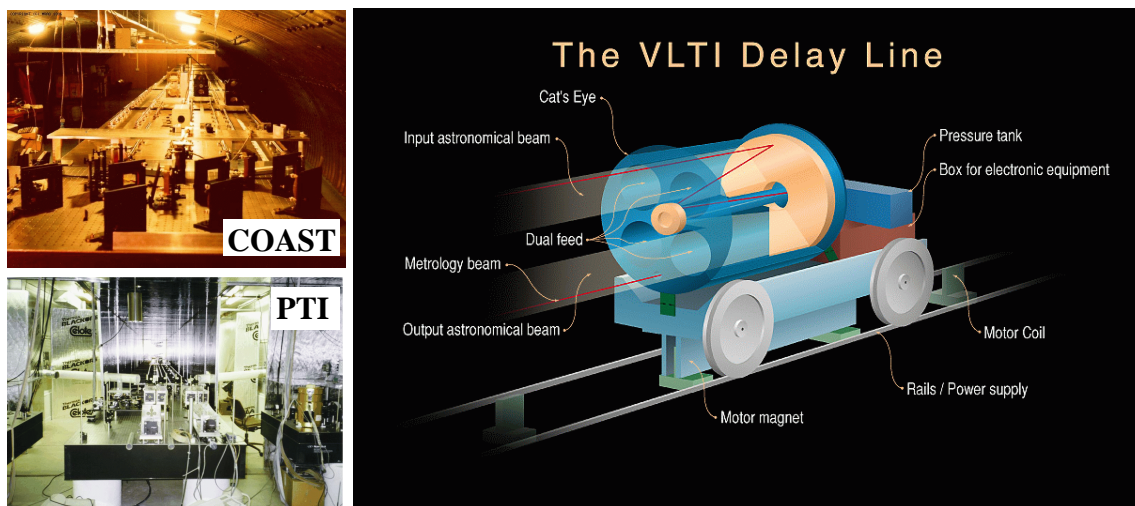


Figure 4.3: Some examples of delay lines

all interferometers have therefore at least a 2-actuator adaptive optics system that corrects from the tip and the tilt (IOTA, NPOI, PTI). Large interferometers with aperture diameter larger than 1 m have plans for higher correction of the wavefront (VLTI/VIMA, KI-main, GI2T, LBT, CHARA). The goal is to stabilize the light and to increase the Strehl ratio of individual beams, i.e. the quality of the central peak. One should note that GI2T currently works in multi-speckle mode and therefore does not formally require AO systems to properly work, even if it would increase its sensitivity performance.

- **Delay lines.** When the object observed is traveling across the sky, the external optical path difference (OPD) between two arms is equal to $B \sin z$, where B is the baseline length and z is the zenith angle. To achieve the fringe detection, the two arms should be equal at the level of the micrometer. In the first experiment by [Labeyrie 1975], the stabilization of the OPD was performed by moving the beam combination table. Nowadays, most interferometers prefer to use optical delay lines (DL) using cat's eyes located on movable chart. Moving a DL either in one arm or another compensates the sidereal motion of the star, exactly like telescope mounts follow the stars displacements. For very long delays, one often has to design and build long DLs that offer only optical delays by steps of a few meters coupled with DLs with shorter strokes (KI, CHARA).
- **Optical path difference stabilization.** The atmospheric turbulence produces not only wavefront corrugation at the level of individual apertures but also at the level of the interferometer called atmospheric piston. The consequence is that the OPD is fluctuating and the fringes move back and forth. Using a fringe sensor (a simple beam combiner that measures the OPD at a frequency higher than the typical atmosphere timescale), one is able to send corrective commands to the DLs. This feature is the zero-degree of adaptive optics for an interferometer. A fringe sensor coupled with a DL is called a fringe tracker and allows to stabilize the signal for longer integration.
- **Beam combination.** The interferences between the various beams can be achieved in many ways (see Sect. 4.4). One usually distinguishes the so called co-axial beam combiners (BCs) that combine the light coming from the same optical axis (like with a beam splitter in the laboratory Michelson interferometer) and the multi-axial ones that produce interferences between beams coming from different directions (like in the Young's experiment). The beam combination is usually made with lenses, mirrors and/or beam splitters. However, the optical functions used by the telecommunication industry has given birth to fibered BCs (e.g. FLUOR [Coudé Du Foresto, Mazé, & Ridgway 1993]) and integrated optics ones (see IONIC experiment [Malbet et al. 1999]) using single mode wave-

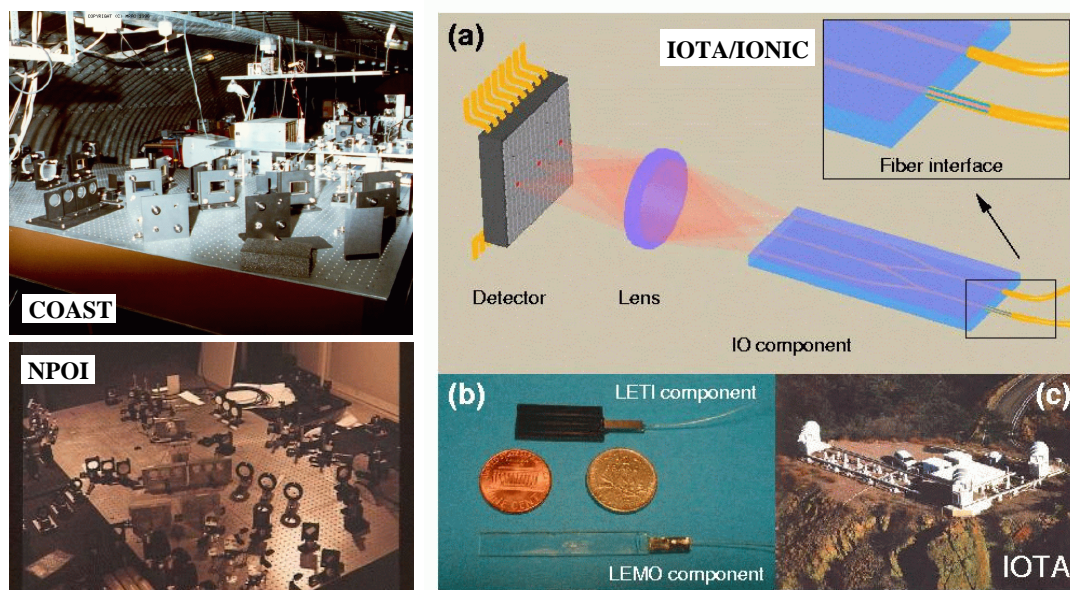


Figure 4.4: Beam combiners. Left: beam combiners in bulk optics. Right: beam combiners using the integrated optics technology.

guides.

- **Detection.** This fundamental step makes use of photon detector either with photo-counting capability in the visible range or CCD with low read-out noise in the infrared. The dispersion of the light can be done just before the detection and the instrument looks similar to a spectrograph.

The schematic layout of the VLTI is displayed on Fig. 4.5. It is typical of most of interferometers. A difference is that the focal plane hosts several instruments: VINCI the commissioning BC based on known technology, AMBER the near infrared spectrograph and MIDI the thermal infrared camera. Smaller interferometers have usually only one dedicated instrument optimized for their astrophysical targets (binaries, stellar diameters, envelopes,...).

4.3.2 Specific applications

I see 5 types of scientific usages of the interferometric light combination.

Interferometry in the past has been most often used with only **two apertures**. Therefore since the atmospheric piston prevents any absolute phase calibration, the astronomers can only measure the amplitude of the complex visibility and a phase difference between two spectral channels when the instrument has some spectroscopic capability. The goal is then to measure the visibility amplitude or a differential phase, also called two-color phase, and to interpret the variations of these measurements with time, with baseline length, or with baseline angle. An important field of application is the measure of stellar diameters and binary orbits, but recently it has been extended to circumstellar envelopes and accretion disks.

The dream of most interferometrists is to perform actual imaging like in the radio domain using **aperture synthesis**. The interferometer COAST has been built with this goal in mind. That is why it is composed of 4 telescopes in order to increase the efficiency of the uv plane coverage, but also to use the technique of closure phases. This closure phase technique, used to be of high importance in radio interferometry, allows to self-calibrate the sum of the phases measured simultaneously by three baselines. This method is very similar also to the bispectrum one in speckle interferometry. However for technical reasons, the beam combination of $N \geq 3$ beams appears to be difficult and only few reconstructed images

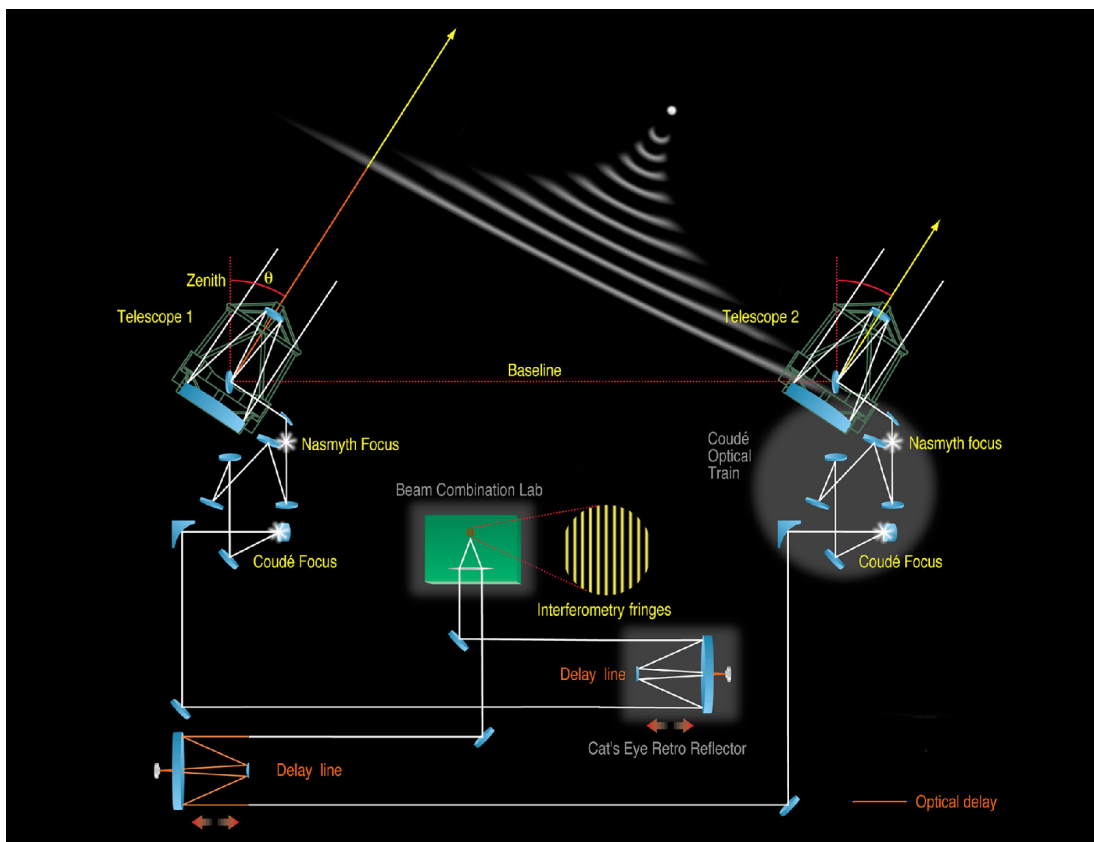


Figure 4.5: VLTI optical layout

have been obtained so far. The outcome of integrated optics might change the situation in the future [Malbet et al. 1999].

The group working on NPOI has been focusing on the **wide-angle astrometry** for a long time (previously at the Mark III interferometer, ancestor of PTI and NPOI). The idea is simple and once again similar to what is being done in radio: when the interferometer detects fringes, the two paths of the interferometer are equal to a fraction of a micrometer. Since the delay due to the sidereal motion of the stars is given by

$$\delta = \mathcal{B} \cos \theta + C, \quad (4.2)$$

where \mathcal{B} is the length of the baseline, θ is the altitude of the star in the sky and C an internal constant, then the knowledge of \mathcal{B} and C together with the measure of the stroke given to the DL give access to $\cos \theta$. The objective consists in measuring the group delay of several tens of stars at different moments of the night and to fit the curves with cosine of the same amplitude \mathcal{B} . The internal metrology measures the internal constant C . After post-processing, both the position of the stars and the baseline are deduced with a precision of the order of the fringe spacing λ/\mathcal{B} , i.e. about 1 mas.

Recently, following the work on Mark III, [Shao & Colavita 1992] proposed the **narrow-angle astrometry** technique. The idea is to observe two objects sufficiently close so that the atmospheric perturbations affecting the stellar path on each telescope is almost the same for the two objects. The correlations in the perturbations is used to increase the accuracy of astrometric measurements down to $10 \mu\text{as}$ opening the search for the reflex motion of stars due to the presence of planets. To achieve such an objective, one has to separate the field at each aperture in two sub-apertures and to propagate in parallel the light from the two stars in two different interferometric systems. A differential metrology allows to link the two interferometers. When the fringes are detected on the two detectors, the differential metrology gives the

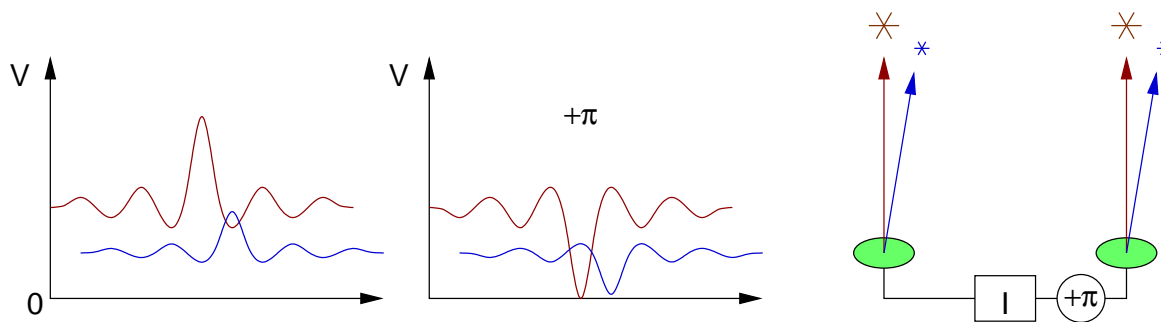


Figure 4.6: Principle of a nulling interferometer (see text for details).

differential delay between the two stars:

$$\Delta\delta = \mathcal{B}\Delta\theta + d, \quad (4.3)$$

Where $\Delta\theta$ and d are respectively the differential angle between the two stars and the internal constant. One interesting application of such a dual interferometer is **phase referencing** like in radio: if a close-by reference star has a zero-phase then the measure $\Delta\delta$ leads to the actual phase of the science target. In radio, the atmosphere is quiet enough to measure the phase reference by depointing the interferometer whereas in the optical domain, the two measurements must be made at the same time. The PTI is the interferometer that hosts this technique.

Finally, many groups are working on the concept of **nulling interferometers**. The idea [Bracewell 1978] is to use the coherence of the light to interferometrically cancel the light arriving in the interferometer boresight. An object located off-axis has translated fringes. In certain directions, the bright peaks of the object fringes are located over the dark zones of the central star fringes. If the nulling in the dark fringes is high enough, the dynamic range of this technique can reach high values (see Fig. 4.6). This application is extremely interesting in the case of the study of extra-solar planets. Those planets are expected to be between 10^4 and 10^9 fainter than their parent stars. Nulling the light of the central star is the only way to detect photons from these worlds. To achieve such performances, the instruments like DARWIN pill up several stages of such nulling interferometers to reach high rejection rate.

4.4 Formation of the interferometric fringes

In this section, I focus on the light combination and the signal detection.

4.4.1 Beam combination

[Mariotti et al. 1992] tried to classify the different types of beam combination (see Fig. 4.7). They have defined 4 levels of criteria:

- **Beam étendue:** what is the field accessible by the detector at each telescope? If this field is limited to the diffraction pattern of the telescope, then the interferometer is called *single-mode*, whereas if the interferometer processes more information than the one in the diffraction pattern it is *multi-mode*. For example in radio, all interferometers are single-mode.
- **Beam direction:** how the light coming from the different arms are combined? If the beams are combined with beam splitters so that they appear to come from the same direction, then the combination is called *co-axial* (see Fig. 4.8a) and gives a flat tint on the detector. If the beams appear to come from various direction (see Fig. 4.8b) like in the Young's experiment the beam combination is called *multi-axial*.

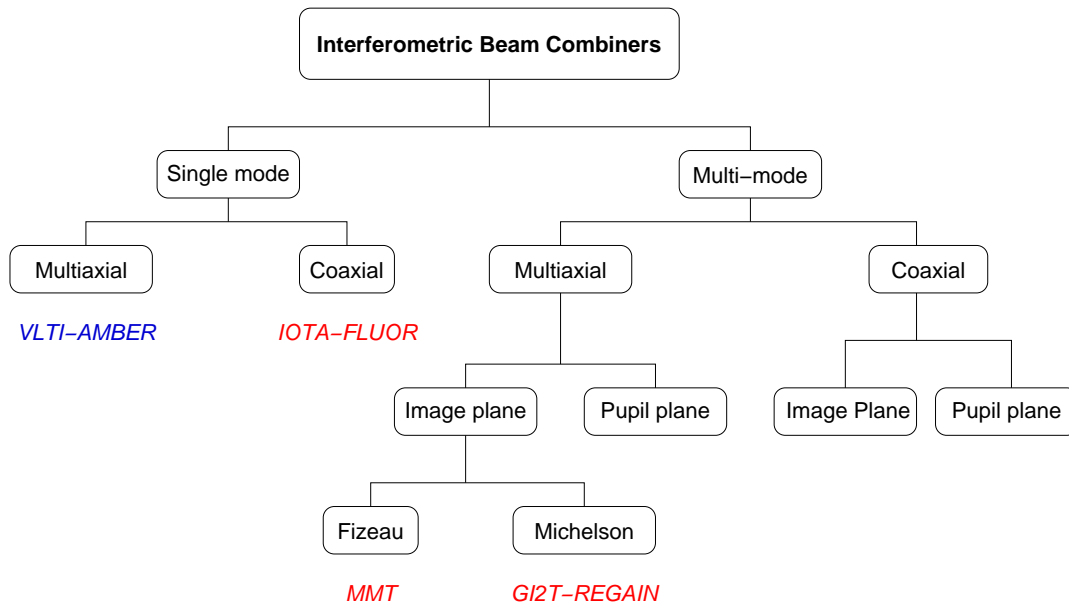


Figure 4.7: Mariotti's classification (adapted from [Mariotti et al. 1992]).

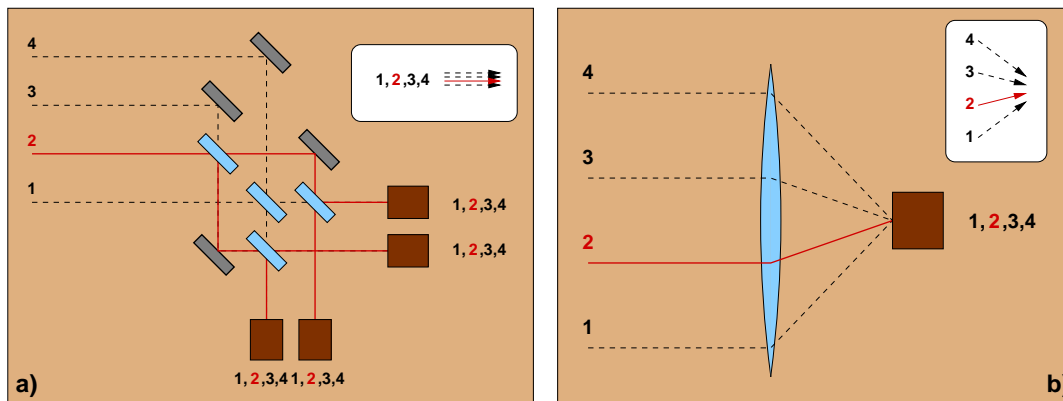


Figure 4.8: All-in-one coaxial (left) and multiaxial (right) 4-way beam combination schemes.

- **Combination plane:** does the beam combination occur in the *image plane*, conjugated with the sky, or, in the *pupil plane*, conjugated with the telescope pupils (see Fig. 4.9)?
- **Relation between the input and output pupils:** what is the interferometric field of view? The answer depends on the relationship between the input / output¹ pupil geometry. One can distinguish 3 cases:
 1. *Fizeau-Stéphan* setup where the input and output pupils are homothetic (both pupil separation and diameters).
 2. *Densified pupil* used by the hyper-telescopes [Pedretti et al. 2000] where the position of the sub-pupils in the output pupil are scaled to the input ones but the diameters of the sub-pupils are magnified.
 3. *Michelson-Pease* setup where there is no link between the input pupils and the output pupils.

The resulting field of view (FoV) are sorted by increasing size: $FoV_1 \geq FoV_2 \geq FoV_3$. The Fizeau-Stéphan set-up gives access to a larger field of view but is difficult to implement since the homothetic relation must be conserved during the transit of the object. It would require continuously reconfigurable beam combiners.

The tree that corresponds to this classification (see Fig. 4.7) shows the complexity of beam combination in optical interferometry. However, all but one current interferometers have been designed to be single-mode, GI2T-REGAIN being the only one using the multi-mode beam combination scheme.

4.4.2 Fringe coding and detection

Once the beams have been combined, one still needs to detect the fringes. Since optical detectors have access only to the intensity of the electric field, the signal must be modulated in phase in order to measure both the amplitude and the phase of the visibility. The signal measured from the combination of two arms A and B is deduced from Eq. (4.1):

$$I(\phi_{\text{mod}}) = I_A + I_B + 2\sqrt{I_A I_B} V_O V_I \cos(\phi_O + \phi_{\text{mod}}). \quad (4.4)$$

The goal is to evaluate the complex visibility $V_O \exp(i\phi_O)$ of the object. One needs to modulate ϕ_{mod} so that the variation of $I(\phi_{\text{mod}})$ in function of ϕ_{mod} leads to the amplitude of the visibility. There are mainly two types of fringe coding: the temporal or spatial coding.

In the multiaxial combination scheme, since the beams from the different arms come from different directions, $\phi_{\text{mod}}(x) = 2\pi(bx/d)/\lambda$. Therefore analyzing the light at different positions on the detector plane, gives the visibility information (see Fig. 4.10). In the coaxial combination scheme, one introduces a variable optical path length on one arm: $\phi_{\text{mod}}(\delta) = 2\pi\delta/\lambda$ (see Fig. 4.11). There exists also other types of coding using the polarization or wavelength dependence of the phase, but they are rarely used.

When combining more than two beams, one has to decide if one uses all-in-one or pairwise beam combination. When the number N of telescopes increases the all-in-one combination is preferred because it involves less optical elements. In a pairwise scheme, all beams must be splitted in $N - 1$ beamlets to be combined with the other telescopes. The all-in-one solution is displayed both for co-axial and multi-axial combinations in Fig. 4.8. However, one has to be cautious on the redundancy of the fringe frequencies so that the signals from two different baselines are not mixed together. That is why in the multi-axial combination the sub-pupils are separated by non-redundant separations, and, in co-axial combination the OPD scan frequencies and amplitudes are also not redundant.

4.5 Main challenges in interferometry

In this section, I address the main difficulties encountered in optical interferometry. The main one is the effect of turbulence due to the atmosphere. I will also tackle the limitation in terms of performance due to the various types of noise.

¹The input pupil is the plane where the electric field coming from the object enters the interferometer. The output pupil is the plane where the electric field exiting from each optical train before being combined on the detector.

4.5.1 Atmosphere turbulence

The main effect of the presence of the atmosphere is the corrugation of the incoming wavefronts. Due to difference of temperature between the ground and the upper layers of the atmosphere, convection occurs and creates turbulent eddies. These eddies are characterized by different temperature and therefore different refractive indices. They move up and down with different spatial scales. When looking to objects through the atmosphere, the light rays are deviated randomly, i.e. the plane incoming wavefront is corrugated by different phase delays depending on the total optical thickness of the atmosphere along the propagation path (see Fig. 4.12). In optical interferometry, this phenomenon called *seeing* yield two main consequences:

- at each telescope pupil entrance, the **local wavefront is corrugated**. One does not get diffraction-limited images of the object, but seeing-limited ones. In short exposure images and for multi-mode interferometers, the image is formed of various speckles (see left panel of Fig. 4.13) and in long-exposure images its typical size is given by the characteristic size of turbulent cells where the light is coherent, i.e. several tenths of meters. In addition, these features move with time at timescale of several milliseconds. In the case of single-mode interferometers, the speckles are spatially filtered at the entrance of the interferometer and are translated in fluctuations of the light coupling. Therefore one has to correct from the photometric fluctuations induced by the turbulence (see right part of Fig. 4.13 and Sect. 4.5.3).
- the atmosphere induces **fluctuations of the optical path differences** for each baseline. The result is that the fringes are not stable at a given optical delay but randomly move around the sidereal position. It is impossible to calibrate the phase of the fringes and their amplitude is also decreased due to smearing during the integration time.

The atmosphere decorrelates the phase between different points of the incoming wavefronts both in space and in time. That is why we usually present the turbulence as yielding coherence volumes inside which the wavefront can be considered as a non-disturbed plane wave. The geometric parameters of the coherence cell are called the Fried's parameters:

- the size of the cell, r_0 , typically 10 cm at $\lambda = 0.5 \mu\text{m}$ and 1 m at $\lambda = 2.5 \mu\text{m}$ depending of the turbulence strength.
- the coherence time, t_0 , typically 10 ms at $\lambda = 0.5 \mu\text{m}$ and 100 ms at $\lambda = 2.5 \mu\text{m}$.

The turbulence occurs at different spatial scales and a popular model is the Kolmogorov model that represents the power spectrum of the turbulence as a power law [Roddiier 1981]. However the turbulence at small spatial frequencies saturates, i.e. the size of the largest eddies is limited. This limit, L is called the outer scale of the turbulence and is important in interferometry since we estimate its size to be of the order of 10 – 100 m, typical lengths of most interferometer baselines. If the baseline is larger than the outer scale then the effect of turbulence is less than predicted by the Kolmogorov model.

4.5.2 Other atmosphere systematics

Optical interferometers must also take into account the atmospheric **refraction** and the **longitudinal spectral dispersion**.

The wavelength dependence of the air refractive index implies wavelength-dependent refraction angles when the light enters the atmosphere. The atmosphere acts like a prism and the images at each aperture are spectrally dispersed. Single mode interferometers spatially filter the incoming wavefront, that means they select a part of the image. Therefore this refraction effect decreases the coupling factor in the interferometer. The larger the telescope size, the smaller the diffraction-limited images: this effect begins to be important for large telescopes. **Atmospheric dispersion correctors** are classical devices made of two prisms that can rotate and compensate the dispersion due to the atmosphere refraction.

The refraction induces chromatic arrival angle, but does it result in chromatic OPD. Fig. 4.15 shows that even if the optical paths are different for two different wavelengths, they are the same for each aperture and the OPD remains zero for all wavelengths. The refraction does not yield a chromatic OPD.

However, the optical delay due to the zenith angle of the observed object has to be compensated by delay lines. If the delay lines are located in vacuum the compensation matches exactly the geometrical delay above the atmosphere, but if the optical delay is performed in air, then the compensation is performed only for one wavelength because of the chromatism of the air refractive index $n(\lambda)$. The resulting OPD given by a delay L of the delay line that matches the geometrical delay δ at $\lambda = \lambda_0$ is then:

$$OPD(\lambda) = \left(\frac{n(\lambda)}{n(\lambda_0)} - 1 \right) \delta \quad (4.5)$$

Therefore the location of the zero-OPD changes with wavelength. At high spectral resolution, the main effect is to twist the fringes, whereas at low spectral dispersion the contrast of the fringes can be severely decreased. To overcome this effect and besides using vacuum delay lines, two translating prisms produce a variable glass thickness that compensates exactly the chromatic OPD. This device is called a **longitudinal dispersion compensator**.

4.5.3 Fighting the atmosphere: complexity and accuracy

The previous sections show that the propagation in the air implies several problems. The chromatic effect of the air refractive index can be compensated by an atmospheric dispersion compensator and a longitudinal dispersion corrector. These phenomena are completely predictable and therefore can easily be controlled by computer in function of the zenith angle.

However the effect of the turbulence is much more difficult to control since the time scale is of the order of several milliseconds and the spatial scales are small. Adaptive optics (or tip-tilt compensation) and fringe trackers are therefore required to increase the sensitivity of optical interferometers (see Sect. 4.3). However the correction is never perfect and some residuals can still affect the signal.

One solution is to use speckle techniques to calibrate those residuals. GI2T has proven that one can use several speckles to calibrate the visibility of an object. Another method is to filter out the incoming wavefront. The principle is well-known by the opticians: they clean up images by placing so-called *spatial filters* in the Fourier plane associated to the images. With a pinhole at the focus of a telescope, the wavefront in the exit pupil is then cleaned up and flat. The wavefront corrugation is transferred in intensity fluctuations since the speckle image on the pinhole is not stable. Optical waveguides, like optical fibers, are optical devices that behave like infinitively small pinholes but with a high coupling efficiency (typically 70%). The signal that exits from a waveguide is an electric field whose shape is given by the geometry of the waveguide (and therefore is fixed) and for which only two parameters can vary: the global amplitude and the phase. By measuring the variations for the photometry for each beam, we can compute a visibility corrected from the atmospheric perturbations. The visibility estimator,

$$V_{\text{corr}} = \frac{2\sqrt{I_A I_B}}{I_A + I_B} V_{\text{mes}}, \quad (4.6)$$

little depends on the turbulence with V_{mes} the raw visibility, I_A and I_B the intensities measured for each beam.

This method has proven to be very accurate in measuring visibilities. FLUOR reaches 0.3% for some targets [Coudé Du Foresto, Ridgway, & Mariotti 1997]. However, one should keep in mind that the measured visibility is not exactly the object visibility except if the object is not resolved by the individual apertures. When the object is larger than the projected size of the spatial filter on the sky, one has to apply a visibility correction using the information given by the image obtained with the resolution of the individual apertures.

4.5.4 Noise sources - Sensitivity

The signal measured with an optical interferometer is affected by several sources of noises. In the case of the instrument AMBER on the VLTI these sources of noises are:

- the **photon noise** is the fundamental noise associated to the detection of the photons. It follows a Poisson-type statistics.

- the **detector read-out noise** is the noise of the electronics that reads the signal. It is an additive Gaussian noise with a characteristic level called the read-out noise (RON).
- the **thermal noise** is the noise that comes from the detection of background photons. The background level is measured and subtracted. The background estimation gives an error due to the photon statistics.
- the **instrument OPD stability** is not a noise that affects the detected photons, but the measured visibility. The residual motions of the optics in the instrument induce a blurring of the fringes at a small level. In AMBER, we expect this level to be lower than 10^{-4} of the unit visibility.
- the **atmosphere fluctuations**, even corrected by simultaneous measurements of the photometry induce degradation of the signal-to-noise ratio. The obvious situation is the case where no photons are coupled into the interferometer.

Computing the error propagation in the final signal allows to calculate a signal-to-noise ratio (SNR) for different type of situations. To illustrate the consequence of the source brightness on the performance of an interferometer, I show in Fig. 4.17 the SNR curve for different star magnitudes in the case of the AMBER instrument on the unit telescope of the VLTI with different typical values of the site.

For bright objects the dominant noise source is the instrument stability. When observing faintest objects, the limitations become first the photon noise, then depending on the integration time, either the thermal background noise or the read-out noise.

4.6 Conclusion

I have presented some elements of the present state of the art in optical interferometry focusing on the functional description, some design choices and the various limitations with the objective to give to the readers the keys to compare this technique with radio interferometry at millimeter wavelengths.

We see that optical interferometry is a younger technique than the radio interferometry because of the complexity of the systems mainly due to the struggle against the atmosphere. It leads to smaller spatial resolution but has still to learn from the radio experience.

We are entering a new era where optical interferometers with large telescopes and increased sensitivity become general user instruments (KI, VLTI). I did not address the topic of optical interferometry in space that faces other challenges. However the search for extra-solar terrestrial planets is certainly driving this area with two main projects: the Space Interferometry Mission (SIM) dedicated to astrometry and the TPF/DARWIN mission focused on nulling interferometry.

Note: To obtain exhaustive and todate information on optical interferometers, I advise the reader to browse **OLBIN**, the **optical long baseline interferometry newsletter** managed by P. Lawson. The address is <http://olbin.jpl.nasa.gov>.

Figure credits

Fig. 4.1: L. Rarogiewicz, Mount Wilson Observatory.

Fig. 4.2: Département Fresnel, Observatoire de la Côte d'Azur; Smithsonian Astrophysical Observatory and Harvard University Center for Astrophysics, University of Massachusetts; Georgia State University; European Southern Observatory.

Fig. 4.3: Mullard Radio Astronomy Observatory, University of Cambridge; Jet Propulsion Laboratory, Palomar Observatory; European Southern Observatory.

Fig. 4.4: Mullard Radio Astronomy Observatory, University of Cambridge; US Naval Observatory, Naval Research Laboratory, Lowell Observatory; Laboratoire d'Astrophysique, Observatoire de Grenoble.

Fig. 4.5: European Southern Observatory.

Fig. 4.7: European Southern Observatory [Mariotti et al. 1992].

Fig. 4.10: right panel, Infrared Interferometry Group, Max-Planck Institut für Radioastronomie.

Fig. 4.11: right figure, Laboratoire d'Astrophysique, Observatoire de Grenoble.

Fig. 4.13: Annual review of astronomy and astrophysics [Labeyrie 1978]; Laboratoire d'Astrophysique, Observatoire de Grenoble.

Fig. 4.14: AMBER consortium OCA, LAOG, UNSA, MPIfR, OAA (AMB-OSM-007 report).

Fig. 4.16: Astronomy & Astrophysics Supplement Series, EDP Sciences [Coudé Du Foresto, Ridgway, & Mariotti 1997]; DESPA, Observatoire de Paris-Meudon.

Fig. 4.17: AMBER consortium OCA, LAOG, UNSA, MPIfR, OAA (Instrument Analysis PDR Report).

Internet resources

The following web sites have been used for some figures of this chapter.

- Mount Wilson Observatory, 20ft interferometer: <http://www.mtwilson.edu/Tour/100inch/20ftI> (Fig. 4.1)
- GI2T: <http://www.obs-nice.fr/fresnel/gi2t> (Fig. 4.2)
- IOTA: <http://cfa-www.harvard.edu/IOTA> (Fig. 4.2)
- CHARA: <http://www.chara.gsu.edu/CHARA> (Fig. 4.2)
- VLTI: <http://www.eso.org/projects/vlti> (Figs. 4.2, 4.3, 4.5)
- COAST: <http://www.mrao.cam.ac.uk/telescopes/coast> (Figs. 4.3, 4.4)
- PTI: <http://huey.jpl.nasa.gov/palomar> (Fig. 4.3)
- NPOI: <http://ad.usno.navy.mil/npoi> (Fig. 4.4)
- IONIC: <http://www-laog.obs.ujf-grenoble.fr/activites/hra/ionic> (Figs. 4.4, 4.13)
- MPIfR: <http://www.mpifr-bonn.mpg.de/div/ir-interferometry> (Fig. 4.10)
- AMBER: <http://www.obs-nice.fr/amber> (Figs. 4.14, 4.17)
- FLUOR: <http://despa.obspm.fr/fluor> (Fig. 4.16)

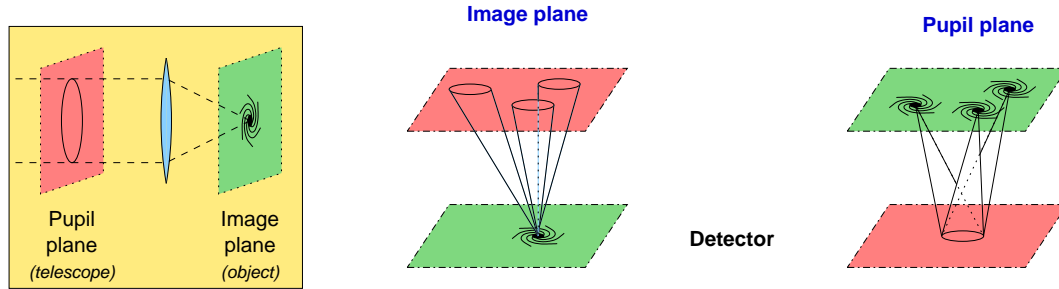


Figure 4.9: Combination planes.

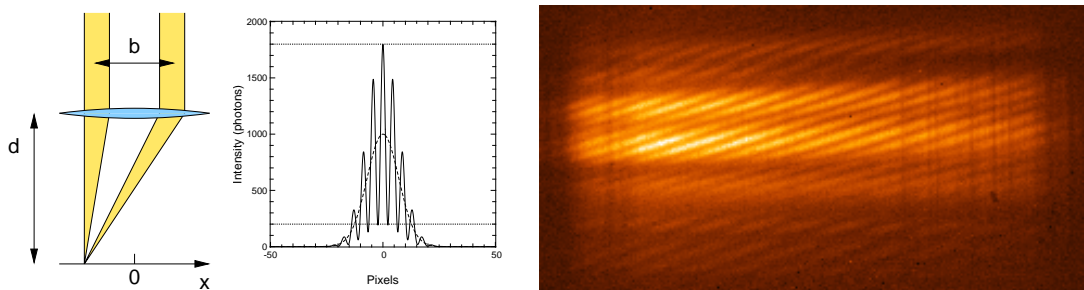


Figure 4.10: Multiaxial beam combination and spatial coding of two-aperture fringes. Left: the OPD changes with the x -position on the detector. Center: the fringes appear superposed to the beam shape. Right: fringes (y -axis) spectrally dispersed (x -axis) in the IR channel of GI2T [Weigelt et al. 2000].

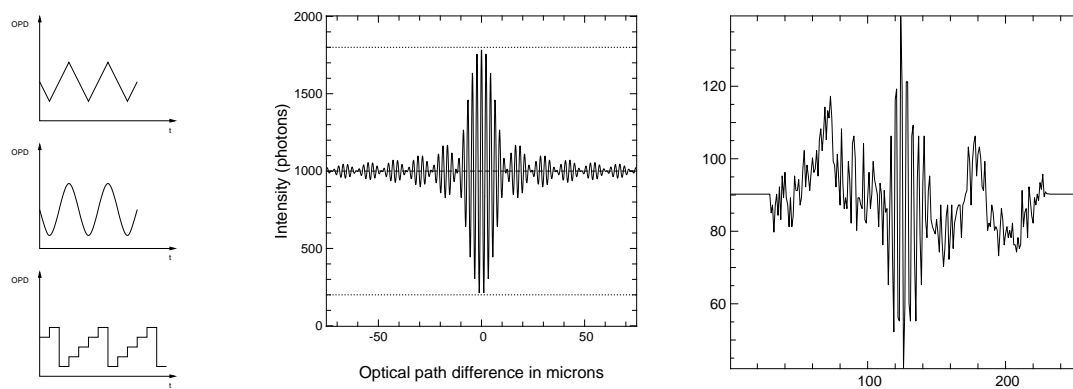


Figure 4.11: Coaxial beam combination and temporal coding of two-aperture fringes. Left: different types of OPD modulation. Center: theoretical signal. Right: signal observed with the IR table at IOTA.

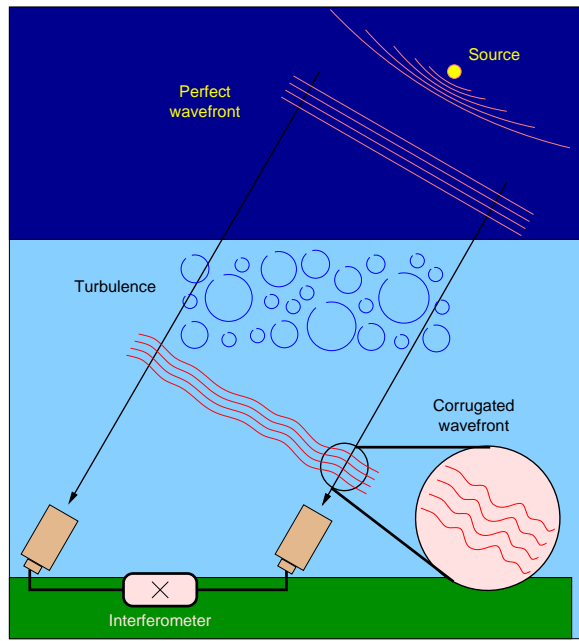


Figure 4.12: Effect of the atmosphere turbulence on the incoming wavefronts.

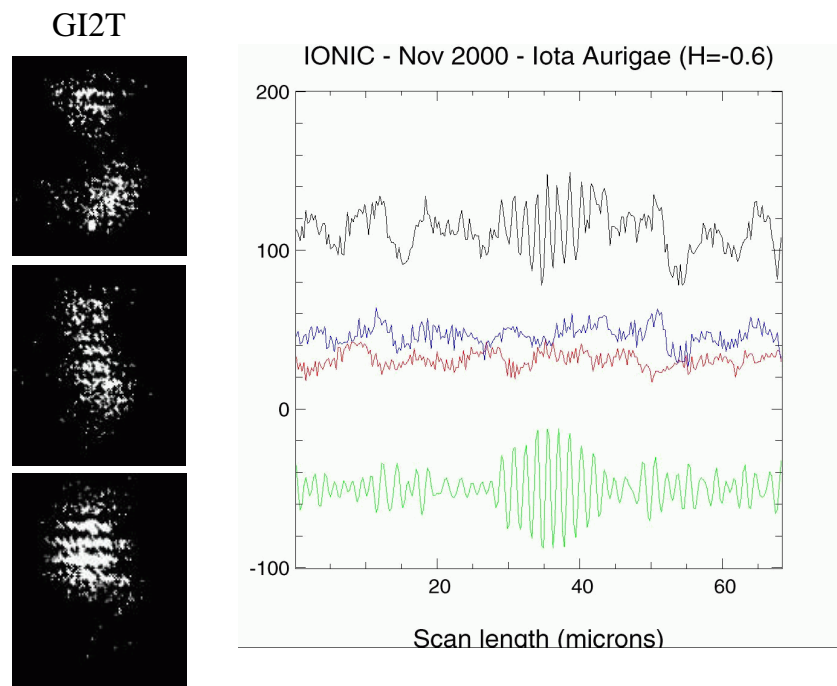


Figure 4.13: Effect of the turbulence of each aperture. Left: in multi-mode beam combination, the image is formed of speckles with fringes at different phases (GI2T, adapted from [Labeyrie 1978]). Right: in single-mode beam combination, the wavefront corrugation is translated into photometric fluctuations (IONIC, [Berger et al. 2001]). Upper curve: raw interferometric signal; center curves: photometric signals; lower curve: photometry-corrected interferometric signal (see also Sect. 4.5.3)

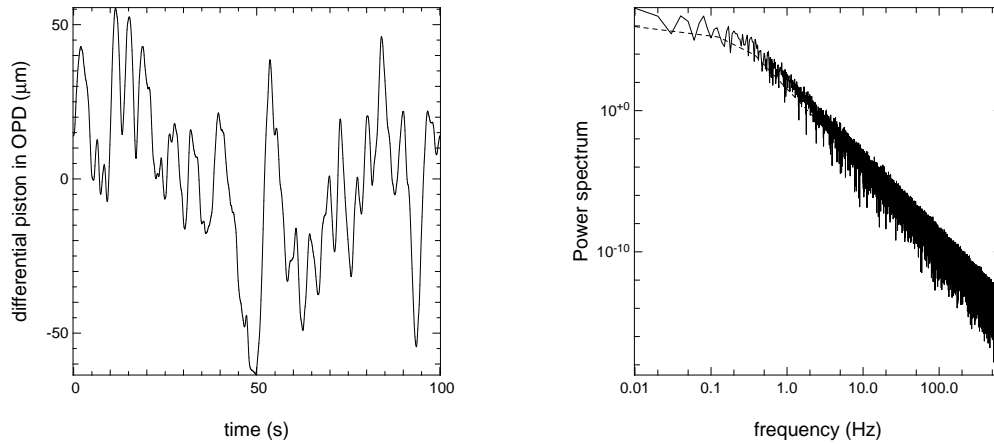


Figure 4.14: Optical path fluctuations due to the turbulence. Left: simulations of the fluctuations for two Unit Telescopes at the VLTI with typical seeing parameters (in microns). Right: the power spectrum of the fluctuations follows a Kolmogorov law with a saturation at low frequency due to the outer scale.

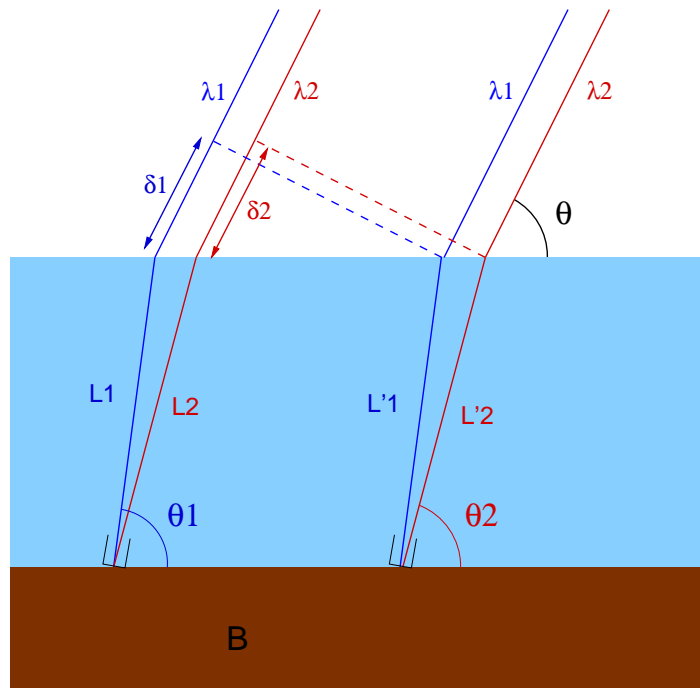


Figure 4.15: Effect of the atmosphere refraction. The object image at each telescope entrance is in fact a small spectrum. However there is no effects on the optical delay since the optical path for the two beams in the atmosphere is the same at each wavelength λ_1 and λ_2 , and, the resulting OPD does not depend on wavelength. Even if $L_1 \neq L_2$, we have $L_1 = L'_1$ and $L_2 = L'_2$, and $\delta_1 = \delta_2$.

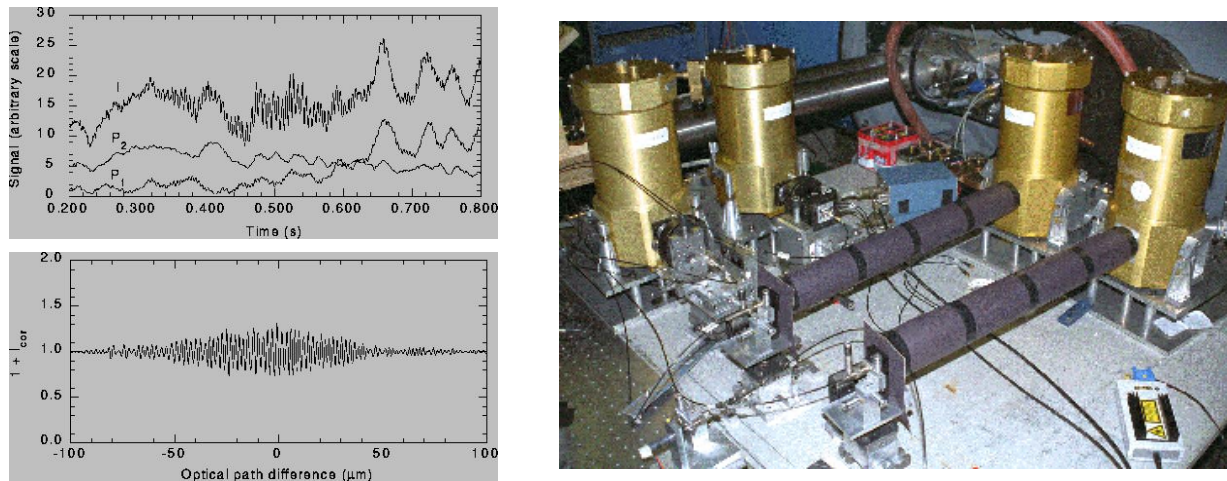


Figure 4.16: The FLUOR fiber beam combiner (right). Example of incoming signals: left top panel shows the raw signal with two photometry channels that monitors the coupling in the fibers; left bottom panels shows the corrected interferogram from [Coudé Du Foresto, Ridgway, & Mariotti 1997].

K-UT ($V_{\text{obj}}=1$, Seeing=0.5", $N_{\text{bact}}=64$, $R_{\text{disp}}=70$, $t=100\text{s}$, $N=1$, FT=1, OFF=0)

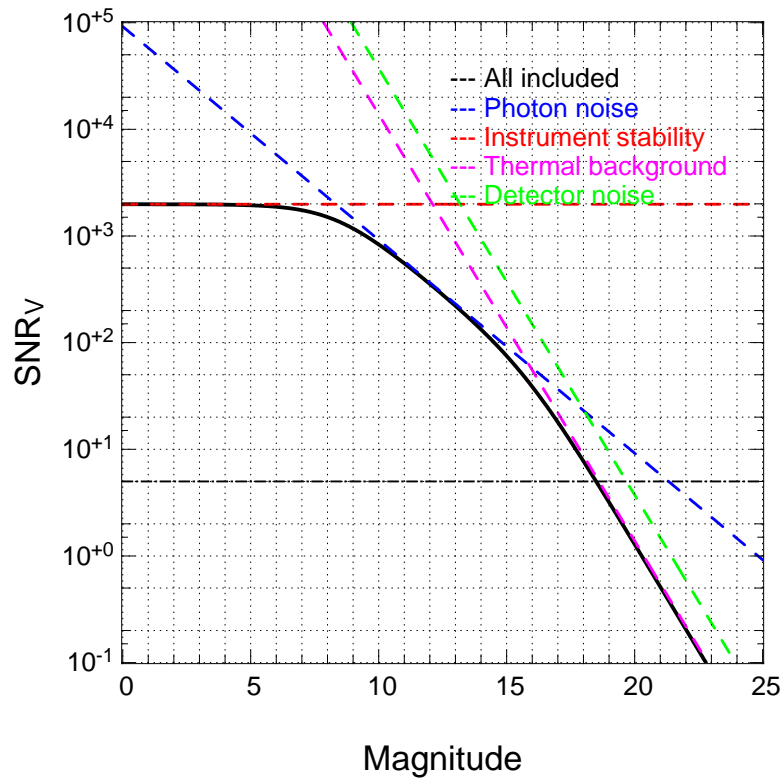


Figure 4.17: Signal-to-noise ratio computed for the AMBER instrument at the VLTI in the K band ($2.2 \mu\text{m}$) for an object of visibility of 1, a seeing of $0.5''$, a low dispersion, and a long exposure using fringe tracking.

Chapter 5

Receivers : an overview for non-specialists

Bernard Lazareff

`lazareff@iram.fr`

IRAM, 300 rue de la Piscine, F-38406 Saint Martin d'Hères, France

5.1 Introduction

The purpose of a receiver is to collect efficiently the astronomical signal that has been concentrated by the antenna near its focal point, and to amplify it with a minimum of extra noise to a level suitable for further processing by the spectrometers or continuum detectors. This is illustrated by figure 5.1.

Figure 5.2 shows the main subsystems of a receiver, that we will discuss below.

5.2 Coupling optics

Up to and including the antenna, the astronomical signal propagates in free space. On the other hand, the first signal processing unit —the mixer— requires the electromagnetic energy to be confined by metallic walls, in a waveguide. The transition between these two modes of propagation occurs at the *horn*.

Assume for a moment that the horn would be placed at the Cassegrain focus of the antenna. Good matching would be difficult to achieve because the field amplitude from a point source (Airy pattern) exhibits radial oscillations alternating between positive and negative values, and has a scale size proportional to wavelength.

These problems are avoided by coupling —via suitable relay optics— the horn to an *image of the aperture*. This fulfills the condition of *frequency-independent illumination*. In other words, imagine that we propagate the horn mode back to the antenna aperture as if we were dealing with a transmitter, then the illumination pattern is independent of frequency. Using suitably designed corrugations on the inner

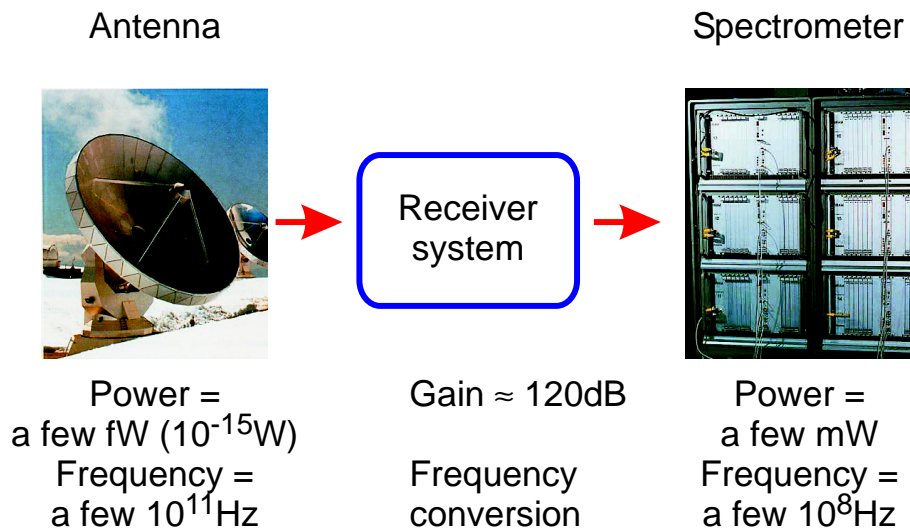


Figure 5.1: Orders of magnitude for frequencies and power levels delivered by the antenna to the receiver, and by the receiver to the spectrometer. The main roles of the receiver are to down-convert the signal frequency to a range suitable for analysis, and to amplify it while adding as little noise as possible.

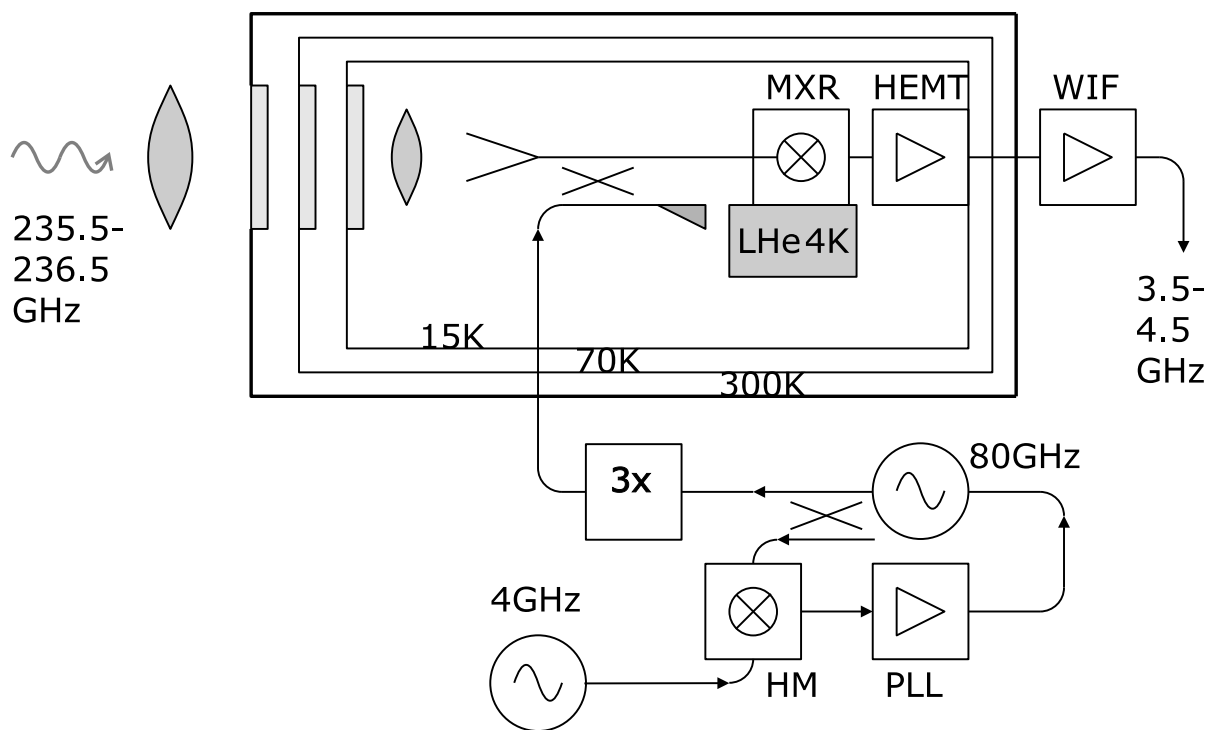


Figure 5.2: Synoptic diagram of a typical receiver. This diagram is grossly simplified; for instance, the optics involves mirrors, elliptical and planar, and also grids; the LO/PLL system is actually more complicated than shown.



Figure 5.3: A corrugated horn for the 150GHz band. The phase-correcting lens normally present at the aperture has been removed to reveal the corrugations. The diameter of the aperture is about that of a typical coin (1DM/100Ptas/1F). All the waves collected by the 30-m antenna converge to the horn with a precise phase relationship and are then squeezed into a waveguide 2 x 1 mm across. The ratio of areas is three hundred million!



Figure 5.4: Frequency down-conversion by mixing. Left: schematic diagram. Right: representation in frequency space.

wall of the horn (see fig. 5.3) the TE₁₀ mode of the rectangular waveguide couples to a mode at the aperture of the horn whose amplitude has circular symmetry, and whose polarization is pure linear.

5.3 Why we need heterodyne receivers

In the present context, *heterodyne* refers to receivers where the frequency of the input signal is shifted to lower frequencies. This is done by adding to the (small) input signal a (relatively) strong monochromatic signal, called the *local oscillator* (LO) and passing the sum through a non-linear device, whose output contains (among others) the difference frequency. Although a non-linear device is involved, the transformation from input to output is linear for the small signal. This process is called mixing or down-conversion. The output signal is called the *intermediate frequency* (IF). Actually the complete signal processing at a radiotelescope can involve up to four heterodyne conversions. The process of mixing is illustrated by figure 5.4 and by the simple equations below.

$$\begin{aligned}
 v_{LO} &= V_{LO} \cos(\omega_{LO}t) \\
 v_S &= V_S \cos(\omega_S t + \phi_S) \\
 v_{IF} &= A (v_{LO} + v_S)^2 \\
 &= A V_{LO} V_S \cos((\omega_S - \omega_{LO})t + \phi_S) + \dots \\
 &= A V_{LO} V_S \cos((\omega_{LO} - \omega_S)t - \phi_S) + \dots
 \end{aligned}$$

Interferometric observers, take a look at the last two lines, and note that, if you insist on keeping positive angular frequencies (and you really should), the signal phase enters in the IF phase with a positive sign in USB ($\omega_S > \omega_{LO}$), and a negative side in LSB.

The first reason why heterodyne down-conversion is needed is that only few signal processing devices exist at millimeter frequencies, and definitely not the fully parallel spectrometers (as opposed to multiplex devices such as FTS) that are routinely used for spectroscopic observations.

Then arises the question of where in the signal processing chain to operate the down-conversion. Basically we have no choice, because hardly any amplifiers are available in the millimeter range, except in the 3mm band, where they do not match the low noise properties of SIS mixers (to be discussed below). So we *must* perform a down-conversion before we can amplify the signal.

Before we leave the topic, it is worth noting that *heterodyne* means different things to different people. For engineers, it means that a mixer is used for down-converting the signal frequency; that's how the word is used above. For astronomers, heterodyne receivers are associated with spectroscopic observations; yet, there is only a quantitative difference, but no essential difference, between bolometer detection with a 80-GHz bandpass, and observing with a filterbank having 1-MHz bandpass. Finally, for physicists, heterodyne means with phase-preserving. In that sense, indeed, a bolometer is not phase-preserving, while a "heterodyne" receiver is phase-preserving only if it is defined *without* the final detector.

5.4 Local oscillator system

All the local oscillators in the IRAM telescope use Gunn oscillators. A Gunn diode is a semiconductor device that exhibits negative dynamic resistance over a suitable range of frequencies. Output powers of the order of 10–50mW can be obtained between 60 and 120 GHz. To achieve oscillation at a precise frequency, two means are combined. First, the Gunn diode is coupled to a coaxial cavity that defines the oscillation frequency, and whose high quality factor provides a good spectral purity. Its resonant frequency can be adjusted mechanically; this allows the desired frequency to be approached within ≈ 10 MHz. Secondly, a fraction of the millimetric radiation from the Gunn oscillator is used to produce a beat with a reference microwave oscillator at a frequency of a few GHz; actually, the Gunn oscillator signal beats with a harmonic ($n=17-65$, depending on the systems) of the reference frequency. The beat signal is used to “servo” by electronic tuning the Gunn oscillator to a multiple of the reference. Actually, not only the frequency, but also the phase of the local oscillator is locked to the reference oscillator, which is essential for interferometry, whether connected-array or VLBI. This description of the *phase-lock* system is over-simplified.

Local oscillator frequencies above 120GHz can generally not be generated directly by Gunn oscillators. In that case, the Gunn power is fed to a *frequency multiplier*, which is a non-linear device like the mixer, but based on non-linear capacitance, and optimized to produce a certain harmonic ($\times 2$, $\times 3$ or $\times 4$ in the case of IRAM systems) of the input frequency. The efficiency of the multiplication process is typically a few percent.

5.5 Local oscillator injection

As mentioned above, the local oscillator power must be added to the astronomical signal before it enters the mixer. When the mixers were based on Schottky diodes (10 years ago and more), they required an LO power of almost a mW. As a consequence, the LO power was coupled via a *diplexer*, which is like a frequency-selective coupler, allowing the mixer to be coupled with close to unity efficiency to *both* the input signal and the LO. With the advent of SIS mixers, and due to their modest LO power requirements (read below), a new method can be used, based on frequency-independent couplers. A fraction f (typically 1%) of the LO power is coupled into the signal path; the rest is wasted! The fraction f must be kept small because the same amount f of room-temperature blackbody noise is also coupled into the signal path. The coupler requires no adjustment and is located close to the receiver, inside the *cryostat* (discussed below).

5.6 Photon-assisted tunneling

All mixers in IRAM receivers are based on SIS junctions. An SIS junction consists of two layers of superconducting metal (Niobium) separated by a few nanometers of insulator (Aluminum oxide). The insulator is so thin that charged particles can tunnel through the barrier. The area of a junction is typically one to a few μm^2 . SIS junctions operate at the boiling temperature of He: 4.2K (at sea level).

Two kinds of charged particles can exist in a superconductor: a) ordinary electrons; b) so-called Cooper pairs, consisting of two electrons interacting and weakly bound together by the exchange of phonons (lattice vibrations); breaking a Cooper pair costs an energy 2Δ . Correspondingly, two kinds of currents can flow across the junction: the Josephson current, consisting of Cooper pairs, and the so-called quasi-particle current, consisting of “ordinary” electrons (presumably “electron” did not sound fancy enough). To keep this digression into SIS physics short, let’s just state that the Josephson current can be ignored. At the operating temperature of the mixer, and in an unbiased junction, the population of quasi-particles is virtually negligible. But, if the bias voltage is raised to the *gap voltage*

$$V_g = 2\Delta/e$$

the flow of quasi-particles across the junction becomes possible because the energy gained across the drop of electrical potential compensates for the energy spent in breaking a Cooper pair. See on figure 5.5 the “LO off” I-V characteristic.

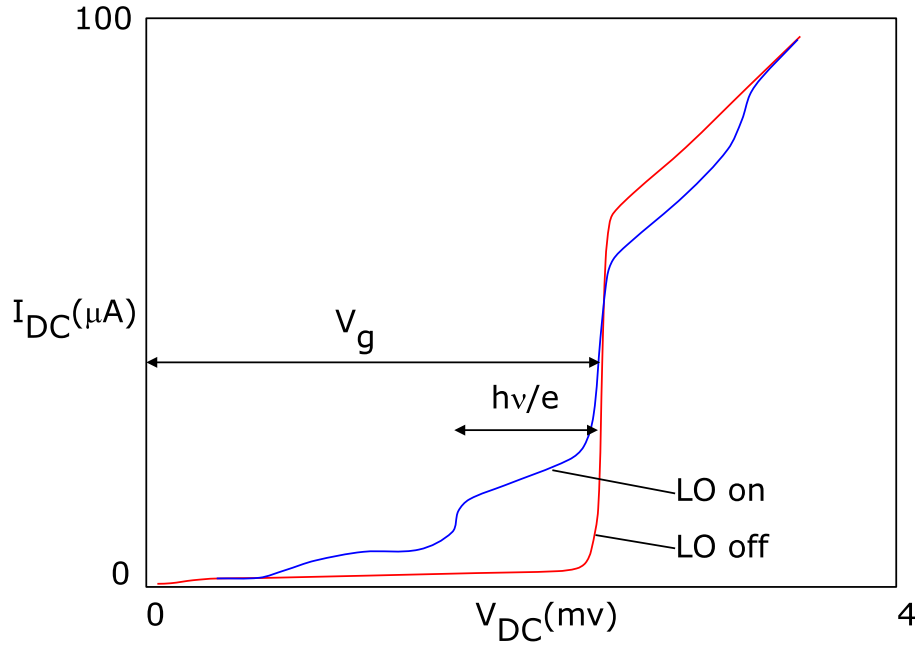


Figure 5.5: Current-voltage characteristics of an SIS junction operating in a mixer. The two curves were measured without and with LO power applied (frequency 230GHz); they have been slightly idealized (for pedagogical reasons, of course).

In the presence of electromagnetic radiation, the situation is modified as follows. If a RF photon is absorbed, its energy $h\nu$ can contribute to the energetic budget, which can now be written as:

$$eV_{\text{bias}} + h\nu = 2\Delta$$

or, equivalently:

$$V_{\text{bias}} + h\nu/e = V_g$$

In other words, the onset of conduction occurs at $V_g - h\nu/e$. The region of the I-V curve below the gap voltage where photon-assisted tunneling occurs is called the *photon step*. See the “LO on” curve on figure 5.5. Figure 5.5 is based on actual measurements of a 2-junction series array: the voltage scale has been scaled $\times \frac{1}{2}$ to illustrate a single junction. For a more detailed analysis of SIS junctions and their interaction with radiation see e.g. [Gundlach 1989].

So far I’ve shown you qualitatively that an SIS junction can function as a total power detector. The responsivity (current generated per power absorbed) can even be estimated to be of the order of one electron per photon, or: $D \approx e/h\nu$. How does that relate to frequency down-conversion? Assume that a power detector is fed the sum of a local oscillator (normalized to unit amplitude for convenience) $v_{LO} = \cos \omega_{LO} t$ and a much smaller signal at a nearby frequency: $v_S = \epsilon \cos \omega_S t$. Assume this functions as a squaring device and discard high-frequency terms in the output:

$$v_{\text{out}} = (v_{LO} + v_S)^2 \longrightarrow \frac{1}{2} \epsilon \cos(\omega_{LO} - \omega_S) t$$

So, a power detector can also function as a frequency down-converter (subject to possible limitations in the response time of the output).

The LO power requirement for an SIS mixer can be estimated as follows. A voltage scale is defined by the width of the photon step: $h\nu/e$. Likewise, a resistance scale can be defined from R_N , the resistance of the junction above V_g ; junctions used in mixers have $R_N \approx 50\Omega$. So, the order of magnitude of the LO power required is:

$$P_{LO} \approx (h\nu/e)^2 / R_N$$

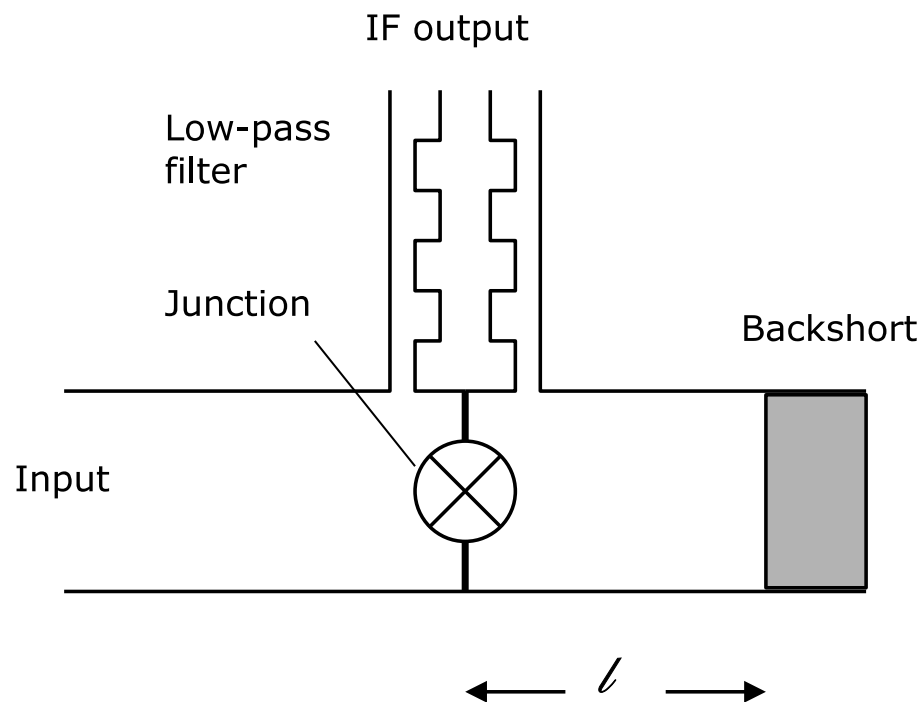


Figure 5.6: Rough sketch of the main elements of a mixer

about 20 nW for a 230 GHz mixer. This makes it possible to use the wasteful coupler injection scheme discussed above.

Because the insulating barrier of the junction is so thin, it possesses a capacitance of about $65 \text{ fF } \mu\text{m}^{-2}$. At the RF and LO frequencies, the (imaginary) admittance of that capacitance is about 3–4× the (approximately real) admittance of the SIS junction itself. Therefore, appropriate tuning structures must be implemented to achieve a good impedance match (i.e. energy coupling) of the junction to the signals.

The minimum theoretical SSB noise for an SIS mixer is $h\nu/k$, 11K at 230GHz; the best IRAM mixers come within a factor of a few ($\approx 4\times$) of that fundamental limit. These numbers are for laboratory measurements with minimal optics losses; practical receivers have a slightly higher noise.

5.7 Mixer

A sketch of a mixer is shown on figure 5.6, again grossly over-simplified. The junction is mounted across the waveguide, in the direction of the electric field. One side of the junction is connected to the outside of the mixer block, both to bring out the IF beat signal, and to provide the DC bias. That connection is made through a low-pass filter to avoid losing precious RF energy.

One end of the waveguide is the input of the mixer; the other end must be terminated somehow. At the zero-order approximation, one would like the junction to “see” an open circuit when “looking into” the rear end of the waveguide. More generally, the junction should see a pure imaginary impedance, so that no energy is wasted. A simple calculation shows that a transmission line having a length l , and terminated into a short-circuit, has an apparent impedance:

$$Z_{BS} = j Z_0 \tan(2\pi l/\lambda)$$

where Z_0 and λ are respectively the propagation impedance and wavelength in the waveguide, and l is the distance to the short-circuit. In particular, for $l = (\frac{n}{2} + \frac{1}{4})\lambda$, the apparent impedance is an open circuit. More generally, by adjusting l , an arbitrary imaginary impedance can be placed in parallel with the junction. Together with the tuning structures mentioned in the previous section, such an *adjustable backshort* contributes to achieve the best possible match of the junction impedance.

For various reasons (one of which is reducing the noise contribution from the atmosphere) it is desirable that the mixer should operate in *single-sideband* mode. We explain how this is achieved with a crude zero-order model. Assume that the best impedance match of the junction is obtained when the apparent impedance of the backshort seen from the junction is an open circuit. Assume we observe in the lower sideband at a frequency $\nu_L = \nu_{LO} - \nu_{IF}$, and want to reject the upper sideband $\nu_U = \nu_{LO} + \nu_{IF}$. That condition can be achieved if, at the frequency ν_U , the junction is short-circuited. So, we must meet the two conditions:

$$l = \left(\frac{n}{2} + \frac{1}{4}\right)\lambda_L \quad \text{lower sideband}$$

$$l = \left(\frac{n}{2} + \frac{1}{2}\right)\lambda_U \quad \text{upper sideband}$$

for some integer n ; we gloss over the distinction between free-space and waveguide wavelengths. The two conditions (one unknown) can be *approximately* met for some l close to

$$l_{\text{reject}} = \frac{1}{8} \frac{c}{\nu_{IF}}$$

Because for current mixers in the 100GHz band, the IF frequency is relatively low (1.5GHz), single-sideband operation requires additional tricks...

Returning to practicalities, tuning a receiver requires several steps (which used to make astronomers a bit nervous at the 30-m telescope when all was done manually). First the local oscillator must be tuned and locked at the desired frequency. Then the backshort is set at the appropriate position, and the junction DC bias voltage is set. Finally the LO power is adjusted to reach a prescribed junction DC current (of the order of $20\mu A$). These adjustments are made by a combination of table lookup and optimization algorithms under computer control. Altogether this involves between 11 and 13 adjustments, mechanical or electrical, yet this process takes only a few minutes with the current systems.

5.8 Cryostat

First, conducted heat would quickly evaporate the helium. Second, a big icicle of water, nitrogen, oxygen, etc... would condense around the reservoir. Conduction and condensation are avoided by operating the receiver in a vacuum enclosure (labelled 300K in figure 5.2). But infrared radiation must also be blocked. Your body is receiving about 700W from the surroundings! (and radiating back about the same amount). A typical 4-liter reservoir of liquid He, exposed to the same flux, would evaporate in 2 minutes! Yet the hold time of a cryostat is one to several weeks, four orders of magnitude more. This is achieved via the two radiation screens labelled 70K 15K in figure 5.2, as well as by reducing to a minimum all conduction losses. The radiation screens are kept cold by a closed-cycle cryogenic machine involving the compression and expansion of helium gas. The 15K stage is also used to cool the first stages of IF amplification. Future receivers will feature fully closed-cycle cryogenics, including the 4K stage.

5.9 Actual receivers

Figure 5.7 shows the performance of one of the Plateau de Bure 230GHz receivers. The present LO/IF system dictates a 1.5GHz IF, therefore, these receivers are operated in DSB mode; in the interferometer, the sidebands can be separated due to their different fringe rates.

Figure 5.8 gives you a chance to peek at the cold RF assembly of one of the dual-channel receivers in operation at the 30-m telescope since May 1998.

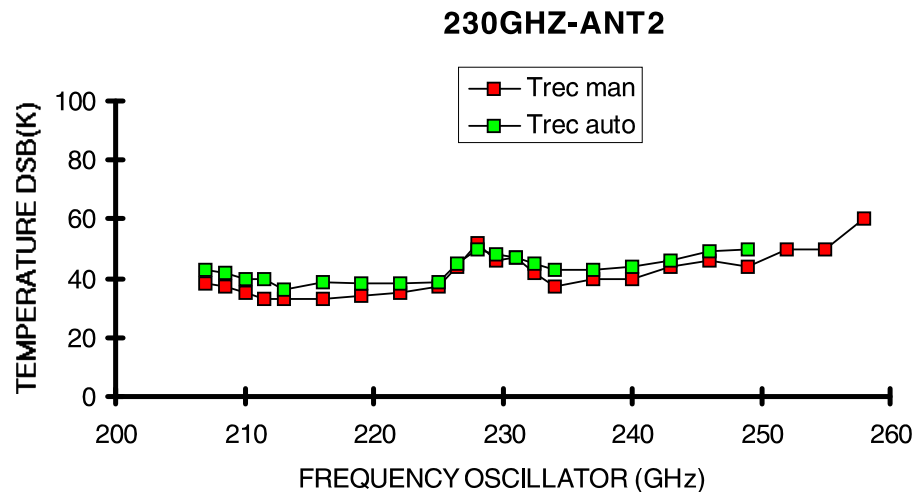


Figure 5.7: DSB noise performance of one of the 230GHz receivers in operation at the PdB interferometer

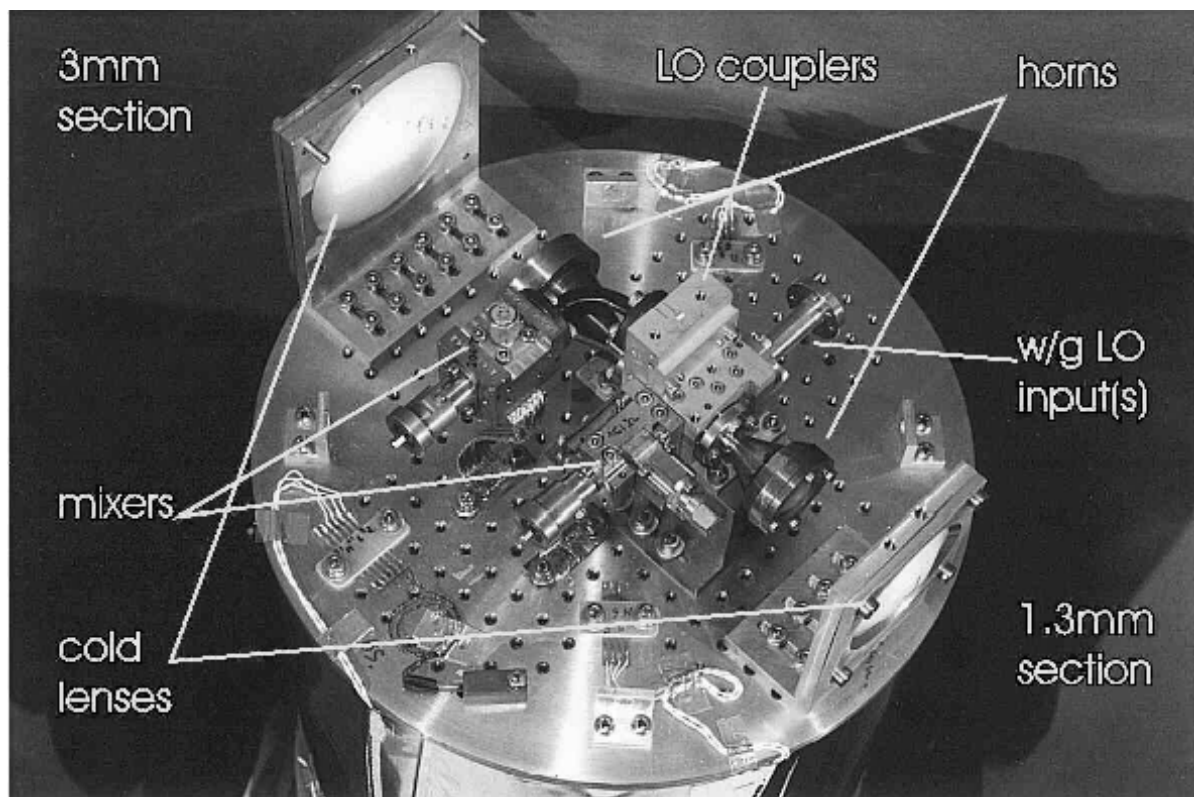


Figure 5.8: The cold RF assembly for a dual-channel receiver used at the 30-m telescope.

Chapter 6

Cross Correlators

Helmut Wiesemeyer

wiesemey@iram.fr

IRAM, 300 rue de la Piscine, F-38406 Saint Martin d'Hères, France

6.1 Introduction

As we already learned in the lecture on radio interferometry by S. Guilloteau (Chapter 2), the interferometer measures the complex cross-correlation function of the voltage at the outputs of a pair of antennas (i, j). This quantity, $R_{ij}(\tau)$ is defined as

$$R_{ij}(\tau) = \langle v_i(t)v_j(t + \tau) \rangle \quad (6.1)$$

(the brackets indicate the time average, see Appendix A). The cross-correlation function is related to the visibility function $V = |V| \exp(i\varphi_{\text{SKY}})$ by

$$R_{ij} = A_0 |V| \Delta\nu_{\text{IF}} \cos(2\pi\nu_{\text{IF}}\tau_{\text{G}} - \varphi_{\text{SKY}}) \quad (6.2)$$

where A_0 is the collecting area of the antenna. Eq. 6.2 only holds for a quasi-monochromatic signal, $\Delta\nu_{\text{IF}} \ll \nu_{\text{IF}}$ (i.e. the bandpass may be represented by a δ -function). The signal phase varies with time due to source structure and atmospheric perturbations (expressed by φ_{SKY}), and due to the geometric delay τ_{G} . The timescale that is needed to fully sample a spectral line, given by the sampling theorem (see below), is much shorter. Here are examples of the different timescales:

1. timescale for phase variation by 1° due to source structure (for a point source at 100 GHz with $\Delta\alpha = 10''$ offset from phase reference center, east-west baseline of 180 m during transit): **10 min**
2. timescale for phase variation due to atmospheric perturbations: (depending on atmospheric conditions and baseline length): **1 sec – several hours**
3. sampling time step for a 80 MHz bandwidth: **6.25 ns**

4. maximum time lag needed for a 40 kHz resolution: **25 μ s**

The sampling time step in the above example is that short that the signal will be dominated by noise. Any deterministic contribution will show in the correlation products. We have to assume that the noise is due to a stationary random process (within a time interval given by the maximum time lag).

In the following, I will discuss digital techniques to evaluate $R_{ij}(\tau)$. Analog methods of signal processing are highly impractical in radio interferometry, for mainly two reasons:

1. In time domain, high precision is needed.
2. The signal needs to be identically copied, in order to cross-correlate the output of one antenna with the outputs from all other antennas. This can be more easily done with digital techniques, than with analog ones.

The first signal processing steps are analog, beginning with the mixing in the heterodyne receivers. For reasons that will become clear later (see R. Lucas, Chapter 7), only the case of single-sideband reception is considered. The sidebands may be separated by a periodic phase shift of $\pi/2$ applied to the local oscillator. The signals are demodulated in two different ways by the correlator. At the entry of the correlator, filters are inserted, that are used to select the intermediate frequency bandpass. The following signal processing steps are digitally implemented, and are performed within the correlator:

1. Sampling the signal: in order to digitize the signal, it needs to be sampled. Bandwidth-limited signals (i.e. containing frequencies between zero and $\Delta\nu$) may be sampled without loss of information if the samples are taken at time intervals $\Delta t \leq 1/(2\Delta\nu)$.
2. In order to numerically compute the cross correlation function, the signals have to be discretized. The data are affected by such a quantization, but may be corrected for it. However, the loss of information cannot be recovered and degrades the correlator sensitivity.
3. Delay compensation: the geometric delays are eliminated for signals received from the direction of the pointing center. Remaining delays are due to source structure.
4. Until now, everything is done in the time domain. However, for spectroscopic applications, the desired output is the cross power spectral density, and not the cross correlation function. These quantities are Fourier-transform pairs (Wiener-Khintchine theorem)¹. The transformation can be efficiently done by a processor performing a *Fast Fourier Transform*.

The plan of this lecture is as follows: after the basic theory, I will talk about the correlator in practice. Both the intrinsic limitations and system-dependent performance will be discussed. For further reading, the book of [Thompson et al. 1986] (chapters 6 – 8), and the introduction by [D’Addario 1989] are recommended. Finally, as an example, the current correlator system on Plateau de Bure will be presented.

6.2 Basic Theory

The “heart” of a correlator consists of the sampler and the cross-correlator. Eq.6.2 represents an over-simplified case, because the bandwidth of the signals is neglected. The correlator output is rather modified by the Fourier transform of the bandpass function. For the sake of simplicity, let us assume an idealized rectangular passband of width $\Delta\nu_{\text{IF}}$ for both antennas, centered at the intermediate frequency ν_{IF} , i.e.

$$|H_i(\nu)| = |H_j(\nu)| = \begin{cases} H_0, & |\nu - \nu_{\text{IF}}| < \Delta\nu_{\text{IF}}/2 \\ 0, & |\nu - \nu_{\text{IF}}| > \Delta\nu_{\text{IF}}/2 \end{cases} \quad (6.3)$$

¹Note that the Fourier transform of a time series is not defined. However, in this context, we only work with finite sections of a time series.

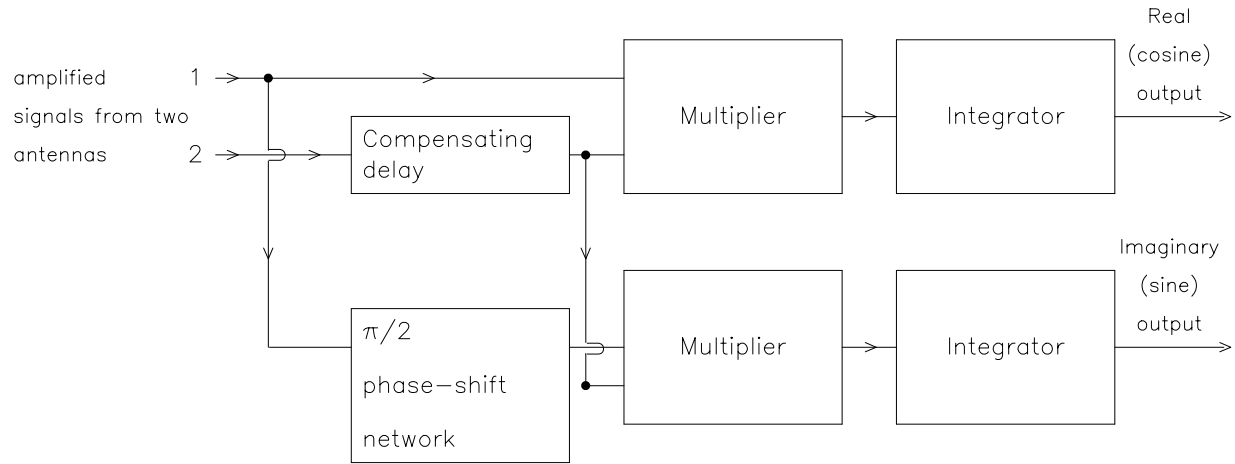


Figure 6.1: Architecture of a complex continuum cross correlator.

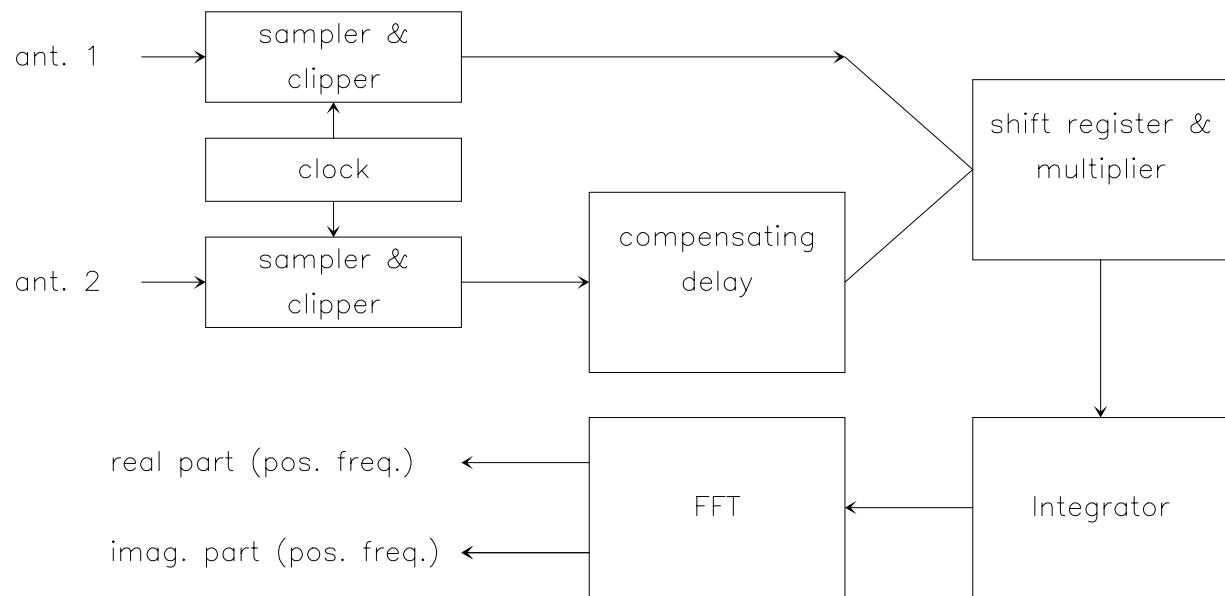


Figure 6.2: Architecture of a complex spectroscopic cross correlator.

(this assumption will be relaxed later). The correlator response to this bandpass is the Fourier transform of the cross power spectrum $H_i(\nu)H_j(\nu)^*$, which is shown in Fig. 6.3:

$$\int_0^\infty H_i(\nu_{\text{IF}})H_j^*(\nu_{\text{IF}}) \exp(2\pi i\nu_{\text{IF}}\tau) d\nu_{\text{IF}} = H_0^2 \Delta\nu_{\text{IF}} \frac{\sin(\pi\Delta\nu_{\text{IF}}\tau)}{\pi\Delta\nu_{\text{IF}}\tau} \exp(i2\pi\nu_{\text{IF}}\tau) \quad (6.4)$$

The correlator output consists of an oscillating part, and a $\sin(x)/x$ envelope (a *sinc* function). If the delay τ becomes too large, the sensitivity will be significantly decreased due to the sinc function (see Fig. 6.3). Strictly speaking, this is the response to the real part of the bandpass, which is symmetric with respect to negative frequencies. The imaginary part of the bandpass is antisymmetric with respect to negative frequencies, thus the correlator response is different. The separation of real and imaginary parts in continuum and spectroscopic correlators will be discussed below.

This example shows that accurate delay tracking (fringe stopping) is needed, if the bandwidth is not anymore negligible with respect to the intermediate frequency. In other words, the compensating delay τ_1 needs to keep the delay tracking error $\Delta\tau = \tau_G - \tau_1$ at a minimum. The offset $k\Delta t$ introduced in correlator channel k needs to be applied with respect to a fixed delay. In the following, the correlator response to a rectangular bandpass will be expressed by the more general instrumental gain function $G_{ij}(\tau)$, defined by

$$A_0 \int_0^\infty H_i(\nu)H_j^*(\nu) \exp(2\pi i\nu\tau) d\nu = G_{ij}(\tau) \exp(2\pi i\nu_{\text{IF}}\tau) \quad (6.5)$$

$G_{ij}(\tau) = |G_{ij}(\tau)| \exp(i\Phi_G)$ is a complex quantity, including phase shifts due to the analog part of the receiving system (amplifiers, filters)². After fringe stopping, the single-sideband response of correlator channel k becomes (for details, see R. Lucas, Chapter 7)

$$\begin{aligned} R_{ij}(k\Delta t) &= |V||G_{ij}| \operatorname{Re} \{ \exp(\pm 2\pi i\nu_{\text{IF}}(\tau + k\Delta t) - i\varphi_{\text{SKY}} \pm i\varphi_G) \} \\ &= |V||G_{ij}| \cos(\pm 2\pi\nu_{\text{IF}}(\tau + k\Delta t) - \varphi_{\text{SKY}} \pm \varphi_G) \end{aligned} \quad (6.6)$$

where the plus sign refers to upper sideband reception, and the minus sign refers to lower sideband reception. From Eq. 6.6, we immediately see that the residual delay error (due to a non-perfect delay tracking) enters as a constant phase slope across the bandpass (with opposed signs in the upper and lower sidebands). The effect of such a phase slope on sensitivity will be discussed later. In order to determine the phase of the signal, the imaginary part of $R_{ij}(\tau)$ has to be simultaneously measured. In a continuum correlator (Fig. 6.1), a $\pi/2$ phase shift applied to the analog signal yields the imaginary part. The signals are then separately processed by a cosine and a sine correlator³. In other words: the pattern shown in Fig. 6.3 is measured in the close vicinity of two points, namely at the origin, and at a quarter wave later, i.e. at $\tau = 1/(4\nu_{\text{IF}})$. Note, however, that due to the sinc-envelope, the decreasing response function cannot be neglected if the bandwidth is comparable to the intermediate frequency.

In a spectroscopic correlator (Fig. 6.2), the imaginary part can be entirely deduced from the digitized signal: if N_{ch} is the number of complex spectral channels, $2N_{\text{ch}}$ time lags are used, covering delays from $-N_{\text{ch}}\Delta t$ to $(N_{\text{ch}}-1)\Delta t$. The correlator output is a real signal with even and odd components (with respect to time lags of opposed signs). The N complex channels of the Fourier transform at positive frequencies yields the cross-power spectrum:

$$r_{ij,k}(\nu_{\text{IF}}) = r_{ij}(k\delta\nu_{\text{IF}}) = \int_{-\infty}^{\infty} R_{ij}(t) \exp(2\pi i\nu_{\text{IF}}t) dt \quad (6.7)$$

$$= \sum_{l=-N_{\text{ch}}}^{N_{\text{ch}}-1} \langle v_i(t)v_j(t + \tau + l\Delta t) \rangle \exp(2\pi ilk/2N_{\text{ch}}) \quad (6.8)$$

(for channel k of a total of N_{ch} complex channels, spaced by $\delta\nu_{\text{IF}}$). The last expression represents the discrete Fourier transform. According to the symmetry properties of Fourier transforms, the even component of the correlator output becomes the real part of the complex spectrum, and the odd component becomes the imaginary part. The Fourier transform is efficiently evaluated using the Fast-Fourier algorithm. In practice, it is rather the digital measurement of the cross-correlation function that is non-trivial. It will

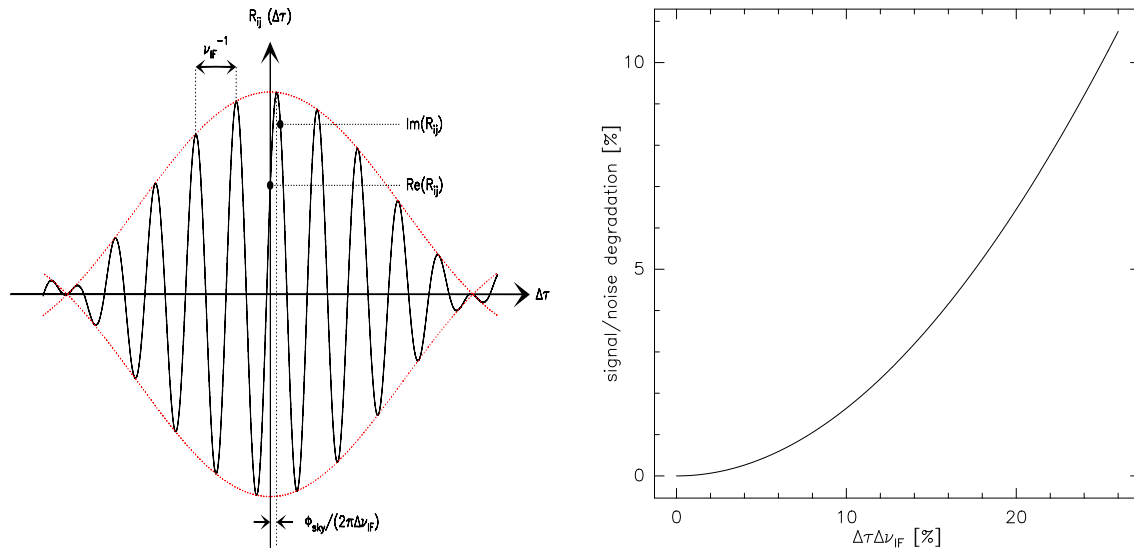


Figure 6.3: Left: Correlator output (single-sideband reception) for a rectangular passband with $\Delta\nu_{\text{IF}}/\nu_{\text{IF}} = 0.2$. Due to the signal phase φ_{SKY} , the oscillations move through the sinc envelope by $\varphi_{\text{SKY}}/2\pi\nu_{\text{IF}}$. The shift may also be due to the phase of the complex gain (in this case, the shift would be in opposed sense for USB and LSB reception). Right: Sensitivity degradation due to a delay error $\Delta\tau$ (with respect to the inverse IF bandwidth). The effect is due to the fall-off of the sinc envelope.

be discussed in detail in Section 6.3.3. The ensemble of cross-power spectra $r_{ij}(\nu_{\text{IF}})$, after tracking the source for some time, becomes (after calibration and several imaging processes) a channel map.

6.3 The Correlator in Practice

In order to numerically evaluate the cross-correlation function R_{ij} , the continuous signals entering the cross correlator need to be sampled and quantized. According to Shannon’s sampling theorem [Shannon 1949], a bandwidth-limited signal may be entirely recovered by sampling it at time intervals $\Delta t \leq 1/(2\Delta\nu_{\text{IF}})$ (also called sampling at Nyquist rate). The discrete Fourier transform of the sufficiently sampled cross-correlation function theoretically yields the cross-power spectrum without loss of information. However, in practice, two intrinsic limitations exist:

- In order to discretize a signal, it is not only sampled, it also has to be quantized. The cross-correlation function, as derived from quantized signals, does not equal the cross-correlation function of continuous signals. Moreover, the sampling theorem does not hold anymore for quantized signals. The reasons will become clear below.
- Eq. 6.7 theoretically extends from $-\infty$ to $+\infty$. In practice (Eq. 6.8), only a maximum time lag can be considered: limited storage capacities and digital processing speed are evident reasons, another limiting factor are the different timescales mentioned before. The abrupt cutoff of the time window affects the data.

These “intrinsic” limitations are discussed in Sections 6.3.1 and 6.3.2. The system-dependent performance will be addressed in Section 6.3.3.

²Because τ is restricted to a maximum time lag, this instrumental gain factor does not describe long-term variations.

³For the sake of completeness, it should be mentioned that this is a special case of the so-called *Hilbert* transform, which property is to change signal phases by $\pi/2$, but to leave amplitudes unchanged.

6.3.1 Digitization of the input signal and clipping correction

As already mentioned, sampling at the Nyquist rate retains all information. However, quantizing the input signal leads to a loss of information. This can be qualitatively understood in the following way: in order to reach the next discrete level of the transfer function, some offset has to be added to the signal. If the input signal is random noise of zero mean, the offset to be added will also be a random signal of zero mean. In other words, a “quantization” noise is added to the signal, that leads to a loss of information. In addition, the added noise is not anymore bandwidth limited, and the sampling theorem does not apply: oversampling will lead to improved sensitivity.

Many quantization schemes exist (see e.g. [Cooper 1970]). It is entirely sufficient to use merely a few quantum steps, if the cross-correlation function will be later corrected for the effects of quantization. For the sake of illustration, the transfer function of a four-level 2-bit quantization is shown in Fig. 6.5. Each of the four steps is assigned a sign bit, and a magnitude bit. After discretizing the signal, the samples from one antenna are shifted in time, in order to compensate the geometric delay $\tau_G(t)$. The correlator now proceeds in the following way: for each delay step Δt , the corresponding sign and magnitude bits are put into two registers (one for the first antenna, and one for the second). The second register is successively shifted by one sample. In this way, sample pairs from both antennas, separated by a successively longer time lag, are created. These pairs are multiplied, using a multiplication table. For the case of four-level quantization, it is shown in Fig. 6.5. Products which are assigned a value of $\pm n^2$ are called “high-level products”, those with a value of $\pm n$ are “intermediate-level products”, and those with a value of ± 1 “low-level products”. The products (evaluated using the multiplication table in Fig. 6.5) are sent to a counter (one counter for each channel, i.e. for each of the discrete time lags). After the end of the integration cycle, the counters are read out.

In practice, the multiplication table will be shifted by a positive offset of n^2 , to avoid negative products (the offset needs to be corrected when the counters are read out). This is because the counter is simply an adding device. As another simplification, low-level products may be deleted. This makes digital implementation easier, and accounts for a loss of sensitivity of merely 1% (see Table 6.1). Finally, not all bits of the counters’ content need to be transmitted (see Section 6.3.2).

Before the normalized contents of the counters are Fourier-transformed, they need to be corrected, because the cross-correlation function of quantized data does not equal the cross-correlation function of continuous data. This “clipping correction” can be derived using two different methods. As an example for the case of full 4-level quantization:

- Four-level cross-correlation coefficient according to the multiplication table Fig. 6.5. The cross-correlation coefficient ρ is a normalized form of the cross-correlation function (see Appendix A):

$$\rho_4 = \frac{2n^2(N_{01,01} - 2N_{01,11}) + 4n(N_{00,01} - N_{00,11}) + 2(N_{00,00} - N_{00,10})}{2(n^2N_{01,01} + N_{00,00})_{\rho=1}} \quad (6.9)$$

where $N_{ij,kl}$ is the number of counts with sign bit i and magnitude bit j at time t (first antenna), and sign bit k and magnitude bit l at time $t + \tau$ (second antenna). $\pm n$ is the product value assigned to intermediate-level products.

- Clipping correction, first method: evaluate the $N_{ij,kl}$ in Eq. 6.9, using joint probabilities $P_{ij,kl}$ (see Appendix A for the definition of the jointly Gaussian probability distribution), such as

$$N_{01,01} = NP_{01,01} = \frac{N}{2\pi\sigma^2\sqrt{1-\rho^2}} \int_{v_0}^{\infty} \int_{v_0}^{\infty} \exp\left[\frac{-(x^2 + y^2 - 2\rho xy)}{2\sigma^2(1-\rho^2)}\right] dx dy \quad (6.10)$$

(N is the number of signal pairs, separated by the time lag of the channel under consideration, v_0 is the clipping voltage, see Fig. 6.4).

- Clipping correction, second method: using Price’s theorem for functions of jointly random variables.

Table 6.1: Correlator parameters for several quantization schemes

method	n	v_0 [σ_{rms}]	$\eta_{\text{q}}^{(1)}$ for sampling rate	
			$2\Delta\nu_{\text{IF}}^{(2)}$	$4\Delta\nu_{\text{IF}}^{(3)}$
two-level	–	–	0.64	0.74
three-level	–	0.61	0.81	0.89
four-level	3	1.00	0.88 ⁽⁴⁾	0.94
	4	0.95	0.88	0.94
∞ -level	–	–	1.00	1.00

Notes:

(1) The correlator efficiency is defined by Eq. 6.13.

The values are for an idealized (rectangular) bandpass and after level optimization.

(2) Nyquist sampling,

(3) oversampling by factor 2

(4) 0.87 if low level products deleted (case of Plateau de Bure correlator)

The result, derived in Appendix B, is shown in Fig. 6.4:

$$R_4 = \frac{\sigma^2}{\pi} \int_0^\rho \frac{1}{\sqrt{1-r^2}} \left\{ (n-1)^2 \left[\exp\left(\frac{-v_0^2}{\sigma^2(1+r)}\right) + \exp\left(\frac{-v_0^2}{\sigma^2(1-r)}\right) \right] + 4(n-1) \exp\left(\frac{-v_0^2}{2\sigma^2(1-r^2)}\right) + 2 \right\} dr. \quad (6.11)$$

Although the discrete, normalized cross-correlation function and the continuous cross-correlation coefficient are almost linearly dependent within a wide range, the correction is not trivial. An analytical solution is only possible for the case of two-level quantization (“van Vleck correction” [Van Vleck 1966]).

In practice, several methods are used to numerically implement Eq. 6.11 (in the following, the index k means k -level quantization). The integrand may be replaced by an interpolating polynomial, allowing to solve the integral. One may also construct an interpolating surface $\rho(R_k, \sigma)$. As already discussed, the clipping correction cannot recover the loss of sensitivity due to quantization. The loss of sensitivity for k -level discretization may be found by evaluating the signal-to-noise ratio

$$\mathfrak{R}_{\text{sn},k} = \frac{R_k}{\sigma_k} = \frac{R_k}{\sqrt{\langle R_k^2 \rangle - \langle R_k \rangle^2}} \quad (6.12)$$

In order to minimize the loss of sensitivity, the clipping voltage (with respect to the noise σ) needs to be adjusted such that the correlator efficiency curve in Fig. 6.4 is at its maximum. The correlator efficiency is defined with respect to the signal-to-noise ratio of a (fictive) continuous correlator, i.e.

$$\eta_k = \frac{\mathfrak{R}_{\text{sn},k}}{\mathfrak{R}_{\text{sn},\infty}} = \frac{\mathfrak{R}_{\text{sn},k}}{\rho\sqrt{N_{\text{q}}}} \quad (6.13)$$

where N_{q} is the number of samples. Table 6.1 summarizes the results for different correlator types and samplings.

Due to the discretization of the input voltages (as shown in Fig. 6.5), any knowledge of the absolute signal value is lost. The signal amplitude is recovered by a regularly performed calibration (using a calibration load of known temperature, for details, see Chapter 12 by A. Dutrey). Fig. 6.6 shows the signal processing steps from the incoming time series to the derived spectrum.

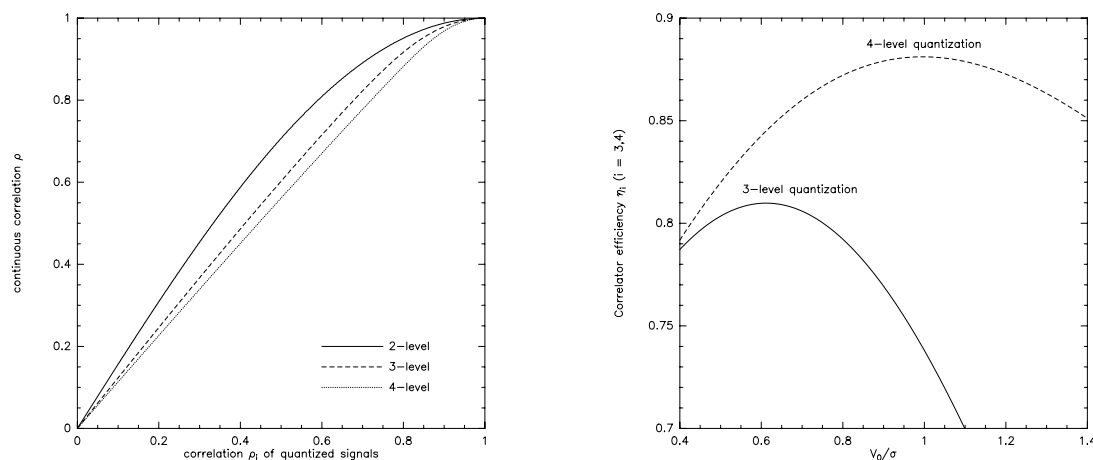


Figure 6.4: Left: Clipping correction (cross correlation coefficient of a continuous signal vs. cross correlation coefficient of a quantized signal) for two-, three- and four level quantization (with optimized threshold voltage). The case of two level quantization is also known as *van Vleck correction*. For more quantization levels, the clipping correction becomes smaller. Right: Correlator efficiency as function of the clipping voltage, for three-level and four-level quantization (at Nyquist sampling).

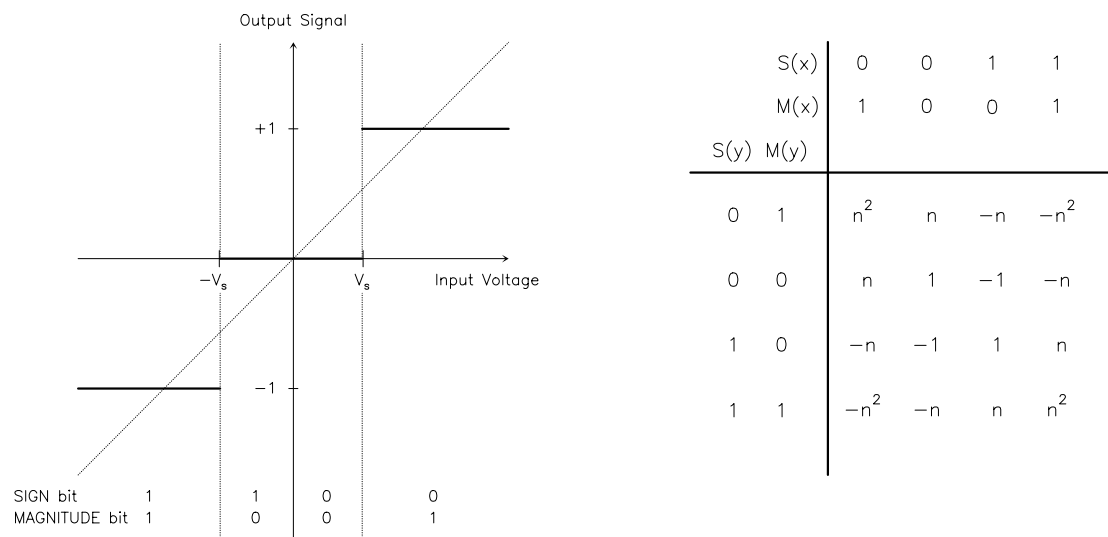


Figure 6.5: Left: Transfer function for a 4-level 2-bit correlator. The dashed line corresponds to the transfer function of a (fictive) continuous correlator with an infinite number of infinitesimally small delay steps. Right: Multiplication table. $S(x)$ is the signal bit at time t , $M(x)$ is the magnitude bit at time t (respectively $S(y)$ and $M(y)$ at time $t + \tau$).

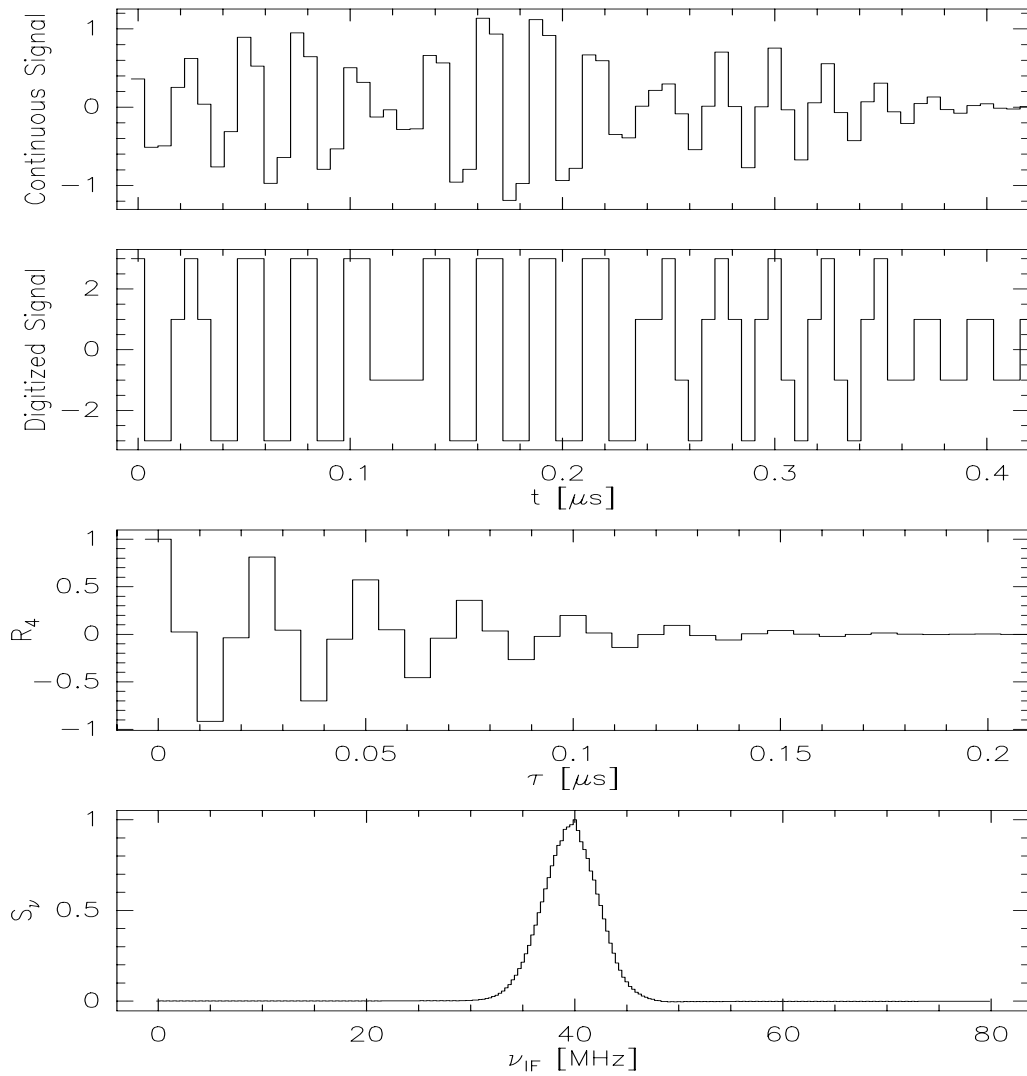


Figure 6.6: The signal processing in a 3-level 2-bit correlator. From top to bottom: the original time series (sampled in discrete time steps, but continuous in amplitude), the digitized time series (with high-level weight 3), the digital correlation R_4 , the reconstructed spectral line.

Table 6.2: Time lag windows

Description	Lag window	Spectral window
rectangular	$w(t) = 1$ for $ t \leq \tau_m$, else 0	$\hat{w}(\nu) = 2\tau_m \frac{\sin(2\pi\nu\tau_m)}{2\pi\nu\tau_m}$
Bartlett	$w(t) = 1 - \frac{ t }{\tau_m}$ for $ t \leq \tau_m$, else 0	$\hat{w}(\nu) = \tau_m \left(\frac{\sin(\pi\nu\tau_m)}{\pi\nu\tau_m} \right)^2$
von Hann	$w(t) = \frac{1}{2} \left(1 + \cos\left(\frac{\pi t}{\tau_m}\right) \right)$ for $ t \leq \tau_m$, else 0	$\hat{w}(\nu) = \tau_m \cdot \frac{\sin(2\pi\nu\tau_m)}{2\pi\nu\tau_m} \cdot \frac{1}{1-(2\nu\tau_m)^2}$
Welch	$w(t) = \left(1 - \left(\frac{t}{\tau_m}\right)^2 \right)$	$\hat{w}(\nu) = \frac{1}{(\pi\nu)^2 \tau_m} \left(\frac{\sin(2\pi\nu\tau_m)}{2\pi\nu\tau_m} - \cos(2\pi\nu\tau_m) \right)$
Parzen	$w(t) = \begin{cases} 1 - 6 \left(\frac{t}{\tau_m}\right)^2 + 6 \left(\frac{ t }{\tau_m}\right)^3 & \text{for } t \leq \tau_m/2 \\ 2 \left(1 - \frac{ t }{\tau_m}\right)^3 & \text{for } \tau_m/2 < t \leq \tau_m \end{cases}$	$\hat{w}(\nu) = \frac{3}{4} \tau_m \left(\frac{\sin(\pi\nu\tau_m/2)}{\pi\nu\tau_m/2} \right)^4$

6.3.2 Time lag windows and spectral resolution

According to the sampling theorem, we need a sampling timestep $\Delta t = 1/(2\Delta\nu_{\text{IF}})$ if we want to fully recover the cross-power spectral density within a bandwidth $\Delta\nu_{\text{IF}}$. The channel spacing $\delta\nu$ is then determined by the maximum time lag $\tau_{\text{max}} = N_{\text{ch}}\Delta t$ (where N_{ch} is the number of channels), i.e.

$$\delta\nu = \frac{1}{2\tau_{\text{max}}} = \frac{1}{2N_{\text{ch}}\Delta t} \quad (6.14)$$

However, the data acquisition is abruptly stopped after the maximum time lag. After the Fourier transform, the observed cross power spectrum is thus convolved with the Fourier transform $\hat{w}(\nu)$ of the box-shaped time window $w(t)$, producing strong sidelobes:

$$w(\tau) = \left\{ \begin{array}{ll} 1, & |\tau| \leq \tau_{\text{max}} \\ 0, & \text{else} \end{array} \right\} \Leftrightarrow \hat{w}(\nu) = 2\tau_{\text{max}} \frac{\sin(2\nu\tau_{\text{max}})}{2\nu\tau_{\text{max}}} \quad (6.15)$$

These oscillations are especially annoying, if strong lines are observed. They may be minimized, if the box-shaped time lag window is replaced by a function that rises from zero to peak at negative time lags, and decreases to zero at positive time lags (apodization). Such a window function suppresses the sidelobes, at the cost of spectral resolution. A comparison between several window functions is given in Fig. 6.7, together with sidelobe levels and spectral resolutions (defined by the full width at half-power, FWHP, of the main lobe of the spectral window). Table 6.2 summarizes the various functions in time and spectral domains. The default of the Plateau de Bure correlator is the Welch window, because it still offers a good spectral resolution. Moreover, the oscillating sidelobes partly cancel out the contamination of a channel by the signals in adjacent channels. Of course, the observer is free to deconvolve the spectra from this default window, and to use another time lag window.

Note: If you apodize your data, not only the effective spectral resolution is changed. Due to the suppression of noise at large time lags, the sensitivity is increased. The variance ratio of apodized data to unapodized data,

$$\int_{-\infty}^{\infty} |w(t)|^2 dt = \int_{-\infty}^{\infty} |\hat{w}(\nu)|^2 d\nu = 1/B_n \quad (6.16)$$

defines the noise equivalent bandwidth B_n . It is the width of an ideal rectangular spectral window (i.e. $\hat{w}(\nu) = 1/B_n$ with zero loss inside $|\nu| \leq B_n/2$, and infinite loss outside) containing the same noise power

Table 6.3: Effects of delay pattern on the sensitivity

Intermediate frequency bandwidth	$\nu_{\text{IF}} = 160 \text{ MHz}$
Baseline	$b = 100 \text{ m}$
Zenith distance of source in direction \mathbf{s}	$\Theta = 30^\circ$
Results in geometric delay:	$\tau_{\text{G}} = \mathbf{b} \cdot \mathbf{s}/c = 0.17 \mu\text{s}$
Attenuation according to Eq. 6.4	1 %

as the actual data. For sensitivity estimates of spectral line observations, the channel width to be used is thus the noise equivalent width, and neither the channel spacing, nor the effective spectral resolution. Fig. 6.7 gives the noise equivalent bandwidths B_n for commonly used time lag windows.

6.3.3 Main limitations

In real life, cross-correlators are subject to the performance of the whole receiving system. This comprises the “analog part” (the signal path from the receivers to the IF filters at the correlator entry), and the “digital part” (everything behind the sampler). Although the analog part is out of the correlator, its performance requires to change our assumptions concerning the input data. This complicates the analysis of the correlator response. The following discussion refers to instantaneous errors only. However, in interferometric mapping, scan-averaged visibilities are used, and the data may be less affected.

Analog part

The shape of the bandpass function (amplitude and phase) at the correlator output is mainly due to the correlator’s response to the filters inserted in the IF band at the correlator entry. So far, for the sake of simplicity, rectangular passbands, centered at the intermediate frequency ν_{IF} , have been assumed. A more complex (and more realistic) case may be an amplitude slope where the logarithm of the amplitude varies linearly with frequency. Although the bandpass function will be calibrated (see Eq. 6.17, and R. Lucas Chapter 7), the effect of such a slope on sensitivity remains. A derivation of the signal-to-noise ratio for that case is beyond the scope of this lecture. To give an impression of the order of magnitude: a slope of 3.5 dB (edge-to-edge) leads to a 2.5 % degradation of the sensitivity calculated for a rectangular passband. A center frequency displacement of 5 % of the bandwidth leads to the same degradation.

As already demonstrated, delay-setting errors linearly increase with the intermediate frequency (Eq. 6.6). Table 6.3 gives an impression of the decrease of sensitivity due to a delay error. The effect is also shown in Fig. 6.3 for a range of delay errors. For example, a delay error of $0.12/\Delta\nu_{\text{IF}}$ accounts for a 2.5 % degradation. Delay errors are mainly due to inaccurately known antenna positions (asking for a better baseline calibration), or due to errors in the transmission cables.

Phase errors across the bandpass may also be of random nature. A phase fluctuation of 12.8° (rms) per scan leads to a degradation of $(1 - \exp(-\sigma_\phi^2/2)) \times 100\% = 2.5\%$. Fluctuations across the bandpass also appear as ripples. They may have several reasons, and are mainly due to the *Gibbs phenomenon*, and due to reflections in the transmission cables. A sinusoidal bandpass ripple of 2.9 dB (peak-to-peak) yields a 2.5 % degradation in the signal-to-noise ratio. The *Gibbs phenomenon* also occurs in single-dish autocorrelation spectrometers. For the sake of illustration, let us again assume a perfectly flat response of receivers and filters. However, the filter response function is only flat across the IF passband. Towards its boundary, steep edges occur. We already learned that strong spectral lines may show ripples, if no special data windowing in time domain is applied. The Gibbs phenomenon is due to a similar problem (but now the spectral line is replaced by the edge of a flat rectangular band extending in frequency from zero to $\Delta\nu_{\text{IF}}$). The output of the cosine correlator is symmetric, but the sine output (imaginary part) is antisymmetric, thus including an even steeper edge. Convoluting this edge with the sinc function (i.e. the spectral window) results in strong oscillations. Let us call this function $f(\nu)$. For calibration purposes, the Gibbs phenomenon has to be avoided: the problem is that calibration uses the system response to a flat-spectrum continuum source. A source whose visibility is $V(\nu)$ is seen as $f(\nu) * [G_{ij}(\nu)V(\nu)]$ (where

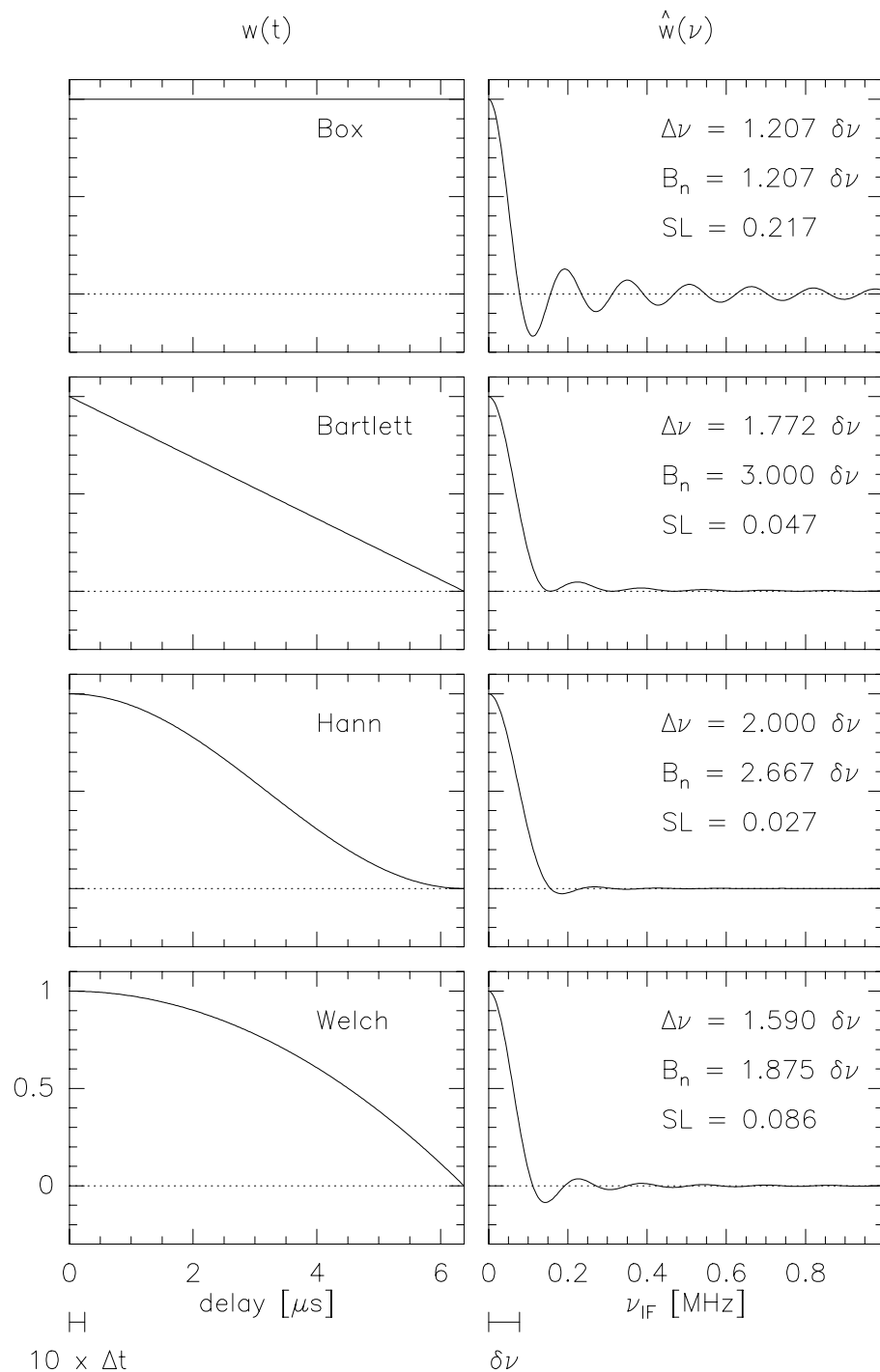


Figure 6.7: Several time lag windows, and their Fourier transforms (normalized to peak). The sidelobe levels SL are indicated, as well as the spectral resolution (defined as the FWHP of the main lobe), and the noise equivalent width. The delay step size, and channel spacing are indicated for the following example: 256 channels, clock rate 40 MHz, resulting in a channel spacing of 78.125 kHz.

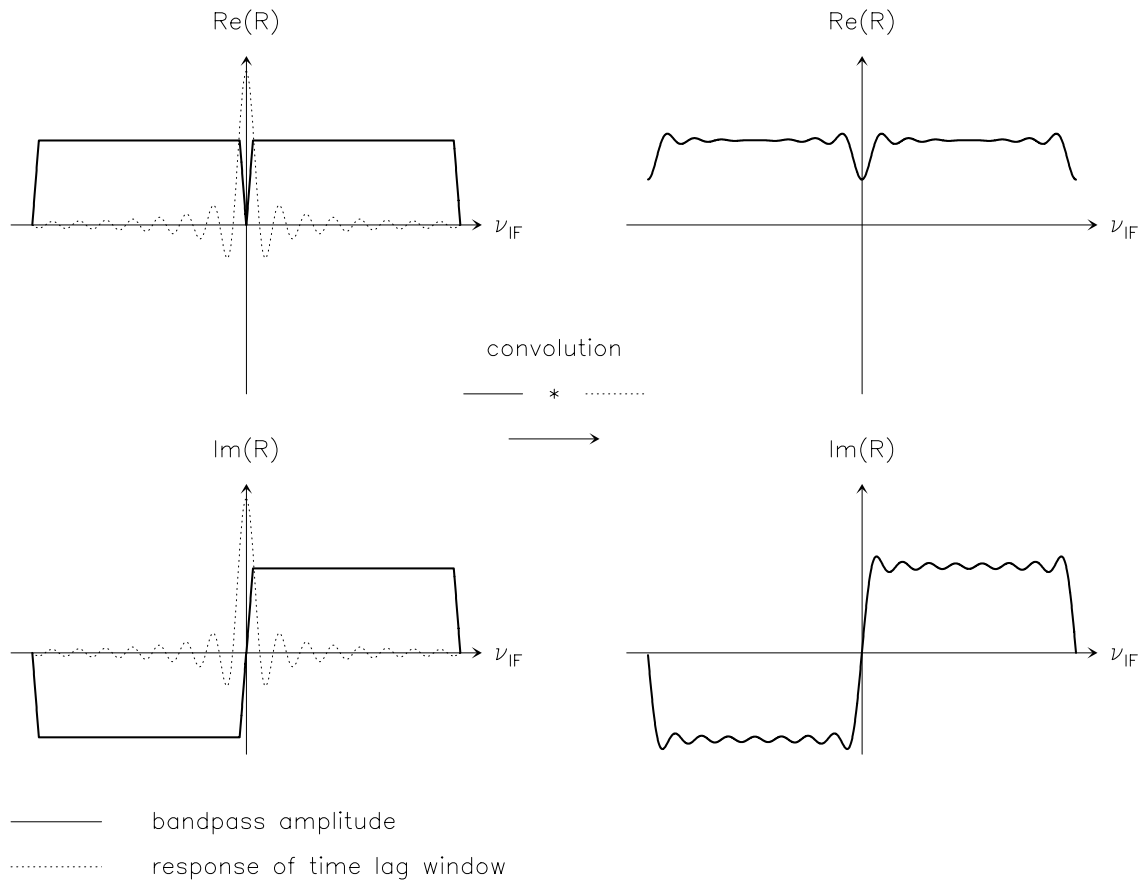


Figure 6.8: The Gibbs phenomenon. The convolution of the bandpass with the (unapodized) spectral window (sinc function) is shown for the real and imaginary parts. Note that for the real part, the phenomenon is stronger at the band edges, whereas for the imaginary part, it contaminates the whole bandpass.

Table 6.4: Maximum integration time of a 16-bit counter

clock frequency:	80 MHz
weight for intermediate-level products:	$n = 3$
positive offset:	$n^2 = 9$
weight for autocorrelation product:	18 (using offset multiplication table)
carry out rate of a 4-bit adder	$18/2^4 = 1.125$
maximum integration time:	$2^{16}/(80 \text{ MHz} \times 1.125) = 0.73 \text{ ms}$
same with a 4-bit prescaler:	$2^{16} \times 2^4/(80 \text{ MHz} \times 1.125) = 11.7 \text{ ms}$

G_{ij} is now a frequency-dependent complex gain function). After calibration it becomes

$$\hat{V}(\nu) = \frac{f(\nu) * [G_{ij}(\nu)V(\nu)]}{f(\nu) * G_{ij}(\nu)} \quad (6.17)$$

Due to the convolution product the complex gain $G_{ij}(\nu)$ does not cancel out, as desired, and $\hat{V}(\nu) \neq V(\nu)$. Automatic calibration procedures have to flag the channels concerned. As shown in Fig. 6.8, for the real part, the effect is stronger at the band edges, but the output of the imaginary part also shows ripples in the middle of the band (thus, the problem is of greater importance for interferometers than for single-dish telescopes using auto-correlators). If the bandwidth to be observed is synthesized by two adjacent frequency windows, the phenomenon is stronger at the band center. You should avoid to place your line there, if it is on top of an important continuum (see Section 6.4.1 for the case of the Plateau de Bure system).

The above summary of the system-dependent performance of a correlator is not exhaustive. For example, the phase stability of tunable filters, which depends on their physical temperature, is not discussed. Alternatives to such filters are image rejection mixers (as used in the Plateau de Bure correlator).

Digital part

Errors induced by the digital part are generally negligible with respect to the analog part. In digital delays, a basic limitation is given by the discrete nature of the delay compensation, which accuracy in turn is limited by the clock period of the sampler. However, digital techniques allow for high clock rates, keeping this error at a minimum.

Evidently, a basic limitation is given by the memory of the counters, setting the maximum time lag (which in turn defines the spectral resolution, as already discussed): with $2K$ bits, we can exactly represent $N = 2^{2K}$ numbers. However, the information contained in the bits is not equivalent. For the 3-level 2-bit correlator, the output of each channel $i = 1, \dots, N$ is

$$R(i) = \frac{1}{2} \left(N \pm \sqrt{N} \sqrt{1 - \text{erf}(v_0/\sqrt{2})} \right) \quad (6.18)$$

(assuming white, Gaussian noise of zero mean and of unit variance, and neglecting the weak contribution of the astrophysical signal). The 1σ -precision of the output is $\approx \sqrt{N}/2$, contained in the last $K - 1$ bits, which thus do not need to be transmitted. The maximum integration time before overflow occurs is set by the number of bits of the counter, and the clock frequency. Table 6.4 shows an example.

The only error cause due to the correlator that is worth to be mentioned is the sampler, i.e. the analog-to-digital conversion. As already shown, the threshold levels are adjusted with respect to the noise in the unquantized signal. However, the noise power may change during the integration. In that case, the correlator does not operate anymore at its optimum level (see Fig. 6.4). This error cause can be eliminated with an automatic level control circuit. However, slight deviations from the optimal level adjustment may remain. Without going too far into detail, the deviations can be decomposed in an even and an odd part: in one case, the positive and negative threshold voltages move into opposed directions (even part of the threshold error). The resulting error can be equivalently interpreted as a change of the signal level with respect to the threshold v_0 , and leads to a gain error. In the other case, the positive and negative

threshold voltages move into the same direction (odd part of the threshold error). This error, however, can be reduced by periodic sign reversal of the digitized samples (if the local oscillator phase is simultaneously shifted by π , the correlator output remains unaffected). Combining the original and phase-shifted outputs, the error cancels out with high precision. Such a phase shift is implemented in the first local oscillators of the Plateau de Bure system (for details see Chapter 7 by R. Lucas). Note also that threshold errors of up to 10 % can be tolerated without degrading the correlator sensitivity too much: the examination of Fig. 6.4 shows that such an error results in a signal-to-noise degradation of less than 0.2 % for a 3-level system, and of less than 0.5 % for a 4-level system (the maxima of the efficiency curves are rather broad).

Another problem is that the nominal and actual threshold values may differ. The error can be described by “indecision regions”. By calculating the probability that one or both signals of the cross-correlation product fall into such an indecision region, the error can be estimated. With an indecision region of 10 % of the nominal threshold value, the error is negligibly small.

Finally, it should be noted that strict synchronisation of the time series from different antennas is mandatory: any deviation will introduce a phase error.

6.4 The correlator on Plateau de Bure

As an example of a cross-correlator used in mm-wave interferometry, I briefly introduce the correlator system on Plateau-de-Bure. Only a spectroscopic correlator is in use. Continuum bands are synthesized by channel averages covering the desired bandwidths. Aspects concerning concrete observing projects are addressed in Chapter 8 by R. Neri.

6.4.1 The third-generation correlator

The third-generation correlator for the Plateau de Bure interferometer will allow for more flexibility, due to the following improvements:

- global bandwidth: 2.56 GHz (vs. 0.96 GHz in the second generation system),
- flexibility: 8 units with channel spacings in powers-of-2 sequence (vs. 6 units, channel spacing in powers-of-4 sequence)
- global digital performance: 9.8 Teramultiplications per second (vs. 1.3 TM s^{-1}).

These improvements are made possible by using new, more integrated technology at both analog and digital signal processing steps.

The cross-correlator comprises eight independent units. Each consists of three parts: an IF processor (frequency setting, low-pass filter selection, oscillator phase control – i.e. the analog functions), a digital part, controlled by a master processor (i.e. delay steps, clipping correction, FFT, small delay corrections, bandpass correction), and a satellite micro reading out and further processing the correlations. Each unit can be placed in the [100, 1100] MHz IF band⁴, in steps of 0.625 MHz (by using a third frequency conversion). There are seven combinations of bandwidth and channel spacing. The channel spacing follows a power-of-two sequence. Three out of the seven modes are synthesized by the adjacent upper and lower sidebands of an image rejection mixer. These bandwidths show the Gibbs phenomenon right in the middle of the band (i.e. at the edges of the IRM sidebands). The central two channels are flagged by default, the observer should avoid to place the most important part of the line there. The highest possible spectral resolution (channel spacing 0.039 MHz) is produced by slowing down the clock rate from 40 to 20 MHz.

The spectroscopic capabilities of the cross-correlator at Plateau de Bure are summarized in Table 6.5. Part of the flexibility is achieved by using the “time-multiplexing” technique. For example, a time-multiplexing factor four means that the data, arriving at a rate of 160×10^6 samples/s, are alternately put into four shift-registers. The shift registers are read out at the clock frequency of 40 MHz, thus creating four data

⁴Note that at Bure the total IF bandwidth available is limited by the receivers to the range [100, 650] MHz

Table 6.5: The Complex Cross Correlator on Plateau de Bure

Bandwidth [MHz]	Sub-band of IRM ⁽¹⁾	Clock Rate [MHz]	Time Multiplex Factor	Number of Lags (2)	Complex Channels	Channel Spacing [MHz]	Spectral Resolution [MHz]	
							(3)	(4)
2 × 160 MHz	LSB + USB	80	4	2 × 128	2 × 64	2.500	3.018	3.975
1 × 160 MHz	LSB or USB	80	4	1 × 256	1 × 128	1.250	1.509	1.988
2 × 80 MHz	LSB + USB	80	2	2 × 256	2 × 128	0.625	0.754	0.994
1 × 80 MHz	LSB or USB	80	2	1 × 512	1 × 256	0.312	0.377	0.497
2 × 40 MHz	LSB + USB	80	1	2 × 512	2 × 256	0.156	0.189	0.248
1 × 40 MHz	LSB or USB	80	1	1 × 1024	1 × 512	0.078	0.094	0.124
1 × 20 MHz	LSB or USB	40	1	1 × 1024	1 × 512	0.039	0.047	0.062

Notes: (1) image rejection mixer (2) with negative & positive time lags (3) box-shaped time-lag window (4) Welch time-lag window

streams taken at a rate that is lower by a factor of four (as compared to the sampling speed). Equivalently, a time-multiplex factor two means two data streams at a rate of 80 MHz each.

For further technical specifications see the Correlator Web page⁵.

6.5 Appendix

6.5.1 Summary of definitions

- Cross-correlation function of voltage outputs v_i and v_j from antenna pair (i, j) :

$$R_{ij}(\tau) = \langle v_i(t)v_j(t + \tau) \rangle = \lim_{T \rightarrow \infty} \frac{1}{T} \int_0^T v_i(t)v_j(t + \tau) dt \quad (6.19)$$

- Covariance of two jointly random variables:

$$\mu = \langle xy \rangle - \langle x \rangle \langle y \rangle \quad (6.20)$$

For signals of zero mean, and again identifying $x = v_i(t)$ and $y = v_j(t + \tau)$,

$$\mu = R_{ij}(\tau) \quad (6.21)$$

- Cross-correlation coefficient of two jointly random variables x, y of variance σ_x^2 and σ_y^2 :

$$\rho = \frac{\mu}{\sigma_x^2 \sigma_y^2} \quad (6.22)$$

For jointly normal random variables of zero mean and of variance $\sigma^2 = \langle x^2 \rangle - \langle x \rangle^2 = \langle x^2 \rangle$, and with $x = v_i(t)$ and $y = v_j(t + \tau)$, the cross-correlation function $R_{ij}(t)$ and the cross-correlation coefficient are related by

$$R_{ij}(\tau) = \rho \sigma^2 \quad (6.23)$$

- Bivariate Gaussian Probability Distribution:

Assume two Gaussian random variables x and y , both of zero mean, and variance σ^2 . The probability $p(x, y) dx dy$ that the value of x is between x_0 and $x_0 + dx$, and that simultaneously the value of y is between y_0 and $y_0 + dy$, is given by the jointly gaussian probability distribution

$$p(x_0, y_0) = \frac{1}{2\pi\sigma^2\sqrt{1-\rho^2}} \exp\left(\frac{-(x_0^2 + y_0^2 - 2\rho x_0 y_0)}{2\sigma^2(1-\rho^2)}\right) \quad (6.24)$$

In our case, the variable x is assigned to the output voltage of antenna i at time t , and y the output voltage of antenna j at time $t + \tau$.

⁵<http://iram.fr/TA/backend/cor6A>

6.5.2 Clipping correction for 4-level quantization

The following determination of the clipping correction is due to [Hagen et al. 1973]:

Given two jointly normal random variables x and y with covariance μ , and given some arbitrary function $g(x, y)$, Price's theorem states that

$$\frac{\partial^m \langle g(x, y) \rangle}{\partial \mu^m} = \left\langle \frac{\partial^{2m} g(x, y)}{\partial x^m \partial y^m} \right\rangle = \int_{-\infty}^{\infty} \int_{-\infty}^{\infty} \frac{\partial^{2m} g(x, y)}{\partial x^m \partial y^m} p(x, y) dx dy \quad (6.25)$$

For random signals of zero mean, the covariance μ is identical with the cross-correlation function $R_{ij}(\tau)$ defined in Eq. 6.1. As shown by Eq. 6.1, we need to accumulate products of the voltage outputs of two antennas (i, j), but using the quantized signals rather than the continuous ones. Thus, with the identification $x = v_i(t)$ and $y = v_j(t + \tau)$, and using \tilde{x} and \tilde{y} for the quantized signals, we can apply Price's theorem to the 4-level cross-correlation function $R_4 = \langle \tilde{x}\tilde{y} \rangle$ such that

$$\frac{dR_4}{d\rho} = \sigma^2 \frac{dR_4}{dR} = \sigma^2 \frac{d\langle \tilde{x}\tilde{y} \rangle}{d\mu} = \sigma^2 \int_{-\infty}^{\infty} \int_{-\infty}^{\infty} \frac{\partial \tilde{x}}{\partial x} \cdot \frac{\partial \tilde{y}}{\partial y} p(x, y) dx dy \quad (6.26)$$

($R = \rho\sigma^2$ denotes the continuous cross correlation function, for the sake of simplicity, antenna indices are omitted). The partial derivatives in the integrand are easily found by using the transfer function shown in Fig. 6.5:

$$\tilde{x} = \Theta(x) + (n-1) [\Theta(x-v_0) - \Theta(-x-v_0)] \Theta(-x) \quad (6.27)$$

where $\Theta(x) = 1$ for $x > 0$, and 0 else. Thus,

$$\frac{\partial \tilde{x}}{\partial x} = 2\delta(x) + (n-1) [\delta(x-v_0) + \delta(x+v_0)] \quad (6.28)$$

Re-writing Price's theorem, we find

$$\begin{aligned} \frac{dR_4}{d\rho} &= \sigma^2 \int_{-\infty}^{\infty} \int_{-\infty}^{\infty} (2\delta(x) + (n-1) [\delta(x-v_0) + \delta(x+v_0)]) \\ &\quad \cdot (2\delta(y) + (n-1) [\delta(y-v_0) + \delta(y+v_0)]) p(x, y) dx dy. \end{aligned} \quad (6.29)$$

Inserting the jointly normal distribution $p(x, y)$, and evaluating the integral yields

$$\begin{aligned} \frac{dR_4}{d\rho} &= \frac{\sigma^2}{\pi} \frac{1}{\sqrt{1-\rho^2}} \left\{ (n-1)^2 \left[\exp\left(\frac{-v_0^2}{\sigma^2(1+\rho)}\right) + \exp\left(\frac{-v_0^2}{\sigma^2(1-\rho)}\right) \right] \right. \\ &\quad \left. + 4(n-1) \exp\left(\frac{-v_0^2}{2\sigma^2(1-\rho^2)}\right) + 2 \right\}, \end{aligned} \quad (6.30)$$

or, alternatively, the integral form given in Eq. 6.11.

Chapter 7

LO System and Signal Transport

Robert Lucas

lucas@iram.fr

IRAM, 300 rue de la Piscine, F-38406 Saint Martin d'Hères, France

7.1 An Heterodyne Interferometer

7.1.1 The simple interferometer

This is composed of 2 antennas, a multiplier, an integrator (Fig. 7.1); we directly multiply the signals, and average in time. $\tau_G = 2\pi\mathbf{b}\cdot\mathbf{s}/c$ is the geometrical delay. Provided the geometrical delay is compensated in the hardware, after filtering out the high frequency terms, the output of the correlator is the real part of the visibility:

$$r(t) = A \cos \varphi(t) \tag{7.1}$$

A complex correlator using a quadrature network can be used to measure the imaginary part; or (equivalently) one uses a spectral correlator.

7.1.2 The heterodyne interferometer

We now consider a more realistic two antenna system (Fig. 7.2), which includes two frequency conversions: e.g. one in the SIS mixer, and one to move the IF band to baseband for numerical sampling and digital correlation. This again is a simplification, but includes all the important effects. The PdB system has in fact 4 frequency conversions (see below).

Let us first consider the effect on phase of a simple frequency conversion.

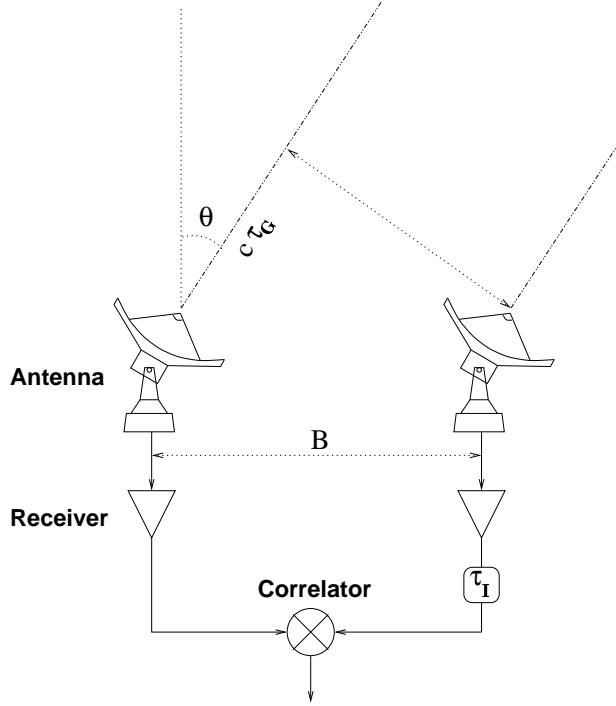


Figure 7.1: A simple, two-antenna interferometer

7.1.3 Frequency conversion

The input signal to the mixer is $U(t) = E \cos(\omega t + \phi)$, and the first LO signal (LO1) is $U_{LO1}(t) = E_{LO1} \cos(\omega_{LO1} t + \varphi_{LO1})$. Mixer output is proportional to $[U(t) + U_{LO1}(t)]^2$ and we select by a filter a band $\Delta\omega$ centered on ω_{IF} . We note: $\omega_U = \omega_{LO1} + \omega_{IF}$, and $\omega_L = \omega_{LO1} - \omega_{IF}$ the angular frequencies in the upper sideband and in the lower sideband, respectively.

The IF output is

$$\begin{aligned} U_{IF}(t) &\propto E_U \cos[(\omega_U - \omega_{LO1})t + \varphi_U - \varphi_{LO1}] + E_L \cos[(-\omega_L + \omega_{LO1})t - \varphi_L + \varphi_{LO1}] \\ U_{IF}(t) &\propto E_U \cos(\omega_{IF} t + \varphi_U - \varphi_{LO1}) + E_L \cos(\omega_{IF} t - \varphi_L + \varphi_{LO1}) \end{aligned} \quad (7.2)$$

After the frequency conversion the phase is the difference of the signal phase and the LO phase, with a sign reversal if the conversion is lower sideband:

	USB	LSB
frequency:	$\omega_{IF} = \omega_U - \omega_{LO1}$	$\omega_{IF} = -\omega_L + \omega_{LO1}$
phase:	$\varphi_{IF} = \varphi_U - \varphi_{LO1}$	$\varphi_{IF} = -\varphi_L + \varphi_{LO1}$

7.1.4 Signal phase

One antenna is affected by the geometrical delay τ_G , and by the phase (φ_U in the upper sideband, φ_L in the lower sideband), which is the quantity to be measured. We apply a compensating delay τ_I in the second IF (IF2), as well as a phase φ_{LO1} to the first LO and a phase φ_{LO2} on the second LO (LO2). We note $\Delta\tau = \tau_I + \tau_G$ the delay tracking error. In a 2-antenna system, we may assume that the signal path through the first antenna suffers no delay of phase offset terms. Obviously the compensating delay τ_I in the second antenna may need to be negative, if the second antenna is closer to the source: in that case one will apply the positive delay $-\tau_I$ on the first antenna. In a N antenna system, one will apply phase and delay commands to all the antennas; a common delay will be applied to all the antennas since no negative delay can be built with current technology.

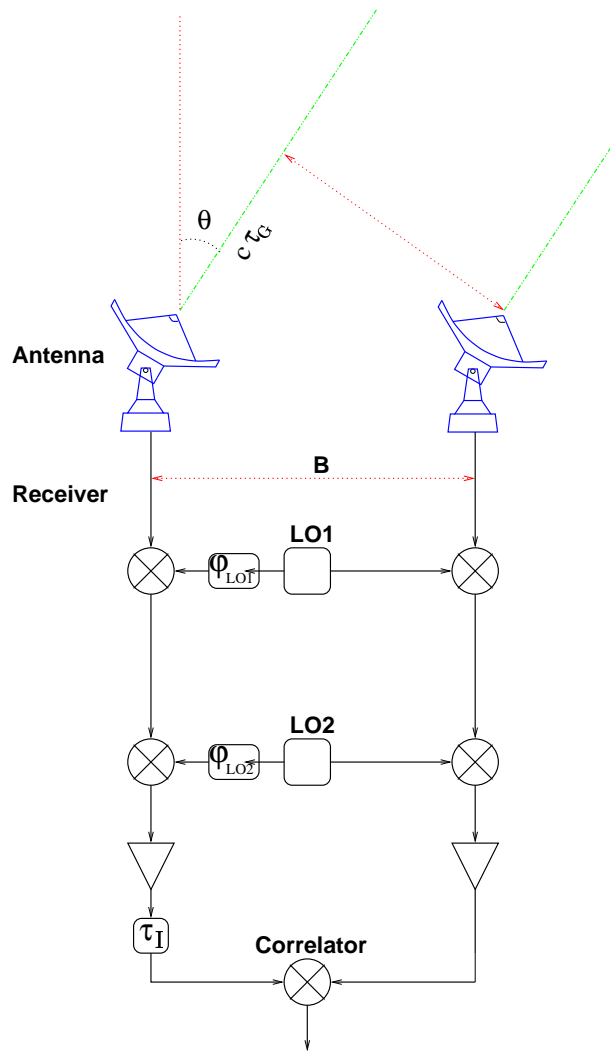


Figure 7.2: A heterodyne, two-antenna interferometer, with two frequency conversions

Let us first consider the upper sideband of the first LO (second LO conversion is assumed upper sideband for simplicity):

	USB	LSB
HF Frequency (RF)	ω_{USB}	ω_{L}
HF Phase	$\varphi_{\text{U}} + \omega_{\text{U}}\tau_{\text{G}}$	$\varphi_{\text{L}} + \omega_{\text{L}}\tau_{\text{G}}$
LO1 Frequency	ω_{LO1}	ω_{LO1}
LO1 Phase	φ_{LO1}	φ_{LO1}
IF1 Frequency	$\omega_{\text{IF1}} = \omega_{\text{U}} - \omega_{\text{LO1}}$	$\omega_{\text{IF1}} = \omega_{\text{LO1}} - \omega_{\text{L}}$
IF1 Phase	$\varphi_{\text{U}} + \omega_{\text{U}}\tau_{\text{G}} - \varphi_{\text{LO1}}$	$-\varphi_{\text{L}} - \omega_{\text{L}}\tau_{\text{G}} + \varphi_{\text{LO1}}$
LO2 Frequency	ω_{LO2}	ω_{LO2}
LO2 Phase	φ_{LO2}	φ_{LO2}
IF2 Frequency	$\omega_{\text{IF2}} = \omega_{\text{U}} - \omega_{\text{LO1}} - \omega_{\text{LO2}}$	$\omega_{\text{IF2}} = \omega_{\text{LO1}} - \omega_{\text{L}} - \omega_{\text{LO2}}$
IF2 Phase	$\varphi_{\text{U}} + \omega_{\text{U}}\tau_{\text{G}} - \varphi_{\text{LO1}} - \varphi_{\text{LO2}}$	$-\varphi_{\text{L}} - \omega_{\text{L}}\tau_{\text{G}} + \varphi_{\text{LO1}} - \varphi_{\text{LO2}}$
after τ_{I}	$\varphi_{\text{U}} + \omega_{\text{U}}\tau_{\text{G}} - \varphi_{\text{LO1}} - \varphi_{\text{LO2}} + \omega_{\text{IF2}}\tau_{\text{I}}$	$-\varphi_{\text{L}} - \omega_{\text{L}}\tau_{\text{G}} + \varphi_{\text{LO1}} - \varphi_{\text{LO2}} + \omega_{\text{IF2}}\tau_{\text{I}}$
Final	$\varphi_{\text{U}} + \omega_{\text{IF2}}\Delta\tau$ $-(\varphi_{\text{LO1}} + \omega_{\text{LO1}}\tau_{\text{G}})$ $-(\varphi_{\text{LO2}} + \omega_{\text{LO2}}\tau_{\text{G}})$	$-\varphi_{\text{L}} + \omega_{\text{IF2}}\Delta\tau$ $+(\varphi_{\text{LO1}} + \omega_{\text{LO1}}\tau_{\text{G}})$ $-(\varphi_{\text{LO2}} + \omega_{\text{LO2}}\tau_{\text{G}})$

To stop the fringes in both sidebands we need the following conditions:

$$\Delta\tau = \tau_{\text{I}} + \tau_{\text{G}} = 0 \quad (7.3)$$

$$\varphi_{\text{LO1}} + \omega_{\text{LO1}}\tau_{\text{G}} = 0 \quad (7.4)$$

$$\varphi_{\text{LO2}} + \omega_{\text{LO2}}\tau_{\text{G}} = 0 \quad (7.5)$$

One sees that *delay tracking* in the second IF imposes a *phase tracking* on the first and second oscillators. The delay error $\Delta\tau$ appears as a phase term proportional to frequency in the IF2 band ω_{IF2} .

The condition that e.g. $\varphi_{\text{LO1}} = -\omega_{\text{LO1}}\tau_{\text{G}}$ means that φ_{LO1} must be commanded to vary at a rate

$$\dot{\varphi}_{\text{LO1}} = -\omega_{\text{LO1}}\dot{\tau}_{\text{G}} \sim 2\pi \frac{b}{\lambda_1} \frac{2\pi}{86400} \quad (7.6)$$

which is about 10 turns per second for $\lambda_1 = 1\text{mm}$ and $b = 1\text{km}$. The condition is much easier for the second LO. In practice the phase is commanded typically every second, as well as its rate of change during the next second (the real curve is approximated by a piecewise linear curve). Note that a linear drift with time of the phase is strictly equivalent to a small frequency offset.

7.2 Delay lines requirements

7.2.1 Single sideband processing in a finite bandwidth

Assume that the conversion loss is negligible for the lower sideband. At a given IF2 frequency ω_{IF2} the directly correlated signal is:

$$V_r = A \cos(\varphi + \omega_{\text{IF2}}\Delta\tau) \quad (7.7)$$

while the sine correlator would give:

$$V_i = A \sin(\varphi + \omega_{\text{IF2}}\Delta\tau) \quad (7.8)$$

$$V = V_r + iV_i = A e^{i(\varphi + \omega_{\text{IF2}}\Delta\tau)} \quad (7.9)$$

Assume we use a correlator with a finite bandwidth $\Delta\nu$. The correlator output is obtained by summing on frequency in the IF passband:

$$V = \int A e^{i(\varphi + \omega_{\text{IF2}}\Delta\tau)} B(\omega_{\text{IF2}}) d\omega_{\text{IF2}} \quad (7.10)$$

where $B(\omega_{\text{IF}2})$ is a complex passband function characteristic of the system: gain of the amplifiers and relative phase factors.

$$V = A e^{i\varphi} \int e^{i\omega_{\text{IF}2}\Delta\tau} B(\omega_{\text{IF}2}) d\omega_{\text{IF}2} \quad (7.11)$$

We have assumed that the source visibility is constant across the band; the source visibility, when the delay error varies, is multiplied by the Fourier transform of the complex passband.

The delay error must be kept much smaller than the inverse of the instantaneous bandwidth to limit the signal loss to a small level. The delays are usually tracked in steps, multiples of a minimum value. To limit the loss to 1%, the minimum delay step must be $\sim 0.25/\Delta\nu$ (0.5 ns for a 500 MHz bandwidth).

7.2.2 Double sideband system

In that case the signals coming from the upper and lower sidebands have similar attenuation in the RF part and similar conversion loss in the mixers. They will have similar amplitudes in the correlator output. The result for the cosine correlator is:

$$\begin{aligned} V = & A_U e^{i[\varphi_U + \omega_{\text{IF}2}\Delta\tau - (\varphi_{\text{LO}1} + \omega_{\text{LO}1}\tau_G) - (\varphi_{\text{LO}2} + \omega_{\text{LO}2}\tau_G)]} \\ & + A_L e^{i[-\varphi_L + \omega_{\text{IF}2}\Delta\tau + (\varphi_{\text{LO}1} + \omega_{\text{LO}1}\tau_G) - (\varphi_{\text{LO}2} + \omega_{\text{LO}2}\tau_G)]} \end{aligned} \quad (7.12)$$

Assuming the same visibility in both sidebands:

$$V = A \cos(\varphi - \varphi_{\text{LO}1} - \omega_{\text{LO}1}\tau_G) e^{i(\omega_{\text{IF}2}\Delta\tau - \varphi_{\text{LO}2} - \omega_{\text{LO}2}\tau_G)} \quad (7.13)$$

If the delays are tracked, and the LO phases rotated as above, the exponential term is 1 and only the real part of the visibility is measured. Some trick is thus needed to separate the signal from the sidebands.

7.3 sideband separation

The sideband separation by mixer rejection is difficult for low IF frequencies, and currently works only at 3mm. The image rejection varies with frequency. There are other methods that cancel the signal in the unwanted side band by a larger factor. They are based on the fact that the LO1 phase $\varphi_{\text{LO}1}$ appears with a different sign on the USB and LSB signals.

7.3.1 Fringe rate method

One might choose to drop the phase rotation on the second LO and let the fringes drift at their natural fringe rates. These rates are opposed in sign for the USB and LSB, and they might be separated electronically. However the natural fringe rate sometimes goes to zero (when the angular distance between source and baseline direction is minimum or maximum), and at least in these cases the method would fail.

It would be more practical to offset the LO1 and LO2 phase rates $\dot{\varphi}_{\text{LO}1}$ and $\dot{\varphi}_{\text{LO}2}$ from their nominal values by the same amount ω_{OFF} . If the offsets have the same sign, they will compensate for the USB and offset the fringe rate by $2\omega_{\text{OFF}}$ in the LSB. If ω_{OFF} is large enough, the LSB signal will be cancelled. Note that offsetting $\varphi_{\text{LO}1}$ by a fixed amount is equivalent to offsetting the LO1 frequency.

This is a simple method to reject the unwanted sideband. Note that the associated noise is not rejected.

7.3.2 Phase switching method

Assume a variable phase offset ψ_1 is added to the LO1 phase command appropriate for compensating the geometrical delay variation:

$$\varphi_{\text{LO}1} = -\omega_{\text{LO}1}\tau_G + \psi_1 \quad (7.14)$$

ψ_1 will be subtracted to the phase of the USB signal, and added to that of the LSB signal. If ψ_1 is switched between 0 and $\pi/2$, the relative phase of the USB and LSB will be switched between 0 and π , and the signals may be separated by synchronous demodulation:

ψ_1	Signal
0	$V_1 = A_U e^{i\varphi_U} + A_L e^{-i\varphi_L}$
$\pi/2$	$V_2 = A_U e^{i(\varphi_U - \pi/2)} + A_L e^{i(-\varphi_L + \pi/2)}$

Then one may compute the visibilities in each sideband:

$$\begin{aligned} A_U e^{i\varphi_U} &= (V_1 + iV_2)/2 \\ \text{and } A_L e^{-i\varphi_L} &= (V_1 - iV_2)/2 \end{aligned} \quad (7.15)$$

We have assumed here that we have a complex correlator (sine + cosine), or equivalently a spectral correlator measuring positive and negative delays (see Chapter 6).

One may also switch the phase by π , in which case the sign of all the correlated voltages is reversed. This has the advantage of suppressing any offsets in the system. Actually both switching cycles are combined in a 4-phase cycle:

ψ_1	Signal
0	$V_1 = A_U e^{i\varphi_U} + A_L e^{-i\varphi_L}$
$\pi/2$	$V_2 = A_U e^{i(\varphi_U - \pi/2)} + A_L e^{i(-\varphi_L + \pi/2)}$
π	$V_3 = -V_1$
$3\pi/2$	$V_4 = -V_2$

$$\begin{aligned} A_U e^{i\varphi_U} &= (V_1 + iV_2 - V_3 - iV_4)/4 \\ \text{and } A_L e^{-i\varphi_L} &= (V_1 - iV_2 - V_3 + iV_4)/4 \end{aligned} \quad (7.16)$$

In a N antenna system one needs to switch the relative phases of all antenna pairs. This could be done by applying the above square-wave switching on antenna 2, then on antenna 3 at twice the switching frequency, and so on. In practice the switching waveforms are orthogonal Walsh functions.

7.4 The PdB Signal and LO transport system

A block diagram of the Plateau de Bure interferometer system is shown in Fig. 7.3.

7.4.1 Signal path

The signal path is outlined in Fig. 7.3. It shows the signal and LO paths for one antenna and one receiver band. The high frequency part (receiver) was described in Chapter 5. The amplified first IF output (1275-1775 MHz) is down-converted to the 100 – 600 MHz band and transported to the central building in a high-quality cable. Before down-conversion, the band shape is modified by a low-pass filter; since the LO2 is at a higher frequency than the IF2, the bandpass will be reversed in the conversion, and this by anticipation compensates for the frequency dependent attenuation in the cable (which is of course higher at the high-frequency end of the bandpass).

The 100 – 600 MHz band arriving in the central building is directed to the correlator analog IF processor inputs (with a division by 6 since there are 6 identical correlator units) and to total power detectors which are used for the atmospheric calibration and for the radiometric phase correction.

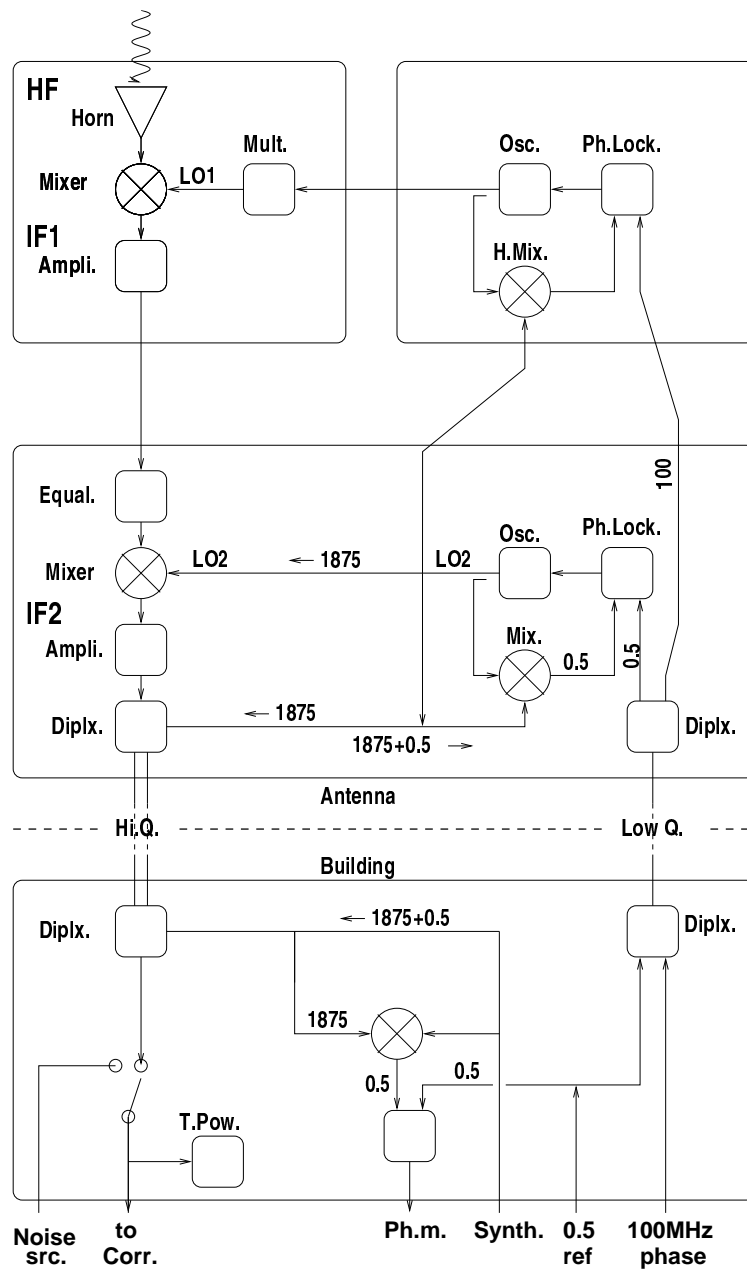


Figure 7.3: The Plateau de Bure interferometer system

7.4.2 LO generation

The first local oscillator is a Gunn oscillator (a tripler is used for the 1.3mm receiver). The Gunn is phase-locked by mixing part of its output with a harmonic of a reference signal (used also as the second LO): the harmonic mixing produces a 100MHz signal, the phase of which is compared to a reference signal at frequency $\epsilon_1 = 100\text{MHz}$, coming from the central building. That reference signal is used to carry the phase commands to be applied to the first LO: a continuously varying phase to compensate for earth motion and phase switching used to separate the side-bands and suppress offsets.

The LO1 signal at ν_{LO1} may be locked either 100MHz above (“High Lock”) or below (“Low Lock”) the N_{H}^{th} harmonic of the LO2 frequency ν_{LO2} :

$$\nu_{\text{LO1}} = (N_{\text{H}}\nu_{\text{LO2}} \pm \epsilon_1)N_{\text{M}} \quad (7.17)$$

The multiplication factor N_{M} is 1 for the 3mm receiver and 3 for the 1.3mm receiver.

The second local oscillator, at $\nu_{\text{LO2}} = 1875 \pm 25\text{ MHz}$, is phase locked $\epsilon_2 = 0.5\text{ MHz}$ below the frequency sent by the synthesizer in the central building (which is under computer control and common to all antennas):

$$\nu_{\text{LO2}} = \nu_{\text{SYN}} - \epsilon_2 \quad (7.18)$$

The ϵ_2 reference frequency is sent to all antennas from the central building in a low quality cable, together with the $\epsilon_1 = 100\text{MHz}$ reference frequency for the first LO. The ν_{SYN} is sent to the antennas via the same high-Q cable that transports the IF2 signal. No phase rotation is applied on the second local oscillator. The relation between the RF signal frequencies (in the local rest frame) in the upper and lower sidebands and the signal frequency in the second IF band is thus (for high lock):

$$\nu_{\text{U}} = \nu_{\text{LO1}} + (\nu_{\text{LO2}} - \nu_{\text{IF2}}) = (N_{\text{M}}N_{\text{H}} + 1)\nu_{\text{LO2}} + N_{\text{M}}\epsilon_1 - \nu_{\text{IF2}} \quad (7.19)$$

and in the lower sideband:

$$\nu_{\text{L}} = \nu_{\text{LO1}} - (\nu_{\text{LO2}} - \nu_{\text{IF2}}) = (N_{\text{M}}N_{\text{H}} - 1)\nu_{\text{LO2}} + N_{\text{M}}\epsilon_1 + \nu_{\text{IF2}} \quad (7.20)$$

7.4.3 Further signal processing

In each correlator a variable section of the IF2 band is down-converted to baseband by means of two frequency changes, with a fixed third LO (LO3) and a tunable fourth LO (LO4). It is on that LO4 that the phase rotations needed to compensate for residual phase drifts due to the geometrical delay change are applied (in fact that LO4 plays the role of the second frequency conversion in the above analysis). No phase rotation is applied on the second and third local oscillators.

The phase rotation applied on the fourth LO's is:

$$\varphi_{\text{LO4}} = (\omega_{\text{LO2}} + \omega_{\text{LO3}} - \omega_{\text{LO4}})\tau_{\text{G}} \quad (7.21)$$

since the second and third conversions are LSB while the fourth is USB. It is different in the different correlator units since the ω_{LO4} frequencies are different.

7.4.4 Phase stability requirements

Short term phase errors in the local oscillators (jitter) will cause a decorrelation of the signal and reduce the visibility amplitude by a factor

$$\eta_{12} = e^{-(\sigma_1^2 + \sigma_2^2)/2} = \sqrt{e^{-\sigma_1^2} e^{-\sigma_2^2}} = \sqrt{\eta_1 \eta_2} \quad (7.22)$$

where σ_1 is the rms phase fluctuation of the LO in one of the antennas (σ_2 in the other). $\eta_1 = e^{-\sigma_1^2}$ is the decorrelation factor for one antenna; typical requirements on σ_1 are:

η_1	0.99	0.98	0.95	0.90
σ_1 (degrees)	5.75	8.1	13.0	18.5

The phase stability required on the LO2 is $\sigma_1/(N_{\text{M}}N_{\text{H}}) \sim 0.1^\circ$ for a 0.95 efficiency at 1.3mm: very stable oscillators are needed.

7.4.5 Cable electrical length control

The ϵ_2 reference frequency is also used for a continuous control of the electrical length of the High-Q cables transporting the IF2 signal from the antennas to the correlator room in the central building. A variation ΔL in the electrical length of the High-Q cable will affect the signal phase by $360\Delta L/\lambda_{\text{IF2}}$; for a length of 500m and a temperature coefficient of 10^{-5} we have a variation in length of 5mm or 17ps, which translates into a phase shift of 4 degrees at the high end of the passband: this is a very small effect.

The same length variation induces a phase shift of $360 \times 0.017 \times 1.875 = 11.5$ degrees at the LO2 frequency. This signal being multiplied by $(N_H + 1)N_M \sim \nu_U/\nu_{\text{LO2}} \sim 120$ for the 1.3mm receiver, we have a totally unacceptable shift of about 4 turns. The cables are buried in the ground for most of their length; however they also run up the antennas and suffer from varying torsions when the sources are tracked, and in particular when the antenna is moved from the source to a phase calibrator.

For this reason the electrical length of the cables is under permanent control. The LO2 signal is sent back to the central building in the High Q cable, and there it is mixed with the $\nu_{\text{LO2}} + \epsilon_2$ signal from the synthesizer. The phasemeter measures every second the phase difference between the beat signal at 0.5 MHz and a reference 0.5 MHz signal.

The measured phase difference is twice the phase offset affecting the LO2, it is used by the computer to correct the LO1 phase φ_{LO1} after multiplication by $\nu_{\text{LO1}}/\nu_{\text{LO2}}$.

7.5 Next generation instruments

Next generation instruments will operate at higher frequencies, and need higher bandwidths, and better angular resolution. The major changes expected are:

- Use of optical fibers rather than cables. Actually this is already the case in some interferometers.
- Digitize higher in the signal chain. transporting digital signals require more bandwidth but is more accurate.
- Possibly generate LO signals using infrared lasers rather than by multiplying lower frequency signals.

Chapter 8

The Plateau de Bure Interferometer

Roberto Neri

`neri@iram.fr`

IRAM, 300 rue de la Piscine, F-38406 Saint Martin d'Hères, France

8.1 History

The design of the millimeter wave interferometer started in June 1979, in the year of the foundation of IRAM, the Institut de Radioastronomie Millimétrique. The construction of the first antenna was completed in June 1987, and three years later an interferometer consisting of three antennas was opened to guest observers. First fringes at 230 GHz were obtained in April 1995, the five antenna configuration of the interferometer was attained one year later, and the six antenna correlator installed end summer 2000. Work is in progress for the construction of the sixth antenna and is foreseen to extend the north-south track. Starting with the commissioning period in 1990 up to the end of 1999, the Plateau de Bure interferometer was able to carry out more than 500 different projects which involved more than 200 investigators from all around the world.

8.2 Description

The Plateau de Bure interferometer is located in the South of the French Alps, near St-Etienne en Dévoluy in the Département of Hautes Alpes. The interferometer's altitude is 2552 m (2560 m at the intersection of the azimuth and elevation axes of the telescopes) and its longitude and latitude at the array phase center are 05:54:28.5 E and 44:38:02.0 N. After the cable-car accident, two means of transport to Plateau de Bure have been made available: transport by helicopter or on the ground using a four-wheel drive in summer, a rattrack in winter time, and a final foot-path to get atop the Plateau. A hangar in which the sixth antenna is currently under construction, is used for antenna maintenance, overhaul periods and, in general, for antenna repair work which needs to be carried out in between times but under safety conditions. The hangar houses a few workshops for cryogenics, mechanics, electronics, a power station which provides

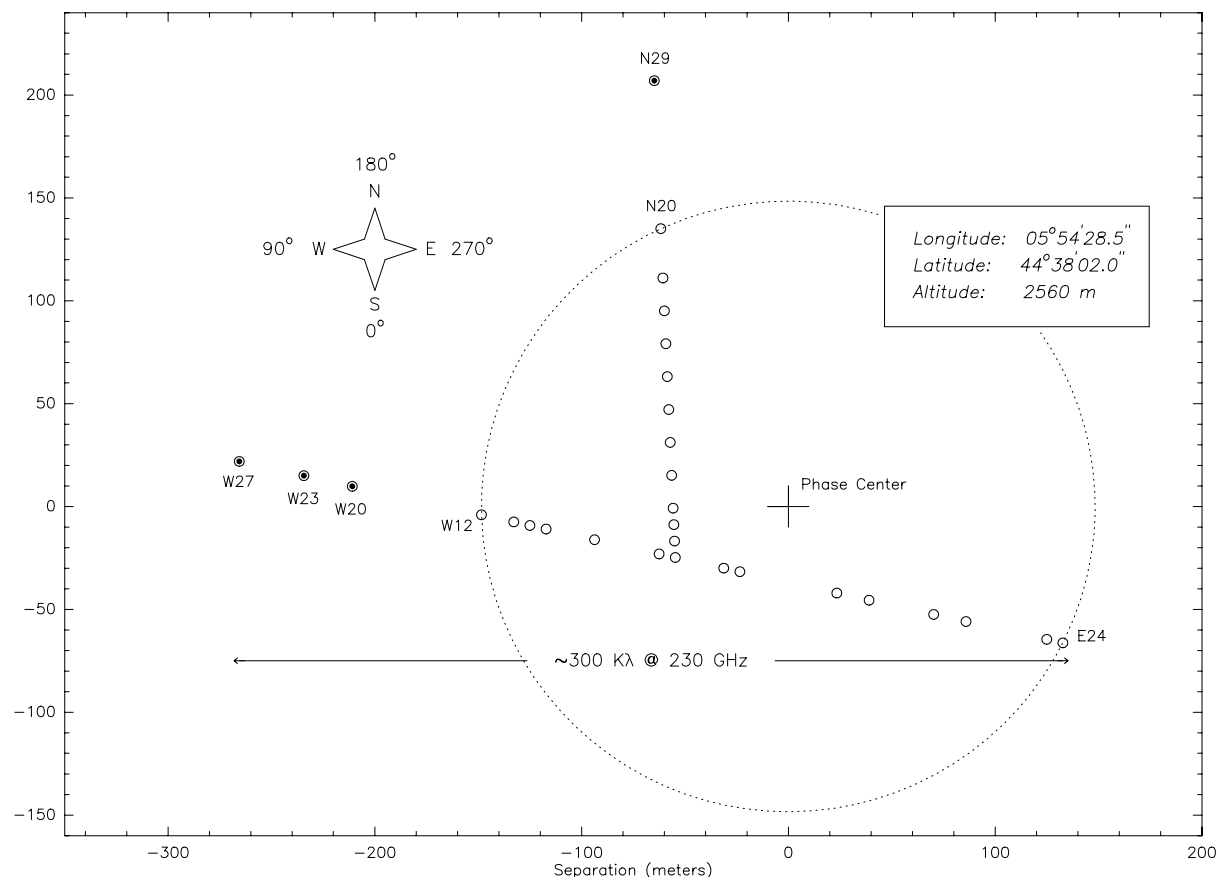


Figure 8.1: PdB interferometer station layout as of March 2001. The interferometer origin is defined as the center of the circle which goes through the stations N20, E24 and W12, the so-called IRAM phase center, and thus gives a unique vector definition to each station.

electric autonomy in case of interruptions in the external power supply and finally, the correlator room and the control room for remote array operation. Almost adjacent to the hall are the living quarters for the staff who supports the uninterrupted round the clock operation of the interferometer.

Currently, the interferometer consists of five antennas arranged in a T -shaped pattern extending over a maximum of 408 meters east-west and 232 meters north-south. A sixth antenna is expected to be ready for 2002, and the extension of the northern track is still under construction.

The antennas are conceptually identical: they all have a fully steerable alt-az mount which incorporates a self-propelled transporter for moving the antennas (130 tons) along the tracks between stations. Each antenna is a 15 m diameter Cassegrain telescope with the backstructure and quadrupod legs largely made of carbon fiber for high thermal stability. The high precision of the reflecting antenna surface ($40\text{--}60\mu\text{m}$) guarantees best performance: all antennas have essentially the same sensitivity ($22\text{ Jy}\cdot\text{K}^{-1}$ at 3 mm, $35\text{ Jy}\cdot\text{K}^{-1}$ at 1 mm – see Chapter 12 by A.Dutrey), and very similar pointing and focussing characteristics.

All the antennas are equipped with dual-frequency SIS receivers operating simultaneously in the 82 GHz–115 GHz and 205 GHz–245 GHz range. Typical double sideband receiver noise temperatures are between 25 K and 50 K at 3 mm and between 40 K and 60 K at 1 mm. The receivers upper and lower sidebands are separated by the correlators with a rejection better than 26 dB. The lower to upper sideband gain ratio depends on the receiver and varies typically between 0.2 and 4.0 under standard operating conditions in the 3 mm band, and yields essentially a double-side band tuning in the 1 mm band. Pure single sideband tuning (with rejection 15 to 25 dB) is also possible in the 3 mm band, with receiver temperatures around 60 to 80 K.

Eight totally independent correlators units are available that provide an 87% correlation efficiency

(for more details see Chapter 6 by H. Wiesemeyer). Each correlator unit provides by default 7 choices of bandwidth/channel configurations down to a nominal velocity resolution of 50 m.s^{-1} at 230 GHz. The correlators can independently be connected either to the 3 mm or to the 1 mm receiver (100-650 MHz) IF2.

A central control computer coordinates the entire interferometer (antennas, receivers and correlators and quite some other equipment) and makes the data acquisition. Raw data corresponding to the individual dumps of the correlator buffers will not be available as real-time jobs apply automatic calibrations (clipping correction, apodization, FFT, sideband separation, small delay correction, bandpass correction and other corrections) and make automatic data quality assessments (marking bad data, shadowing, phase lock, just to cite a few flags) before data is written to disk. A second workstation provides the software resources for offline data analysis and for data archiving before transfer to the Grenoble headquarters.

8.3 Array operation

8.3.1 Array calibration

The astronomical setup of the interferometer involves a number of steps that are done under the joint responsibility of the array operator and of the astronomer on duty (AoD). The goal of the setup is to maximize the interferometer performance in view of sensitivity and positional precision.

Change of array configuration

A change of configuration is the responsibility of the operators and of the technical staff. Since most projects, as mapping, mosaicing and snapshot observations, require more uv -coverage than a single configuration can provide, the antennas are moved typically every three weeks or so, to a new configuration. Every additional configuration increases the mapping sensitivity and the uniformity of the uv -coverage by adding $N(N - 1)/2$ baselines to the sampling function (these are 10 baselines during the winter period, 6 baselines during the summer period when the array is operated with only 4 antennas). Configurations are usually selected among six types according to several criteria: antenna availability, project type, atmospheric seeing, uv -coverage, pressure in local sidereal time, sun avoidance and other factors.

Six primary configurations are needed to cover the desired range of angular resolution at the two operating frequencies with 5 antennas:

Configuration	Stations
D	W05 W00 E03 N05 N09
C1	W05 W01 E10 N07 N13
C2	W12 W09 E10 N05 N15
B1	W12 E18 E23 N13 N20
B2	W23 W12 E12 N17 N29
A	W27 W23 E16 E24 N29

The configurations can be combined to produce five sets of configurations for different angular resolution:

Set	Configurations	Purpose
D	D	detection / lowest resolution
CD	D, C2 or C1	$3.5''$ at 100 GHz
CC	C1, C2	higher resolution than CD
BC	B1, C2	$2.0''$ at 100 GHz
BB	B1, B2, C2	higher resolution and sensitivity
AB	A, B1, B2	$1.0''$ at 100 GHz

Special configurations and sets of configurations are used during the annual antenna maintenance period which is usually between May and October. During this period observations at 1 mm are for most of the

time not feasible, specially in the two extended B configurations. Observations in the A configuration whether at 3 mm or 1 mm will in general only be scheduled during the winter period. Requested non-standard configurations are considered only in exceptional cases.

Antenna focus

Sensitivity is one of the most important concerns. As a rule of thumb, an axial displacement of the secondary by $\sim \lambda/3$ results in a 20% loss of sensitivity. To avoid losses larger than 3%, the position of the secondary needs to be measured to much better than $\lambda/10$ on regular time intervals. The positional precision, however, depends on the source strength, the operating wavelength, the sampling of secondary positions and, finally, on atmosphere stability. In general, the focus is measured at 3 mm on a strong quasar by displacing the secondary in steps of 1 mm (in steps of 0.45 mm if done at 1 mm). This is systematically done by the operators at the beginning of every project and is automatically verified by the system every hour during project execution.

Antenna pointing

A high pointing accuracy is demanded in view of sensitivity and mapping quality. Antenna pointing errors affect the global sensitivity of the interferometer and may lead to severe errors in the image restoration process. As a rule, a pointing precision of $\Delta\theta \sim \theta_{\text{FWHP}}/20$ is desirable at the highest frequency. The good pointing accuracy results from an optimized structural design: a good knowledge of the gravitational load, a good positional stability of the receivers (a good alignment is needed for dual-frequency observations), a precise control of the secondary, high precision bearings and position encoders, a good servo system, ... and a good software control for repeatable antenna pointing errors. The quality of a pointing model is generally limited by wind and thermal load effects. The absolute pointing accuracy achievable with the IRAM antennas is in general below the 2-3'' rms at each axis with a slightly higher uncertainty in elevation. Such a pointing accuracy leads to very small intensity variations, most of the time with negligible effects on the image reconstruction. Higher accuracy is obtained by regular relative pointing measurements every hour.

Each antenna is characterized by a fixed set of pointing parameters. These are measured only in certain circumstances: when an antenna is going to see first light, when modifications are made which may affect the pointing of an antenna, or more generally in cases of suspected pointing problems. In these cases a precise interferometric pointing session, eventually with a preceding less sensitive full-sky single-dish session, is required to derive the full set of antenna pointing parameters. Such pointing sessions are reduced with a dedicated non-linear fitting program in use at Plateau de Bure.

The pointing model is actually based on 5 parameters only, all others being negligibly small. These parameters are: IAZ and IEL (the azimuth and elevation encoder zero point correction), COH (the antenna horizontal collimation), and IVE and IVN (the antenna East-West and North-South inclination). IAZ, IEL, IVE and IVN are in station dependent, while COH is in principle an antenna constant. IAZ, IEL and COH are measured in interferometric mode by pointing on a few low elevation and high elevation sources. In general, three strong quasars at 3 mm are fully sufficient. The remaining two parameters, IVE and IVN are measured on every project start with an inclinometer by making an antenna turn through 360°.

Delay measurements

Delay measurements aim at the correction of cable length (electric path) differences between two antennas after compensation of the geometrical path length. An improper knowledge of the difference in cable length is visible as a frequency dependent phase slope in the intermediate frequency bands (IF1 and IF2), and, depending on the amplitude of the slope, may result in a more or less important loss of sensitivity. The delay is measured by a cross-correlation on a strong radio source at the beginning of every project.

Baseline lengths measurements

The goal is to measure the position of each antenna i relative to a common reference point (distances X_{ij}, Y_{ij}, Z_{ij} between antennas i and j or distances dX_i, dY_i, dZ_i with respect to the theoretical station

position) in order to subtract the phase term $2\pi w$ (see Chapter 2 by S.Guilloteau) at any hour angle and declination from the observed phase. The absence of a good baseline solution is equivalent to having large uncertainties in the baseline separation between different antennas. As a consequence, the geometrical delay might improperly be compensated and large time-variable phase errors might affect the observations.

Though the quality of a baseline solution is easily found out – the calibrator’s visibility phase shouldn’t vary with reference to the phase tracking center as function of hour angle and declination – a good baseline solution is truly indispensable for the purpose of phase calibration. Phase errors can often be more deleterious on compact configurations where source visibilities are stronger than on extended configurations. As a reference, winter conditions allow baselines in the D configuration to be measured at 3 mm with a $5^\circ - 8^\circ$ phase accuracy and with $5^\circ - 20^\circ$ in the A configuration. In summer conditions the accuracy is often 2 – 3 times lower.

Though no high accuracy is needed for antenna positioning (offset position from the target location is routinely within a wavelength), the actual antenna position has to be known with high precision: within a small fraction of a wavelength (70-300 μ m). The precision is limited essentially by the atmosphere and by thermal effects.

The baseline parameters can be obtained to high accuracy from observations of a number k of relatively strong point sources, well-distributed in hour-angle and declination, for which accurate positions are available. The analysis of these observations is usually carried out with CLIC, the calibration program, using a least-square-fit analysis on the geometric phase difference for antenna pairs (i, j) :

$$\begin{aligned} \phi_{ij}^g &= \phi_{ij}^s + \phi_{ij}^a = 2\pi w = \\ &= \frac{2\pi}{\lambda} \underbrace{(X_{ij}, Y_{ij}, Z_{ij})}_b \cdot \underbrace{\begin{pmatrix} \cos H \cos \delta \\ -\sin H \cos \delta \\ \sin \delta \end{pmatrix}}_s + \phi_{ij}^a \\ \rightarrow \Delta\phi_{ijk}^g &= \frac{2\pi}{\lambda} (\Delta b_{ij} \cdot s_k + \underbrace{b_{ij} \cdot \Delta s_k}_{\simeq 0}) + \Delta\phi_{ijk}^a \end{aligned}$$

where ϕ_{ij}^s is the assumed geometrical phase between the two stations, H and δ the hour angle and declination of the source, and where $\Delta\phi_{ijk}^a = O_{ij} \cos \text{El}_k$ are elevation dependent correction terms for the non-intersection of the elevation and azimuth axes in the nodal point of the antennas. These terms are well-known and stand for non-negligible elevation dependent variations of the visibility phase which need to be removed as accurately as possible before solving for the baselines.

In theory, three sources are sufficient to measure the actual baseline lengths, in practice 10-12 sources are necessary to obtain an accurate measurement. Since a displacement by $1''$ at 100 GHz on a baseline of 100 m translates already to a phase offset of $\sim 58.2^\circ$ (~ 1 rad), the positions of the radio sources used for baseline measurements need to be known with an accuracy Δs_k better than $0.02''$.

The baseline equation implies that positional errors are equivalent to phase errors. Since baseline length errors scale with the angular separation between calibrator and source, the aim is to have calibrators as close as possible to minimize the phase errors.

Sometimes, accurate baselines are not required as in the case of self-calibration projects. Sometimes, however, even if good baselines are required, they simply cannot be determined precisely enough after a change of configuration. Projects observed in the meantime will then need to wait for a better baseline model. Such projects will in general not be phase-calibrated by the astronomer on duty, but phase-calibration has to be done later on by the proposers of the observations.

Gain measurements

Gain measurements (GAIN scans) are cross-correlations on strong radio sources which are essentially used to measure the image to signal sideband ratios for both the 3 mm and 1.3 mm receivers. The required sideband ratio depends on the project, the achievable sideband ratio depends on the receiver and the frequency. An accurate measurement of the receiver gain is necessary for a good estimate of the atmospheric opacity and of the associated thermal noise with which the atmosphere contributes during the observations.

Therefore, results of a gain measurement are followed by an atmospheric calibration (scan CALI).

Receiver stability

As a rule, a high receiver stability $\leq 3 \cdot 10^{-4}$ is never required. Sometimes, however, depending on atmospheric conditions, array configuration and observing frequency, a higher stability may be desirable in view of a very promising radiometric phase correction. Though such a high stability is not always achievable on all the receivers, it makes possible an improvement in data quality when the atmospheric phase correction technique becomes practical (see Chapter 11 by M.Bremer). Experience at Bure from the last three years shows that the radiometric phase correction is quite efficient under clear sky conditions: from spring to autumn essentially during the evening and morning hours, in winter almost always when the weather allows to observe.

Since observations on more compact baselines suffer less from the effects of the atmospheric phase noise – for reference, an rms of less than 10° rms at 3 mm is routinely obtained on the shortest baselines – a high receiver stability in compact configurations is only exceptionally required. Typically, under average observing conditions with a receiver stability of $3 \cdot 10^{-4}$ we may already correct atmospheric phase fluctuations with a precision of 10° at 115 GHz.

8.3.2 Array observations

Setting up a project

Since projects are spread over typically a few months, it is impractical that astronomers actually come to the interferometer for their observations. In some exceptional case, however, when observations require rapid decisions, the presence of a visiting astronomer may become necessary. Up to now and after ten years of operation, only a handful of projects required the presence of a visiting astronomer. Only non-standard observations like mapping of fast moving objects, coordinated observations may require a member of the project team to be present on the site. All observations are currently carried out “in absentee”, and a *local contact* is assigned to each project.

The observer has to specify all aspects of his/her program in an observing procedure. For routine observations, this is usually done with the help of the local contact by parameterizing the general observational procedure. Once the procedure is written, a copy is made available to the operation center at Plateau de Bure. Before start, further verifications will be made by the scientific coordinator and, to finalize the procedure, by the astronomer on-duty who makes a last check by looking at the technical details in the proposal, at the technical report and at the recommendations made by the programme committee.

Quite some time, however, may pass between the preparation of an observational procedure and the actual observations. Depending on the requirements, between a few hours and a few months may go for the decision to start the observations. On average 90% of the projects are completed within 6 months from their acceptance.

Observations

For the observations, the array is operated by an operator with the assistance of an astronomer and under the supervision of the scientific coordinator. The operator has the full responsibility for conducting all observations following pre-established observing procedures or with the help of the astronomer in case of unpredicted events.

The operator will execute the observing procedure according to a pre-established planning which allows for some flexibility in the scheduling, and to a few criteria (as the maximum amount of precipitable water in the atmosphere, the required atmospheric phase stability, the requested observing frequencies, the declination of the targets, the sun avoidance limit and a few other aspects) which will help both the operator and the astronomer in their final decision-making on which project to carry out as next. As a rule, excellent atmospheric conditions will be used for high grade projects requesting sensitivity at high frequencies while the remaining time will in general be devoted to projects which require less stringent atmospheric conditions.

Once a project is selected, the operator will start the observing procedure which sets up the needed equipment configuration (essentially sky frequencies, correlator settings and target coordinates according with the observer’s wishes) and will start preparing the interferometer for the observations: the receivers are

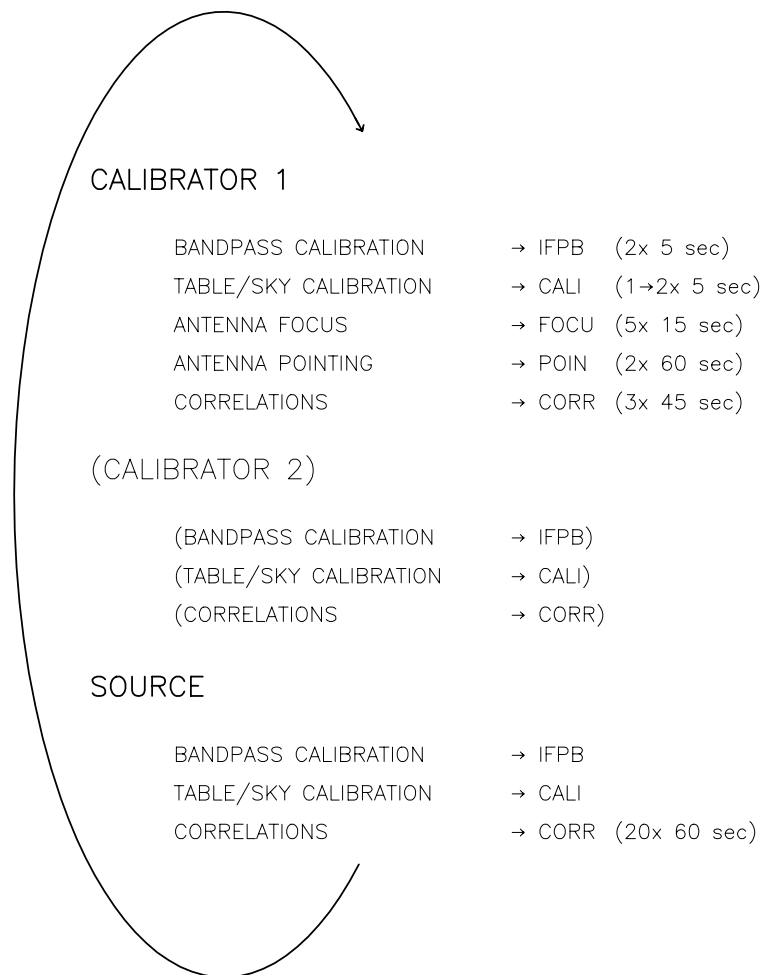


Figure 8.2: Standard observations: a cyclic sequence of measurements. IFPB scans aim at calibrating the IF passband, CALI are auto-correlations on a hot load (290 K) and on the sky (on a 15 K load only at the beginning of every project) to adjust the temperature response of the array, FOCU and POIN scans measure focusing and pointing offsets (done only every 45 minutes) and CORR scans are cross-correlations (complex visibilities). In projects requesting two calibrators every other calibration is made on the second calibrator.

tuned, the gains and the zero-delay of the receiving antenna is adjusted and verified, the antenna pointed and focused, the RF passband is measured and the temperature scale of the interferometer calibrated. The flux of the primary calibrators are then verified, eventually replaced if their flux density has dropped too much, and the observations started.

As soon a project is started, the astronomer on-duty will monitor the execution of the project and the data quality by examining the visibility amplitude and phase of the calibration sources, the antenna tracking in presence of wind, the antenna pointing corrections, and all time-dependent instrumental and atmospheric parameters which could have some implications on the observations. Furthermore, to avoid further observing on a target with wrong coordinates, the astronomer will verify the presence or absence of line and/or continuum emission according to the expected values quoted in the proposal. Finally, the astronomer on-duty will provide pre-calibrated data on a best effort basis. Depending on project complexity and needs, further data analysis is sometimes required on the site to decide on follow-up observations.

When the observations are running, commands are regularly issued to the antennas and to the peripheral equipment (phase rotators, correlators and others) following a well-defined, cyclic sequence as shown

in Figure 8.2. This sequence may slightly change depending on the number of calibrators and on the number of phase centers (i.e. the fields of view requested for different sources or for mosaic-type observations) the observer wishes to track in a single run. Typical observations at Plateau de Bure fall in one of the following categories:

- **Detection:** deep integrations aiming at measuring the flux densities of faint targets (continuum emission and/or line emission/absorption) with the interferometer mostly in compact configurations.
- **Snapshot:** observations in one or more configurations, aiming at measuring apparent sizes in a small sample of targets, in some cases even allowing for mapping. The observational procedure sets up short integrations on individual objects in a cyclic manner.
- **Mapping:** observations generally in two or more configurations aiming at mapping a single object.
- **Mosaic:** similar to snapshot observations, except that the array switches between adjacent, half-beam spaced phase centers to map field of views which are more extended than the primary beam of the antennas.

Monitoring project execution

Under normal circumstances only a few parameters of interest are regularly verified and corrected (mostly automatically) during the observations, but instantaneous (every second) and much more detailed information can be obtained at any time by connecting to the equipment (receivers, antenna control parameters, digital correlator units and others). During the operation the array status is continuously monitored so that the operator can provide fast feedback in response, at any time when necessary. An automatic data quality assessments (flagging bad data, antenna shadowing, receiver phase lock and others) before writing data to disk. The astronomer on-duty has the responsibility of periodically monitoring the data acquisition and to write a few notes assessing the data quality during and after the observations. Monitoring the progress of a project by making intermediate data reductions, however, is the responsibility of the observer. This is not the responsibility neither of the astronomer on-duty nor of his/her local contact.

8.4 Proposal submission and contact people

Quite some people are required to run such a complex instrument as an interferometer. Sooner or later you will meet some of these people, but for most of the projects only a few will play an essential role.

At proposal submission time, you will first get in touch with the scientific secretary who will address you a confirmation of the proposal reception shortly after the deadline. Once a proposal is registered it is sent to the members of the Programme Committee (eight members: two from each country of the IRAM partner organizations plus two external) and, at the same time, its feasibility assessed by the scientific coordinator. Technical considerations as observing strategy, observational risk factors and other issues are communicated to the Programme Committee, only if necessary and only at the time of the meeting to avoid any technical remark to influence the scientific evaluation. Shortly after the meeting, during which the Programme Committee expresses its recommendations, a global proposal evaluation is made by the IRAM director who takes the final decision. Thereupon, a notification is addressed to you which contains the final recommendation and a technical report. If the proposal is not rejected from the beginning, a local contact (a staff astronomer) will be appointed to the project and his name communicated to you.

In the course of the observations, only four persons will play a role for the principal investigator who proposed the observations: the local contact, the scientific coordinator, the astronomer on-duty and the array operator. The local contact, who is the direct interlocutor of the observer, is a staff astronomer whose role is to help the observer in a concerted effort to prepare his/her observations and, later on, in the Grenoble headquarters to help (if needed) the observer in calibrating the data.

Finally, once the observations are completed and before coming to Grenoble, the principal investigator or one of his team members will need to get in touch with two persons: the local contact and the coordinator for the data reduction activities who will finalize the stay of the visiting astronomer at the Grenoble headquarters.

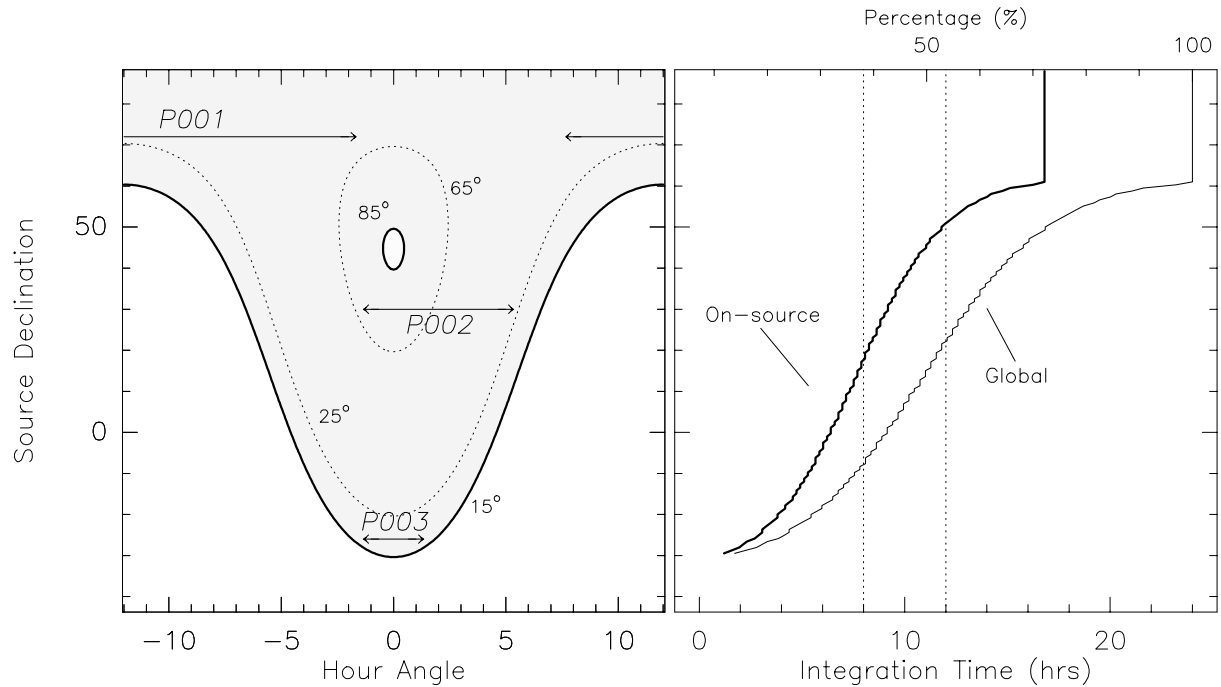


Figure 8.3: Source visibility and effective observing time. The scheduling priority is in general inversely proportional to the declination (observations of low declination sources tend to be more difficult, as they cannot be carried out at any time – the shaded region is the sky above 15 degree elevation). The total observing time per track for depends on the declination of the source and is usually limited to 8-12 hrs for sources of the northern hemisphere. For standard mapping projects, observational overhead counts in by 28% of the time. This is equivalent to an effective on-source integration time of about 6-9 hrs.

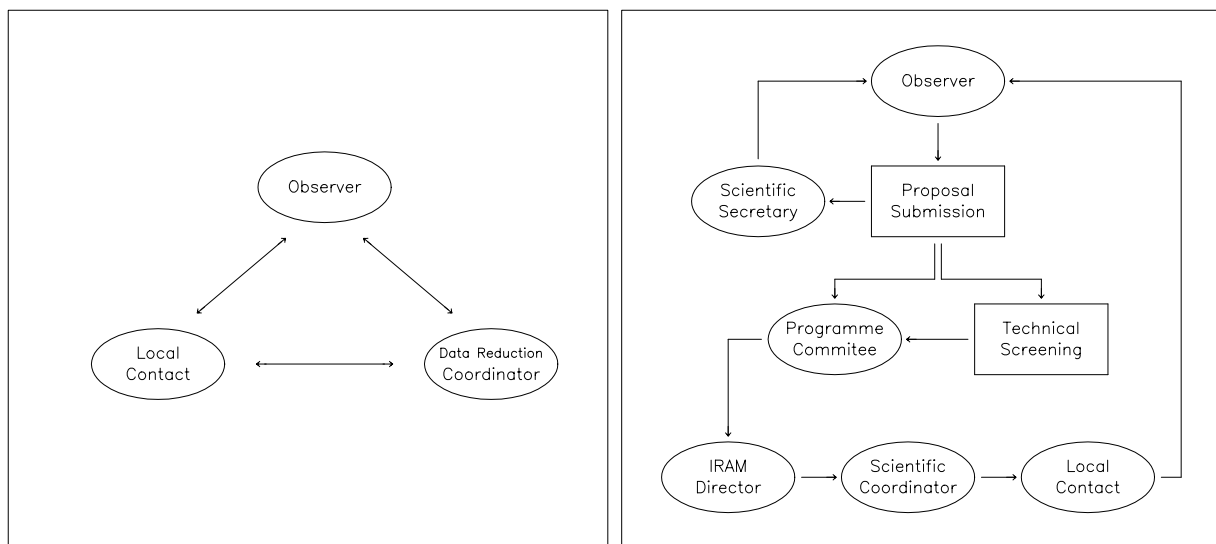


Figure 8.4: Proposal submission and contact persons at IRAM

Chapter 9

Bandpass and Phase Calibration

Robert Lucas

lucas@iram.fr

IRAM, 300 rue de la Piscine, F-38406 Saint Martin d'Hères, France

9.1 Definitions and formalism

As has been seen in the previous lectures, each interferometer baseline provides a measurement of the source visibility at a given point in the u, v plane of spatial frequencies; the source brightness distribution can then be reconstructed by an appropriate Fourier Transform.

In reality things are not so simple. Interferometers are designed with a lot of care; however many electronic components will have variable gains both in amplitude and in phase; these variations will affect the results and have to be taken out. It is generally sometimes more efficient to have a slightly varying instrument response, and a more sensitive instrument, than a very stable one with less sensitivity, provided the varying terms in the response are slow and may be easily calibrated out. At millimeter wavelengths the atmospheric absorption and path length fluctuations will dominate the instrument imperfections in most cases.

For a given observation, if we interpret the correlator response (amplitude and phase) as the source visibility, ignoring any imperfections, we have an observed (apparent) visibility $\tilde{V}_{ij}(t)$, where i, j are antenna numbers, ν the frequency and t is time. If the true source visibility is $V_{ij}(t)$, we may define :

$$\tilde{V}_{ij}(t) = \mathcal{G}_{ij}(t)V_{ij}(t) + \epsilon_{ij}(t) + \eta_{ij}(t) \tag{9.1}$$

where the $\mathcal{G}_{ij}(\nu, t)$ are the complex gains of each baseline. $\eta_{ij}(t)$ is a noise term resulting from thermal fluctuations in the receivers; $\epsilon_{ij}(t)$ is an offset term. This assumes that the system is linear. π phase switching applied on the first local oscillators is a very efficient method of suppressing the offsets $\epsilon_{ij}(t)$; they are generally negligible and will not be considered any further.

9.1.1 Baseline based vs antenna based gains

Since amplitude and phase distortions have different physical origins it is generally useful to write

$$\mathcal{G}_{ij}(t) = g_i(t)g_j^*(t) = a_i(t)a_j(t)e^{i(\phi_i(t)-\phi_j(t))} \quad (9.2)$$

Here we have split the gains into antenna based factors. This is generally legitimate since the gains represent properties of the data acquisition chains which are in the analogue part of the system. The correlator itself is a digital machine and we assume it is perfectly working (including the clipping correction). This assumption is certainly valid when considering a single frequency and a single instant. When we start averaging in time or frequency, the average of the product may not be the product of averages, and we may have some baseline-based effects.

The baseline-based gains can be determined by observing a point source. This is usually a strong quasar. In that case the true visibilities $V_{ij}(t)$ should all be equal to the quasar flux density S . Then

$$\mathcal{G}_{ij}(t) = \frac{\tilde{V}_{ij}(t)}{S} \quad (9.3)$$

The antenna gains $g_i(t)$ can also be deduced from the non-linear set of equations:

$$g_i(t)g_j^*(t) = \frac{\tilde{V}_{ij}(t)}{S} \quad (9.4)$$

This is a system with N complex unknowns and $N(N-1)/2$ equations. In terms of real quantities there are $N(N-1)$ measured values (amplitudes and phases; there are only $2N-1$ unknowns since one may add a phase factor to all complex gains without affecting the baseline-based complex gains. When N is larger than 2 the system is over determined and may be solved by a method of least squares.

If we note $\tilde{V}_{ij} = \tilde{A}_{ij}e^{i\tilde{\varphi}_{ij}}$, the equations for phases are simply:

$$\phi_i - \phi_j = \tilde{\varphi}_{ij} \quad (9.5)$$

It can be shown that the least-squares solutions (when the same weight is given to all baselines, and if we impose the condition $\sum_{j=1,N} \phi_j = 0$), is given by:

$$\phi_i = \frac{1}{N} \sum_{j \neq i} \tilde{\varphi}_{ij} \quad (9.6)$$

For the amplitudes we can define in order to get a linear system:

$$\gamma_i = \log g_i, \quad \tilde{\alpha}_{ij} = \log \tilde{A}_{ij} \quad (9.7)$$

$$\gamma_i + \gamma_j = \tilde{\alpha}_{ij} \quad (9.8)$$

This time the least square solution is, when the same weight is given to all baselines:

$$\gamma_i = \frac{1}{N-1} \sum_{j \neq i} \alpha_{ij} - \frac{1}{(N-1)(N-2)} \sum_{j \neq i} \sum_{k \neq i, > j} \alpha_{jk} \quad (9.9)$$

Obviously this antenna gain determination needs at least three antennas. For three antennas it reduces to the obvious result:

$$g_1 = \frac{\tilde{A}_{12}\tilde{A}_{13}}{\tilde{A}_{23}} \quad (9.10)$$

These formulas can be generalized to the cases where the baselines have different weights.

It can be seen in the above formulas that the precision to which the antenna phases and amplitudes is determined is improved by a factor \sqrt{N} over the precision of the measurement of the baseline amplitudes and phases.

9.1.2 Gain corrections

The determination of antenna-based gains (amplitudes and phases) has an obvious advantage: the physical cause of the gain variations are truly antenna-based. One may solve for the gains at the time of the observations, and correct the occurring problems to improve the quality of the data. One may re-point or re-focus the antennas to correct for an amplitude loss, correct for an instrumental delay (affecting the frequency dependence of the phases) . . .

9.2 Bandpass calibration

In the previous section we have considered a monochromatic system. We have actually finite bandwidths and in principle the gain coefficients are functions of both frequency and time. We thus write:

$$\tilde{V}_{ij}(\nu, t) = \mathcal{G}_{ij}(\nu, t)V_{ij}(\nu, t) = g_i(\nu, t)g_j^*(\nu, t)V_{ij}(\nu, t) \quad (9.11)$$

If we make the assumption that the passband shape does not change with time, then we should have for each complex baseline-based gain:

$$\mathcal{G}_{ij}(\nu, t) = \mathcal{G}_{Bij}(\nu)\mathcal{G}_{Cij}(t) \quad (9.12)$$

The same decomposition can also be done for the antenna-based gains:

$$g_i(\nu, t) = g_{B_i}(\nu)g_{C_i}(t) \quad (9.13)$$

$g_{B_i}(\nu)$ is the antenna complex passband shape, which by convention we normalize so that its integral over the observed bandpass is unity; then $g_{C_i}(t)$ describes the time variation of the complex gains.

Frequency dependence of the gains occurs at several stages in the acquisition chain. In the correlator itself the anti-aliasing filters have to be very steep at the edges of each subband. A consequence is that the phase slopes can be high there too. Any non-compensated delay offset in the IF can also be seen as a phase linearly dependent on frequency. The attenuation in the cables strongly depends on IF frequency, although this is normally compensated for, to first order, in a well-designed system. The receiver itself has a frequency dependent response both in amplitude and phase, due the IF amplifiers, the frequency dependence on the mixer conversion loss. Antenna chromatism may also be important. Finally the atmosphere itself may have some chromatic behavior, if we operate in the vicinity of a strong line (e.g. O₂ at 118 GHz) or if a weaker line (e.g. O₃) happens to lie in the band.

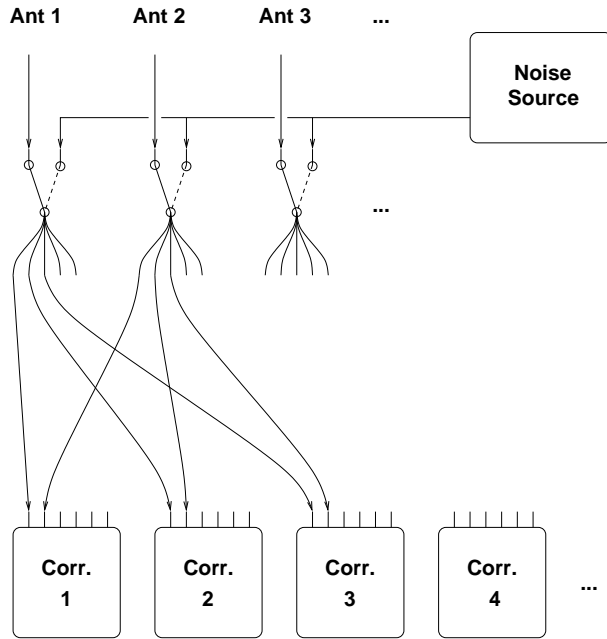
9.2.1 Bandpass measurement

Bandpass calibration usually relies on observing a very strong source for some time; the bandpass functions are obtained by normalizing the observed visibility spectra by their integral over frequency. It is *a priori* not necessary to observe a point source, as long as its visibility can be assumed to be, on all baselines, independent on frequency in the useful bandwidth. If there is some dependence on frequency, then one should take this into account.

9.2.2 IF passband calibration

In many cases the correlator can be split in several independent subbands that are centered to different intermediate frequencies, and thus observe different frequencies in the sky. In principle they can be treated as different receivers since they have different anti-aliasing filters and different delay offsets, due to different lengths of the connecting cables. Thus they need independent bandpass calibrations, which can be done simultaneously on the same strong source.

At millimeter wavelengths strong sources are scarce, and it is more practical to get a relative calibration of the subbands by switching the whole IF inputs to a noise source common to all antennas (Fig. 9.1). The switches are inserted before the IFs are split between subbands so that the delay offsets of the subbands are also calibrated out. This has several advantages: the signal to noise ratio observed by observing the noise



IF Passband calibration setup

Figure 9.1: IF passband calibration scheme

source is higher than for an astronomical source since it provides fully correlated signals to the correlator; then such a calibration can be done quite often to suppress any gain drift due to thermal variations in the analogue part of the correlator. Since the sensitivity is high, this calibration is done by baseline, so that any closure errors are taken out.

When such an “IF passband calibration” has been applied in real time, only frequency dependent effects occurring in the signal path before the point where the noise source signal is inserted remain to be calibrated. Since at this point the signal is not yet split between subbands, the same passband functions are applicable to all correlator subbands.

At Plateau de Bure an “IF passband calibration” is implemented. Of course when the noise source is observed the delay and phase tracking in the last local oscillators (the one in the correlator IF part) are not applied. The precision in phase is $360/\sqrt{\Delta\nu\Delta t} = 0.5^\circ$ at 100 kHz resolution which is sufficient for most projects.

9.2.3 RF bandpass calibration

To actually determine the functions $g_{B_i}(\nu)$ we observe a strong source, with a frequency-independent visibility. The visibilities are

$$\tilde{V}_{ij}(\nu, t) = g_{B_i}(\nu)g_{B_j}^*(\nu)g_{C_i}(t)g_{C_j}^*(t)V_{ij}(t) \quad (9.14)$$

Then

$$g_{B_i}(\nu)g_{B_j}^*(\nu) = \frac{\tilde{V}_{ij}(\nu, t)}{\int \tilde{V}_{ij}(\nu, t)d\nu} \quad (9.15)$$

since the frequency independent factors cancel out in the right-end side. One then averages the measurements on a time long enough to get a sufficient signal-to-noise ratio. One solves for the antenna-based coefficients in both amplitude and phase; then polynomial amplitude and phase passband curves are fitted to the data.

Applying the passband calibration The passband calibrated visibility data will then be:

$$\tilde{V}_{c_{ij}}(\nu, t) = \tilde{V}_{ij}(\nu, t) / g_{B_i}(\nu) g_{B_j}^*(\nu) \quad (9.16)$$

the amplitude and phase of which should be flat functions of frequency.

Accuracy The most important here is the phase precision: it sets the uncertainty for relative positions of spectral features in the map. A rule of thumb is:

$$\Delta\theta / \theta_B = \Delta\phi / 360 \quad (9.17)$$

where θ_B is the synthesized beam, and $\Delta\theta$ the relative position uncertainty. The signal to noise ratio on the bandpass calibration should be better than the signal to noise ratio of the spectral features observed; otherwise the relative positional accuracy will be limited by the accuracy of the passband calibration.

The amplitude accuracy can be very important too, for instance when one wants to measure a weak line in front of a strong continuum, in particular for a broad line. In that case one needs to measure the passband with an amplitude accuracy better than that is needed on source to get desired signal to noise ratio. Example: we want to measure a line which is 10% of the continuum, with a SNR of 20 on the line strength; then the SNR on the continuum source should be 200, and the SNR on the passband calibration should be at least as good.

9.2.4 Sideband calibration

A millimeter-wave interferometer can be used to record separately the signal in both sidebands of the first LO (see Chapter 7). If the first mixer does not attenuate the image sideband, then it is useful to average both sidebands for increased continuum sensitivity, both for detecting weaker astronomical sources and increasing the SNR for calibration.

However the relative phases of the two sidebands can be arbitrary (particularly at Plateau de Bure where the IF frequency is variable since the LO2 changes in frequency in parallel with the LO1). This relative phase must be calibrated out. This is done by measuring the phases of the upper and lower sidebands on the passband calibrator observation. These values can be used later to correct each sideband phase to compensate for their phase difference.

During the passband calibration one calculates:

$$e^{i\phi_U} = \frac{\int \tilde{V}_{ij,USB}(\nu, t) d\nu}{|\int \tilde{V}_{ij,USB}(\nu, t) d\nu|} \quad (9.18)$$

and

$$e^{i\phi_L} = \frac{\int \tilde{V}_{ij,LSB}(\nu, t) d\nu}{|\int \tilde{V}_{ij,LSB}(\nu, t) d\nu|} \quad (9.19)$$

Then at any time the double sideband visibility is:

$$\tilde{V}_{ij,DSB}(\nu, t) = e^{-i\phi_U} \tilde{V}_{ij,USB}(\nu, t) + e^{-i\phi_L} \tilde{V}_{ij,LSB}(\nu, t) \quad (9.20)$$

As a result the two terms on the right hand side have zero phase at the time of the pass band calibration and they keep the same phase during the whole observing session.

At observing time, offsets on the first and second LOs can be introduced so that both ϕ_U and ϕ_L are very close to zero when a project is done. This is actually done at Plateau de Bure, at the same time when the sideband gain ratio is measured (see Chapter 12).

9.3 Phase calibration

We now turn to the more difficult problem of correcting for the time dependence of the complex gains, contained in the functions $g_{c_i}(t)$. Variations occur in both amplitude and phase. Let us summarize the various effects to be calibrated:

- **Interferometer geometry:**
Small errors in the baseline determination will cause slow phase drifts (period 24 hours); unfortunately these errors are dependent on the source direction so they cannot be properly calibrated out by phase referencing on a calibrator, only reduced by a factor of the order of the source to calibrator distance expressed in radians.
- **Atmosphere**
The atmosphere introduces phase fluctuations on time scales 1s to a few hours, depending on baseline length and atmospheric conditions (see Chapter 11). The effect of fluctuations on short time scales is to cause loss of amplitude by decorrelation, while on the long term the phase fluctuations can be mistaken for structure in the source itself. The critical time there is the time it takes for the projected baseline vector to move by half the diameter of one antenna:

$$\Delta t_C = \frac{D}{2} \frac{86400}{2\pi b} = 224 \frac{D}{15} \frac{450}{b} \quad (9.21)$$

This time ranges from 4 minutes to 1 hour for Plateau de Bure, depending on the baseline length. The phase fluctuations on short time scales may be corrected by applying the radiometric phase correction method, if it is available.

- **Antennas**
The antennas may cause variations in amplitude gains due to degradation in the pointing and in the focusing due to thermal deformations in the antennas. These can be corrected to first order by amplitude calibration but it is much better to keep the errors low by proper frequent monitoring of the pointing and focus, since these errors affect differently sources at the center and at the edges of the field. Focus errors also cause strong phase errors due to the additional path length which is twice the sub reflector motion in the axial direction.
- **Electronics**
Phase and amplitude drifts in the electronics are kept low by efficient design (see Chapter 5 and Chapter 7). The electronics phase drifts are generally slow and of low amplitude, except for hardware problems.

A detailed analysis can be found in [Lay 1997].

9.3.1 Phase referencing by a nearby point source

This is the standard, traditional way to calibrate the phases with current interferometers. A point source calibrator is typically observed for T_1 (a few minutes) every T_C (20-30 minutes). One fits a gain curve to the data observed on the calibrator, this gain curve is an estimate of the actual gain curve $g_{C_i}(t)$. This enables removing most long-term phase drifts from the observation of the target source.

Decorrelation It can be shown that the decorrelation factor for a given baseline is approximated by:

$$f \sim 1 - \frac{1}{2} \int_{-\log 2.5T_1}^{\infty} \nu P_\phi(\nu) d(\log \nu) \quad (9.22)$$

The decorrelation is fundamentally a baseline-based quantity: it cannot generally be expressed as a product of antenna-based factors. Both the target source and the calibrator are affected, so amplitude referencing will correct for decorrelation. However, the amount of decorrelation will vary from an integration to the next, so that the amplitude uncertainty is increased.

Phase referencing The slow component of $g_{C_i}(t)$ to be calibrated out is sampled at intervals T_C so that only variations with periods longer than $2T_C$ can be followed. However one fits a slow component into the data points so one is sensitive to errors due to the presence of the fast component: the fast component is *aliased* into a slow component. **It is essential to fit a curve that does not go through the points.**

Fast phase referencing One may reduce T_C as much as possible to remove a larger part of the atmospheric fluctuation spectrum. Time scales of the order of 10s may be used, at the expense of:

- the time efficiency is decreased (relatively more time is spent on the calibrator resulting in a larger overhead)
- caution must be taken that the time T_C may become comparable to the time it takes to water eddies to drift along the apparent distance between source and calibrator.

Water vapor radiometry A radiometry system may be used to monitor the emission of water vapor at a suitable frequency in front of all antennas (dedicated instrument or astronomy receiver; water line or quasi continuum). The fluctuations in the path length can be of a few % of the total path length due to water vapor.

The fluctuations of the water emission are converted into fluctuations of path length by using an atmospheric model (see lecture by M. Bremer, Chapter 11). In principle one could hope to correct for all phase fluctuations this way. However limitations due to receiver stability, to variations in emission from the ground, and to uncertainty in the determination of the emission to path length conversion factor have the consequence that it is not yet possible to consistently correct for the variation of path length between the source and the calibrator.

So far this method at IRAM/Plateau de Bure is used only to correct for on-source fluctuations. Its main effect is to remove the decorrelation effect due to short-term phase fluctuations, improving the precision of amplitude determination.

9.3.2 Phase referencing by a point source in the primary beam

We now consider the simple case where the field contains a strong point source: it can be a continuum source (quasar) or a line source (maser). In that case all phase fluctuations with period longer than $\sim 2T_1$ are removed, where T_1 is the integration time. However statistical errors may be mistaken for true atmospheric phase fluctuations, causing additional decorrelation.

This method gives good results, but for very specific projects which can be observed in very poor atmospheric conditions (e.g. observation of radio emitting quasars, of stars with strong maser lines).

9.3.3 Phase referencing using another band or another frequency

It is generally easier to measure the path lengths fluctuations at a lower frequency (even though the phase scales like frequency), due to both better receiver sensitivity and larger flux of the referencing source. Moreover, in marginal weather conditions, if the rms phase fluctuations at 100 GHz is $\sim 40^\circ$, then at 230 GHz they are of $\sim 100^\circ$, and the phase becomes impossible to track directly due to 2π ambiguities.

If two receivers are available simultaneously, one may subtract to the high frequency phase the phase measured at the low frequency. The atmospheric fluctuations are cancelled and only a slow instrumental drift remains. The gain curve at the high frequency is then determined as the sum of two terms: the low frequency gain curve (including the slow atmospheric terms) plus that slow instrumental drift (which represents any phase fluctuation affecting one of the signal paths of the two receivers).

This method is currently used at Plateau de Bure.

Chapter 10

Atmospheric Absorption

Juan Pardo^{1,2}

pardo@isis.iem.csic.es

¹ CALTECH, Astronomy Department, Mail Stop 320-47 1200 E., California Blvd., Pasadena, CA 91125, USA

² Inst. Estructura de la Materia Dpto. Física Molecular Serrano, 121 Madrid, E-28006 Spain

This lecture is partially adapted from the IMISS1 course “ Atmospheric Absorption” By Michel Guélin (sections 10.1 and 10.4.1). It also includes a description of the phase correction methods (sections 10.5.3 and 10.5.4) by Martina Wiedner. The author would like also to acknowledge the contributions of the following people: J. Cernicharo, E. Serabyn and S. Matsushita.

10.1 The physical and chemical structure of the Atmosphere

10.1.1 Constituents of the atmosphere

In order to study the effect of the atmosphere on the outgoing longwave radiation, it is convenient to subdivide it into a “clean dry” component, water vapor, and aerosols (water droplets, as well as ice crystals, salt grains & dust particles, which serve as condensation seeds for water).

Abundances Table 10.1 gives the standard composition of the “clean dry” air in the troposphere (i.e. at altitudes ≤ 20 km). Except for CO₂, whose abundance at ground level may vary between day and night by up to a factor of 2, this composition is remarkably homogeneous and constant. Other trace components, most of which are unstable (SO₂, O₃, NO, CO, ...) have abundances (in volume) that never exceeds 10⁻⁵.

The abundance of water is highly variable, but hardly exceeds 1% in mass, even locally. Most of the water in the air is in the form of vapor. Even inside the clouds, precipitation and turbulence insure that

Name	Molec. mass amu	Normal abund. (% in volume)	Name	Molec. mass amu	Normal abund. (% in volume)
N ₂	28.013	78.084	He	4.003	0.0005
O ₂	32.000	20.946	Kr	83.8	0.0001
Ar	39.948	0.934	CH ₄	16.043	0.0002
CO ₂	44.010	0.033 ^v	H ₂	2.016	0.00005
Ne	20.183	0.0018	N ₂ O	44.013	0.00005

Table 10.1: Main constituents of the dry air in the troposphere.

the mass of water droplets per cm^{-3} seldom equals that of water vapor. In addition the water vapor mixing ratios above 15-20 km are under 10 ppmv making it just another trace gas there.

Overall picture of the atmospheric spectrum Despite the above facts, water, which has a large absorption cross section in the IR and a large specific heat of vaporization, ($L_w \sim 600$ cal/g), ozone, which has UV photodissociation bands playing a key role in the stratosphere, and carbon dioxide, which has large IR absorption cross sections, are the major actors of the thermal balance of the air.

Ozone and to much less extent molecular Oxygen are responsible for most of the absorption of the solar radiation in the UV, especially between 180 and 290 nm, thanks to these processes: $O_3 + h\nu(\lambda < 310 \text{ nm}) \rightarrow O_2(^1\Delta_g) + O(^1D)$ (Hartley band), $O_2(^3\Sigma_g^-) + h\nu(\lambda < 175 \text{ nm}) \rightarrow O(^3P) + O(^1D)$ (Schuman-Runge band), and $O_2(^3\Sigma_g^-) + h\nu(\lambda < 242 \text{ nm}) \rightarrow O(^3P) + O(^3P)$ (Herzberg band),

In the visible, the air is fairly transparent except for scattering by aerosols, mostly water droplets, ice crystals and dust particles. In the infrared, H₂O, CO₂ (around 15 μm) and O₃ (around 10 μm) are very efficient absorbers of the solar and ground radiation, to the extent that they prevent ground-based observations in large regions of the electromagnetic spectrum.

By clear weather, the atmospheric absorption at millimeter and submillimeter wavelengths is dominated by rotational and fine structure lines of molecules in their ground electronic and low vibrational states.

The strongest molecular rotational resonances appear in polar molecules (H₂O and O₃ being the most important of such molecules in the atmosphere) and are of the type E1 (electric dipole transitions). Intrinsically weaker M1 (magnetic dipole) transitions are of considerable practical importance in the atmosphere due to the high abundance of O₂. We will see that collision induced E2 (electric quadrupole) absorption involving N₂ and O₂ is measurable in the atmosphere. The different atmospheric hydrometeors (water droplets, snow, graupel, hale, ice crystals,...) scatter and absorb following different patterns across the longwave (radio to submm) spectral region. All the mechanisms involved in the radiative transfer of longwave radiation in the atmosphere will be described in this chapter.

10.1.2 Thermodynamics of the air

Gas mixture: Dalton's law A mixture of ideal gases behaves like an ideal gas:

$$\text{Partial pressures : } p_1V = \mathcal{N}_1kT, \quad p_2V = \mathcal{N}_2kT, \quad \dots \quad (10.1)$$

$$\text{Total pressure : } pV = (p_1 + p_2)V = (\mathcal{N}_1 + \mathcal{N}_2)kT + \dots = \mathcal{N}kT \quad (10.2)$$

Dry air is a mixture of N₂, O₂, ... molecules. It behaves indeed very much like an ideal gas: $R_a = c_{p_a} - c_{v_a} = 8.3143$ J/mol-deg (vs 8.3149 for an ideal gas), $\gamma_a = 1.404$ (vs 1.400 for ideal rigid molecules).

Wet air (without clouds) is a mixture of dry air + H₂O molecules. It is customary to denote by e the partial pressure of water vapor, p_a that of dry air, and p' the wet air pressure. The specific heats of water *vapor* are not that different from those of ideal gases: $c_{v_w} = 25.3 + 210^{-3}(T - 273)$; $\gamma_w = 1.37$, vs $c_v = 3R = 24.9$ and $\gamma = \frac{4}{3}$ for a rigid asymmetric top.

Then, Dalton's law yields:

$$c'_v = \left(1 - \frac{e}{p'}\right)c_{v_a} + \frac{e}{p'}c_{v_w} \simeq \left(1 + 0.2\frac{e}{p'}\right)c_{v_a} \quad (10.3)$$

The fractional abundance of water vapor and $\frac{e}{p}$ reaching seldom a few percent, the wet air constants are within a small correction term equal to the dry air constants. In particular, introducing the volume density ρ , it is customary to write:

$$p' = \frac{R\rho'T}{M'} = \frac{R\rho T'}{M_a} \quad (10.4)$$

where $T' = \frac{M'T}{M_e} = T(1 - 0.378\frac{e}{p'})^{-1}$, is the *virtual temperature*.

Then, for the adiabatic expansion of a wet air bubble, one has:

$$T' = Cst \times p^{m'} \quad (10.5)$$

m' is equal to m_a within few per mil, so, in practice, the adiabatic curves of dry air can be used for wet air (without clouds), provided one replaces T by T' (the difference could reach a few K and could be important near 0°C). In the following, we drop the ‘prime’ signs, except for the virtual temperature T' .

10.1.3 Hydrostatic equilibrium

At large scales, the air pressure and density depend essentially on the massive and slowly varying dry component and are well described by *hydrostatic equilibrium*. The air temperature, as we have seen, depends significantly on the abundance and distribution of water, CO₂ (and O₃ for the stratosphere).

At equilibrium:

$$dp/dh = -g\rho \quad p = \frac{\rho RT'}{M_a} \quad (10.6)$$

where ρ is the density at an altitude h , p is the pressure, $T' \simeq T$ the air “virtual” temperature. $M_a \simeq 29$ is the average molecular weight, and g the local gravitational field.

$$\frac{dp}{p} = \frac{-gM_a}{RT'} dh \quad (10.7)$$

In the “standard atmosphere” model, T' , the temperature of the air varies linearly with altitude and is given throughout the troposphere (i.e. between $h=0$ and 11 km) by: $T' = T'_o - b(h - h_o)$, where b (in K km⁻¹) is a constant. Let us first consider a relatively small change in altitude: $h - h_o \leq 1$ km, $T' \simeq T'_{ave} = (T'(h) + T'(h_o))/2$; we find Laplace’s hydrostatic formula:

$$\frac{\rho}{\rho_o} \simeq \frac{p}{p_o} \simeq e^{-\frac{gM_a h}{RT'_{ave}}} = e^{-\frac{h}{h_o}} \quad (10.8)$$

where ρ_o is the density at sea level and $h_o = RT/M_ag = 8.4(T/288)$ km, the scale height. The gas column densities (expressed in g.cm⁻²) along the vertical above sea level (N_o) and above a point at altitude h (N) are:

$$N_o M_a = \int \rho dh = \rho_o h_o ; \quad N = N_o e^{-h/h_o} \quad (10.9)$$

For larger altitudes, from Eq.10.7 and $dh = -dT'/b$, then:

$$\frac{dp}{p} = \frac{gM_a}{bR} \frac{dT'}{T'} ; \quad \rho = \rho_o \left(\frac{T'}{T'_o}\right)^{s-1} \quad (10.10)$$

with $s = gM_a/(bR)$.

Although the above equations represent fairly well the density and pressure throughout the troposphere, the temperature distribution can depart significantly from the above linear variation near the ground. This ground heats up faster than the transparent air during the day, and cools off more rapidly during the night. The temperature gradient at low altitudes (up to 1-2 km) can be thus steeper or shallower than described by b (K km⁻¹). Occasionally, it can be inverted, the temperature increasing with altitude. The *inversion*

layer usually stops briskly at 1 or 2 km altitude and the normal temperature gradient resumes above. Inversion layers are common during the night over bare land. They can also be caused by hot winds blowing from the sea.

The local temperature gradient determines stability of the air to vertical motions. A rising bubble of wet air expands adiabatically as long as the water vapor it contains does not condense. Expanding, it cools almost as an ideal gas with:

$$T \propto p^m \text{ and } m = (1 - 0.23q)m_a \simeq m_a \quad (10.11)$$

The pressure is set by the surrounding air (Eq.10.8), and the bubble seen to cool down with an “adiabatic” gradient of

$$\frac{dT}{dh} = -g \frac{M_a}{C_p} = 9.8 \text{Kkm}^{-1}$$

If the actual temperature gradient is smaller than the adiabatic gradient, the bubble becomes cooler, hence denser than the surrounding air and its ascent stops. The air is stable. If the local gradient is larger than the adiabatic gradient, the bubble becomes less dense than the surrounding air; the air is unstable and a thick convection layer develops, a situation likely to happen in a hot summer afternoon.

10.1.4 Water

The scale height of water, h_w , which results from a fast evaporation/condensation process, is small (typically 2 km) compared to the equilibrium scale height $h_o = 8.4$ km. At $h = 2.5$ km, the altitude of the Plateau de Bure, the water vapor column density N_w (or w , “amount of precipitable water”, when expressed in g.cm^{-2} , or cm of water) is normally reduced by a factor of 3-4, with respect to sea level. This factor, as we have seen, is strongly modulated by the local temperature gradient. w is lower in the presence of a low altitude inversion layer which reduces the vertical turbulence and traps most of the water well below the observatory.

10.2 Atmospheric radiative transfer in the mm/submm

Due to space constraints in this book we cannot provide a very detailed overview of all aspects involved in modeling the longwave atmospheric spectrum. The author and co-workers have recently published an in-depth description of their radiative transfer model ATM (Atmospheric Transmission at Microwaves, Pardo et al [2001b]) that can serve as a reference for the information that is missing here. That model has been adopted in this chapter.

10.2.1 Introduction

Accurate modeling of the longwave emission/absorption spectrum of the terrestrial atmosphere is needed in many scientific applications. In the astrophysical domain, it is needed to predict the atmospheric attenuation at a given frequency for ground-based and airborne observatories, to calculate system noise temperatures and to estimate phase delays for interferometry. In remote sensing of the atmosphere and the Earth’s surface, obtaining useful data for meteorological and environmental studies relies upon an accurate knowledge of the atmospheric spectrum.

We will see in this chapter how to model the Earth’s atmosphere longwave spectrum. For millimeter and submillimeter astronomy applications we need to know for a given path through the atmosphere, the opacity, radiance, phase delay and polarization¹.

10.2.2 Unpolarized radiative transfer equation

The unpolarized radiative transfer in non-scattering media is described by a relatively simple differential scalar equation:

¹Polarization can be produced by different mechanisms such as emission of paramagnetic molecules such as O_2 under the effect of the geomagnetic field, by radiation scattering by hydrometeors, or by reflection on a Fresnel-like (ocean) surface.

$$\frac{dI_\nu(\vec{r}, \vec{n})}{ds} = \epsilon_\nu - \kappa_\nu I_\nu(\vec{r}, \vec{n}) \quad (10.12)$$

where I_ν is the radiance (in $\text{W m}^{-2}\text{ster}^{-1}\text{cm}^{-1}$), $\epsilon_\nu d\omega d\nu ds d\sigma$ and $\kappa_\nu I(\vec{r}, \vec{n}, \nu) d\omega d\nu d\sigma ds$ are the amounts of energy emitted and absorbed at frequency ν in a pencil of solid angle $d\omega$ in the direction \vec{r} through a cylinder of length ds and cross-section $d\sigma = d\sigma \vec{n}$. ϵ_ν and κ_ν are the macroscopic absorption and emission coefficients. The absorption coefficient gives the fractional loss of intensity (at a given wavelength) per length through an absorbing medium.

After rearranging equation 10.12 and considering absence of scattering, the radiative transfer problem is unidimensional in the direction of \vec{r} . We can formulate it under *Local Thermal Equilibrium* (LTE) conditions as follows:

$$\frac{dI_\nu(s')}{d\tau_\nu} = -I_\nu(s') + S_\nu(T[s']) \quad (10.13)$$

where s' is a coordinate along the path, $S_\nu = \epsilon_\nu/\kappa_\nu$ is the so-called *source function*, and $d\tau_\nu = \kappa_\nu ds$ is the *differential opacity*.

The solution of this equation can be given in an integral form:

$$I_\nu(s) = I_\nu(0)e^{-\tau_\nu(0,s)} + \int_0^s S_\nu(s')e^{-\tau_\nu(s',s)}\kappa_\nu(s')ds' \quad (10.14)$$

In general, the line-by-line integrated opacity corresponding to a path through the terrestrial atmosphere is calculated in a discrete way as follows:

$$\tau_\nu(s', s) = \sum_{i(\text{layers})} \left[\sum_{j(\text{molec.})} \left(\sum_{k(\text{resonances})} \kappa_{\nu k} \right) \right]_i \cdot \Delta s_i \quad (10.15)$$

where Δs_i is the path through the homogeneous i -th layer in the path from s' to s and no line coupling between different species is assumed. As pressure increases the calculations have to use thinner layers to follow the opacity distribution.

The absorption coefficient of an electric dipole (E1) resonance in the atmosphere is given in general by the following equation:

$$(\kappa_\nu)_{lu} = \frac{8\pi^3 N\nu}{3hcQ} (e^{-E_l/KT} - e^{-E_u/KT}) \cdot |\langle u | \mu | l \rangle|^2 f(\nu, \nu_{l \rightarrow u}) \quad (10.16)$$

where N is the number density in the relevant vibrational state the molecule, E_n the energy level of the state and g_n its degeneracy, Q is the partition function, μ is the dipole operator of the transition and $|u\rangle$, $|l\rangle$ are the wavefunctions of the upper and lower states, and, finally, $f(\nu, \nu_{l \rightarrow u})$ is the line shape function. This the basic expression used in the ATM model.

10.2.3 Spectroscopic parameters

Both transition probabilities $|\langle u | \mu | l \rangle|^2$ and rotational energy levels (from which both resonance frequencies and population factors under LTE are determined) can be obtained from the rotational hamiltonians. The number of rotational constants depends on the type of molecule. The cases to be considered in the atmosphere are diatomic or linear molecules (with no magnetic moment), symmetric rotors in $^3\Sigma$ electronic state, and asymmetric rotors.

Transition probabilities:

The way we parametrize them is the following:

$|\langle J, \tau | \mu | J', \tau' \rangle|^2 = \mu_g^2 \lambda_g(J, \tau, J', \tau')$. J, J' represent rotational quantum numbers, τ, τ' are other quantum numbers, μ_g is the value of the dipole moment (electric or magnetic), and $\lambda_g(J, \tau, J', \tau')$ is a dimensionless parameter called the *oscillator strength* of the particular transition.

Partition function:

The case of symmetric linear or diatomic molecules ($^{16}\text{O}_2$, N_2O or CO) and the general asymmetric rotors must be treated individually. In the first case the energy levels are $\sim hB(J+1)$ where B is the rotational constant of the molecule in the considered vibrational state. There are corrections to this simple rigid rotor expression but for CO , for example, the associated parameter D is five orders of magnitude smaller than B and for other important atmospheric molecules the ratio B/D is even larger. In the case of asymmetric rotors (O_3 , SO_2, \dots) there are three main rotational constants (A, B, C) in the Hamiltonian related with the three principal axes. There are also corrections due to centrifugal and other effects.

Analytical expressions (see Pardo et al [2001b]) can be used in the atmosphere for both types of molecules within an error not larger than 0.4%.

Spectroscopy of H_2O , O_2 , O_3

Of the major molecular constituents of the atmosphere (see Table 10.1) only water vapor and ozone, owing to their bent structure, have a non-zero electric dipole moment. Molecular nitrogen, an homonuclear species, and CO_2 , a linear symmetric species, have no permanent electric or magnetic dipole moment in their lowest energy states. These latter molecules, as is the case for most of gaseous molecules, are singlet states, with electrons arranged two-by-two with opposite spins. O_2 has a permanent magnetic dipole owing to two parallel electron spins. It thus presents magnetic dipole transitions of noticeably intensity due to the large abundance of this molecule in the atmosphere.

We present here the details about the spectroscopy of H_2O , O_2 and O_3 because these molecules dominate the longwave atmospheric spectrum as seen from the ground.

Water vapor Water vapor is a C_{2v} molecule (degree of symmetry: $\sigma=2$) with a relatively high electric dipole moment: $\mu=1.88 \cdot 10^{-19}$ esu·cm. The first vibrational modes of H_2^{16}O are at 3693.8 cm^{-1} (1,0,0), 1614.5 cm^{-1} (0,1,0) and 3801.7 cm^{-1} (0,0,1). The nuclear spins (1/2 for H, 0 for ^{16}O and ^{18}O , 1/2 for ^{17}O , and 0 for D) lead to two spectroscopically separated species of water: $I=1$ (statistical weight $g=3$) [ortho- $^{16,18}\text{H}_2\text{O}$], and $I=0$ ($g=1$) [para- $\text{H}_2^{16,18}\text{O}$]. HDO and H_2^{17}O have a hyperfine structure.

For $^{16,18}\text{H}_2\text{O}$ each level is denoted, as usual for asymmetric top molecules by three numbers $J_{K_{-1}, K_{+1}}$. J , which is a “good” quantum number, represents the total angular momentum of the molecule; by analogy with symmetric tops, K_{-1} and K_{+1} stand for the rotational angular momenta around the axis of least and greatest inertia. Allowed radiative transitions obey the selection rules $\Delta J = \pm 1, \Delta K = \pm 1, 3$, with $K_{-1}, K_{+1} : \text{odd, odd} \leftrightarrow \text{even, even}$ or $o, e \leftrightarrow e, o$. The levels with K_{-1} and K_{+1} of the same parity belong to the *para* species, those of opposite parity belong to *ortho* water.

Molecular oxygen Molecular oxygen, although homonuclear, hence with zero electric dipole moment, has a triplet electronic ground state, with two electrons paired with parallel spins. The resulting electronic spin couples efficiently with the magnetic fields caused by the end-over-end rotation of the molecule, yielding a magnetic dipole moment of two Böhr magnetons, $\mu_{mag}=2\mu_B\delta hr=1.854 \cdot 10^{-2}$ Debyes. The magnetic dipole transitions of O_2 have intrinsic strengths $\sim 10^{2-3}$ times weaker than the water transitions. O_2 , however, is 10^{2-3} times more abundant than H_2O , so that the atmospheric lines of the two species have comparable intensities.

The spin of 1 makes of the ground electronic state of O_2 a triplet state ($^3\Sigma$). \mathbf{N} , the rotational angular momentum couples with \mathbf{S} , the electronic spin, to give \mathbf{J} the total angular momentum: $\mathbf{N} + \mathbf{S} = \mathbf{J}$. The $\mathbf{N} \cdot \mathbf{S}$ interaction (and the electronic angular momentum–electronic spin interaction $\mathbf{L} \cdot \mathbf{S}$) split each rotational

level of rotational quantum number $N \geq 1$ into three sublevels with total quantum numbers

$$J = N + 1, J = N \quad \text{and} \quad J = N - 1$$

the $J = N + 1$ and $J = N - 1$ sublevels lying below the $J = N$ sublevel by approximately $119(N + 1)/(2N + 3)$ GHz and $119/(2N - 1)$ GHz, respectively. Note that the two identical ^{16}O nuclei have spins equal to zero and obey the Bose-Einstein statistics; there are only odd N rotational levels in such a molecule.

The magnetic dipole transitions obey the rules $\Delta N = 0, \pm 2$ and $\Delta J = 0, \pm 1$. Transitions within the fine structure sublevels of a rotational level (i.e. $\Delta N = 0$) are thus allowed. The first such transition is the $(J, N) = 1, 1 \leftarrow 0, 1$ transition, which has a frequency of 118.75 GHz. The second, the $1, 1 \leftarrow 2, 1$ transition, has a frequency of 56.26 GHz. It is surrounded by a forest of other fine structure transitions with frequencies ranging from 53 GHz to 66 GHz. The first "true" rotational transition, the $N = 3 \leftarrow 1$ transitions, have frequencies above 368 GHz (368.5, 424.8, and 487.3 GHz). In addition, the permanent magnetic dipole of this molecule can interact with an external magnetic field, leading to a Zeeman splitting of the energy levels. In our atmosphere this splitting is of the order of 1-2 MHz.

The rare isotopomer $^{18}\text{O}^{16}\text{O}$ is not homonuclear, hence has odd N levels and a non-zero electric dipole moment. This latter, however, is vanishingly small (10^{-5}D).

Ozone The quantum numbers are as in other asymmetric top molecules, such as H_2O . As noted above, ozone is mostly concentrated between 11 and 40 km altitude; it shows large seasonal and, mostly, latitude variation. Because of its high altitude location, its lines are narrow: at 25 km, ρ_a , hence $\Delta\nu$, is reduced by a factor of 20 with respect to sea level; moreover, the dipole moment of ozone ($\mu = 0.53$ Debyes), 3.5 times smaller than that of H_2O , further reduces the ozone line widths. Because of their small widths and despite the small ozone abundance, ozone lines have significant peak opacities, especially as frequency increases. This fact can be seen in the high resolution FTS measurements presented in this chapter.

10.2.4 Line shapes

Absorption

In the lower atmospheric layers (up to ~ 50 km, depending on the molecule and the criteria) the collisional broadening mechanism (also called pressure-broadening) dominates the line shape. One approximation to the problem considers that the time between collisions, τ_{col} ($\propto p^{-1}$), is much shorter than the time for spontaneous emission, τ_{rad} , which is, in the case of a two level system, $1/A_{u \rightarrow l}$ where $A_{u \rightarrow l}$ is the Einstein's coefficient for spontaneous emission. This approximation leads to the so-called Van Vleck & Weisskopf profile, normalized as follows to be included in equation 10.16:

$$f_{VVW}(\nu, \nu_{l \rightarrow u}) = \frac{\nu \Delta\nu}{\pi \nu_{l \rightarrow u}} \left(\frac{1}{(\Delta\nu)^2 + (\nu - \nu_{l \rightarrow u})^2} + \frac{1}{(\Delta\nu)^2 + (\nu + \nu_{l \rightarrow u})^2} \right) \quad (10.17)$$

where $\Delta\nu$ is the collision broadening parameter.

This lineshape describes quite well the resonant absorption in the lower atmospheric layers except for very large shifts from the line centers. For example, all the mm/submm resonances of H_2O and other molecules up to 1.2 THz are well reproduced using this approximation within that frequency range. Some properties of the collision broadening parameters in the atmosphere are:

$$\Delta\nu(p, T) = \Delta\nu(p_0, T_0) \frac{p}{p_0} \left(\frac{T_0}{T} \right)^\gamma \quad (10.18)$$

$$\Delta\nu(M - \text{dry air}) = X_{N_2} \Delta\nu(M - N_2) + X_{O_2} \Delta\nu(M - O_2) \quad (10.19)$$

where X are the volume mixing ratios. Laboratory measurements for individual lines are the only source of precise information about the parameters γ and $\Delta\nu(M - N_2, O_2)$ for the different atmospheric trace

gases M . The exponent γ has been found in most cases to be in the range 0.6 and 1.0. For O_2 and H_2O self-collisions have to be considered.

When the pressure gets very low the Doppler effect due to the random thermal molecular motion dominates the line broadening:

$$\mathcal{F}_D(\nu, \nu_{l \rightarrow u}) = \frac{1}{\Delta\nu_D} \left(\frac{\ln 2}{\pi}\right)^{1/2} \exp\left[-\left(\frac{\nu - \nu_{l \rightarrow u}}{\Delta\nu_D}\right)^2 \ln 2\right] \quad (10.20)$$

where the halfwidth parameter is given by:

$$\Delta\nu_D = \frac{\nu_{l \rightarrow u}}{c} \sqrt{\frac{2 \ln 2 k T}{m}} = 3.58 \cdot 10^{-7} \nu_{l \rightarrow u} \sqrt{\frac{T}{M}} \quad (10.21)$$

M being the molecular weight of the species in g/mol.

If the collisional and thermal broadening mechanisms are comparable the resulting line-shape is the convolution of a Lorentzian (collisional line shape at low pressures) with a Gaussian: a Voigt profile.

Phase delay

Besides absorption, the propagation through the atmosphere also introduces a phase delay. This phase delay increases as the wavelength approaches a molecular resonance, with a sign change across the resonance. The process can be understood as a forward scattering by the molecular medium in which the phase of the radiation changes.

Both the absorption coefficient and the phase delay can be treated in a unified way for any system since both parameters are derived from a more fundamental property, the complex dielectric constant, by means of the Kramers-Krönig relations. A generalized (complex) expression of the VVW profile, which accounts for both the Kramers-Krönig dispersion theory as well as line overlapping effects (parameter δ) is the following ($\nu_{l \rightarrow u} \equiv \nu_{lu}$):

$$\mathcal{F}_{VVW}(\nu, \nu_{lu}) = \frac{\nu}{\pi \nu_{lu}} \left[\frac{1 - i\delta}{\nu_{lu} - \nu - i\Delta\nu} + \frac{1 + i\delta}{\nu_{lu} + \nu + i\Delta\nu} \right] \quad (10.22)$$

the imaginary part of which reduces to equation 10.17 when $\delta=0$.

10.2.5 Non-resonant absorption

H_2O pseudocontinuum

Lines with resonant frequencies up to a given frequency (10 THz in our case) are included in line-by-line calculations. Since the true lineshape is not known accurately beyond a few times the halfwidth from the line centers (this may be due to the finite collision time, the complexity of the calculations and the lack of precise laboratory data), a broadband “continuum”-like absorption term needs to be included for accurate results in the longwave domain.

Dry continuum-like absorption

The non resonant absorption of the dry atmosphere is made up of two components: collision induced absorption due to transient electric dipole moments generated in binary interactions of symmetric molecules with electric quadrupole moments such as N_2 and O_2 , and the relaxation (Debye) absorption of O_2 .

Pseudocontinua in ATM

In the ATM model model, we introduce collisionally-induced dry absorption and longwave (foreign) pseudocontinuum water vapor absorption derived from our previous FTS measurements performed on top of

Mauna Kea, Hawaii. For both terms we use ν^2 frequency power laws, with the coefficients as determined by Pardo et al [2001a].

$$\kappa_{c,H_2O} = 0.031 \cdot \left(\frac{\nu}{225}\right)^2 \cdot \left[\frac{e}{1013} \cdot \frac{p-e}{1013}\right] \cdot \left(\frac{300}{T}\right)^3 m^{-1} \quad (10.23)$$

$$\kappa_{c,dry} = 0.0114 \left(\frac{p-e}{1013}\right)^2 \left(\frac{300}{T}\right)^{3.5} \left(\frac{\nu}{225}\right)^2 m^{-1} \quad (10.24)$$

The validity of these expressions is restricted to frequencies ≤ 1.1 THz (the upper limit of our current data), although there are indications that they can be extended to 2 THz with no important loss of accuracy.

10.2.6 Radiative transfer through atmospheric hydrometeors

The equation describing the transfer of radiation through an atmosphere that contains scatterers is as follows:

$$\mu \frac{dI(z, \mu)}{dz} = K(z, \mu)I(z, \mu) - 2\pi \int_{-1}^1 M(z, \mu, \mu')I(z, \mu')d\mu' - \sigma(z, \mu)B[T(z)] \quad (10.25)$$

where:

- $I=(I,Q,U,V)^T$ is the Stokes vector describing the propagating electromagnetic field.
- K is the extinction matrix.
- M is the zeroth Fourier component of the phase matrix.
- σ is the emission vector.
- $B(T)$ is the blackbody spectrum at temperature T .
- $\mu=\cos(\theta)$ (θ =zenith angle, $0 \Rightarrow$ downwards). The frequency dependence in several of these quantities is implicit. Finally, z is the vertical coordinate in a plane-parallel atmosphere.

K , M and σ are related according to:

$$K(\mu) = 2\pi \int_{-1}^{+1} M(z, \mu, \mu')d\mu' + \sigma(\mu) \quad (10.26)$$

which is a consequence of the detailed energy balance.

The frequency independent (excluding Raman effect or fluorescence) far-field scattering by single non-spherical particles has been incorporated to the ATM model. It is computed using state-of-the-art T-Matrix routines developed by Mishchenko [2000]. For the integration over all possible orientations to be possible, it is necessary to be in the single scattering regime. Then, each particle is in the far-field zone of the others. This implies that the average distance between particle centers is larger than 4 times their radii. This requirement is usually satisfied by cloud and precipitation particles. The scattered fields are then incoherent and their Stokes parameters can simply be added.

For estimates concerning the effect of clouds to ground-based observations a plane parallel geometry is assumed, as a first approach, with thermal emission as the only source of radiation. The hydrometeors can be either totally randomly-oriented or at least azimuthally randomly oriented. In both cases, the radiation field is azimuthally symmetric leading the Stokes parameters U and V to vanish so that the dimension of tensorial equation (10.25) reduces to be 2. This radiative transfer equation can then be integrated using the quite standard method called *doubling and adding*, introduced in the ATM model according to Evans & Stephens [1991].

To illustrate the effect of two different types of clouds, we have performed first a simulation where we add to a clear atmosphere containing 1 mm of water vapor a layer between 6 and 6.5 km that contains spherical water droplets with a radius of 40 μm and a liquid water path of 0.1 km/m^2 . The second simulation replaces the water droplets for spherical ice particles with a radius of 100 μm . The effect of liquid water is quite large since it is a quite effective absorber. The effect of ice is much more related with its scattering properties and becomes more important at shorter wavelengths.

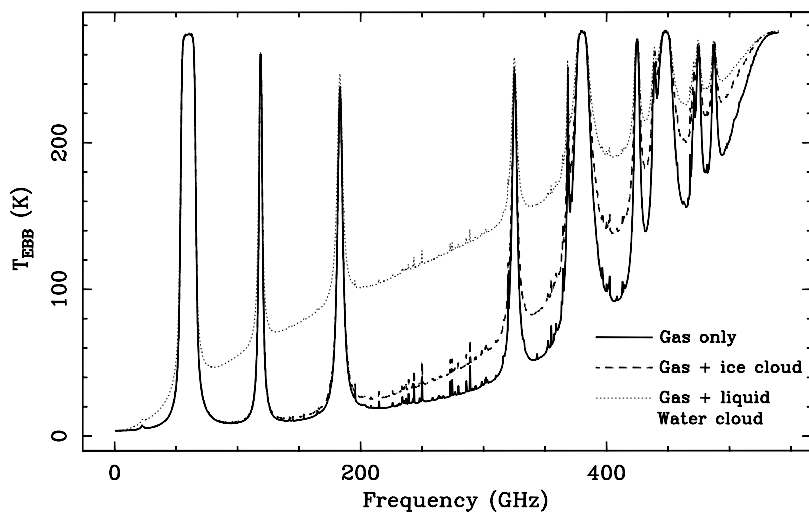


Figure 10.1: Simulations of the effect of clouds in the brightness temperature of the atmosphere at zenith. The liquid water and ice layers have been placed between 6.0 and 6.5 km, the equivalent water path is 0.1 km/m^2 for both but the size of the spherical particles is $40 \text{ }\mu\text{m}$ for liquid water and $100 \text{ }\mu\text{m}$ for ice. The considered atmosphere contains 1 mm of water vapor column.

10.3 Fourier Transform Spectroscopy for site testing

10.3.1 FTS measurements at Mauna Kea

Broadband submillimeter atmospheric measurements with a Fourier-transform spectrometer have been performed in recent years at the Caltech Submillimeter Observatory (CSO) with the primary goal of accurately measuring the atmospheric transmission in the submillimeter-wave domain and using the data to build a state-of-the-art transmission model.

The instrument used for this work has been described in Serabyn & Weisstein [1995]. Recently, new 1.1 THz and 1.6 THz low-pass filters have been installed in front of the ^3He cooled bolometer detector in order to efficiently cover both the full subTHz domain and the supraterahertz windows that are predicted by theory. The first successful measurements on Mauna Kea using the 1.1 THz filter were obtained on the night of 1998 April 1st under extremely dry “El Niño” conditions. It was estimated that the H_2O column was under 0.2 mm , so it is clear that these data offered the best opportunity for a determination of the dry and wet longwave nonresonant terms $[\mathcal{K}_{c,dry}(\nu), \mathcal{K}_{c,H_2O}(\nu)]$. However, to separate one from the other, an independent measurement under the same P/T conditions was needed. This occurred in a second run in July 1999, greatly simplifying our analysis (see Figure 10.2). From these 2 datasets, our goals have been to:

- I) Extract the dry continuum from our measurements and determine its origin.
- II) Determine the H_2O excess absorption in the submillimeter domain in low humidity conditions (when only foreign-gas collisions have to be taken into account), and compare it to proposed formulations.

The separation of these two terms using the data from the upper panel of Figure 10.2 is described in detail in Pardo et al [2001a] and leads to the formulation given in section 10.2.5. This is the first time that such a separation is done successfully in the submillimeter.

Our results indicate that the H_2O and dry continuum-like terms of existing models are not accurate in the submillimeter range and that the models should be updated accordingly. This has been done in Pardo et al [2001b]. The lower panel of Figure 10.5 shows the April 98 data and the separate opacity contributions that add up to fit the observed opacity.

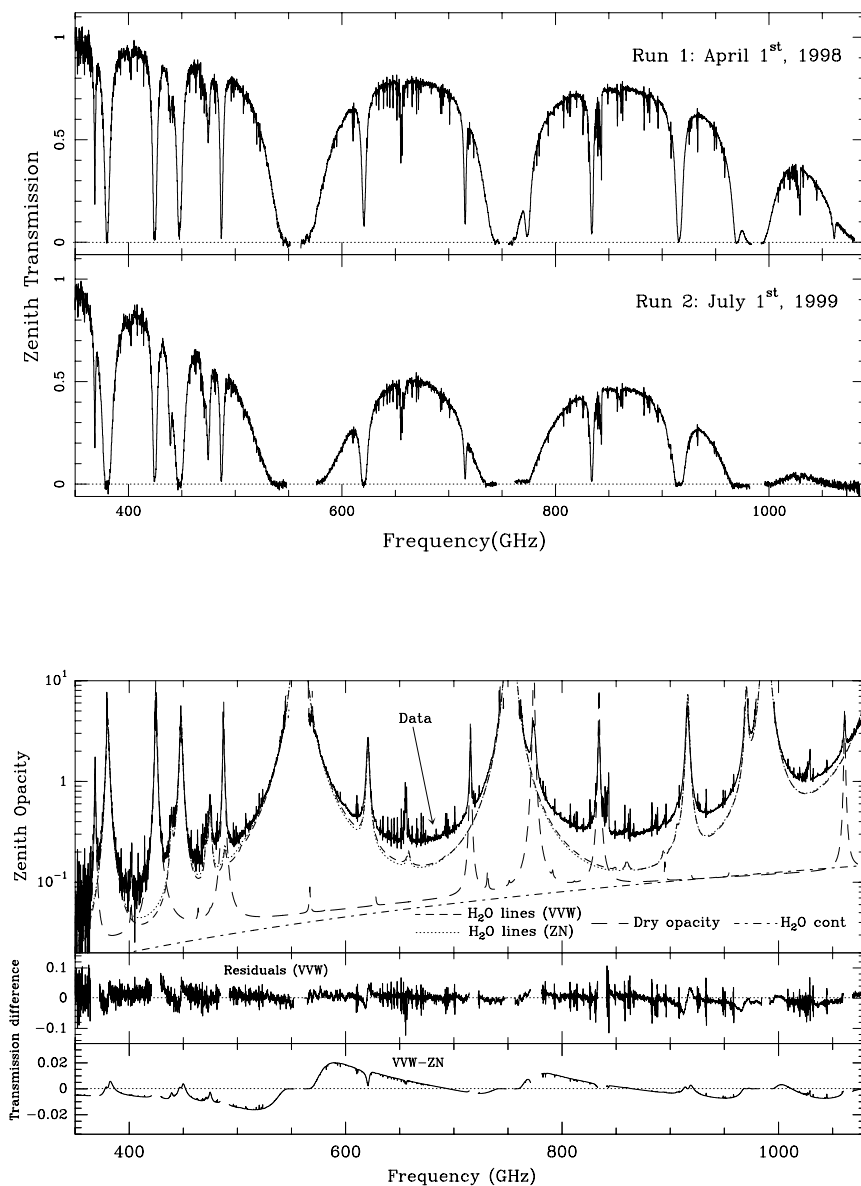


Figure 10.2: Upper panel: High resolution fully calibrated FTS atmospheric zenith spectra ($\Delta\nu=199$ MHz) obtained with the FTS experiment at Mauna Kea (Hawaii). Bottom Panel: Fit of the above April 98 zenith spectrum, shown in terms of opacity on a logarithmic scale. The opacity contributions from the different species and the continua leading to the final fit are plotted separately (assuming a VVW line shape for water). The middle panel shows the fit residual when using a VVW lineshape. The bottom panel is the difference between the fit considering VVW lineshapes and the one considering Zhevakin-Naumov (ZN) profiles.

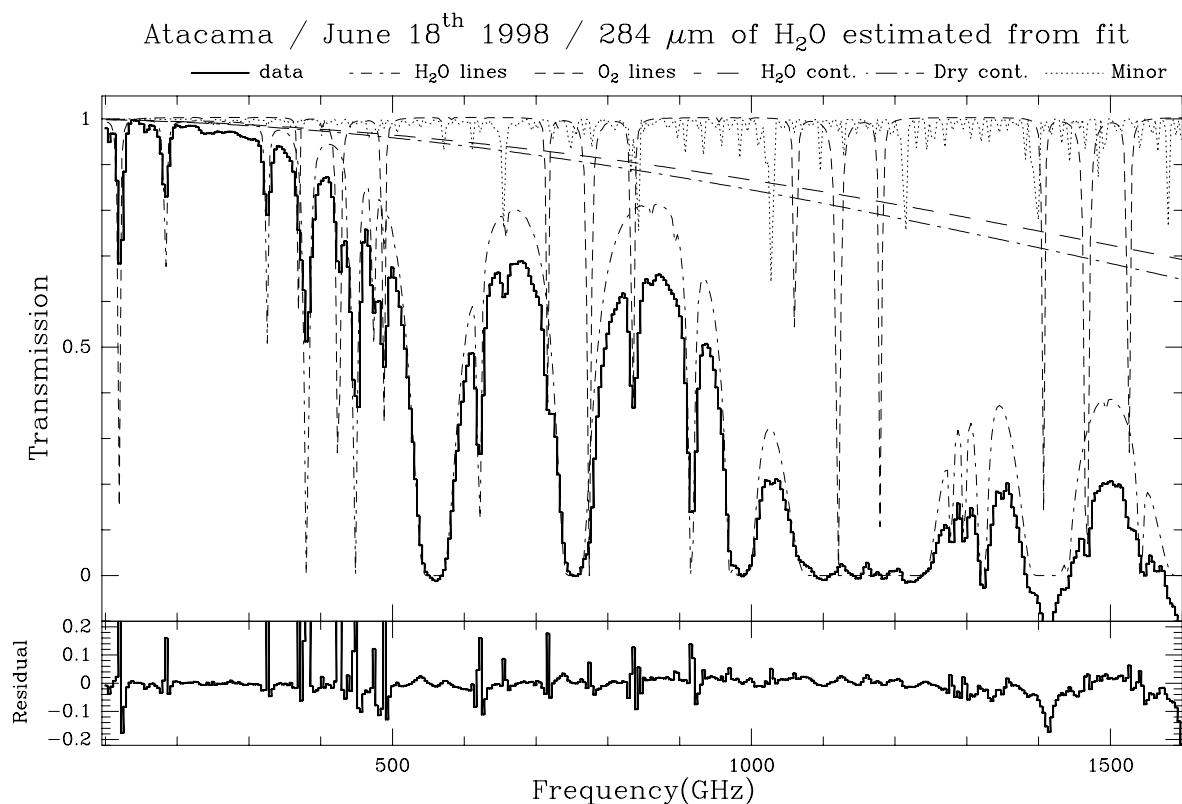


Figure 10.3: Atmospheric transmission spectrum obtained at Pampa La Bola on 1998 June 17 (courtesy of Satoki Matsushita). The absorption line and continuum components from the ATM fit of the data, along with the fit residual are also shown.

10.3.2 FTS measurements at Atacama (future ALMA site)

Two other FTS experiments are reported at sites in the Atacama desert, undergoing site testing measurements in areas selected for the Atacama Large Millimeter Array (ALMA) construction.

The first of such experiments has been operated by Nobeyama Observatory at Pampa la Bola, 4800 m above sea level in northern Chile on September 1997 and June 1998. The instrument is a Martin-Puplett type FTS with an InSb bolometer as detector. The frequency range covered is 150 – 1600 GHz (or 2 mm to slightly under 200 μm wavelength). Further details on the instrument can be found in Matsushita et al [1999].

On the morning of 1998 June 17, the best atmospheric transmission spectrum of the experiment was recorded. (Fig. 10.3, *top*). However, due to the limited sensitivity around 1500 GHz and offset errors in the phase correction of the Fourier-transformed spectra, there are some systematic errors in the transmission spectra around the 1450 – 1600 GHz window (it could be up to 10% in transmission). During the observing run, side-by-side measurements with the second FTS experiment in the area (at Chajnantor [Paine et al 2000]) were performed. The measured transmission spectra showed very good correspondence to each other within an accuracy of $\leq 1\%$ in the 650 GHz and 850 GHz windows.

Again, radiative-transfer calculations using the model ATM were performed to fit the data. The best fit of the June 17th spectrum is shown in Fig. 10.3. The model, that took advantage of what we learned from the Mauna Kea data, fits very well the observed spectrum with only one free parameter (the precipitable water vapor column [$N_{\text{H}_2\text{O}}$] above the site) except for frequencies higher than 1350 GHz, where the measurement suffers from systematic errors. The fit results in a water vapor column of 0.284 mm.

10.4 Atmospheric absorption evaluation

Calculations of zenith atmosphere opacity at 2.5 and 2.9 km, the altitude of the IRAM sites, can be performed with the updated ATM model [Pardo et al. 2001b] (see Figure 10.4). In fact, the model itself has been installed on-line on the IRAM telescopes of Pico Veleta and Plateau de Bure; it is activated at each calibration or skydip and allows to interpret the observed sky emissivity in terms of water and oxygen contributions and of upper and lower sideband opacities. Note that the opacities derived from sky emissivity observations do not always agree with those calculated from the measurement of P, T , and the relative humidity on the site, as water vapor is not at hydrostatic equilibrium.

The typical zenith atmospheric opacities, in the dips of the 1.3 mm and 0.8 mm windows (e.g. at the frequencies of the $J = 2 - 1$ and $3 - 2$ rotational transitions of CO, 230.54 and 345.80 GHz), are respectively 0.15–0.2 and 0.5–0.7 in winter at the IRAM sites. The astronomical signals at these frequencies are attenuated by factors of respectively $\simeq 1.2$ and 2 at zenith, 1.3 and 2.8 at 45 degree elevation, and 1.7 and 6 at 20 degree elevation. Larger attenuations are the rule in summer and in winter by less favorable conditions. The $J = 1 - 0$ line of CO, at 115.27 GHz, is close to the 118.75 GHz oxygen line. Although this latter is relatively narrow, it raises by $\simeq 0.3$ the atmosphere opacity (which is 0.35–0.4). The atmosphere attenuation is then intermediate between those at 230 and 345 GHz (by dry weather, however, it is more stable than the latter, since the water contribution is small). The measurement of accurate CO line intensity ratios (even not considering the problems linked to differences in beam size and receiver sideband gain ratios) requires therefore good weather, a high source elevation, and a careful monitoring of the atmosphere.

During the past few years, new ground-based astronomical observatories have been built to allow access to the submillimeter range of the electromagnetic spectrum. Potential sites are now being tested for more ambitious instruments such as the *Atacama Large Millimeter Array* (ALMA). All of these are remote, high altitude sites. For our simulations we have selected three sites of interest for submillimeter astronomy: Mauna Kea, HI, USA (LAT=19:46:36, LONG=-155:28:18; home of the Caltech Submillimeter Observatory, James Clerk Maxwell Telescope and Submillimeter Array), Chajnantor, Chile (LAT=-23:06, LONG=-67:27; site selected for ALMA) and the Geographic South Pole (site of the Antarctic Submillimeter Telescope and Remote Observatory). The results of this comparison are also shown on Figure 10.4.

10.4.1 Correction for atmospheric absorption, T_A^*

By analogy with the Rayleigh-Jeans approximation, $I = 2kT/\lambda^2$, which strictly applies to long wavelengths, the mm-wave radio astronomers have introduced the concept of “radiation” or “effective” temperatures, which scale *linearly* with the detected power.

The noise power detected by the telescope is the sum of the power received by the antenna, \mathcal{W}_A , and of the noise generated by the receiver and transmission lines, \mathcal{W}_{rec} .

Using Nyquist’s relation $\mathcal{W} = kT\Delta\nu$, \mathcal{W}_A and \mathcal{W}_{rec} can be expressed in terms of the temperatures T_A and T_{rec} of two resistors, located at the end of the transmission line, which would yield noise powers equal to \mathcal{W}_A and \mathcal{W}_{rec} , respectively: $\mathcal{W}_A + \mathcal{W}_{rec} = kT_A\Delta\nu + kT_{rec}\Delta\nu = k(T_A + T_{rec})\Delta\nu$.

T_A is called the “antenna temperature” and T_{rec} the “receiver temperature”. T_A becomes T_{load} when the receiver horn sees a load, instead of the antenna, and T_{gr} when it sees the ground. It should be noted that T_{load} and T_{gr} are not *stricto sensu* equal to the load and ground physical temperatures, but are only “Rayleigh-Jeans” equivalent of these temperatures (they are proportional to the radiated power). For ambient loads, they approach closely the physical temperature, since $h\nu/k \simeq 11$ K at $\lambda = 1.3$ mm.

When observing with the antenna a source and an adjacent emission-free reference field, one sees a change $\Delta T_A = T_A(sou) - T_A(ref)$ in antenna temperature. Because of the calibration method explained below, it is customary, in mm-wave astronomy, to replace ΔT_A , the source antenna temperature, by ΔT_A^* , the source antenna temperature corrected for atmosphere absorption and spillover losses. Both are related through: $T_A = (1 - \eta_f)T_{gr} + \eta_f(T_{sky} + \Delta T_A^* e^{-\tau})$, where τ is the line-of-sight atmosphere opacity. η_f is the forward efficiency factor, which denotes the fraction of the power radiated by the antenna on the sky (typically of the order of 0.9, see also Chapter 1).

The source equivalent “radiation temperature” T_R (often improperly called “brightness temperature” and therefore denoted T_{MB} when it is averaged over the main beam) and ΔT_A^* are related through

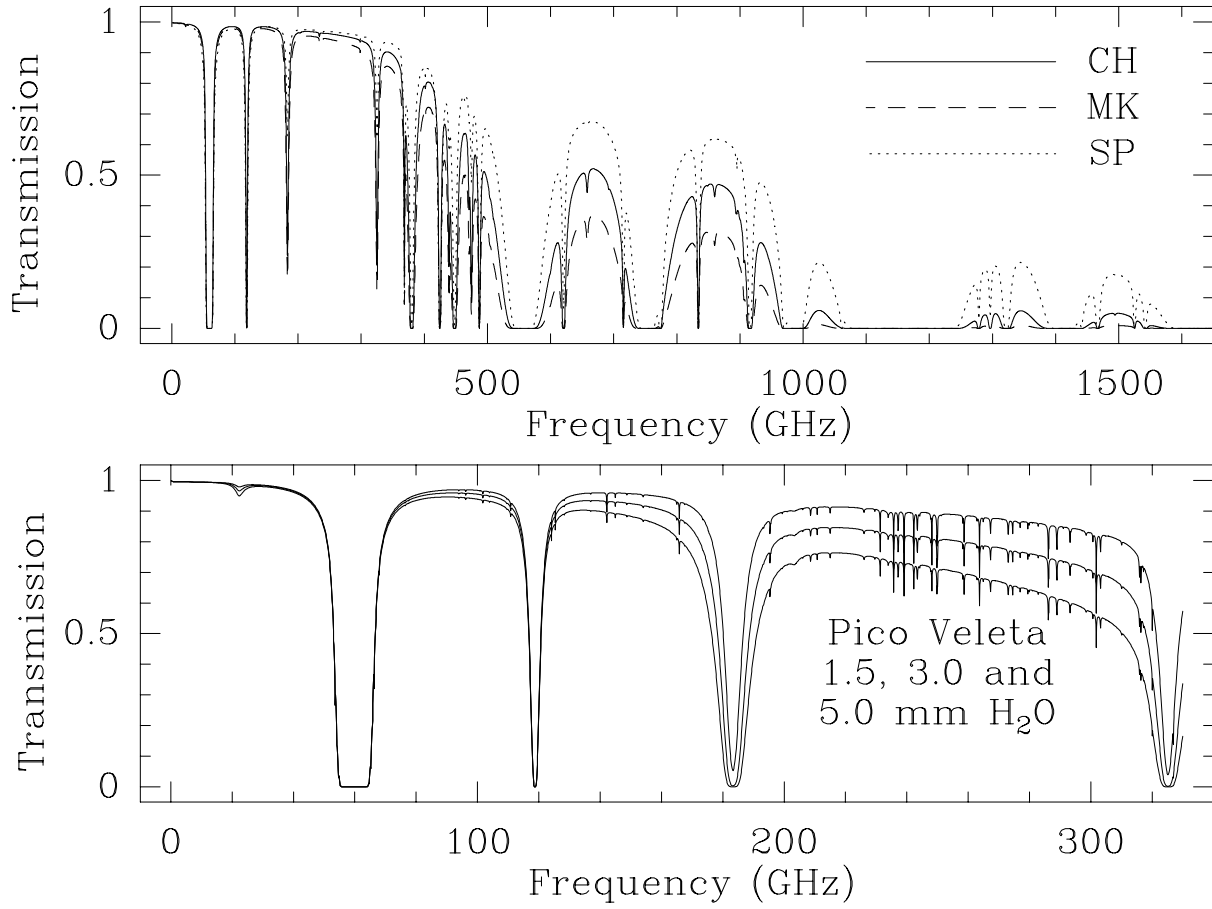


Figure 10.4: Calculated zenith atmospheric transmissions and continuum-like opacities for Mauna Kea, Chajnantor and the South Pole corresponding to the 1st quartile of the cumulative water column statistics for winter time in the three sites. The H₂O cumulative distributions used here were derived from different methods leading probably to a comparative optimistic result for the South Pole. For comparison we have added the expected transmission in the millimeter range for Pico Veleta in winter for 1.5, 3.0 and 5.0 mm of water vapor.

$$\Delta T_A^* = \int_{sour} T_R \mathcal{A}(x, y) dx dy$$

where $\mathcal{A}(x, y)$ is the antenna power pattern. For a source smaller than the main beam, $\Delta T_A^* = \eta_b / \eta_f T_{MB}$ (where η_b is the beam efficiency factor, see also Chapter 1).

When observing a small astronomical source with temperature $\Delta T_R \gg T_{BG} = 2.7$ K, located at an elevation el , one detects a signal \mathcal{V}_{sour} (of scale: \mathcal{G} volt or counts per Kelvin):

$$\frac{\mathcal{V}_{sour}}{\mathcal{G}} = M_{sour} = T_{rec} + (1 - \eta_f)T_{gr} + \eta_f T_{sky} + \eta_b T_{MB} \times e^{-\tau} \quad (10.27)$$

This signal can be compared with the signals observed on the blank sky (T_{atm}), close to the source, and to that observed on a hot load (T_{load}):

$$M_{atm} = T_{rec} + (1 - \eta_f)T_{gr} + \eta_f T_{sky}; \quad T_{sky} = (1 - e^{-\tau})T_{atm}; \quad M_{load} = T_{rec} + T_{load} \quad (10.28)$$

here, we have neglected the cosmic background and assume, in a first step, that the receiver is tuned single sideband.

Simplest case

(e.g. [Penzias & Burrus 1973])

Let's assume that $T_{load} \simeq T_{gr} \simeq T_{atm}$; then:

$$\begin{aligned} M_{load} - M_{atm} &= \eta_f T_{gr} e^{-\tau} \\ M_{sour} - M_{atm} &= \Delta T_A^* e^{-\tau} \\ \Delta T_A^* &= \frac{M_{sour} - M_{atm}}{M_{load} - M_{atm}} \eta_f T_{gr} \end{aligned} \quad (10.29)$$

Note that in Eq.10.29, the measurement of the antenna temperature includes the atmospheric opacity correction, but does not depend explicitly on an assumption on the atmospheric opacity. We can write:

$$\Delta T_A^* = \frac{M_{sour} - M_{atm}}{M_{load} - M_{atm}} T_{cal} \quad (10.30)$$

where we define T_{cal} as $T_{cal} = \eta_f T_{gr} \simeq \eta_f T_{atm}$.

More realistic case

Typically, the mean atmosphere temperature is lower than the ambient temperature near the ground by about 40 K: $T_{atm} \simeq T_{gr} - 40$ K; then, the formula above still holds if we replace T_{cal} by:

$$T_{cal} = (T_{load} - T_{emi}) e^{\tau} \quad (10.31)$$

$$\begin{aligned} \text{with } T_{emi} &= T_{sky} \eta_f + (1 - \eta_f) T_{gr} \\ &= \frac{(T_{load} + T_{rec}) \times M_{atm}}{M_{load}} - T_{rec} \end{aligned} \quad (10.32)$$

$$T_{sky} = (1 - e^{-\tau})(T_{gr} - 40)$$

T_{rec} , the receiver effective temperature is usually calculated by the Y factor method using a cold load (usually cooled in liquid nitrogen, i.e. at 77 K) and an ambient load (e.g. at 290 K).

$$Y = \frac{M_{hot_load}}{M_{cold_load}} \quad T_{rec} = \frac{T_{hot_load} - Y T_{cold_load}}{Y - 1} \quad (10.33)$$

General case

The receiver is not purely single-sideband. Let us denote by G^l and G^u the normalized gains in the receiver lower and upper sidebands, $G^l + G^u = 1$. The atmosphere opacity per km varies with altitude as does the air temperature.

Then, the above expressions of T_{sky} and T_{emi} should be explicated for each sideband ($j = u$ or l):

$$T_{sky}^j = (1 - e^{-\tau^j}) T_{atm}^j \quad (10.34)$$

$$T_{emi} = T_{sky}^l \eta_f G^l + T_{sky}^u \eta_f G^u + (1 - \eta_f) T_{gr} \quad (10.35)$$

The atmospheric transmission model ATM allows to calculate iteratively τ_ν from a load+ sky measurement. The values of τ^l, τ^u are calculated for the Standard US atmosphere (parameters are: Winter-, Spring-, or Summer-temperature T , altitude, latitude, water vapor w) by summing up the contributions of O_2 , H_2O and O_3 (including rare isotopes and vibrationally excited states). A first guess of the amount of precipitable water is made from the ambient temperature, pressure and humidity. Then, the expected T_{sky} and T_{emi} are calculated from the two expressions above and T_{emi} is compared to its value measured from the the observation of the atmosphere and the load (Eq.10.32). The value of w is changed and the calculation of τ^j, T_{sky}^j and T_{emi} restarted. Normally, the process converges after 2 to 4 iterations. Once w and T_{emi} are known, the calibration factor T_{cal} can be derived

$$T_{cal}^j = (T_{load} - T_{emi}) e^{\tau^j} \quad (10.36)$$

and the data calibrated in the T_A^* scale using Eq.10.30.

10.5 Phase fluctuation evaluation

10.5.1 Cause of Phase Fluctuations

The phase measured by an interferometer is the difference in the arrival times of the signals at the different antennas. The phase difference contains useful information about the location and structure of the source, but is also affected by atmospheric inhomogeneities. The complex dielectric constant fluctuates in time and in space as the distributions of water droplets, ice particles, and atmospheric gases suffer variations. In the case of clear atmosphere (no scatterers present) the main source of phase delay is water vapor. When there is more water vapor along the optical path of one of the telescopes, the incoming radiation will experience an additional delay and the measured phase will increase by $\Delta\phi$. With wind the amount of water vapor in the beam of each telescope will change over time and so will the detected phase. This phase delay has a resonant behavior as seen in section 10.2.4. As a result, the source appears to move around in the sky and, if the signals are integrated over a period of time which is long compared to the time scale of the fluctuations (few to tens of seconds), resolution as well as signal strength will be degraded. Fluctuations in the dry component of the atmosphere can also originate phase delays but these are in general less important.

10.5.2 Simulations of phase fluctuations

Present day radio interferometers are mostly limited to frequencies below 350 GHz. Phase delay increases in importance as the frequency increases into the submillimeter domain because of the strength of the atmospheric lines involved in both absorption and dispersion. Using the complex line shape of equation 10.22 we have calculated the derivative of the phase delay respect to the water vapor column $\frac{\partial\phi}{\partial N_{H_2O}}$ (this derivative will be called the *differential phase* and is provided in deg/ μm here). The differential phase as a function of frequency has been plotted for the Chajnantor site in Figure 10.5 (where the curve is restricted to those frequencies where the transmission is above 10% when the precipitable water vapor column is 0.3 mm, i.e. very good conditions for single-dish submillimeter observations). Another useful quantity plotted in the same figure is the derivate of the phase delay with respect to the sky brightness temperature ($T_{B,sky}$), since this function relates the phase correction between two antennas to a measurable physical parameter ($T_{B,sky}$). Note however that whereas the differential phase described above depends only on ΔN_{H_2O} , this new quantity depends on N_{H_2O} as well. The curve plotted here corresponds to $\frac{\partial\phi}{\partial T_b}(\nu)$ at $N_{H_2O}=0.3\text{mm}$.

As seen in Figure 10.5, the differential phase becomes much more important in the submillimeter domain than it is at millimeter wavelengths, so its correct estimation and the selection of the best means of monitoring water vapor column differences between different antennas are essential for the success of ground-based submillimeter interferometry. For example, the differential phase is 0.0339 deg/ μm at 230 GHz whereas it is -0.4665 and 0.2597 deg/ μm at 650 and 850 GHz respectively, roughly an order of magnitude larger.

10.5.3 Phase Correction Methods

There are basically two different phase correction methods:

A) The phase offset due to the atmosphere can be measured *directly* by observing a calibrator, i.e., a strong point source whose position and hence theoretical phase are well known. Assuming instrumental errors are small the difference between the measured and the theoretical phase gives the phase offset introduced by the atmosphere. The phase offsets, which are interpolated between measurements on the calibrator, are subtracted from the measured phase of an astronomical source.

B) The correction can be determined indirectly by detecting the emission from water molecules and calculating the phase error from the differences in the amounts of water along the paths to the individual antennas using a model as presented on Figure 10.5. There are two different approaches to determine the amount of water vapor: (i) *Total Power Method*, where the astronomical receivers measure the continuum emission; and (ii) *Radiometric Phase Correction*, where the emission from water lines is measured by dedicated instruments. So far, radiometers monitoring the 22 GHz and the 183 GHz lines have been built

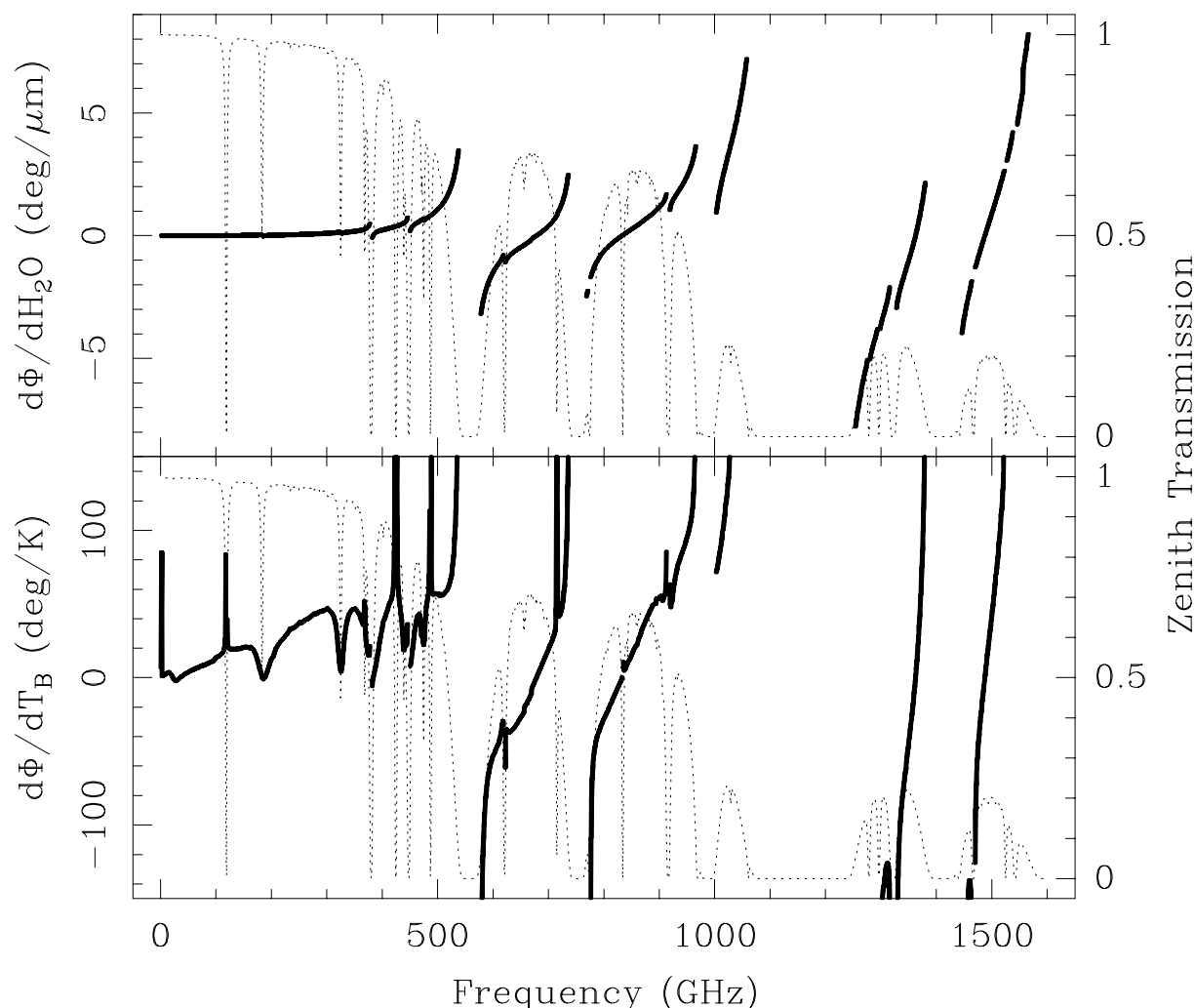


Figure 10.5: Upper panel: Derivative of the phase delay respect to the water vapor column (*differential phase* in text; this derivative is independent of the water vapor column) as a function of frequency, superposed on the Chajnantor atmospheric transmission curve for 0.3 mm of water vapor. Lower panel: Derivative of the phase delay respect to the sky brightness temperature for 0.3 mm H₂O column.

and tested. Receivers at 22 GHz typically have lower noise temperatures than those at 183 GHz, but on (very) dry sites, such as Chajnantor, the 183 GHz monitors will be ideal to measure the optical path with higher accuracy due to the much higher conversion factors from sky brightness temperature in K to optical path length in mm.

10.5.4 Example of phase correction

Fig. 10.6 shows typical phase correction results in normal night time weather for Mauna Kea (2.2 mm N_{H_2O}): The CSO-JCMT interferometer observed bright hydrogen recombination line maser emission towards the source MWC349 at 354 GHz. The solid curve in the top plot displays the measured phase after Doppler correction, it represents the atmospheric phase fluctuations and some electronic phase noise. The dashed line shows the phase predicted by the water vapor monitors. The measured and the predicted phase agree well and their difference is plotted in the lower graph. Phase correction reduces the rms phase fluctuations from 60° (140 μm) to 26° (60 μm) over 30 minutes. If one would integrate on source for 30 minutes 42% of the astronomical flux would be lost due to decorrelation, but with phase correction the

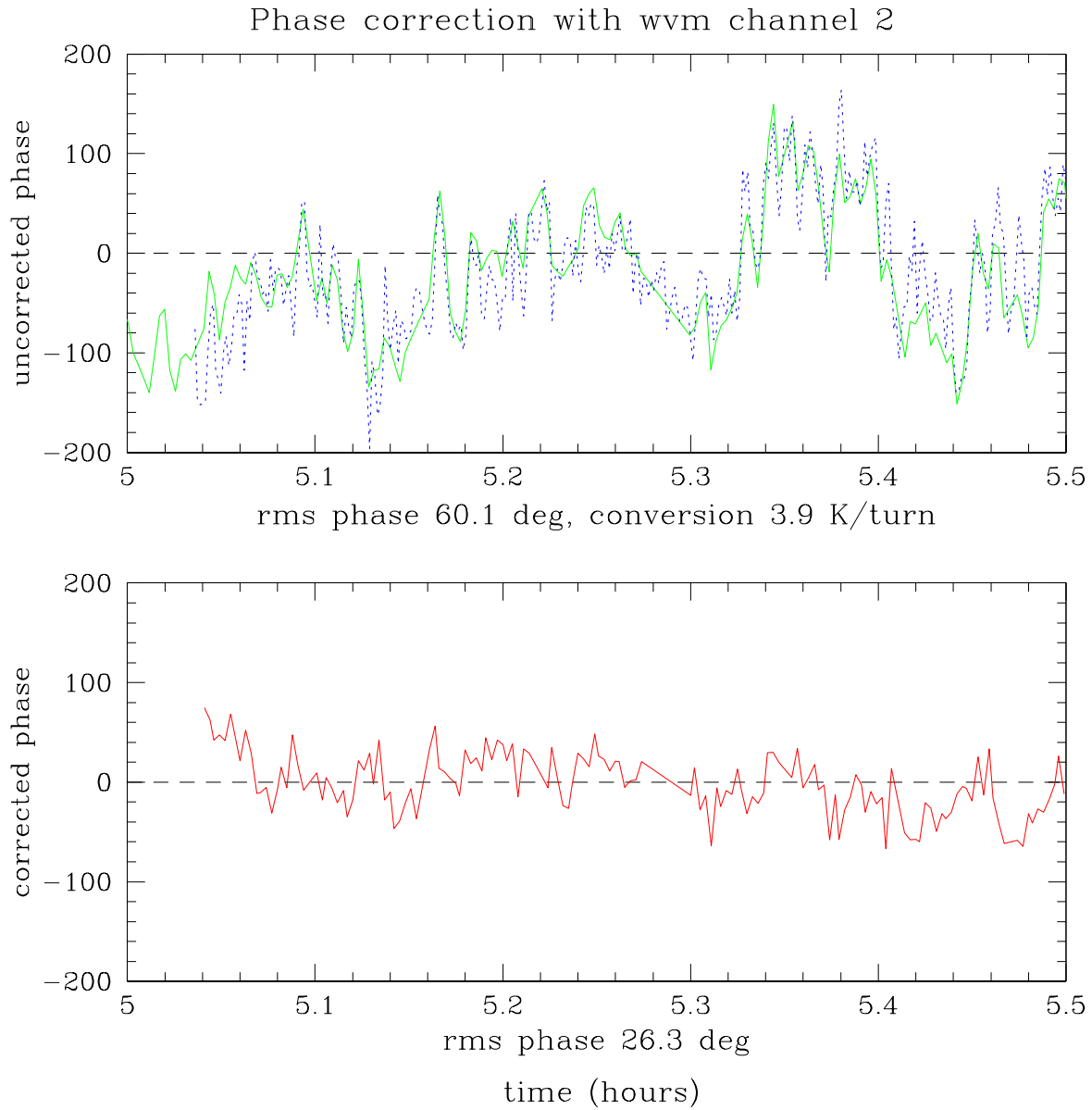


Figure 10.6: Phase correction results for the CSO-JCMT interferometer using 183.31 GHz 3-channel water vapor monitors (courtesy of Martina Wiedner).

loss would amount to only 10%.

Chapter 11

Atmospheric Fluctuations

Michael Bremer

bremer@iram.fr

IRAM, 300 rue de la Piscine, F-38406 Saint Martin d'Hères, France

11.1 Introduction

We have already encountered the effects of atmospheric absorption in the lecture by Michel Guélin (Chapter 10). Even under low opacity conditions, observations can be difficult or impossible due to atmospheric phase fluctuations. In principle, integration of an interferometric signal is like the adding up of vectors. The amplitude is the length of a vector, and its orientation is given by the phase. Errors in the phase will cause part of the amplitudes to cancel each other out according to Eq. 11.1

$$\overline{V_{ij}^m} = V_{ij} \exp(-\sigma_\phi^2/2) \quad (11.1)$$

where V_{ij} are the ideal visibilities, $\overline{V_{ij}^m}$ the integrated ones, and σ_ϕ the phase noise in radian (assuming a Gaussian noise distribution).

If our eyes were sensitive in the millimeter range with a resolving power of some arc seconds, we would not only see a luminous sky where sources are difficult to make out on the background: we would notice refracting bubbles of sizes between some centimeters to several kilometers drifting with the wind, merging, separating and distorting the view behind them. It is water vapor which has not attained the concentrations necessary for cloud formation, and mixes badly with dry air. Even in the case of low opacity and a sky clear for human perception, these distortions - which are shifts and tilts in the incoming phase front - can be so important that they make observations impossible.

In this lecture we will study the physics behind this effect and possible ways to correct for it which have become available in recent years.

The phases of a wave front that reaches ground-based observatories have been modified by their journey through refractive index variations in the Earth's atmosphere. The instrument itself has no way to tell

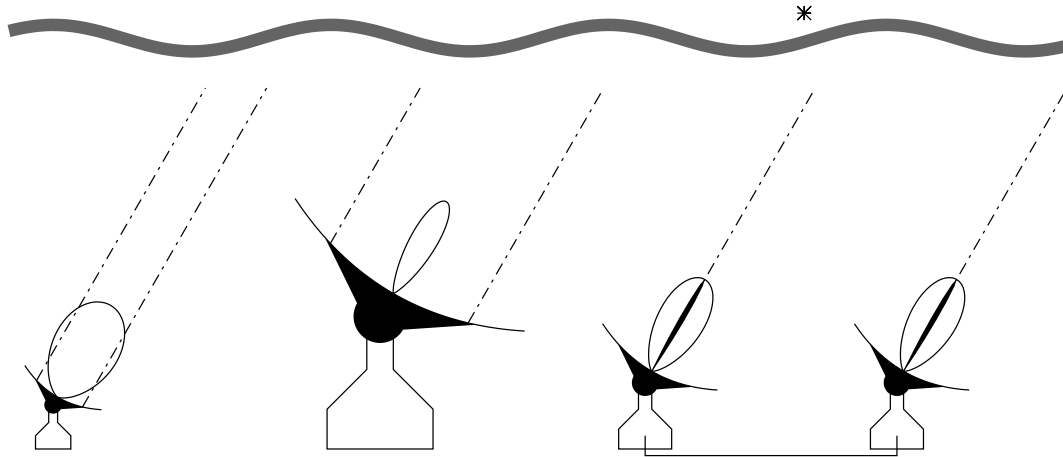


Figure 11.1: Two single dish radio telescopes and one synthesis array observing a source. Angular resolution and the effects of atmospheric turbulence increase with the diameter of an instrument. An interferometer's synthesized beam has the same problems that a single dish with a projected baseline's diameter would experience.

which part of the phases are due to valuable structure in the astronomical source and which part was caused during the last kilometers in front of the telescope.

As a result, the apparent position of a point source keeps moving, so that details of an extended source become blurred ("seeing"). The perturbations become progressively decorrelated with increasing separation between two lines of sight.

Depending on turbulence scale, wavelength and telescope size, a ground-based observer will be confronted with different effects. To some extent, one can reduce unwanted perturbations by choosing an observatory's site carefully. But there are always some days which are better than others.

- If the telescope diameter is much larger than a typical turbulence cell and if phase shifts over a turbulent cell are less than 1 radian, one works in the **diffractive** regime: some power is scattered into an error beam, but the diffraction limited resolution of the instrument is conserved. These conditions can be found for very long baseline interferometry at cm wavelengths under good conditions.
- In the **refractive** regime, the turbulence cells are much larger than the telescope so that the whole image seems to move around. Phase shifts can be several radians. *This is the case we have to cope with at the Plateau de Bure interferometer.*
- In the **intermediate** case, one gets speckles on short integration times which average into an image convolved with a seeing disk (an effect well-known to optical and near infrared observers).

For a small radio telescope, the phase noise passes unnoticed (Fig.11.1). Its beam size is bigger than the apparent position shifts induced by seeing, and the ray paths leading to the opposing outer edges of the reflector will not differ much. For a big single dish, the effect can become noticeable: under unstable conditions, a source may wander in and out of the beam, disturbing not only the observations of the target of interest but also pointing and focus. An interferometer suffers even more from seeing because the distances between individual antennas are large. This has the double effect of making the synthesized beam smaller and of increasing the differences in the atmospheric turbulence pattern between the optical paths. In the optical and near infrared, it is the dry atmosphere which causes the phase shifts. In the centimeter radio range, it is the tropospheric water vapor and the ionospheric plasma irregularities, and mainly water vapor in the millimeter radio range.

The interest of interferometric phase correction is to determine and remove the atmospheric phase noise. Each individual antenna has to correct a time variable "piston" in the incoming wave front, which is the equivalent of adaptive optics for the synthesized dish.

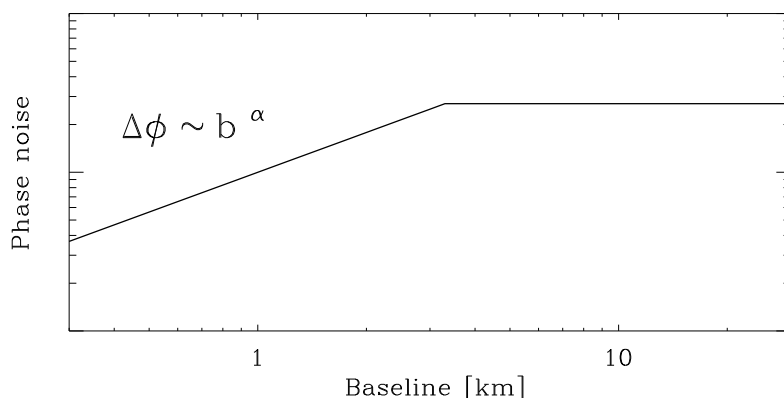


Figure 11.2: Atmospheric phase noise as a function of baseline length. The position of the break and the maximum phase noise are weather dependent.

Most of the water vapor is confined to the troposphere (<10 km) with an exponential scale height of 2 km. Its molecular weight is 18.2 g/mol so that it has the tendency to rise above dry air (28.96 g/mol). Our planet retains the water vapor due to the negative vertical temperature gradient in the troposphere, and the fact that H₂O is close to the transition points to liquid and solid under terrestrial pressure and temperature conditions. Venus is an example for a planet with a hot troposphere (extreme CO₂ and H₂O greenhouse effect) who lost most of its water long ago.

Under Earth's environmental conditions, water vapor mixes badly with dry air and tends to form bubbles with sizes up to several kilometers, which are broken up by turbulent motions. When choosing high and dry sites for millimeter astronomy, one must keep in mind that high phase noise can be induced even by low amounts of precipitable water.

Parameters that influence interferometric phase noise strongly are:

- wind speed,
- projected baseline length,
- the time of the day (nights are typically more stable due to the missing solar energy input to turbulence),
- topographic effects, e.g. the turbulent wakes of mountains.

The leveling off of the phase noise on a high, constant value corresponds to the outer scale size of the turbulence, where the fluctuations along two lines of sight become totally decorrelated, i.e. as bad as they can possibly get (Fig. 11.2). Increasing the baselines will not increase the phase noise any more, and this is why very long baseline interferometry can work.

In the following, some fundamentals about turbulence will be explained, and how one can analyze the properties of a turbulent atmosphere. Possible methods to monitor the phase fluctuations will be discussed, with emphasis on the phase monitoring system on the Plateau de Bure. Some examples with observational data will be presented, demonstrating its benefits and current limitations.

11.2 Hydrodynamical basics of turbulent motion

Turbulence has its origin in the non-linearities of the hydrodynamical equations of motion. These equations are not derived from first principles, but present the easiest consistent way of describing the motion of compressible (gases) or incompressible (liquids) media. Given the complexity of observed hydrodynamical phenomena (white water rivers, curling smoke, ...) it was doubted for more than a century if the equations could really be as simple as given below.

Scepticism was nourished by the fact that some stationary (i.e. time invariant) solutions were mathematically valid but not observed experimentally, which can be understood today by checking the solutions for their stability. It is an interesting fact that stationary solutions are *not* always the most stable ones – this assumption might appear “natural”, but is in fact quite misleading. To find out under which conditions one has to expect turbulence, we must have a closer look into the equations of hydrodynamics.

In a free flow (i.e. no outer confinements like tubes) and under sub-sonic conditions, one can treat air as an incompressible medium. This allows to use the Navier-Stokes equations which describe such a medium with viscosity (Eq. 11.2).

$$\underbrace{\frac{d\vec{V}}{dt}}_1 + \underbrace{\frac{grad P}{\rho}}_2 + \underbrace{grad U}_3 - \underbrace{\frac{\eta}{\rho} \Delta \vec{V}}_4 = 0 \quad (11.2)$$

The respective terms describe:

1. This part is the complete derivative in time, containing non-linear terms:

$$\frac{d\vec{V}}{dt} = \frac{\delta\vec{V}}{\delta t} + \underbrace{(\vec{V} grad)}_{kin. Energy} \vec{V} = \frac{\delta\vec{V}}{\delta t} + \underbrace{\frac{1}{2} grad (\vec{V} \cdot \vec{V})}_{kin. Energy} - \underbrace{\vec{V} \times (\nabla \times \vec{V})}_{Vortices} \quad (11.3)$$

2. The pressure term describes the reaction to external forces, and is related to density and temperature through the equation of state.
3. External forces, described by the gradient of a Potential U . This form makes it easier to include this term into the others. We are interested here in cases where U is constant in good approximation, so we can leave this term out in the following.
4. Energy dissipation. Viscous terms, with the Laplacian operator $\Delta = \nabla^2 = div grad$. The material constant η is the viscosity coefficient for incompressive media (there is a term with a second coefficient for compressive media, but it can be neglected here).

To solve Equation 11.2, one needs:

- the equation of state for the gas,
- the conservation of mass and energy,
- the boundary conditions.

We will not have to deal with these equations directly. If you have to solve them for some reason: There is a whole class of numerical methods and library codes in the literature, which avoid non-evident pitfalls concerning different coordinate systems and numerical stability. For the current discussion, we are only interested in the question of similarity.

Flow problems resemble each other for certain combinations of flow velocity, spatial dimension and viscosity. This allows to predict the general properties of a hydrodynamic system (and if it is turbulent or not) from small models or other well-studied cases where the geometries are the same. It is convenient to change to dimensionless equations by expressing lengths and velocities in units of the system's typical length scale l_0 (e.g. the size of an obstacle) and the unperturbated flow velocity V_0 .

One obtains not only $V' = V/V_0$ and $l' = l/l_0$, but must change all other units which are combinations of the two: $t' = t \cdot v_0/l_0$, $\rho' = \rho \cdot l_0^3$ and $P' = P \cdot l_0^3/v_0^2$. As a result, we get the dimensionless equation Eq.11.4:

$$\frac{dV'}{dt'} + \frac{grad P'}{\rho'} - \frac{1}{Re} \Delta V' = 0 \quad (11.4)$$

Medium	η [g/cm s]	$\nu = \eta/\rho$ [cm ² /s]
Water	0.010	0.010
Air	0.00018	0.150
Alcohol	0.018	0.022
Glycerin	8.5	6.8
Mercury	0.0156	0.0012

Table 11.1: Examples for viscosity and the kinetic viscosity η/ρ various media at 20°C (adapted from [Landau & Lifshitz 1959]). The viscosity changes little with altitude, so that the density dependency of ν dominates and satellites above ≈ 300 km altitude experience a non-turbulent, laminar flow.

which contains **Reynold’s number** $Re = l_0 \cdot V_0 \cdot \rho/\eta$. It determines the relative influence of the energy dissipating term relative to the non-linear turbulent term. A high Reynold’s number will reduce the effect of $\Delta V'$, so that turbulence will develop. Each problem has its specific **Critical Reynold’s number** Re_c , which lies typically between 10 and 100. For a given geometry and a $Re > Re_c$, no stable solution exists (e.g. Figure 41-6 from [Feynman et al. 1964]).

With Eq.11.4 and the viscosities from Tab.11.1, we find that for ambient conditions, wind moving faster than 1 cm/s hitting an obstacle bigger than 1 cm generates a turbulent flow. A house (10 m) in a 10 m/s wind has $Re \approx 6 \cdot 10^6$, mountains $Re \approx 1 \cdot 10^9$.

This means that turbulence is something quite common in our environment. In our daily life, we encounter many turbulent systems which defy detailed prediction: leaves of wind-moved trees, eddies in flowing water, the structure of clouds, to name only a few. All these effects are non-linear and will never repeat themselves exactly, although their parameters stay within certain limits.

It may be surprising that these phenomena have been neglected by classical physics for centuries, to become finally popular in the wake of chaos theory and the development of powerful computers. One reason for this was surely the problem of repeating an experiment with inherent chaos exactly, and the sheer bulk of work for doing the calculations. Linear physics were favored not because they are more abundant in nature, but because they were easier to understand and reproduce.

Even chaos theory has a hard time with the atmosphere. The famous “strange attractors” which describe non-repetitive curves in solution spaces are not very useful for turbulence, because one is not sure if the number of solution space dimensions is finite or not in this case.

Meteorology is a well-known (and sometimes notorious) example for predictions of a non-linear system. In spite of a network of measurement stations and satellite data, boundary conditions are not known precisely enough for long term forecasts. This is the famous “butterfly effect”: A butterfly moving its wings in South America may change the weather in Europe six months later.

But don’t start hunting butterflies to prevent storms right now: this example only illustrates that non-linear systems do not obey the “small cause - small effect” rule of linear physics but a rather imprecise “small cause at the right place may have a big effect” rule. So it could be a butterfly, a spoken word, a thought, or a tree falling in a forest, or all of them together that may tip a balance.

For all practical applications, the interactions are too complex to backtrack the cause – but nevertheless, the history that makes a leaf move right now in a unique way outside your window contains somewhere the gravitational pull of faraway galaxies, and your mere presence will leave traces in the turbulent structures all over the universe (no liabilities implied, fortunately).

A small perturbation may set off a non-linear cause-and-effect chain, but this is only because a turbulent system can have multiple macroscopically different states without violating the conservation of energy. Using a statistical approach, we will now discuss turbulence’s energy distribution on different scale sizes. This is an important step to understand how atmospheric parameters (including phase noise) change with time and distance.

11.3 Statistical properties of turbulence

We start with a simple model of turbulence. It must explain why the scale size of the finest turbulence structures becomes smaller and smaller with increasing Re , and should allow to treat the finest details in

a homogeneous way. It cannot explain why certain structures form and not others, but it describes the average flow of energy across the scale sizes of turbulence.

- Kinetic energy enters the medium on large scales, in the form of convection or friction on an obstacle (**energy range**).
- The energy is transferred towards smaller scale sizes over eddy fragmentation, while the Reynolds number decreases (**inertia range**).
- The smallest eddies have sub-critical Re 's, dissipate heat, and are stable (**viscous range**).

[Kolmogorov 1941] advanced a hypothesis for high ($Re > 10^6 - 10^7$) Reynold's numbers, postulating that turbulence in the inertia range was determined only by one parameter ϵ (kinetic energy converted to heat by viscous friction per unit time and unit mass). In the viscous range, it would only depend on ϵ and the already discussed viscosity η . This model treats cases like the seemingly amorph eddies-within-eddies part in the Fig.41-6 (d),(e) (from [Feynman et al. 1964]). As we have derived in the previous section, (d) and (e) are indeed the cases to be expected in the troposphere.

The inertia range is interesting for us because it corresponds to spatial dimensions of some meters to 2-3 kilometers, i.e. the baselines of the PdBI fall into this range.

For the mathematical treatment of highly developed turbulence, one can use a formalism based on random variations.

Most "classical" statistics represent a given distribution of probability (binomial, Poisson, Gaussian, ...) around a most likely measurement value. For atmospheric parameters like e.g. temperature and wind velocity, we must make a more general approach: the most likely measurement values vary with time and space, which means they can be represented by *non-stationary random processes*. The classical average and its variation are not very useful to describe these systems.

An instrument for the characterization of non-stationary random variables are *structure functions*, which were first introduced by [Kolmogorov 1941]. A scalar structure function has the form given in Eq.11.5,

$$D_f(x_i, x_j) = \overline{(f(x_i) - f(x_j))^2} \quad (11.5)$$

i.e. a function $f(x)$ is measured at the positions x_i and x_j , squared and averaged over many samples to obtain a $D_f(x_i, x_j)$. When the average level of f changes, the average differences between $f(x_i)$ and $f(x_j)$ stay constant.

The structure function formalism can even be used to describe vector parameters like the turbulent wind velocity, in this case one simply needs 3×3 tensors of structure functions for their description. We won't need tensors in the following discussion, however. The detailed mathematical formalism of random fields would be too much for this course (see [Tatarski 1971] for details). We will only discuss the basic concepts and their application to phase shifts.

Real atmospheric parameters are functions of time and space. For time dependency, Taylor's hypothesis of frozen turbulence has been quite successful (Eq.11.6). It states that the pattern of refractive index variations stays fixed while it is moving with the wind.

$$f(x, t + t') = f(x - V_{al} \cdot t', t) \quad (11.6)$$

This means that for the structure functions, one can either measure at two different sites simultaneously or measure in one place and compare different times. Time-like structure functions are often easier to determine because the sampling is continuous and instrumental effects are reduced by averaging. The velocity V_{al} is also called "Velocity aloft" and can differ notably from measurements of a ground-based meteorological station: wind speeds increase with altitude and change direction due to the diminishing effect of ground friction.

For two measurement points which are a distance r apart from each other, one finds that the structure functions of many atmospheric parameters (temperature, refractive index, absolute wind velocity, ...) obey a $r^{2/3}$ power law. This law can be derived from the theory of random fields, but the easiest way is as follows:

Consider a velocity fluctuation δV_r (where δV_r may be large) which occurs on a scale size r and a time $t = r/\delta V_r$:

- its energy per mass unit is $\propto (\delta V_r)^2$
- The energy per mass and time: $\epsilon \propto \delta V_r^2/t = \delta V_r^3/r$
- Stationary transport of this energy from large to small scale sizes, where it is finally dissipated
- Approximately, $D_{rr}(r) = \overline{(V(r_l + r) - V(r_l))^2}$ is dominated by eddies of size r , i.e. $D_{rr}(r) \approx (\delta V_r)^2$
- Therefore, the formula for intermediate scale sizes is:

$$D_{rr}(r) \propto (\epsilon \cdot r)^{2/3} \quad (11.7)$$

For a thin layer, refractive index fluctuations and phase fluctuations are identical. This is the *thin screen approximation*.

$$D_\varphi(r) = C \cdot (\epsilon \cdot r)^{2/3} \quad (11.8)$$

In a thick turbulent layer, the phase front encounters multiple refractive index fluctuations and the power law index changes. This problem can be solved by analyzing the irregular refracting medium over its Fourier transform. After [Tatarski 1961], the spectral density of the function

$$D(r) = r^p \quad (11.9)$$

with $0 < p < 2$ is in the three dimensional case

$$F'(\kappa) = \frac{\Gamma(p+2)}{4\pi^2} \sin(\pi p/2) \kappa^{-(p+3)} \quad (11.10)$$

An important condition is that the fluctuations must have an outer limit, i.e. that the power law does not increase indefinitely. To get the phase fluctuations from the refractive index spectrum, we take

$$D_\varphi(r) = 4\pi \int_0^\infty [1 - J_0(\kappa r)] F'(\kappa) \kappa d\kappa \quad (11.11)$$

with the Bessel function J_0 and finally obtain the power law for thick screen turbulence:

$$D_\varphi(r) \propto (\epsilon \cdot r)^{5/3} \quad (11.12)$$

For the phase noise ($\Delta\varphi(r) = \sqrt{D_\varphi(r)}$), one has therefore to expect power laws with exponents between 1/3 and 5/6. The absolute scaling factor for the power law and the position of the break where the phase noise levels off depend on the observing site, and of course on the weather.

Due to the quasi-random nature of phase fluctuations, forecasts and inter/extrapolations can be considered inadequate for a phase correction system. Direct measurements of the water vapor column along the line of sight are therefore the most reliable approach.

11.4 Remote sounding techniques

These methods were originally developed for meteorology and control of industrial emissions.

1. **LIDAR**: compares laser back scattering or transmission. DIAL: differential absorption LIDAR, works at two frequencies (on and off the atmospheric line of interest), detects 0.01 g/m³ water vapor. Disadvantage: works best from aircraft, expensive equipment.
2. **SODAR**: Remote sounding with sound waves. Detects turbulence, but gives little quantitative results.
3. **IR window**: H₂O line absorption in front of a strong continuum source (Sun, Moon, Jupiter). Disadvantage: Directions of observing and monitoring beam differ. The phase correction degrades as a function of the separation angle and the distance of the dominant turbulent layer.

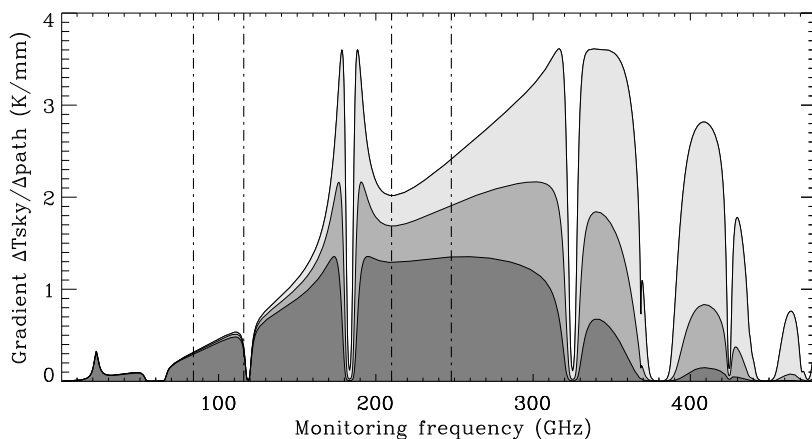


Figure 11.3: Gradient $\Delta T_{sky}/\Delta path$ (K/mm) as a function of frequency and total precipitable water under clear sky conditions. The atmospheric model assumed an ambient temperature of 275 K, pressure 780 mbar, elevation 45° , an observing frequency of 90 GHz and various amounts of water vapor. Light grey: 3 mm water, middle grey: 5 mm water, dark grey: 8 mm water. Dash-dotted lines indicate the receiver tuning ranges of the PdBI.

4. **Radiometric:** Uses the atmospheric emission. Dedicated monitors operate mostly near the 22 GHz or 183 GHz lines (several spectral channels). The inter-line regions of the 1mm and 3mm windows are also sensitive enough, but make it difficult to remove cloud emission.

For the radiometric approach, it is useful to study the sensitivity as a function of frequency, i.e. by how much the sky emission changes for a fixed fluctuation of water vapor, which corresponds to a fixed wet path fluctuation. Fig.11.3 shows what change in T_{sky} one must measure under conditions of various humidity.

There are two reasons to use the 22.2 GHz line: Clouds are easier corrected at this frequency, and receiver components are less expensive.

One notices that the 84-116 GHz window is 1-2 times as sensitive as the 22.2 GHz line, and the 210-248 GHz window 4.5-8.3 times. A dedicated receiver near the 183 GHz water line would have the highest sensitivity, but can suffer from temperature dependent saturation effects. It is better adapted for sites where the total amount of water above the instrument is typically less than 3 mm.

11.5 Current phase correction at IRAM

Remote sounding is done with the astronomical 1mm receivers in the inter-line region at the chosen observing frequency. One uses the total power channel (bandwidth 500 MHz). Advantages of this approach are the close coincidence of observed and monitored line of sight, and the fact that no additional monitoring equipment is needed.

First success was on April 18, 1995, with the installation of the present receiver generation on the PdBI [Bremer 1995]. Critical advantages were the improved total power stability of the receivers and the capability to observe in the 1mm window. The necessary stability for a 30° phase rms at 230 GHz is about $\Delta M/M = 2 \cdot 10^{-4}$.

Steps of the method:

1. Calibration of the total power counts M_{atm} to T_{sky} as given in the lecture on amplitude and flux calibration.
2. Iterate the amount of precipitable water vapor in an atmospheric model to reproduce T_{sky} . There is no “learning phase” of the algorithm on a quasar, just the model prediction.

RF: Fr.(A) CLIC - 07-MAY-1999 15:09:02 - i--1 N05W00W05E03 No Avg.
 Am: Rel.(A) 99 4436 I038 0836+710 P CORR CONT3 4D1 18-MAY-1998 13:53 -2.7 Vect.Avg.
 Ph: Rel.(A) Atm. 149 4476 I038 J0753+5352 P CORR CONT3 4D1 18-MAY-1998 14:14 -1.5

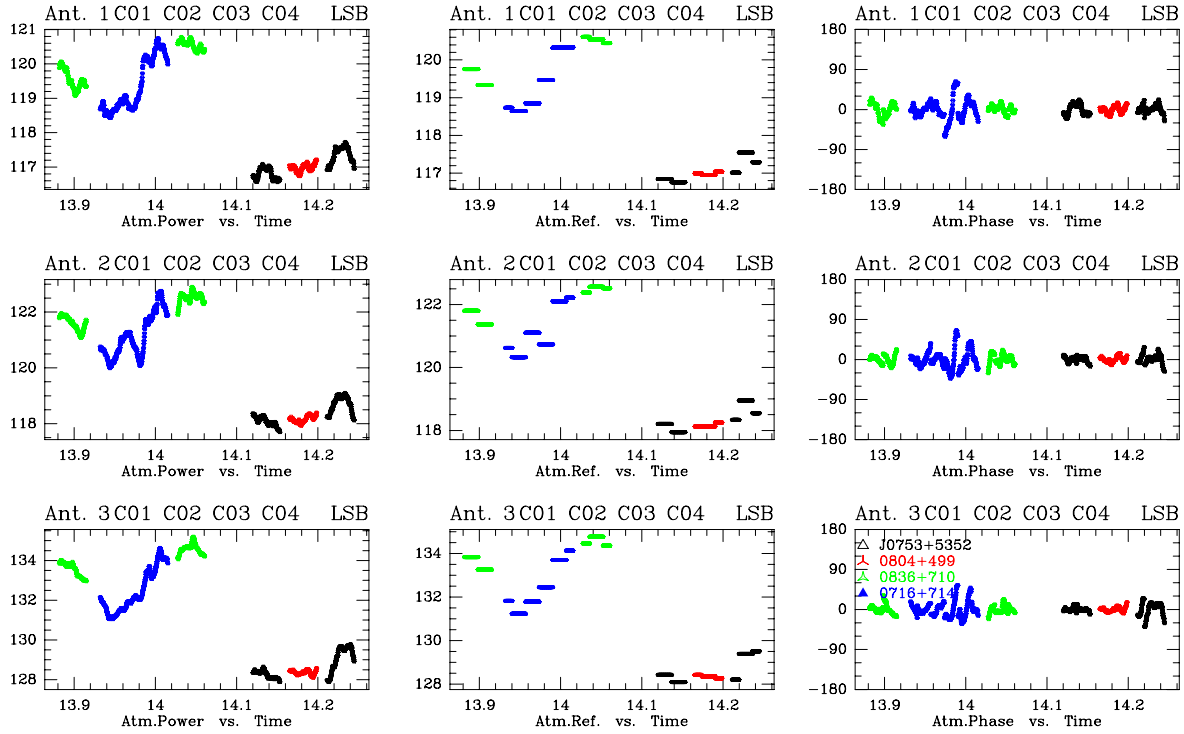


Figure 11.4: Antenna based total power at 228.3 GHz, the reference value to calculate the differential correction, and the model-based phase shift per antenna at 86.2 GHz.

3. The amount of water vapor along the line of sight is proportional to the wet path length.

$$path \approx 6.7 \cdot water(\text{Zenith}) \cdot airmass(\text{Elevation}) \quad (11.13)$$

However, wet path length and opacity have different dependencies on frequency, atmospheric pressure and temperature which should be taken into account. The main increase of the refractive index n of water vapor relative to dry air happens in the infrared, which makes it difficult to use the Cramers-Kronig relations linking it to opacity (integration over many transitions). For simplicity, we use the calculations by [Hill & Clifford 1981] for the frequency dependency and the temperature and pressure dependencies by [Thayer 1974] instead. These references use not n but the refractivity N , which is defined over the excess path length L relative to vacuum propagation over the line of sight s :

$$L = 10^{-6} \int N_\nu(s) ds \quad (11.14)$$

$$N(P, T) = 77.493 \frac{P_{atm}}{T} - 12.8 \frac{pV}{T} + 3.776 \times \frac{pV}{T^2} \quad (11.15)$$

Hill and Clifford calculate $N(\nu)$ for $T = 300$ K, $P = 1013.3$ mbar, 80% humidity

$$N(p, T, \nu) = 77.493 \frac{P_{atm}}{T} - 12.8 \frac{pV}{T} + N(\nu) \frac{pV}{28.2} \left(\frac{300.}{T} \right)^2 \quad (11.16)$$

4. Subtract the average over a time interval (default: the duration of a scan) to remove residual offsets due to receiver drift and ground pickup, which can be different for each antenna (see Fig.11.4).

5. Convert the antenna specific path shifts into phase at the observed wavelength, $\Delta\phi_i$
6. Calculate the baseline specific phase shifts $\Delta\phi_{ij} = \Delta\phi_i - \Delta\phi_j$. A corrected and an uncorrected version are calculated and stored during the real time reduction which compresses the spectra over one scan. The precision of the correction in relative pathlength is about $65\mu\text{m}$ per antenna (hence $90\mu\text{m}$ per baseline, i.e. $\sqrt{2}$ larger).
7. During the off-line data reduction, the user can choose freely between the corrected and uncorrected sets. The phase correction can fail under the following conditions:
 - Clouds: the model only works for clear sky conditions, and will over-estimate the phase shifts seriously in the presence of clouds.
 - Very stable winter conditions: The phase noise of the observations can be below 25° at 230 GHz, which is the intrinsic noise of the correction method.
 - Total power instabilities: For some frequencies, the receivers are difficult to tune. One can get a nice gain in the interferometric amplitude, but an unstable total power signal with an intrinsic noise well above 25° at 230 GHz.

Even for the cases above, the observer has lost nothing because the uncorrected scans are still there. Software tools are available which help to decide when to apply the correction.

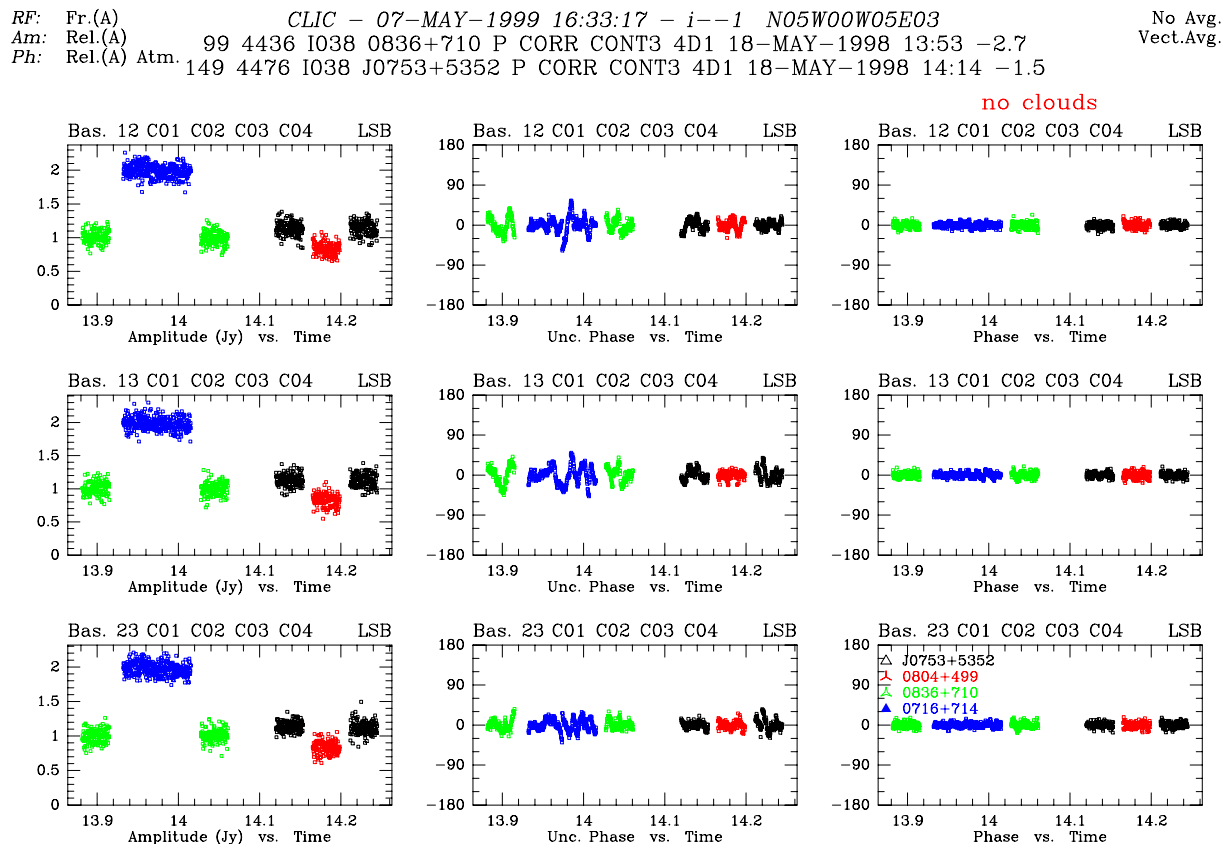


Figure 11.5: Baseline based amplitudes, uncorrected phase and monitor corrected phase at 86.2 GHz with a time resolution of 1 s. The data correspond to the antenna based section in Fig.11.4. The phase calibration applied in columns 2 and 3 was obtained using STORE PHASE /SELF on a one minute time scale, thereby setting the mean phases to zero.

RF: Fr.(A) CLIC - 07-MAY-1999 16:01:03 - i--1 N09W01E03 No Avg.
 Am: Rel.(A) 295 9621 1038 B0749+5400 P CORR CONT3 4D2-W10 22-MAY-1998 14:56 -.6 Vect.Avg.
 Ph: Rel.(A) Atm. 367 9666 1038 B0749+5400 P CORR CONT3 4D2-W10 22-MAY-1998 15:28 .0

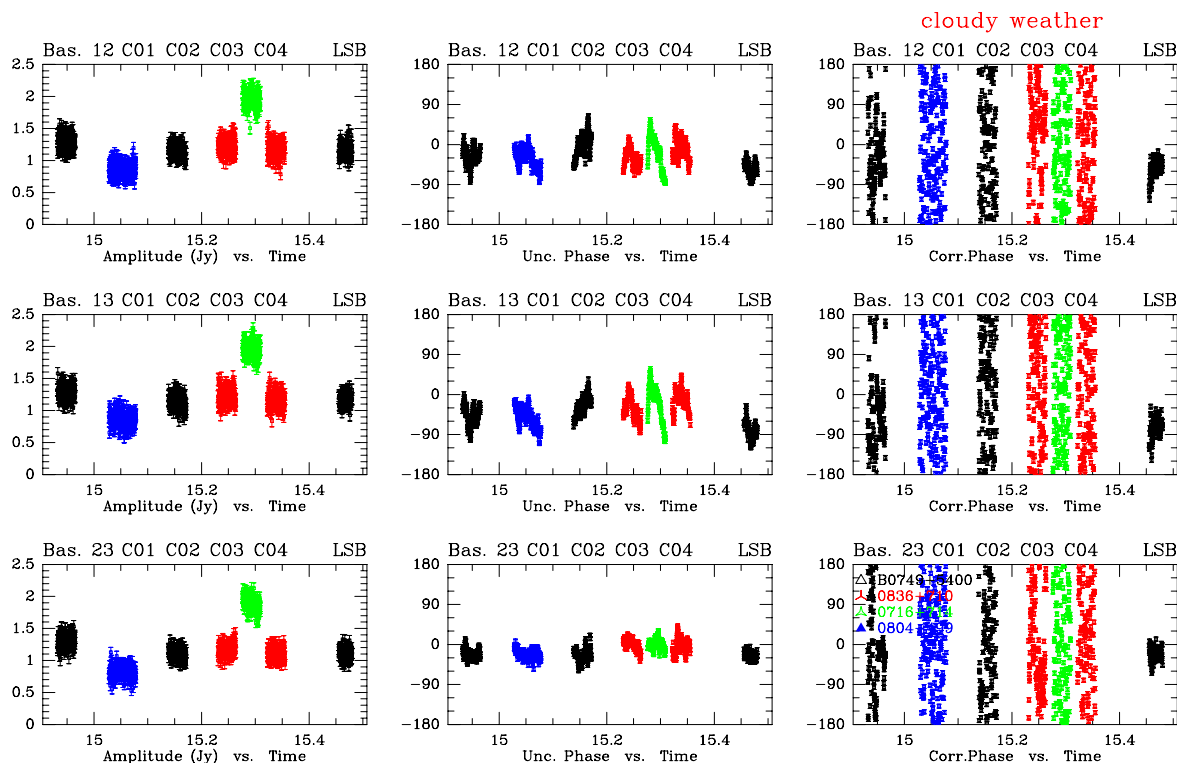


Figure 11.6: Baseline based amplitudes, uncorrected phase and monitor corrected phase at 86.2 GHz for a cloudy data section. The clear sky model over-estimates the correction and would result in serious amplitude loss. The off-line data reduction software will identify those parts and disable the correction there.

11.6 Phase correction during off-line data reduction

In a typical data reduction session, the atmospheric phase correction hides behind two unobtrusive buttons (Fig.11.7). The default of the PHCOR button will calculate the phase correction on a scan basis, i.e. only the corrected amplitudes will be used and not the phases. There are two reasons to be cautious about the corrected phases:

- As we have learned from turbulence theory, averages are *not* good in describing data which obey a structure function. Adjusting the monitored phases to zero average can introduce random-like offsets due to slow (large-scale) components of the atmospheric fluctuations. You can only rely on averages if the outer scale of turbulence have passed several times over the instrument. This can be true on your source (typically 20 min integration time), but is doubtful on the calibrators (integrations of typically 3 min). It may work for compact configurations depending on wind speed, i.e. it depends on the weather. There may be an improvement, but it cannot be guaranteed.
- Nearly linear changes in total power can be due to a big water vapor bubble in the atmosphere or a gain drift in the receivers. The first will produce a phase shift, the second will not, and the software cannot tell them apart. In most cases, gain drifts happen when the antenna has just moved a large distance in elevation, as pump friction and liquid helium distribution change with the receiver cabin tilt. Such drifts are invisible in the interferometric amplitude (opacity correction), but the phase correction is more sensitive to them.

The part of related header variables is accessible over

CLIC> VARIABLES MONITOR

Some items are scan-based in time resolution, others can be expanded to a time scale of one second over the total power signal. One can plot the following quantities related to the phase correction:

- ATM_POWER: total power counts of the monitoring receiver
- ATM_REFERENCE: the offsets which are subtracted from ATM_POWER
- ATM_EMISSION: the calibrated sky emission in Kelvin
- ATM_PHASE: the modeled atmospheric phase
- ATM_UNCORRPH: the astronomical phase uncorrected from atmosphere
- ATM_CORRPH: the astronomical phase corrected with the model
- ATM_VALIDITY: 0 or 1 whether the phase correction has been declared valid or not. This flag is antenna specific.

In order to check the validity of the phase correction, the standard reduction runs the command

CLIC> STORE CORRECTION AUTO 15

i.e. CLIC will test the phase calibrator observations (type P) if the application of the phase correction improves or degrades the amplitudes, and will declare the correction on source observations (type O) in a ± 15 minutes time window for good.

Apart from AUTO, one can use GOOD and BAD for a manual override of the diagnostics, and SELF to check the amplitude for each scan (indifferent to type O or P) for strong sources.

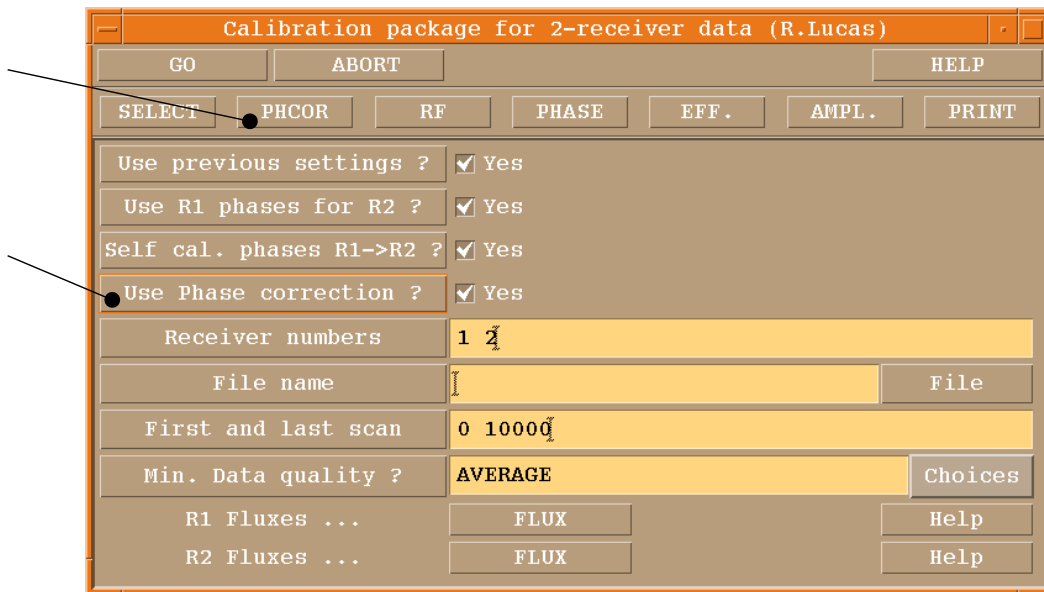


Figure 11.7: The CLIC calibration package menu, with phase correction related items marked.

11.7 Frequently asked questions

- **How often is the phase correction applied?** Statistics have been calculated for all receiver 1 CORR scans in the preliminary data reduction files between September 1997 and March 1999 (a

total of 3120 hours). Over this period, the phase correction was diagnosed “good” during 78.8% of the observing time.

- **Does one gain something on a self calibrated source?** Yes, the monitor corrected spectra are improved on a sub-scan scale, i.e. on one second. An example for this case can be found in Fig. 11.5.
- **How fast can the phase change?** Phases at 3 mm can turn by more than 360° over 30 seconds. Even under calm conditions, it was found that a time resolution of one second for the correction gave better results than an average correction over four seconds.
- **Is dry weather the same as low phase noise weather?** Unfortunately not. Even with 3mm precipitable water, one can have very bad phases if the wind is high (about 10 m/s).
- **Why is the phase correction sometimes disabled under clear sky conditions?** Each correction system has its intrinsic noise. If the atmospheric phase noise is below 10° at 3 mm or 30° at 230 GHz (which happens under stable winter conditions), the added noise will undo the benefits, and the diagnostics will switch the correction off. The same can happen under less favorable conditions if a receiver has an unstable total power signal (this can happen at some frequencies).
- **How does the corrected phase depend on baseline length?** Basically, it becomes independent. Over time scales longer than the monitor time interval, the structure function dependence stays.
- **Are there still changes / improvements in the system?** Yes, we are working on it.

Chapter 12

Amplitude and Flux Calibration

Anne Dutrey^{1,2}

Anne.Dutrey@obs.ujf-grenoble.fr

¹ IRAM, 300 rue de la Piscine, F-38406 Saint Martin d'Hères, France

² LAOG, BP53, F-38041 Grenoble Cedex 9, France

Calibration compensates for imperfections and unknowns in the instrument use, including antenna defects (surface quality, focus), pointing errors, atmospheric transmission and fluctuations, receiver and backend gain and instabilities, etc...All of them are varying in time. In addition, calibrated data are also expressed in a reliable physical unit.

This lecture is then cut in three parts, of equal importance:

1. The single-dish calibration of the amplitude: its errors and biases
2. The flux density calibration which gives the absolute scale of the data
3. The temporal amplitude calibration of interferometric data

12.1 Definition and Formalism

From Lucas lecture (Chapter 9), Eq. 9.1, the baseline-based observed visibility $\tilde{V}_{ij}(t)$ is linked to the true visibility V_{ij} of the source by:

$$\tilde{V}_{ij}(t) = \mathcal{G}_{ij}V_{ij} + \epsilon_{ij}(t) + \eta_{ij}(t) \quad (12.1)$$

In antenna-based calibration, \mathcal{G}_{ij} can also be written as:

$$\mathcal{G}_{ij} = g_i(t)g_j^*(t) = a_i(t)a_j(t)e^{i(\phi_i(t)-\phi_j(t))} \quad (12.2)$$

Hence, for antenna i , the antenna-based amplitude correction for the lower sideband a_i^L is given by

$$a_i^L(t) = T_{cal,i}^L(t)G_i^L(\nu, t)\Gamma_i(t) \quad (12.3)$$

and for the upper sideband:

$$a_i^U(t) = T_{cal,i}^U(t)G_i^U(\nu, t)\Gamma_i(t) \quad (12.4)$$

where $T_{cal,i}^U$ and $T_{cal,i}^L$ are the corrections for the atmospheric absorption (see Chapter 10), in the upper and lower sidebands respectively. Γ_i the antenna gain (affected by pointing errors, defocusing, surface status and systematic elevation effects). Note that Eqs.12.3-12.4 do not include the decorrelation factor f (see Chapter 9 by R.Lucas) because this parameter is baseline-based. We assume here decorrelation is small enough, i.e. $f = 1$; if not, a baseline-based amplitude calibration may be required.

$G_i^L(\nu, t)$ and $G_i^U(\nu, t)$ are the electronics gains (IF chain+receiver) in the lower and upper sidebands, respectively. The receiver sideband gain ratio is defined as $G_i^{UL}(\nu, t) = G_i^U(\nu, t)/G_i^L(\nu, t)$. The sideband gain ratio is to first order independent of the frequency ν within the IF bandwidth. The derivation of the receiver gains is given in Chapter 9. At Bure, the receivers and the IF chain are very stable and these values are constant with time (and equal to G_i^{UL} , G_i^U and G_i^L , respectively, since we also neglected their frequency dependence within the IF bandwidth). They are measured at the beginning of each project on a strong astronomical source. Moreover in Eq.12.3-12.4, we use the fact that for a given tuning, only the receiver gains and the atmospheric absorption have a significant dependence as a function of frequency.

Section 12.2 will focus on the corrections for the atmospheric absorption ($T_{cal,i}^U(t), T_{cal,i}^L(t)$) and the possible biases they can introduce in the amplitude.

In the equations above, the amplitudes can be expressed either in Kelvin (antenna temperature scale, T_A^* , $\eta_f = \eta_b$) or in Jy (flux density unit, $1 \text{ Jy} = 10^{-26} \text{ W m}^{-2} \text{ Hz}^{-1}$). The derivation of the conversion factor between Jy and K, in Jy/K, \mathcal{J}_{iS} (single-dish mode) and \mathcal{J}_{iI} (interferometric mode) and its biases will be detailed in section 12.3 which is devoted to the flux density calibration.

Finally Section 12.4 will deal with the understanding of the terms $\Gamma_i(t)$ and f , the amplitude calibration of interferometric data.

12.2 Single-dish Calibration of the Amplitude

The goal of this part of the calibration is to measure the atmospheric transparency above each antenna.

This calibration is done automatically and in *real-time* but it can be redone *a posteriori* if one or several parameters are wrong using the CLIC command `ATMOSPHERE`. However, for 99 % of the projects, the single-dish calibration is correct. Moreover, we will see in this section that in most cases, even with erroneous calibration parameters, it is almost impossible to do an error larger than $\sim 5\%$.

For details about the properties of the atmosphere, the reader has to refer to Chapter 11 while the transmission of the atmosphere at mm wavelengths is described in Chapter 10. Most of this lecture is extracted from the documentation ‘‘Amplitude Calibration’’ by [Guilloteau 1990] for single-dish telescope and from [Guilloteau et al. 1993].

Since all this part of the calibration is purely antenna dependent and in order to simplify the equations, the subscript i will be systematically ignored. In the same spirit, the equations will be expressed in T_A^* scale taking $\eta_f = \eta_b$ (see [Guilloteau 1990]).

The atmospheric absorption (*e.g.* for the lower side-band T_{cal}^L) can be expressed by

$$T_{cal}^L = \frac{(T_{load}(1 + G^{UL}) - T_{emi}^L - G^{UL}T_{emi}^U)}{\eta_f e^{-\tau^L / \sin(Elevation)}} \quad (12.5)$$

where T_{load} is the hot load and T_{emi}^L and T_{emi}^U are the noise temperature received from the sky in the lower and upper sidebands respectively (for the IRAM interferometer, the difference in frequency between the upper and lower sidebands is $\sim 3 \text{ GHz}$).

The system temperature T_{sys} is given by:

$$T_{sys}^L = T_{cal}^L \times \frac{M_{atm}}{M_{load} - M_{cold}} \quad (12.6)$$

The main goal of the single-dish calibration is to measure T_{cal} (hence T_{sys}) as accurately as possible.

At Bure, during a standard atmospheric calibration, the measured quantities are:

- Phase 1, M_{atm} : the power received from the sky
- Phase 2, M_{load} : the power received from the hot load
- (Phase 3), M_{cold} : the power received from the cold load

T_{rec} , the noise temperature of the receiver, is deduced from the measurements on the hot and cold loads at the beginning of each project and regularly checked. The phase 2 (hot load) is also not systematically done (this remains valid because temperature drifts on the hot load are on timescales of several hours). The receiver sideband ratio G^{UL} is also measured at the beginning of each project (see Chapter 9). T_{emi} , the effective temperature seen by the antenna, is given by

$$T_{emi} = \frac{(T_{load} + T_{rec}) \times M_{atm}}{M_{load}} - T_{rec} \quad (12.7)$$

Moreover, T_{emi} which is measured on the bandwidth of the receiver, can be expressed as the sum of T_{emi}^L and T_{emi}^U (a similar expression exists for T_{sky}):

$$T_{emi} = \frac{T_{emi}^L + T_{emi}^U \times G^{UL}}{1 + G^{UL}} \quad (12.8)$$

T_{emi} is directly linked to the sky temperature emissivity (or brightness temperature) T_{sky} by:

$$T_{sky} = \frac{T_{emi} - (1 - \eta_f) \times T_{cab}}{\eta_f} \quad (12.9)$$

where T_{cab} is the physical temperature inside the cabin and η_f , the forward efficiency, which are both known (or measurable) quantities.

Our calibration system provides then a direct measurement of T_{emi} and hence of T_{sky} , which is deduced from quantities accurately measured. Hence, in Eq.12.5 the only unknown parameter remains τ^L , the opacity of the atmosphere at zenith, which is iteratively computed together with T_{atm} the physical atmospheric temperature of the absorbing layers. This calculation is performed by the atmospheric transmission model ATM (see Chapter 10) and the documentation ‘‘Amplitude Calibration’’).

The opacity τ^L (or more generally τ_ν) comes from two terms:

$$\tau_\nu = A_\nu + B_\nu \times w \quad (12.10)$$

A_ν and B_ν are the respective contributions to O_2 and H_2O , the water vapor content w is then adjusted with T_{atm} by the model ATM to match the measured T_{sky} . The ATM model works as long as the hypothesis done on the structure of the atmosphere in plane-parallel layers is justified, as it is usually the case for standard weather conditions.

12.2.1 Low opacity approximation and implication for T_{cal}

When the opacity of the atmosphere is weak ($\tau_\nu < 0.2$) and equal in both image and signal bands, T_{cal} is mostly dependent of T_{atm} and both of them can be considered as independent of τ_ν and hence w .

In the conditions mentioned above, τ_ν can be eliminated from Eq.12.5. The equation becomes:

$$T_{cal}^L = \frac{\eta_f \times (1 + G^{UL}) \times T_{atm}}{\eta_b \times (1 - \eta_f \times \frac{T_{cab} - T_{atm}}{T_{cab} - T_{emi}^L})} = \frac{(1 + G^{UL}) \times T_{atm}}{(1 - \eta_f \times \frac{T_{cab} - T_{atm}}{T_{cab} - T_{emi}^L})} \quad (12.11)$$

(details about the derivation of Eq.12.11 are given in the documentation ‘‘Amplitude Calibration’’ by S.Guilloteau). In Eq.12.11, the unknown is T_{atm} , the physical temperature of the absorbing layers. T_{atm} is mostly dependent on the outside temperature, pressure and site altitude and weakly on τ_ν . For this reason, T_{cal} and T_{sys} remain correct even if w and hence τ_ν are not properly constrained.

Item	T_{cab}	T_{rec}	η_f
Typical Error	2 K	10 K	0.01
Induced variation (in %)	0.7	0.3	1.3

Table 12.1: Percentage error on amplitude scale introduced by erroneous input parameters.

Figures 12.1 and 12.2 illustrate this point. Thick lines correspond to the exact equation (Eq.12.5) and dashed lines to the approximation (Eq.12.11). The comparison between Eq.12.11 and 12.5 was done for three common cases 1) at 87 GHz, with $G^{UL} = 10^{-2}$, 2) at 115 GHz, with $G^{LU} = 0.5$ and at 230 GHz, with $G^{UL} = 0.5$. For the 15-m dishes, the forward efficiencies used are $\eta_f = 0.93$ at 3 mm and $\eta_f = 0.89$ at 1.3 mm. Fig.12.1 is done for a source at $elevation = 20^\circ$ and Fig.12.2 for a source at $elevation = 60^\circ$.

The following points can be deduced from these figures:

1. As long as $T_{sky}^L = T_{sky}^U$, the equation 12.11 remains valid even at high frequencies > 200 GHz and for $w > 5$ mm.
2. This comes from the fact the T_{atm} is mostly independent of the atmospheric water vapor content.
3. As soon as $T_{sky}^L \neq T_{sky}^U$, the equation 12.11 is not valid. Note also that the error is about constant with the opacity because T_{atm} is mostly independent of the atmospheric water vapor content. Moreover at 115 GHz, the atmospheric opacity is dominated by the 118 GHz Oxygen line and cannot be below 0.2 and the amount of opacity added by the water vapor is small. T_{cal} remains mostly constant with w .

At mm wavelengths, the derivation of the T_{cal} (or T_{sys}) using an atmospheric model is then **quite safe**.

12.2.2 Absolute errors on T_{cal} due to instrumental parameters

The equations above show that T_{cal} is also dependent of the instrumental parameters T_{rec} , η_f and T_{load} . These parameters can also lead to errors on T_{cal} . Derivatives of the appropriate equations are given in the IRAM report ‘‘Amplitude Calibration’’. Applying these equations and taking $T_{atm} = 240$ K, $T_{load} = 290$ K and $T_{emi} = 50$ K, the possible resulting errors are given in the table 12.1.

As a consequence, the most critical parameter of the calibration is the Forward Efficiency η_f . This parameter is a function of frequency, because of optics surface accuracy, but also of the receiver illumination. If η_f is underestimated, T_{sky} is underestimated and you may obtain anomalously low water vapor content, and vice-versa.

The sideband gain ratio G^{UL} is also a critical parameter. G^{UL} is not only a scaling factor (see Eq.12.5), but is also involved in the derivation of the atmospheric model since the contributions from the atmosphere in image and signal bands are considered. This effect is important only if the opacities in both bands are significantly different, as for the J=1-0 line of CO.

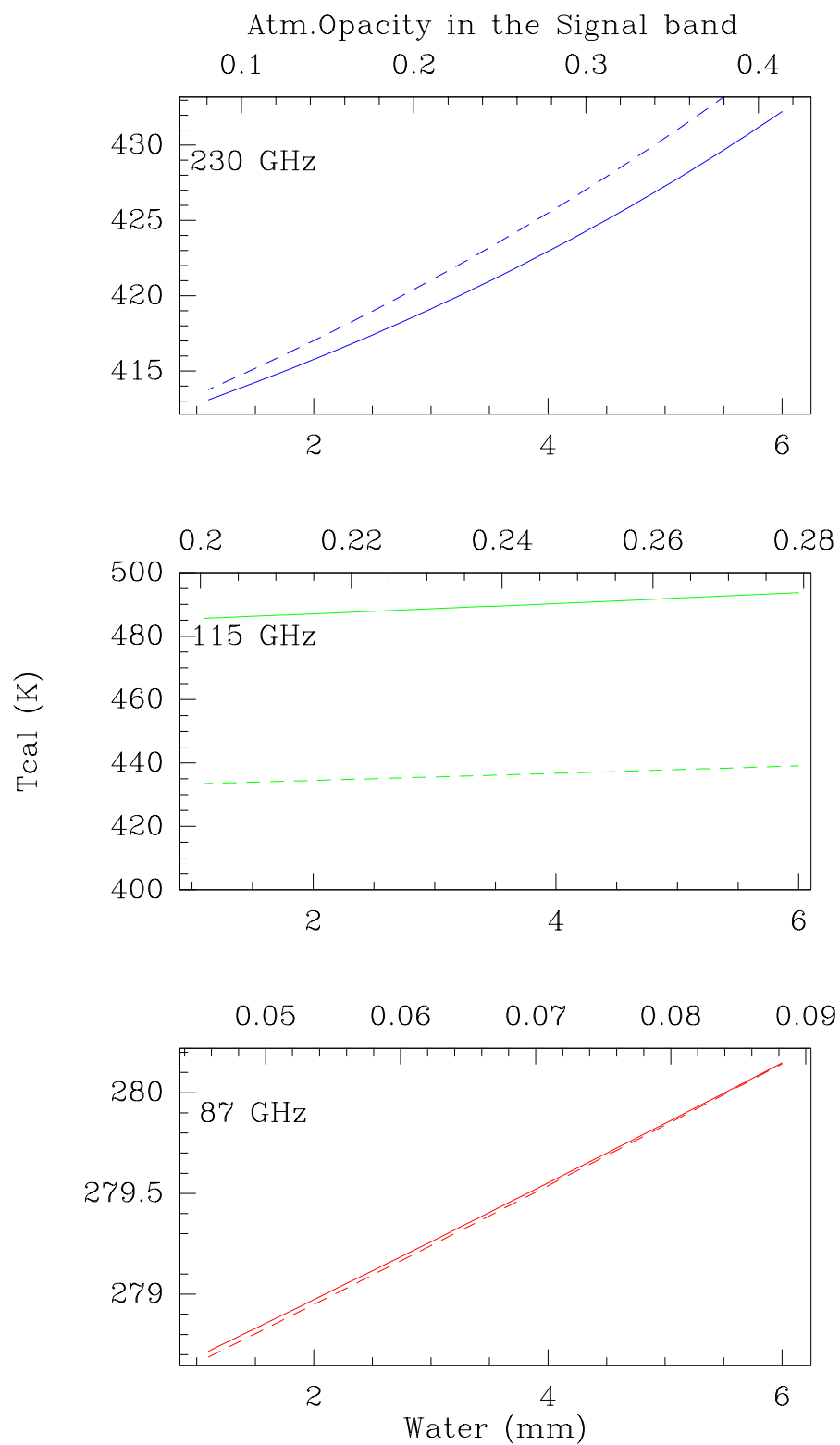
Eq.12.5 shows that as soon as the receivers are tuned in single side band ($G^{UL} < 10^{-2}$ or rejection > 20 dB), the effect on T_{cal}^L is insignificant. Errors can be significant when the tuning is double-side band with values of G^{UL} around $\sim 0.8 - 0.2$. For example, when the emissivity of the sky is the same in both bands ($T_{sky}^U = T_{sky}^L$), the derivative of Eq.12.8 shows that an error of 0.1 on $G^{UL} = 0.5$ leads to $\frac{\Delta T_{cal}}{T_{cal}} \simeq \frac{dG^{UL}}{1+G^{UL}} \sim 6.5\%$.

However, this problem is only relevant to single-dish observations and should not happen in interferometry because as soon as three antennas are working, G^{UL} can be accurately measured (see Chapter 9). At Bure the accuracy on G^{UL} is better than about 1 % and the system is stable on scale of several hours.

12.2.3 Relative errors or errors on T_{cal}^L/T_{cal}^U

Following Eq.12.5, the side band ratio will be affected by the following term:

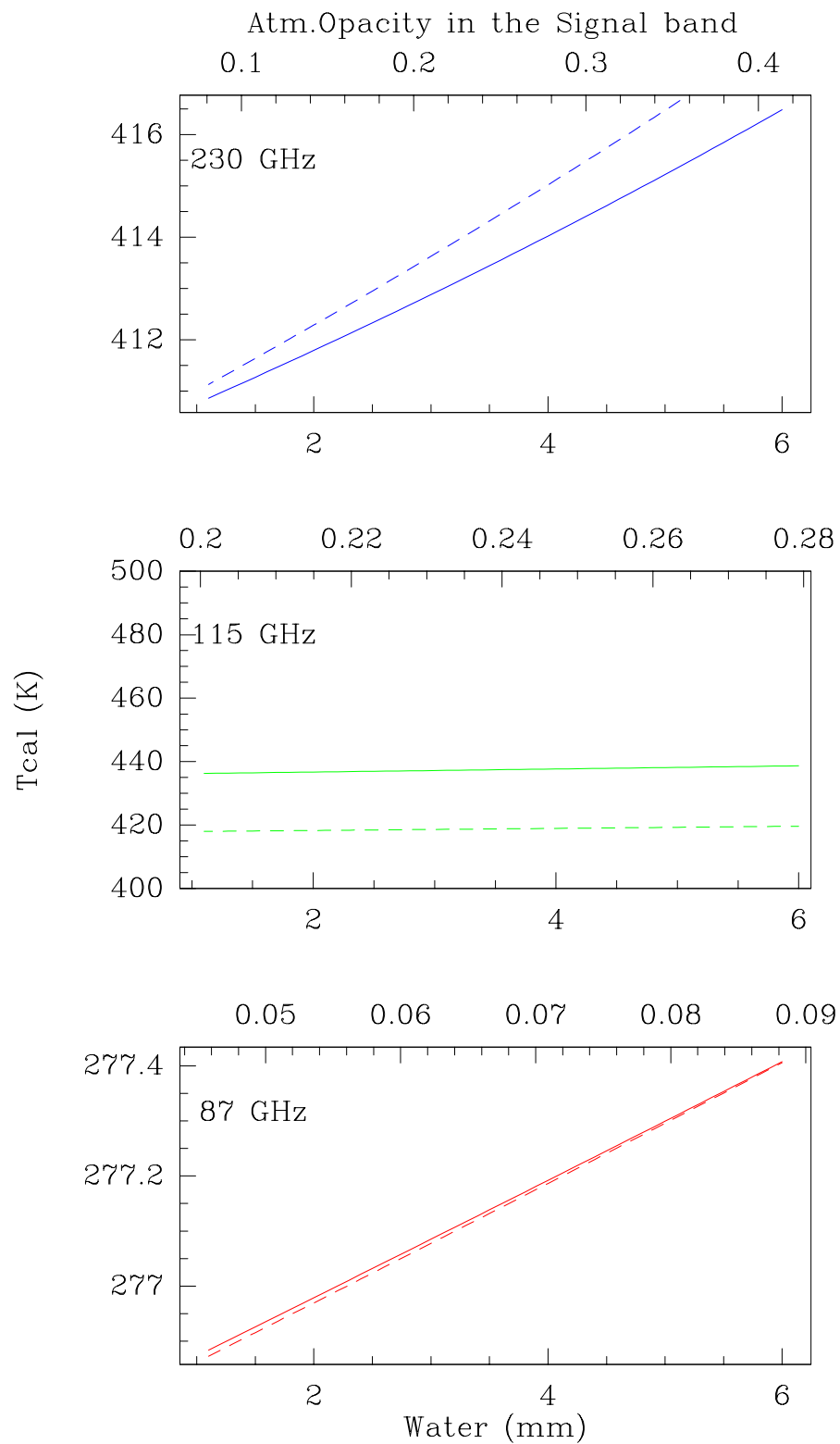
$$T = \frac{e^{(\Delta(\tau^L - \tau^U))}}{\sin(Elevation)} \quad (12.12)$$



Bure Antennas

Elevation = 20°

Figure 12.1: Calibration temperature as function of water vapor (or opacity) at 87, 115 and 230 GHz for a source at 20 degrees elevation. Parameters are taken for the Bure interferometer (see text). Thick lines correspond to the exact equation (Eq.12.5) and dashed lines to the approximation (Eq.12.11).



Bure Antennas

Elevation = 60°

Figure 12.2: Calibration temperature as function of water vapor (or opacity) at 87, 115 and 230 GHz for a source at 60 degrees elevation. Parameters are taken for the Bure interferometer (see text). Thick lines correspond to the exact equation (Eq.12.5) and dashed lines to the approximation (Eq.12.11).

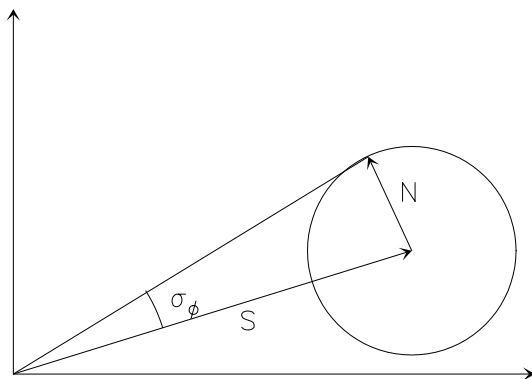


Figure 12.3: Phase error resulting from limited S/N ratio. $\sigma_\phi \approx 1/(S/N)$.

where $\Delta(\tau^L - \tau^U)$ is the error on the sideband zenith opacity difference. This difference is maximum at frequencies corresponding to a wing of an atmospheric line, for example when observing around 115 GHz, near the O₂ line at 118 GHz. As example, taking the frequencies of 112 and 115 GHz for a source at 20° in elevation and a zenith opacity difference $(\tau^L - \tau^U) = 0.150$, an error of 0.030 on this difference (coming from A_ν) will give an error of less than 1% on the gain G^{UL} . Moreover errors on Oxygen lines are very unlikely because the content in Oxygen in the atmosphere is relatively well known and only varying with the altitude of the site.

At the same frequencies, an error of 5 mm (which would be enormous) on the water vapor content will only induce an error of 1% on the gain. Around such low frequency and for small frequency offsets, the water absorption is essentially achromatic. Improper calibration of the water vapor fluctuations will then result in even smaller errors since this is a random effect.

12.2.4 Estimate of the thermal noise

The resulting thermal noise is given by

$$1\sigma = \frac{2kT_{sys}}{\eta A \sqrt{\Delta\nu \times t}} \text{ (K)} \quad (12.13)$$

where k is the Boltzmann's constant, A is the geometric collecting area of the telescope, η the global efficiency factor (including decorrelation, quantization, etc...), $\Delta\nu$ the bandwidth in use and t the integration time. The resulting error on the phase determination is inversely proportional to the signal to noise ratio, as shown in Fig.12.3.

12.3 Flux Calibration (visitor's nightmare)

More details are found in the documentation "Flux measurement with the IRAM Plateau de Bure Interferometer"¹ by A.Dutrey & S.Guilloteau.

12.3.1 Introduction

Because of the focus and pointing errors, and possible drifts in receiver gains, amplitude calibration has always been difficult at mm wavelengths. In addition to these basic single-dish effects, the variable amount of decorrelation introduced by phase noise (atmospheric and/or instrumental) make it difficult, if not impossible, for an interferometer to measure absolute flux densities.

All measurements need to be relative to some source of known flux. In practice, planets are used because they are among the few astronomical objects sufficiently strong at millimeter wavelengths for which flux density predictions are possible and sufficiently accurate. They are then used as primary calibrators to

¹<http://iram.fr/PDBI/flux/flux.html>

Antenna number	3 mm efficiency (Jy/K)	1.3 mm efficiency (Jy/K)
1	22	37
2	21	27
3	21	36
4	21	29
5	22	34

Table 12.2: Conversion factor from K to Jy for the 15-m antennas of Plateau de Bure

bootstrap the flux of the stronger quasars which are point sources. Since the quasars are highly variable, a regular monitoring (each month) is needed. These observations require a very good weather with a small amount of precipitable water vapor (< 4 mm) and a stable atmospheric phase. If not properly taken into account, the quasar variability can produce an error in the flux scale during one configuration which does not result in a simple scale factor in the final image, but introduces artifacts.

12.3.2 Calibration procedure at Bure

Some basic points Because of the physics of quasars, the spectral index may be variable with time as the source intensity. Simultaneous measurements at 2 frequencies are thus needed to estimate it accurately, IRAM instruments (30-m and PdBI) use the frequencies of 86.7 GHz and 228 GHz. At the 30-m, flux density measurements are done during the pointing sessions while they are performed in special sessions at Bure, usually after baseline measurements.

The results of the flux sessions are regularly reduced and published in an internal report (usually each 4 months). These reports are currently available on the web, in the local IRAM page (see²).

How we proceed at Bure In practice, it is impossible (and not necessary) to follow all the quasars used as amplitude calibrator at the IRAM interferometer. Monitoring of the RF bandpass calibrators which are strong quasars with flux density > 2 Jy (no more than 4-8 sources) is enough. In the meantime, planets are observed as primary calibrators. These sessions require to calibrate the atmosphere (T_{sys}) on each source and to check regularly the focus.

At the Bure interferometer, the flux density measurements on quasars are done by pointings in interferometric mode. Pointings on planets are actually done in total power mode because they are resolved by interferometry and strong enough. Total power intensity is not affected by the possible decorrelation due to atmospheric phase noise. However, it is then necessary to accurately determine the efficiencies of the individual antennas (conversion factor in Jy/K) in interferometric mode (\mathcal{J}_I) and in single-dish mode (\mathcal{J}_S).

Determining the antenna efficiencies (Jy/K) For each flux session, \mathcal{J}_S is measured on planets by comparison with the models (see GILDAS programs ASTRO or FLUX).

For a given antenna, the interferometric efficiency \mathcal{J}_I is always $\geq \mathcal{J}_S$. Pointing measurements in interferometric mode are not limited by the atmospheric decorrelation because the timescale of the atmospheric decorrelation is usually significantly larger than the time duration of the basic pointing integration time ($<$ a few sec). On the contrary, all instrumental phase noise on very short timescale can introduce a significant decorrelation and degrades \mathcal{J}_I . This is what may happen from time to time at a peculiar frequency due to a bad optimization of the receiver tuning.

For example, in the initial 1.3 mm observations, strong decorrelation was introduced by the harmonic mixer of the local oscillator system which degraded \mathcal{J}_I by a factor of 2 – 4 depending of the antennas. This problem has been solved recently. Now at 3 mm, it is reasonable to neglect the instrumental noises and take $\mathcal{J}_I = \mathcal{J}_S$. At 1.3 mm, the new harmonic mixers have been installed only recently and statistics on the site are rare but laboratory measurements show that the loss in efficiency should be small. The Table 12.2 gives the antenna efficiencies \mathcal{J}_S , as measured in flux sessions or by holography. These values

²<http://iram.fr/LI/astro.html>

are the current efficiencies (as of November 1997); older values are given in flux reports. They assume that the focus is optimum and do not include any instrumental phase noise. \mathcal{J}_I agrees usually within 10 % at 3 mm and 15 % at 1.3 mm with \mathcal{J}_S , note that \mathcal{J}_I must be $\geq \mathcal{J}_S$.

Being able to cancel out most of the instrumental phase noise even at 1.3 mm makes the IRAM interferometer a very reliable instrument. It is reasonable to think that, in the near future, the flux calibration will be systematically performed at Bure at the beginning of each project by reference to the antenna efficiencies. This is indeed already the case: after pointing and focusing, we systematically measure the flux of calibrators when starting a new project (data labeled FLUX in files). Up to now, for typical weather conditions, most (more than 90 %) of the flux measured at 3 mm are correct within 10 % and more than 60 % at 1.3 mm are within 15 %.

CRL 618 and MWC 349 as secondary flux calibrators Finally, for each project, a complementary flux check is systematically done using the continuum sources CRL 618 or MWC 349 (pointing + cross-correlations). However these sources must be used with some caution. CRL 618 is partially resolved in A and B configurations at 3 mm and in A,B,C at 1.3 mm. Moreover it has strong spectral lines which may dominate the average continuum flux; this must be checked before using it for flux estimates. MWC 349 is unresolved and remains a reliable reference in all antenna configurations. The only strong lines for MWC 349 are the Hydrogen recombination lines. The adopted flux densities are:

For CRL618 (see flux reports 13 and 15):

- CRL618 F(87 GHz) = 1.55 Jy (+/- 0.15)
At 87 GHz, the flux density of CRL 618 (free-free emission from the HII region) has increased since 1990 (where it was ~ 1.1 Jy instead of 1.55 Jy).
- CRL618 F(231.9 GHz) = 2.0 Jy (+/- 0.3),
from [Martin-Pintado et al. 1988]. Since the flux density has increased at 87 GHz, this value needs to be observationally confirmed. Beware of the line contamination which can be high in CRL618.

For MWC349:

- Spectrum of MWC349 $F(\nu) = 1.69(\nu/227 \text{ GHz})^{0.6}$
- MWC349 F(87 GHz) = 0.95 Jy
- MWC349 F(227 GHz) = 1.69 Jy

These values agree within 1 σ with the measurement performed at 87 GHz [Altenoff et al. 1994], (0.87 \pm 0.09 Jy).

12.3.3 Determining the absolute flux scale on a project

The method Fig.12.4 is a printout of the “standard calibration procedure” used in CLIC. This procedure uses the CLIC command SOLVE FLUX which works on cross-correlation only as follows:

1. The flux of the reference source is fixed to $F(\text{Ref})$
2. $F(\text{Ref})$ is used to measure the antenna efficiency by dividing it by antenna temperature of the reference ($T_A^*(\text{Ref})$): $\mathcal{J}_I = F(\text{Ref})/T_A^*(\text{Ref})$
3. \mathcal{J}_I is used to compute the flux of all other sources in the index: $F(\text{source}) = \mathcal{J}_I \times T_A^*(\text{source})$

The flux density of the amplitude calibrators will be used in the final step of the amplitude calibration to fix the flux of the source of astronomical interest.

The practice In the automatic procedure, the reference sources are the calibrators where **Fixed flux** is set to **YES** and the reference values are in the variable **Input Flux**. **Flux in file** corresponds to the value stored with the data (by using the observational command **FLUX**, see Chapter 8 for details). The calculation is performed by clicking on **SOLVE** and the results are displayed inside the variable **Solved Flux**.

If you want to iterate using one of these values as reference, you need to write it in the variable **Input Flux** and set **Fixed flux** to **YES**. Like in the **CLIC** command **SOLVE FLUX**, the individual antenna efficiencies (\mathcal{J}_I) are computed; these values are only averaged values on the time interval using all sources. They are then affected by many small biases like pointing or focus errors and atmospheric decorrelation and they are usually worse than the canonical values given in table 12.2 (for biases, see end of this section).

When you are satisfied by the flux calibration, you need to click on the following sequence of buttons: 1) **Get Results** in order to update the internal variables of the **CLIC** procedure, 2) **Store** to save the flux values inside the header file (**hpb** file) and 3) **Plot** to display the result of your calibration. The plot shows the inverse of the antenna efficiencies ($1/\mathcal{J}_I$) versus time for all selected sources. If the flux calibration is correct, all sources must have the same value *e.g.* $1/\mathcal{J}_I$. This plot is systematically done in mode **amplitude scaled** (written on the top left corner). In this mode, the antenna temperature of each source $T_A^*(source)$ in K is divided by its assumed (variable **Input flux**) flux density $F(source)$ in Jy (the value you have just stored), the result is then $T_A^*(source)/F(source) = 1/\mathcal{J}_I(source)$ which must be the same for all sources and equal to $1/\mathcal{J}_I$. If it is not the case, for example if one source appears systematically lower or higher than the others, this means that its flux is wrong and you need to iterate.

Note that the scan range, applied on all calibrators, which is by default the scan range of the “standard calibration procedure” can be changed. This option is useful when there is some shadowing on one calibrator because the shadowing can strongly affect the result of a **SOLVE FLUX**. If you change the scan range, do not forget to click on **UPDATE**.

12.3.4 Possible biases and remedies

Flux densities are more important than efficiencies In the final amplitude calibration performed on the source (see next section), the flux of the source is determined by reference to the flux of the amplitude calibrator which is usually also the phase calibrator. This means that the averaged efficiencies \mathcal{J}_I computed by **SOLVE FLUX** and the automatic procedure are not directly used and in many case variations of \mathcal{J}_I does not affect the accuracy of the final amplitude calibration because they are corrected. It is then fundamental to have a good estimate of the flux of the amplitude calibrator but not necessarily to know precisely the averaged \mathcal{J}_I .

Possible biases Using the automatic procedure, the following biases may occur:

1. There is some shadowing on the reference source. The estimate of the \mathcal{J}_I can then be wrong: use another reference.
2. One or several antennas are off focus: \mathcal{J}_I is larger than \mathcal{J}_S but flux densities can still be correct if there is no significant focus drift during the time interval used to measure the fluxes. If the data are affected by a significant focus drift, this also affects the accuracy of the flux measurements. Depending of the observation time of the reference and of the sources, the estimated flux densities can be either too low (reference taken at the beginning when the focus is correct, sources at the end when the focus is off) or too high (opposite situation). In both cases, it is necessary to check the focus (or have a look at the **show.ps** file). If no drift occurs, the measured fluxes are correct. If a drift occurs, the flux calibration must be done on a smaller interval of time where the focus drift remains negligible.
3. The pointing on the reference is bad. \mathcal{J}_I is then overestimated implying that the flux of all other sources (with good pointing) is also overestimated. Check the pointing on the possible reference sources (or see the **show.ps** file) and select a better reference.
4. There is a strong atmospheric decorrelation because flux measurements are performed on cross-correlations of about 4 minutes when the atmospheric phase fluctuations are high (check them on

Flux list				
GO	ABORT	HELP		
Solve	Get result	Store	Plot	Calibrate
Receiver: 1 Frequency 110.201 GHz				
Efficiencies:	24.06 22.33 21.91 20.21 22.79			
Scan range ?	0 10000			
Calibrator 0415+379				
Input Flux?	5.508			
Fixed flux?	<input checked="" type="checkbox"/> Yes			
Solved Flux:	5.508			
Flux in File:	5.508			
Calibrator 0528+134				
Input Flux?	2.245			
Fixed flux?	<input type="checkbox"/> No			
Solved Flux:	2.292			
Flux in File:	2.245			
Source CRL618, Model Flux 1.55 Jy				
Input Flux?	1.55			
Fixed flux?	<input type="checkbox"/> No			
Solved Flux:	1.623			
Flux in File:	1.55			

Figure 12.4: User interface of the “standard calibration procedure” of CLIC corresponding to the flux calibration.

an individual cross-correlation taken on a strong quasar *e.g.* the RF calibrator). There are two possibilities: i) when the atmospheric correction works well (as it is usually the case), just apply it to measure the fluxes; ii) if not, the data may be usable at 3 mm by selecting the best scans on a small interval of time but at 1.3 mm data are useless.

5. The interferometric efficiencies \mathcal{J}_I are really very different to \mathcal{J}_S because there is a wonderful mixing of the points mentioned above... Ask to an expert (e.g. your local contact...).

Note that the biases 3) and 4) do not affect flux estimates when they are performed on pointing data (as in sessions of flux measurements).

12.3.5 The program FLUX

This program is not used by the external users of the PdBI but IRAM astronomers to provide reliable flux density of quasars to visitors (see flux reports). A description of the program is given in “Flux measurement with the IRAM Plateau de Bure Interferometer”³ by A.Dutrey & S.Guilloteau

12.4 Interferometric Calibration of the Amplitude

For antenna i , the antenna-based amplitude correction is given by (Eq.12.3 and 12.4).

$$a_i^K(t) = T_{cal_i}^K(t)G_i^K(\nu, t)\Gamma_i(t) \quad (12.14)$$

where $K = U$ or L . The decorrelation factor f (see Chapter 9) is not taken into account here because it is fundamentally a baseline-based parameter.

In a baseline-based decomposition, the complex gain of baseline ij , \mathcal{G}_{ij} is given by:

$$\mathcal{G}_{ij}^K(t) = f \times a_i(t)a_j(t)e^{i(\phi_i(t)-\phi_j(t))} \quad (12.15)$$

and the amplitude of the baseline ij is \mathcal{A}_{ij}

$$\mathcal{A}_{ij}^K(t) = f \sqrt{T_{cal_i}^K T_{cal_j}^K(t)G_i^K(\nu, t)G_j^K(\nu, t)\Gamma_i(t)\Gamma_j(t)} \quad (12.16)$$

We will discuss first the term Γ_i and estimate then the decorrelation factor f , before giving a global scheme of the amplitude calibration.

12.4.1 Correction for the antenna gain $\Gamma_i(t)$

The antenna gain $\Gamma_i(t)$ corresponds to losses due to the antenna, mainly focus (F_i) and pointing (P_i) errors coming from thermal variations of the antenna structure and surface.

$$\Gamma_i(t) = P_i(t) \times F_i(t) \quad (12.17)$$

At Bure, we now check and correct automatically the pointing and the focus each hour. This correction is then done mainly in real time. This has improved a lot the quality of the data at 1.3 mm. However, it is necessary in some cases to add a break in the amplitude (but not in the phase) fitting in order to take into account a focus error or a loss of amplitude due to pointing errors.

Note that an error on the focus of 0.1 mm at 1.3 mm will introduce a phase error of $\frac{4\pi}{\lambda} \times \frac{180}{\pi} \times 0.1 \sim 55^\circ$ and a loss in amplitude of $\sim 3 - 5\%$.

³<http://iram.fr/PdBI/flux/flux.html>

Atmospheric Timescales	Amplitude coherence	Phase correction	Comments
$\Delta t \geq 1 - 2$ hours	No loss	Corrected by temporal phase fitting	Large scales are corrected
$1 \text{ min} \leq \Delta t \leq 1 - 2$ hours 1 min = scan duration	No correction can be partially corrected	rms ($= \Delta\phi$) of temporal phase fit $f = e^{(-\Delta\phi^2/2)}$ Radio Seeing	Loss of flux <i>a-posteriori</i> correction by comparison with some reference sources: images of calibrators of known flux
$\Delta t \leq 1$ min	Usually corrected Radiometric phase correction	“MONITOR 0” \equiv mean value of the phase in 1 min	works usually well except for bad weather conditions

Table 12.3: Useful decomposition of the atmospheric phase fluctuations above the Plateau de Bure interferometer. This qualitative scheme is done to show which timescales are corrected by the calibration of the Bure data and the radiometric phase correction working at Bure.

12.4.2 Estimate of the atmospheric decorrelation factor f

Details about the origin of f are given in Chapter 11. I will discuss here the practical implementation of the atmospheric phase correction done in real-time and in CLIC. More details are given in the IRAM report “Practical implementation of the atmospheric phase correction for the PdBI” by R.Lucas.

The atmospheric phase fluctuations are due to different time varying water vapor content in the line-of-sight of each antenna through the atmosphere. Between antennas i and j , this introduces a decorrelation factor $f \sim e^{-\Delta\phi_{ij}^2/2}$ on the visibility V_{ij} . This term, non-linear, cannot be factorized by antenna. Moreover due to the physical properties of the atmosphere, there are several timescales. One can correct partially some, but not all, of them.

At Bure the basic integration time is 1 second and the scan duration is usually 60 seconds. The radiometric correction works then on timescales of a few seconds to one minute. It corrects only the amplitude: the phase is never changed because phase jumps between individual scans are dominated by instrumental limitations (mainly the receiver stability on a few minutes + ground pickup variations). The implications on the image quality are developed in Chapter 18. Longer atmospheric timescales of about 2 – 8 hours are removed by the spline functions fitted inside the phase and the amplitude.

Intermediate timescales fluctuations from about one minute (the scan duration) to 1 hour are not removed. The resulting rms phase are measured by the fit of the splines in the phase. These timescales are not suppressed by the radiometric correction, and they contribute to the decorrelation factor f (see Eq.12.16), as the main component.

The decomposition of the atmospheric timescales for the PdBI observing method is given in table 12.3.

The method The differences in water vapor content are measurable by monitoring the variations of the sky emissivity T_{sky} . A monitoring of the total power in front of each antenna will then lead to a monitoring of the phase fluctuations. At Bure, we monitor the total power M_{atm} with the 1.3 mm receivers. The variation of T_{sky} , ΔT_{sky} (equal to ΔT_{emi}) is linked to the total power by

$$\frac{\Delta M_{atm}}{M_{atm}} = \frac{(\Delta T_{emi} + \Delta T_{loss})}{T_{sys}} \quad (12.18)$$

The monitoring of the atmospheric phase fluctuation works only when ΔT_{loss} due to the instrumentation is negligible on the timescales at which the phase correction is calculated and applied (typically a few seconds to one minute). Slow drifts on scale of hours have no effects.

With standard atmospheric conditions and following [Thompson et al. 1986] (their Eq.13.20), the variation of the path length through the atmosphere at zenith can be approximated by:

$$\Delta L = 6.3\delta w \quad (12.19)$$

where δw is the variation of water vapor content. ΔL is related to the phase fluctuation ψ_i above the antenna i by

$$\psi_i(t) = \frac{2\pi}{\lambda} \Delta L(t) \quad (12.20)$$

For example, under standard conditions (see fig.12.1 or 12.2), a variation $\delta w = 0.1$ mm corresponds to $\Delta L \simeq 630 \mu\text{m}$, $\Delta T_{sky} \simeq 1.5$ K and $\psi_i \simeq 250^\circ$ at 1.3 mm. This value is enormous and would not allow to produce images of good quality.

To reduce the phase fluctuation to a reasonable value having a negligible impact on the image quality *e.g.* $\psi_i \sim 25^\circ$, one needs to get $\Delta T_{loss} + \Delta T_{sky} \sim 0.15$ K corresponding to a global path length variation of $\sim 60 \mu\text{m}$. For a typical $T_{sys} \sim 150$ K (DSB in the antenna plane, not SSB outside the atmosphere as for astronomical use), the instrumental stability required ($\Delta T_{loss}/T_{sys}$) must then be of order of $\sim 5 \cdot 10^{-4}$.

At Bure, on timescales of a few minutes, ΔT_{loss} is dominated by the stability of the receivers which must be carefully tuned to get the best stability. The 1.3 mm receivers are systematically tuned to get a stability of a few 10^{-4} ; the stability is checked by doing autocorrelations of 60 seconds on the hot load. Achieving the required stability may prove impossible at some frequencies.

Practical implementation Ideally one would like to use T_{emi} measured each second on each antenna to compute $\psi_i(t)$ and correct the measured baseline phases. Practically, it is not so simple because $\psi_i(t)$ can do many turns and instrumental effects affect the measured T_{emi} .

Instead we use a differential procedure: once the antenna tracks a given source, one calibrates the atmosphere to calculate $T_{sys}(t_0)$, $\Delta L(t_0)$ and $\Delta L/dT_{sky}(t_0)$. Phase corrections are then referenced to t_0 .

$$\Delta\psi_i = \frac{2\pi}{\lambda} \frac{d\Delta L}{dT_{emi}} \frac{T_{sys}(t_0)}{M_{atm}(t_0)} (M_{atm}(t) - M_{atm}(\text{Ref})) \quad (12.21)$$

where $M_{atm}(\text{Ref})$ is chosen in order to minimize as much as possible all the slow effects contributing to ΔT_{loss} . A long term atmospheric effect can also be included in $M_{atm}(\text{Ref})$ because these effects are not removed by the radiometric phase correction but by the traditional phase referencing on a nearby calibrator. The main steps are the following:

1. The total power M_{atm} is continuously monitored on calibrators and on sources (every second).
2. Using the standard calibration method (see first part of the lecture) M_{atm} and T_{emi} (measured each second) are used to compute T_{sky} and w .
3. The atmospheric model has also been upgraded to compute the path length ΔL and its derivative $d\Delta L/dT_{emi}$. ΔL is computed by integrating the refractive index of the wet air along the line of sight across the atmosphere.
4. Within the 60 seconds scan, the new phase (Eq.12.21) is computed and the correction applied to the amplitude.

Quasi-real Time Calibration For the quasi-real time correction,

- the default value for $M_{atm}(\text{Ref})$ is the measured atmospheric emission at the time of the last calibration, *i.e.* $M_{atm}(\text{Ref}) = M_{atm}(t_0)$.

RF: Uncal. CLIC - 02-AUG-2001 16:50:27 - dutrey N15E10W12W09N05 Scan Avg.
 Am: Abs. 596 4561 G078 0415+379 P CORR 12CO(2-1 5C2 22-MAR-1997 10:43 -5.2 Vect.Avg.
 Ph: Abs. 1072 4920 G078 0415+379 P CORR 12CO(2-1 5C2 22-MAR-1997 16:46 .9

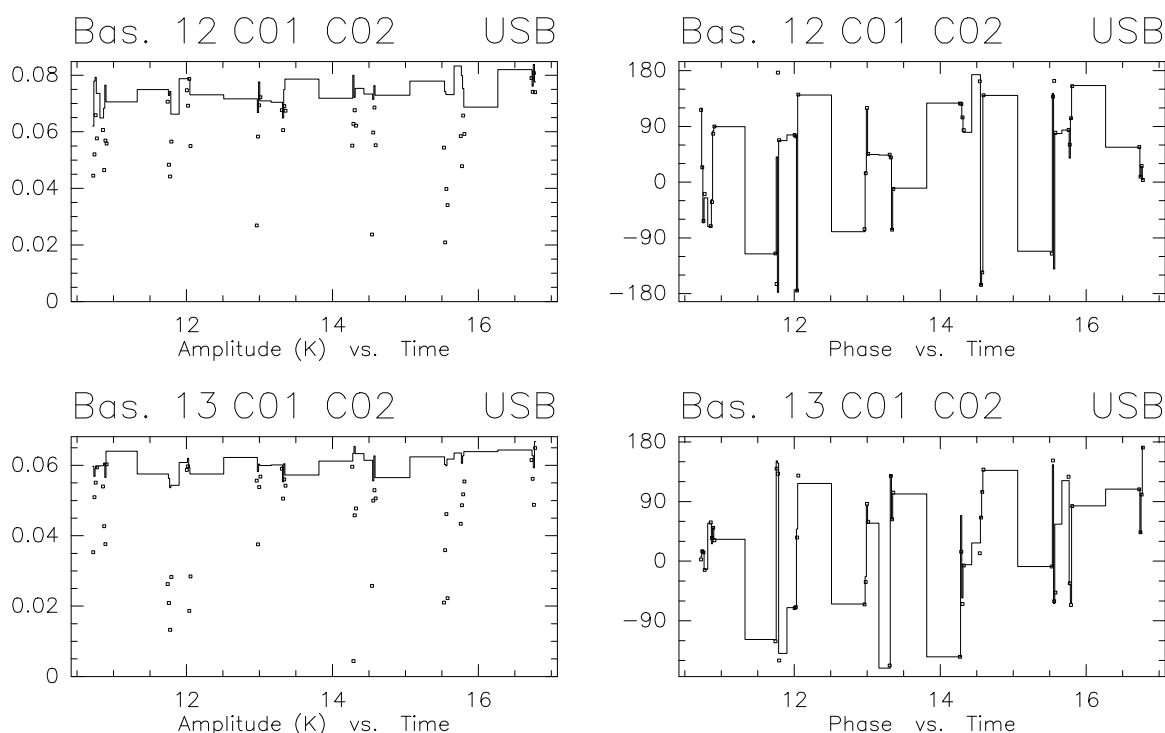


Figure 12.5: The amplitude and phase versus time on baselines B12 and B13 with (histogram) and without (points) the radiometric phase correction. The phase remains unchanged but the amplitude is significantly improved.

Calibrating using CLIC The CLIC command “**MONITOR** [*delta - time*]” allows to re-compute all the parameters. This command is useful when you want to select a better value for $M_{atm}(\text{Ref})$.

- This command is used to prepare the atmospheric radiometric phase correction. It processes the calibration scans to compute the correction factors (i.e. the change of path length for a given change in emission temperature of the atmosphere at the atmospheric monitor frequency (normally 1.3 mm)).
- The scans in the current index are grouped in intervals of maximum duration [*delta - time*] (in seconds); source changes will also be used to separate intervals. In each interval a straight line is fitted in the variation of atmospheric emission as a function of time; this line will be the reference value for the atmospheric correction, i.e. the correction at time t is proportional to the difference between the atmospheric emission at time t and the reference at time t . This scheme is used to avoid contaminating the correction with total power drifts of non-atmospheric origin (changes in receiver noise and gain, and changes in ground noise).
- **MONITOR 0** will use for each scan the average of the atmospheric emission as the reference value (i.e. $M_{atm}(\text{Ref}) = \langle M_{atm}(t) \rangle_{scan}$). This will cause the correction to average to zero in one scan: the average phase is not changed, only the coherence is restored leading to an improved amplitude.

The automatic calibration procedure uses the command **MONITOR 0**.

RF: Fr.(A) CLIC - 03-AUG-2001 15:56:00 - alma W23E23W27E16N29 Scan Avg.
 Am: Rel.(A) 84 4798 G067 0415+379 P CORR HCO+(10) 5A-E24+E23 10-FEB-1997 18:13 -0.3 Vect.Avg.
 Ph: Rel.(A) 335 5026 G067 0415+379 P CORR HCO+(10) 5A-E24+E23 10-FEB-1997 21:53 3.4

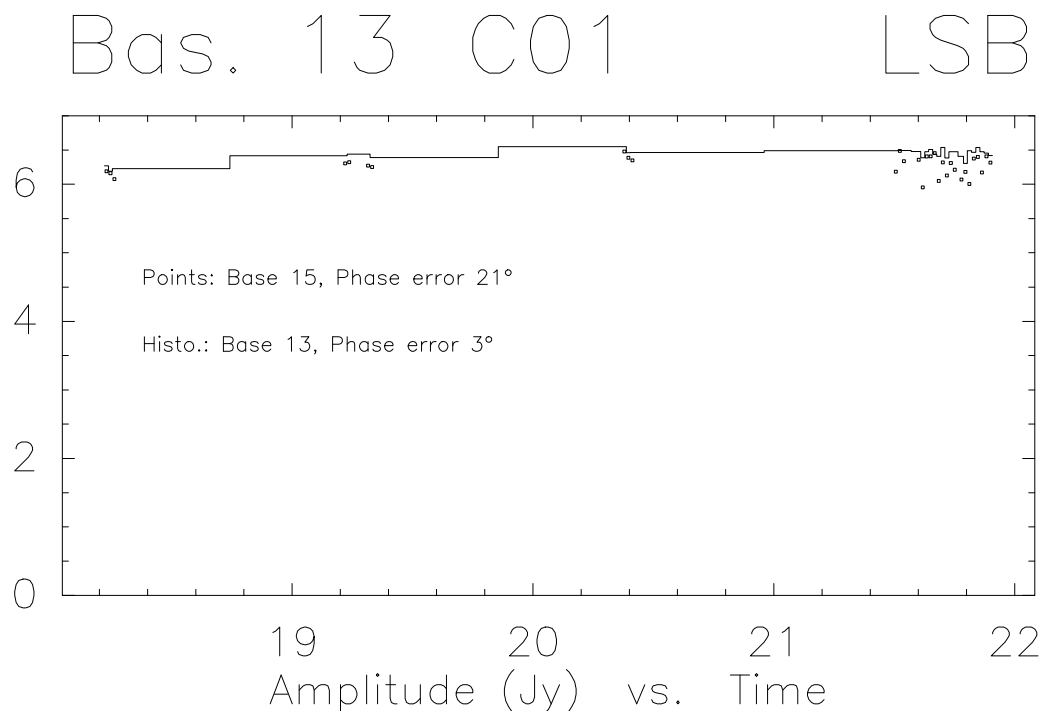


Figure 12.6: Example of calibrated amplitude (Jy) versus time on a short (B13) and a long (B15) baseline. The amplitudes are similar.

12.4.3 Fitting Splines: the last step

In the real-time processing, only the receiver gain and bandpass, the atmospheric transmission and the radiometric correction have been calibrated.

Fitting of the temporal variations of the global antenna gain (the so-called *amplitude calibration*) is performed in CLIC by fitting splines functions with time steps of 3-6 hours (`SOLVE AMPLITUDE [/WEIGHT] [/POL degree] [/BREAK time]`) and can be done either in baseline-based or in antenna-based mode. Note that in the latter case, the averaged amplitude closures are computed, as well as their standard deviations. The amplitude closures should be close to 100%. Strong deviations of amplitude closures from 100% are an indication of amplitude loss on long baselines, due to phase decorrelation during the time averaging. The fit then shows systematic errors; if this occurs, baseline based calibration of the amplitudes might be preferred.

The amplitude calibration involves interpolating the time variations of the antenna gains measured with the amplitude calibrator, assuming the its flux is known. The fitted splines must be as smoothed as possible in order to minimize the errors introduced on the source which is observed in between calibrators.

12.4.4 A few final checks

Once the amplitude calibration curve is stored, one can perform some simple checks on the calibrated data of the calibrator. These checks must be done in Jy (mode “`AMPLITUDE ABSOLUTE RELATIVE`” to the flux density of the calibrator).

RF: Fr.(A) CLIC - 03-AUG-2001 15:53:09 - alma W23E23W27E16N29
 Am: Rel.(A) 84 4798 G067 0415+379 P CORR HCO+(10) 5A-E24+E23 10-FEB-1997 18:13 -0.3
 Ph: Rel.(A) 335 5026 G067 0415+379 P CORR HCO+(10) 5A-E24+E23 10-FEB-1997 21:53 3.4

Scan Avg.
Vect.Avg.

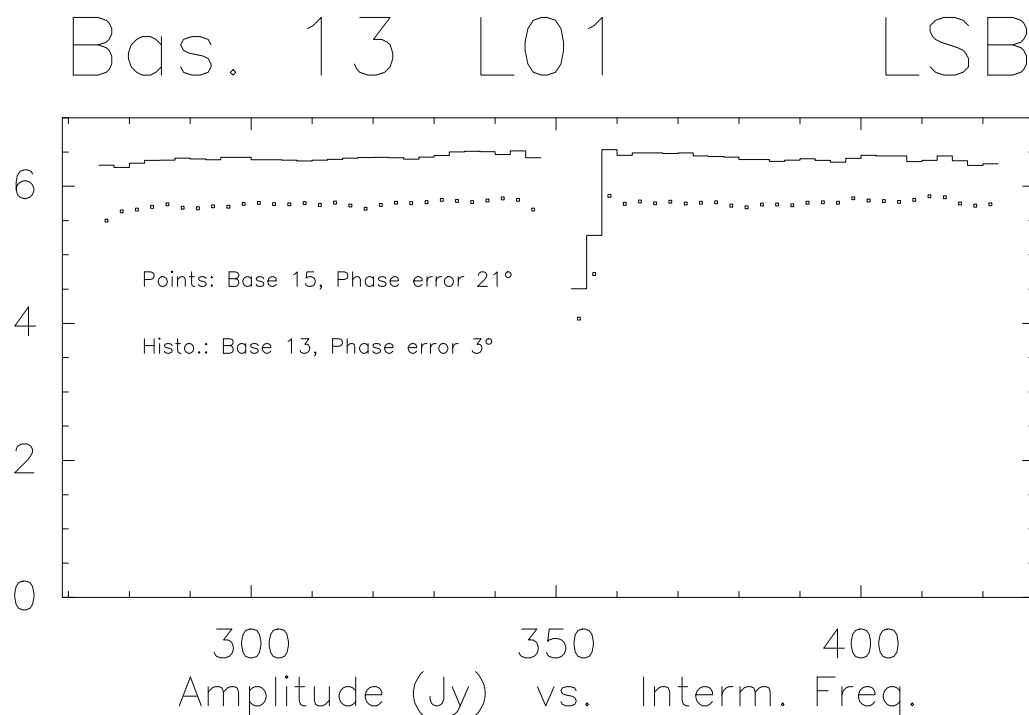


Figure 12.7: Example of calibrated amplitude versus IF frequency on a short (B13) and a long (B15) baseline. There is a significant loss of amplitude on the long baseline. The decorrelation factor is not calibrated out, and varies from short to long baselines. In this case, for the short baseline (B13), the decorrelation is completely negligible (see fig. 12.6).

Amplitude versus time On each baseline, the amplitude curves should be flat and equal to assume the flux density of the calibrator.

Amplitude versus IF frequency On each baseline, the amplitude curves should be flat, but they are not necessarily equal to flux of the calibrator because the decorrelation factor f is not taken into account here. To retrieve the flux density of the calibrator, they must be multiplied by the corresponding $e^{-(\Delta\phi)^2/2}$, where $\Delta\phi$ is baseline rms phase noise determined during the phase calibration.

Chapter 13

Calibration of data in Practice

Anne Dutrey^{1,2} & Roberto Neri¹

Anne.Dutrey@obs.ujf-grenoble.fr & neri@iram.fr

¹ IRAM, 300 rue de la Piscine, F-38406 Saint Martin d'Hères, France

² LAOG, BP53, F-38041 Grenoble Cedex 9, France

13.1 Introduction

13.1.1 Contents of the account

At the first login on a new project account, you should find five directories:

1. **reports**: It contains all the pre-calibration performed by the Astronomer on Duty (AoD) on the site. This subdirectory is in read access only. For a given observing date, you should find the following compressed files: `28-feb-2001-x007.hpb.gz`, the header file containing the calibration curves of the data; `28-feb-2001-x007.ps.gz`, the PostScript file containing the result of this calibration. This file should be carefully read before starting a new calibration. `show-28-feb-2001-x007.ps.gz` is the PostScript file corresponding to a first look of the data. It includes meteo conditions (wind, mm of water, system temperature) but also pointing and focus errors. In many cases, this file can help to interpret dubious data. This file should also be read carefully before starting calibration. The file `x007.note` are notes written by the AoD on the site. This file is updated at each period of observations. It gives important information about the data quality and possible problems.
2. **headers**: It initially contains a copy of reports. Files should be uncompressed and data calibration should be performed in this subdirectory. This is the default directory of CLIC. However before activating CLIC, it is better to move to this subdirectory using the shell command: `“cd /headers”`.
3. **maps**: This subdirectory, empty at the beginning, should contain at the end all the *uv* tables and the maps produced. Using the CLIC procedure `“Write A UV Table”`, the *uv* tables are created by

default in this directory which is also the default directory for GRAPHIC and MAPPING.

4. `tmp/DATA`: This subdirectory contains the raw data files (IPB) and their corresponding log files. In the example presented above, it would contain: `H228X007.IPB`, `H228X007.OBS`, `H228X007.RDI`. Access to this directory and to the raw data files is automatically handled by CLIC.
5. `DATA`: Most of the time this directory is empty. However, it can contain some IPB files and their corresponding log files. Like in the case of `tmp/DATA`, its use is transparent. The reducer does not need to know the exact location of the raw data files on her/his account. CLIC handles it for him/her.

Note that only the directories `reports`, `headers` and `maps` are saved on CDroms by the automatic procedure `savproj`.

13.1.2 Before starting the data reduction

The compressed PostScript files in `headers` containing the calibration curves performed by the AoD must be *gunzipped* and printed. Then, they must be carefully studied in order to determine the general quality of the data and find possible problems which are usually mentioned in the `project.note` file (*e.g.* `x007.note`) written by the AoD during the pre-data reduction process.

13.1.3 Activating the CLIC environment

CLIC is available by typing in the directory `headers`

```
$ CLIC
```

Under CLIC, there are several procedures available:

1. `File`: To open a new header (`hpb`) or data (`IPB`) file
2. `Raw Data File`: To open a raw data file (`IPB`)
3. `Raw Data File Directories`: To define the location of raw data file directories
4. `First Look`: Instrumental and meteorological conditions during the observations (see §2)
5. `Standard Calibration (2 receivers)`: To calibrate raw data (see §3)
6. `Self-Cal on a point source`: To self calibrate the phase
7. `Simple Check`: To do simple checks on the data
8. `Holography Reduction`: To reduce holographic data
9. `Write A UV Table`: To produce the visibility table

Useful procedures to calibrate data are 1) “`First Look`”, 2) “`Standard Calibration (2 receivers)`” and 3) “`Write A UV Table`”.

13.2 The “First Look” procedure

The procedure “`First Look`” provides information about the weather conditions and a few instrumental parameters at the time of the observations. This information is very important as it helps you to make a first data quality assessment even before you may start with the interactive data calibration procedure. The panel of the procedure is shown on Fig.13.1.

Monitoring information is provided on:

- `Meteorology`: the average and maximum wind velocity, the ambient pressure and temperature. Gusty conditions and observations with wind velocities above 10 m/s may show up with high pointing corrections. Take care to tag visibilities which may be affected by such difficult observing conditions.

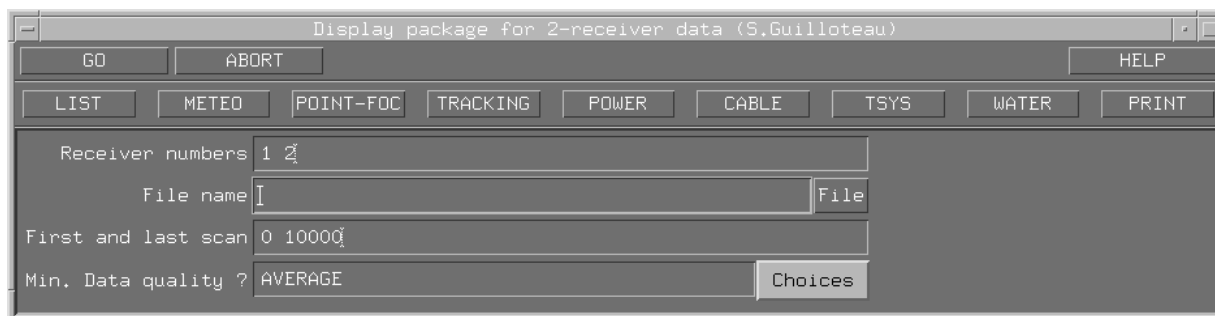


Figure 13.1: “First Look” panel

- **Pointing and Focus:** the applied corrections are shown for all the antennas in the array. Only differential variations in the corrections play a role, not the absolute amount. Sudden pointing corrections by more than $10''$ can considerably spoil the visibilities, especially at the highest observing frequencies. A similar consideration applies for antenna focus corrections, although visibilities are automatically corrected for phase offsets which are generated by focus corrections.
- **Tracking Errors:** The tracking errors in azimuth and in elevation are given for all antennas.
- **Total Power:** a trace of the total incident atmospheric power recorded by the continuum detectors (one for each receiver, each one second), helps in further evaluating the data quality. As a rule, strong and rapid variations in the total power trace the presence of clouds in the line of sight while a sudden up- or down-stepping on one antenna and on one receiver is a sign of a renewed receiver tuning. The total power increases in general with the air mass.
- **Cable Phase:** variations in the electrical length of the cables show up in phase variations (referenced to the LO2 phases). These are measured by a phasemeter. Appropriate corrections for the phases of the LO1 rotators are computed taking n times the corrections measured by the phasemeters of the 3 mm receivers and $3n$ times the corrections measured by the phasemeters of the 1 mm receivers, where n is the harmonic number of the tuned frequency. Strong and rapid variations while a source is tracked may indicate a fault in a cable (these data should perhaps be flagged), whereas a sudden but steady change is mostly related to a shift in the antenna pointing.
- **System Temperature:** dependent on the observing conditions and on the frequency. As for the total power detectors, strong and rapid variations in the system temperature trace atmospheric instability, whereas a sudden but steady change on one receiver is a sign of a renewed receiver tuning.
- **Water vapor:** the content of precipitable water vapor in the atmosphere is a critical parameter on which the quality of most of the high frequency observations depend. Should the measured water vapor content not be consistent (or roughly) on all the high frequency receivers, please check the receiver gain.

Finally, the “First look” procedure produces a short list of all the scans recorded at the time of the execution of a project. Such a listing allows you to trace back the sequence of operations during an observing run. Note that the range of scan validity for the calibration procedure sets up with the last GAIN scan in the short list.

Looking at the results of the procedure (called in the example above `show-28-feb-2001-x007.ps.gz`) should be done simultaneously with the reading of the project.note file (here `x007.note`).

13.3 The “Standard Calibration (2-receivers)” procedure

We describe here, step by step the inputs and actions (or outputs) of the procedure “Standard Calibration (2 receivers)”. The associated panel is given in Fig.13.2.

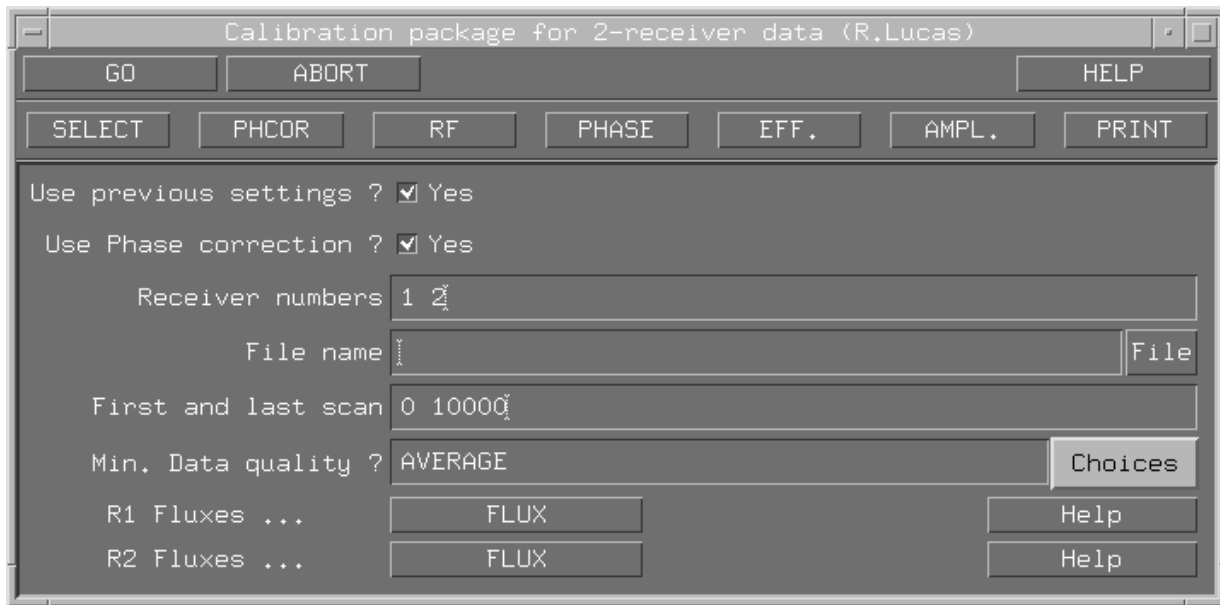


Figure 13.2: “Standard Calibration (2 receivers)” panel

13.3.1 Inputs

On the panel, the reducer should select with the mouse the “File name” of the header file. Other parameters are automatically selected by the procedure if the flag “Use previous settings” is set to YES which is the default. Never change it if your data are correct (no editing). The parameters “First and last scan” are selected automatically when “Use previous settings” is set to YES. The default value for the flag Min. Data quality is AVERAGE. The flag “Use Phase correction” must also be set to the default: YES. The current procedure uses by default the phase calibration of the receiver 1 to calibrate the instrumental phase of the receiver 2 because the experience has shown that it is the most efficient way to proceed (see R.Lucas lecture on phase calibration). Therefore, the calibration of the receiver 2 (1.3 mm) cannot be dissociated from the calibration of the receiver 1 (3 mm) and the flag “Receivers numbers” must be set to 1 2, except when observations were done at 3 mm only.

Finally, the inputs “R1 Fluxes” and “R2 fluxes” are associated (when needed) to the action EFF)

13.3.2 Actions or Outputs

To calibrate your data, you need to do the following actions leading to the output calibration, in order:

1. SELECT: Select the calibration parameters
2. PHCOR: Radiometric phase correction, equivalent to a “Monitor 0”, see A.Dutrey lecture.
3. RF: Radio Frequency calibration
4. PHASE: Instrumental phase calibration versus time
5. EFF: Efficiency (Jy/K) calibration, to determine the flux densities of the amplitude calibrator. The inputs “R1 Fluxes” and “R2 Fluxes” should be used here.
6. AMP: Amplitude calibration versus time
7. PRINT: To produce the LaTeX and PostScript files containing the calibration curves (*e.g.* 28-feb-2001-x007.ps).

By typing GO, all the actions listed above are done sequentially. The reducer has just to type `continue` under CLIC (or use the “Continue” button in the top left menu) at each step of the calibration process.

13.3.3 Results of the calibration

After a few general comments about quality of the data, including the measurement of the seeing (deduced from the rms of the fit of the temporal phase), the pages 1 and 2 summarize the calibration as follows:

- §1.1 The estimated flux densities of the calibrators at the observed frequencies.
- §1.2 The efficiencies of the antennas for receivers 1 and 2 (which are deduced by fixing the flux of one or several calibrators).
- §1.3 The hour angle observed on the source
- §1.4 The table of the rms obtained on the RF calibration for receivers 1 and 2 in both upper and lower sidebands
- §1.5 The table of the rms obtained the temporal fit for the phase and the amplitude per baselines. Note that for receiver 2, the rms given in Col.1 is exactly the product of frequency ratio (rece 2/rece 1) times the rms obtained on receiver 1 because the phase on the receiver 1 is used to calibrate the phase on the receiver 2. After applying this phase correction, a second fit is performed on the residuals, its rms is displayed on Col.2. Col.3 gives the rms obtained on the amplitude (in %).

Chapter 14

UV Plane Analysis

Robert Lucas

lucas@iram.fr

IRAM, 300 rue de la Piscine, F-38406 Saint Martin d'Hères, France

14.1 *uv* tables

After calibration with CLIC, the calibrated data may be stored in a particular file called a '*uv* table'. This is useful because much of the data in the CLIC data file are not needed any more: atmospheric parameters, total powers, image sideband visibilities, data from other receivers may be discarded at this stage. All that counts is: the data that are needed to describe the source itself, the sky frequency that was observed, ... One may for instance create a *uv* table for the continuum and one for each line that was observed.

These *uv* tables are just special GILDAS tables suited for *uv* data handling that are created by CLIC. Mapping consists of transforming these tables into something more meaningful for the astronomer, either images or numbers like positions, flux densities, sizes, etc. However a good part of the data evaluation and analysis can be directly performed on the *uv* data itself, before performing any of the complex operations involved in creating an image (Fourier transform and deconvolution). Direct analysis of the *uv* data is the subject of this Lecture.

14.1.1 *uv* table contents

A *uv* table is a file in the Gildas Data Format, of dimensions $[3N_C+7, N_V]$, for N_C spectral channels and N_V visibilities. The $3N_C + 7$ lines contain:

1. u in meters
2. v in meters
3. Scan number

4. Observation date (integer CLASS day number)
5. Time in seconds since above date
6. Number of start antenna of baseline
7. Number of end antenna of baseline
8. First frequency point (real part)
9. First frequency point (imaginary part)
10. First frequency point (weight)
11. Same for second frequency point, and so on

Thus for a given scan with N_A antennas, $N_A(N_A - 1)/2$ visibilities are recorded.

The table header has the standard form of a GILDAS Image. The header is available (for instance) by declaring:

```
GRAPHIC> SIC\DEFINE HEADER T co10.uvt READ
GRAPHIC> EXAMINE T%
```

For a table named `co10.uvt`. Some keywords convey a more precise meaning for *uv* tables:

T%NDIM should be 2

T%DIM contains $3N_C+7$ and N_V

T%RA, T%DEC coordinates (radians) of the pointing center (the center of the primary beam).

T%A0, T%D0 coordinates (radians) of the phase tracking center (a point source at this point should have zero phase); they are identical to RA and DEC when a table is first produced.

T%EPOCH The epoch of those coordinates. Should be 2000.0

T%VELOFF, T%VELRES The velocity of the reference channel, and the channel separation in velocity units (km/s)

T%RESTFRE, T%FREQRES The rest frequency, and the channel separation in frequency units (MHz)

T%CONVERT[1,1] the reference channel

T%CONVERT[1,2] the actual observing frequency at the reference channel (MHz); the one used to scale angular displacements from u, v coordinates in meters.

One may also examine directly the header by typing simply :

```
GRAPHIC> HEADER co10.uvt
```

14.1.2 How to create a *uv* Table

uv Tables are created by CLIC using the command TABLE.

A set of commands to create a *uv* table may look like:

```
! Reset the default options:
SET DEFAULT
! find the useful scans:
FILE IN 21-JAN-1998-H126
SET SOURCE IRC+10216
SET RECEIVER 1
SET PROCEDURE CORRELATION
```



```

SET QUALITY AVERAGE
FIND
! calibration options:
SET AMPLITUDE ANTENNA RELATIVE
SET PHASE ANTENNA RELATIVE INTERNAL ATMOSPHERE
SET RF ANTENNA ON
! table creation:
SET SELECTION LINE LSB L01
TABLE HCN NEW /FREQUENCY HCN 88631.85 /RESAMPLE 19 10 -27 2.12 V

```

All but the last two commands should be familiar at this point.

- The first new command, SET SELECTION, prepares the last one TABLE. It selects that the next table to be created will be a line table (i.e. with more than one spectral channel). The lower sideband data will be used, and only the first subband of the correlator: L01.
- The last command TABLE, actually creates the table named `hcn.uvt`. The rest frequency, 88631.85 MHz, is set to be the reference used for the velocity scale. The data will be resampled to a velocity grid of 19 channels; the reference channel 10 will correspond to the LSR velocity -27 km/s; the channel spacing will be 2.12 km/s. Without /RESAMPLE, one would have got all the channels in the subband L01 with their original velocity separation. Without /FREQUENCY, the rest frequency present in the data (in the observing procedure) would have been used.

Using /RESAMPLE, one may avoid creating tables with too many channels (by discarding unused parts of correlator subbands) and choose the resolution that is actually needed.

If the data is spread on several files, one may go on by opening the other files, finding the data scans, and appending to the table:

```

FILE IN 12-FEB-1998-H126
FIND
TABLE
FILE IN 21-FEB-1998-H126
FIND
TABLE
...

```

(the arguments to TABLE need not to be repeated).

For continuum tables one may use:

```

SET SELECTION CONTINUUM DSB L01 TO L05 -
/WINDOW 214405 214726 217476 217796 217837 217875
TABLE CONT-1MM NEW

```

Here we are using data from all the line subbands, but only in the three frequency windows: 214405 to 214726 MHz, 217476 to 217796MHz, and 217837 to 217875. This is of course to avoid the line emission of some molecules.

A standard menu is available under the CLIC main menu (“Create a UV Table”). After execution, a specific procedure is created to keep track of the options and parameters used. This procedure can subsequently be edited to add new data files (data files can also be added from the menu).

14.2 uv data plots

A procedure is available to do various plots from a continuum or line table. Its name is UVALL and it is called by clicking on “Interferometric UV operations” in the GRAPHIC standard menu. One has to select the first and last channel to be plotted (0 0 to get all channels) and the name of the parameters to be plotted in abscissa and ordinate. The following examples are the most useful plots:

Figure 14.1: “Create a UV Table” menu in CLIC

uv coverage: to get an idea of the imaging quality that may be obtained, to check if one configuration has been forgotten, ...

weight vs. number: check if some data got strange weights (e.g., zero) for any reason

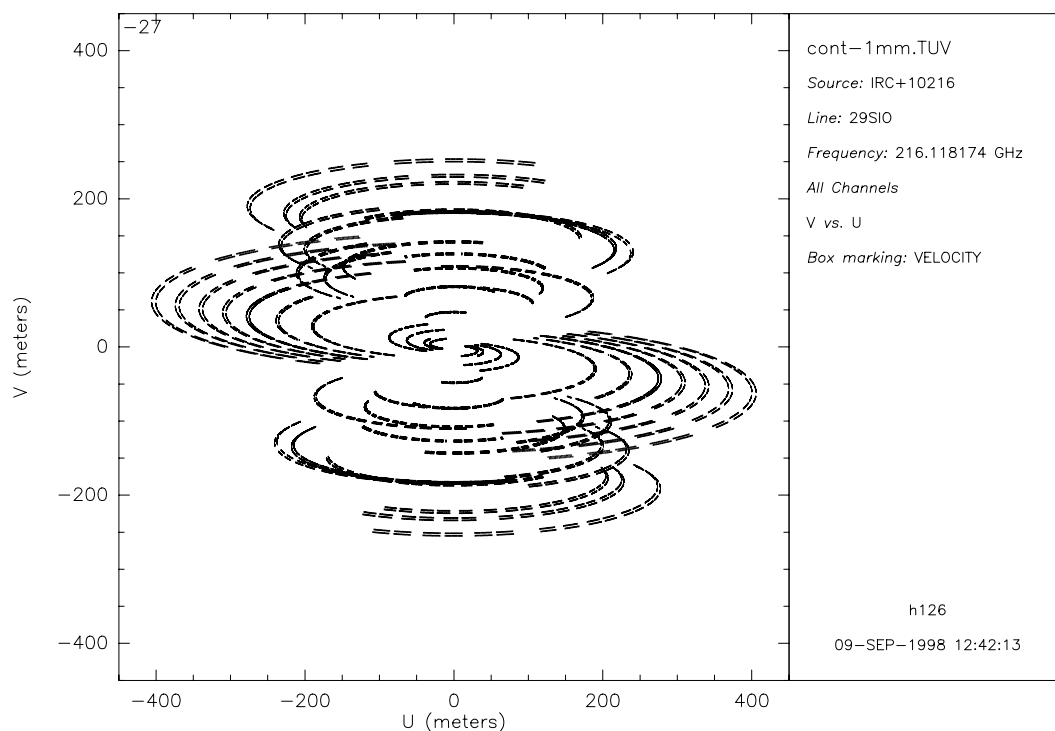
Amplitude vs. antenna spacing: quite useful if a source is strong to see if it looks resolved. Also check for spurious high amplitude points.

Amplitude vs. weight: another useful check: spurious high-amplitude points with non-negligible weight can cause a lot of harm in a map.

These plotting facilities are also implemented in the MAPPING program as a command (SHOW UV).

14.3 Data editing

Editing the interferometer data is not very flexible when done in the *uv* tables. If a problem occurs, it is not easily diagnosed since many of the parameters associated with the data acquisition are not present: atmospheric data, total powers, ... It is however useful when something strange occurs in the mapping process to do *uv* plots of the input table to look for the faulty data. Using time or scan number as X coordinate is recommended. One then may go back to the CLIC program and flag the faulty data, tag the

Figure 14.2: Example of a uv coverage plot

corresponding scans, and keep a log of these problems so that they are not encountered again when the uv tables are reconstructed for any reason.

Two tasks have been written that may directly edit the data in uv tables:

UV_CLIP flags all visibilities larger than a given flux: this deletes visibility points with totally wrong numbers, if any.

UV_FLAG deletes visibility points in a given time interval for a given baseline.

Both tasks work by setting the corresponding weight to zero: their action is irreversible (you will have to reconstruct the uv table to go back).

The **MAPPING** program provides a more efficient, simpler and reversible interactive tool to flag parts of a uv data set (command **UV_FLAG**).

14.4 Position shift

For the purpose of further data reduction it may be necessary to change the phase center of the uv data. This is done by a simple rotation of the phases (multiplication by a complex factor). One uses the task **UV_SHIFT** for this purpose.

14.5 Averaging

14.5.1 Data compression

One may simply wish to average several channels to increase the signal to noise ratio (use tasks **UV_COMPRESS** and **UV_AVERAGE**).

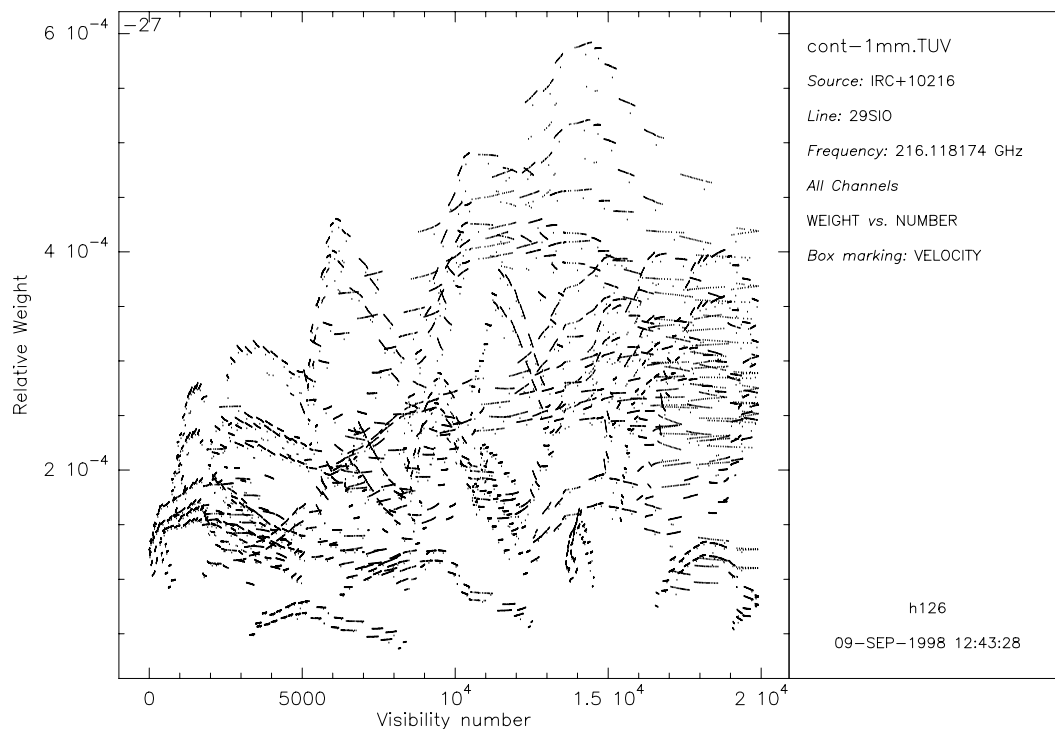


Figure 14.3: Weight versus visibility number plot

14.5.2 Circular averaging

For sources with circular symmetry it may be necessary to obtain the variation of amplitude with antenna spacing, in order to compare the amplitude data with models. For this purpose, with task `UV_CIRCLE` one takes the mean of all the visibilities in concentric rings in the uv plane. The output has the format of a uv table (except that all v 's are zero), and may be plotted with `UVALL` (fig. 14.5).

Use this sort of averaging with caution: the phase center must accurately coincide with the source position or the amplitude of the visibility average will decrease on long spacings (use `UV_FIT` and `UV_SHIFT`). One may also do this kind of averaging in separate sectors in the uv plane, to check for asymmetries, provided the uv plane is well sampled (task `UV_CUTS`).

14.6 Model fitting

Model fitting is the oldest way of analyzing interferometer data. It was effectively used in the times where the coverage of the uv plane was too scarce to even think of creating an image by Fourier transform. One assumes a simple source model depending of a few parameters (source position, flux, size) and fits the visibility function of that model to the visibility data. Of course one may use a linear combination of several source models since the Fourier transform is linear. This is performed using the `GILDAS` task `UV_FIT`. The result may be displayed with the procedure `PLOTFIT`. Both are available in the panel “Interferometric UV operations” from the `GRAPHIC` standard menu.

Table 14.1 gives examples of a few models and their visibility functions. For source models with a circular symmetry, the visibility function is split into a radial dependent amplitude and a phase factor which depends only on the source position.

Some sources are actually so simple that this method may be used to a good accuracy (fig. 14.6).

Quite often this method is used for sources that are unresolved or not well resolved at a given frequency; for instance a SiO maser may consist of several point-source components at different velocities. Fitting a point source in each channel one derives a “spot map” (figs 14.7,14.8).

Parameters:		Variables:	
x_0	RA position	x, y	sky position
y_0	DEC position	r	$\sqrt{(x - x_0)^2 + (y - y_0)^2}$
S	Source flux	u, v	projected spacing
b	HP size	q	$\sqrt{u^2 + v^2}$

Name	Model	Visibility
Point source	$S \delta(x - x_0, y - y_0)$	$S e^{-2i\pi(ux_0 + vy_0)}$
Gaussian	$\frac{4S}{\pi b^2 \log 2} e^{-4 \log 2 \frac{r^2}{b^2}}$	$S e^{-\pi^2/4 / \log 2 (bq)^2} e^{-2i\pi(ux_0 + vy_0)}$
Disk	$\frac{4S}{\pi b^2}$ where $ r < b$	$S J_1(\pi bq) e^{-2i\pi(ux_0 + vy_0)}$

Table 14.1: A few simple source models and their visibility functions

14.6.1 Position measurement

For a source with central symmetry the task `UV_CENTER` determines the source position by using only the phases. Alternatively the task `UV_FIT` may be used to fit the amplitudes and phases at the same time, or e.g. to simultaneously fit a pair of sources.

14.7 Continuum source subtraction

It is straightforward to subtract a point source at the phase center in the uv data: one simply subtract a real number (the source flux) from all the visibilities.

The task `UV_SUBTRACT` subtracts a time-averaged continuum uv table from a spectral line table (this assumes that the continuum and the line have been observed simultaneously), providing a new table with the line emission. Note that if the source is too complex, the time averaging (needed to avoid increasing the noise level in the resulting table), may affect the structure of the subtracted continuum image.

If the continuum data was not observed in the same session, or is known only from other sources, one may build a uv table of the continuum using the task `UV_MODEL`. This task computes that table from a model image or data cube; it computes the corresponding visibilities at uv coordinates taken from a reference uv table (e.g. the table out of which one wants to subtract the continuum model).

14.8 Self calibration by a point source

In some cases the continuum is a point source, and is strong enough to be used to reference the phases and amplitudes of the line data. The phase and amplitude referencing can be done in `CLIC` command `STORE PHASE /SELF` or in the uv tables using task `UV_ASCAL`.

For this one creates separately a line table and a continuum table. Naturally both must have been observed simultaneously. It is strongly advised to self-calibrate the phase first, then the amplitude using a longer smoothing time. `UV_ASCAL` allows in addition to subtract (part of) the input reference source, typically to provide continuum-free spectral line maps.

Note that this operation will work also if the source is somewhat extended, but with central symmetry; in that case only the phases can be self-calibrated.

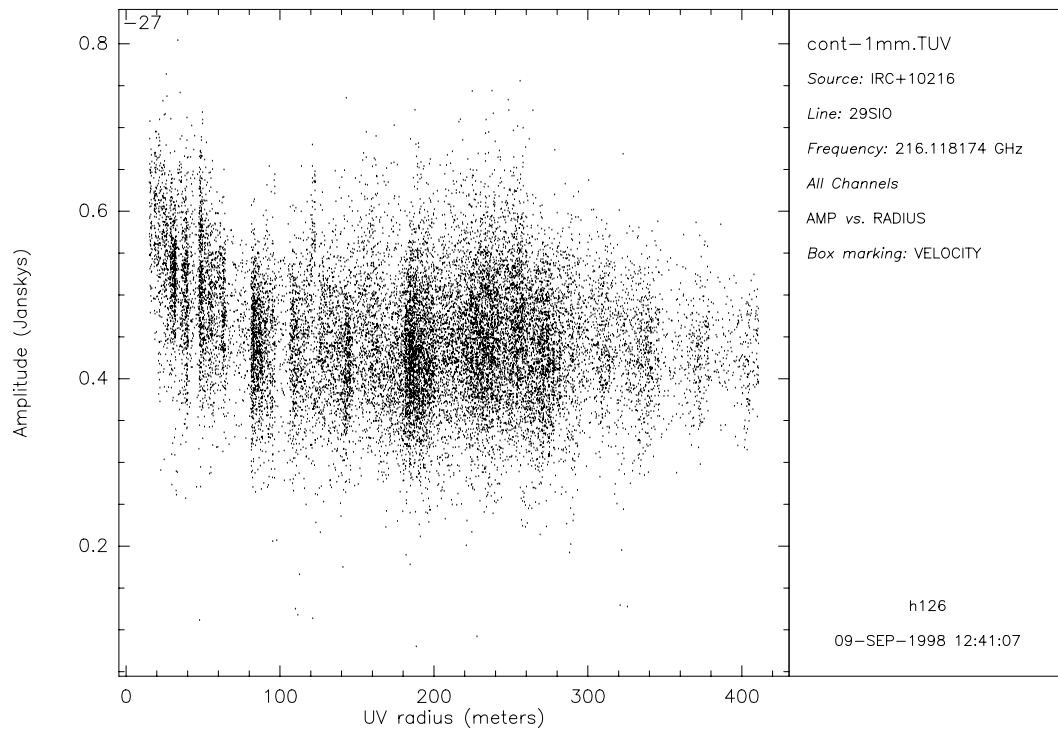


Figure 14.4: Amplitude versus antenna spacing plot

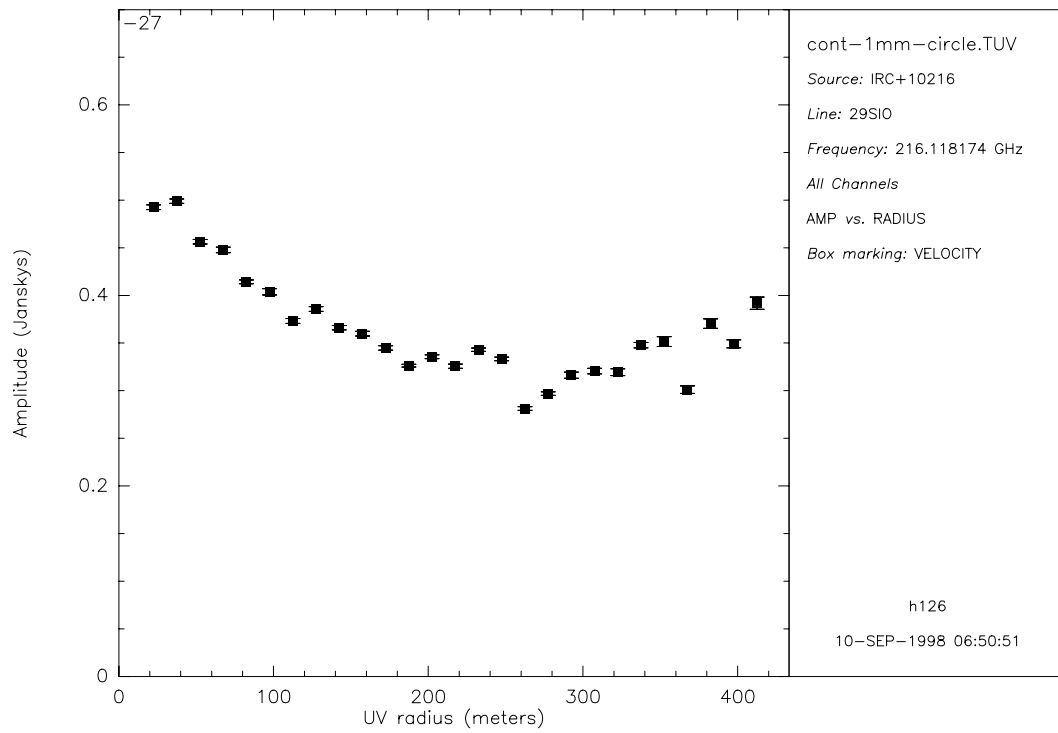


Figure 14.5: Example of a circular average plot (same data as fig. 14.4)

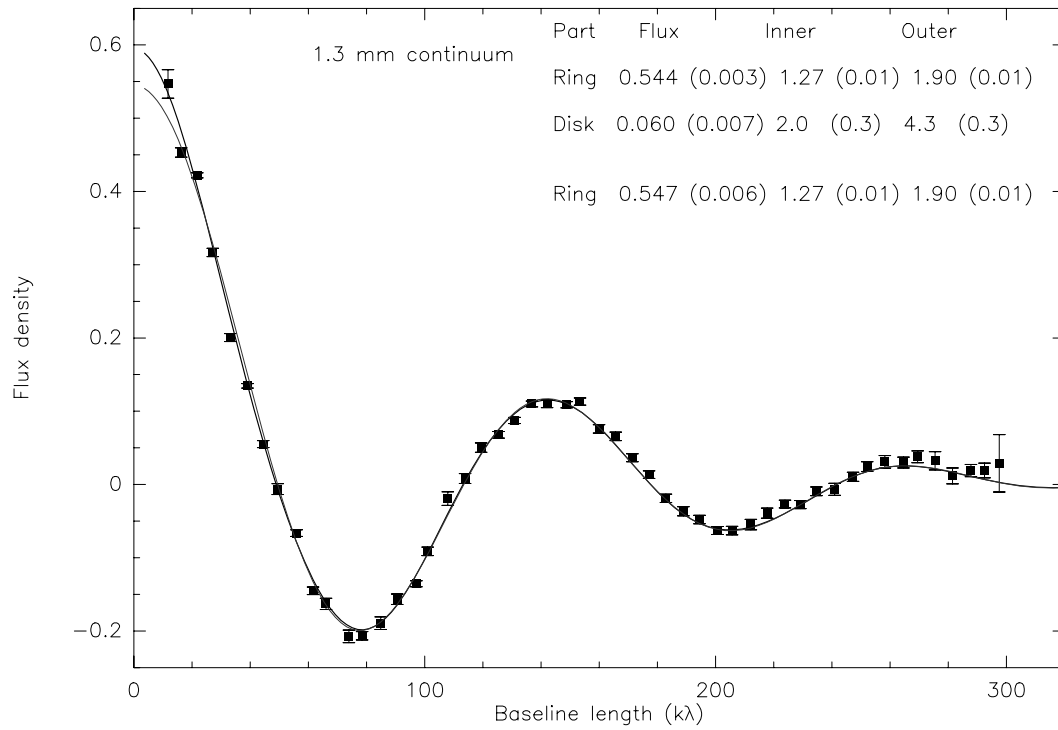


Figure 14.6: uv -plane fit to the disk around GG Tau at 1.3 mm (from [Guilloteau et al. 1999]).

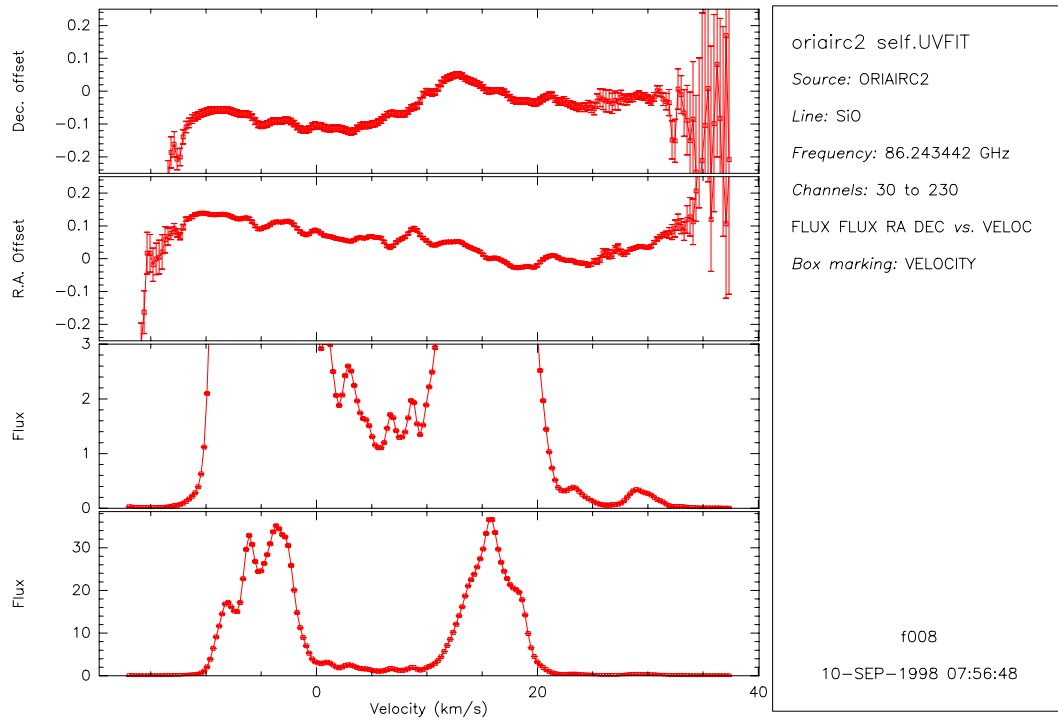


Figure 14.7: Result of a multi-channel point source fit to the Orion SiO ($v=2$, $J=2-1$) maser

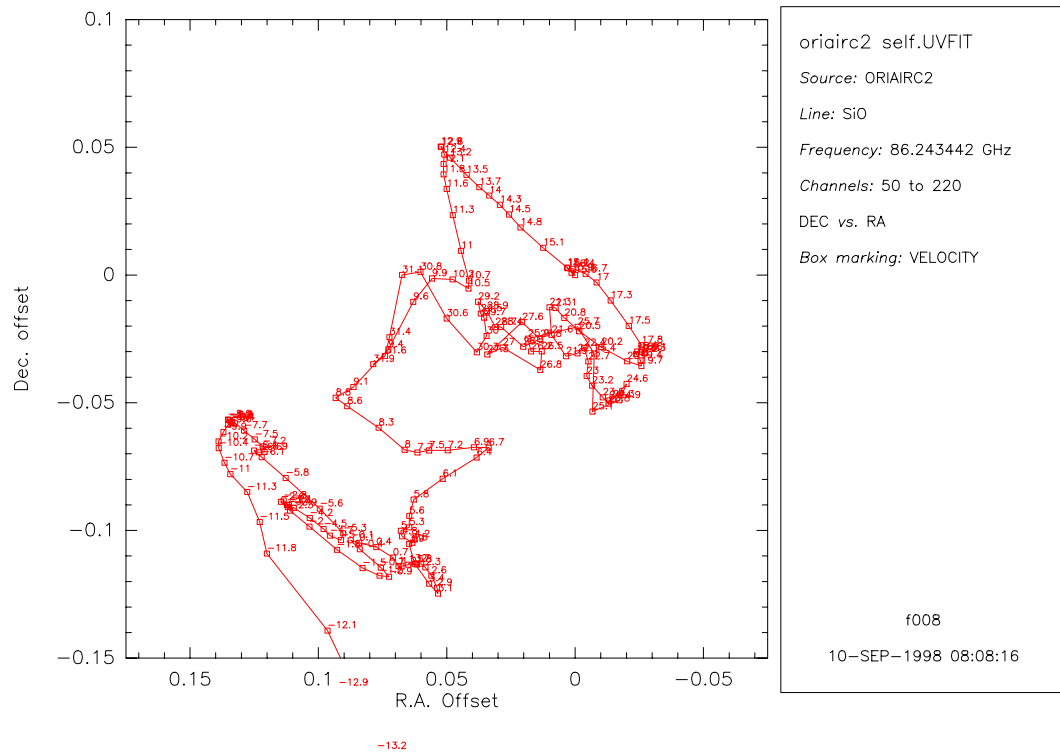


Figure 14.8: “Spot map” of the Orion SiO ($v=2, J=2-1$) maser

Chapter 15

The Imaging Principles

Stéphane Guilloteau

guillote@iram.fr

IRAM, 300 rue de la Piscine, F-38406 Saint Martin d'Hères, France

Assuming identical antennas, we have shown in previous lectures that an interferometer measures the *visibility function*

$$V(u, v) = \iint B(x, y) I(x, y) e^{-2i\pi(ux+vy)} dx dy \quad (15.1)$$

over an ensemble of points $(u_i, v_i), i = 1, n$, where $B(x, y)$ is the power pattern of the antennas and $I(x, y)$ the sky brightness distribution.

The imaging process consists in determining as best as possible the sky brightness $I(x, y)$. Since Eq.15.1 is a convolution, the imaging process will involve deconvolution techniques.

Let $S(u, v)$ be the sampling (or spectral sensitivity) function

$$\begin{aligned} S(u, v) \neq 0 &\iff \exists i \in 1, n (u_i, v_i) = (u, v) \\ S(u, v) = 0 &\iff \forall i \in 1, n (u_i, v_i) \neq (u, v) \end{aligned} \quad (15.2)$$

The spectral sensitivity function S contains information on the relative weights of each visibility, usually derived from noise predicted from the system temperature, antenna efficiency, integration time and bandwidth.

Let us define

$$I_w(x, y) = \iint S(u, v) W(u, v) V(u, v) e^{2i\pi(ux+vy)} du dv \quad (15.3)$$

where $W(u, v)$ is an arbitrary *weighting function*. Since the Fourier Transform of a product of two functions is the convolution of the Fourier Transforms of the functions, $I_w(x, y)$ can be identified with

$$I_w(x, y) = (B(x, y)I(x, y)) ** (D_w(x, y)) \quad (15.4)$$

where

$$D_w(x, y) = \iint S(u, v) W(u, v) e^{2i\pi(ux+vy)} du dv = \widehat{SW} \quad (15.5)$$

$D_w(x, y)$ is called the *dirty beam*, and is directly dependent on the choice of the *weighting function* W , as well as on the spectral sensitivity function S . $I_w(x, y)$ is usually called the *dirty image*.

Fourier Transform, which allows to directly derive I_w from the measured visibilities V and spectral sensitivity function S , and **Deconvolution**, which allows to derive the sky brightness I from I_w , are thus two key issues in imaging (see Eq.15.4).

15.1 Fourier Transform

The first step in imaging is to evaluate the dirty image, using Fourier Transform. Several techniques are available.

15.1.1 Direct Fourier Transform

The simplest approach would be to directly compute sin and cos functions in Eq.15.4 for all combinations of visibilities and pixels in the image. This is straightforward, but slow. For typical data set from the VLA, which contain up to 10^5 visibilities per hour and usually require large images (1024×1024 pixels), the computation time can be prohibitive. On the other hand, the IRAM Plateau de Bure interferometer produces about 10^4 visibilities per synthesis, and only require small images (128×128). The Direct Fourier Transform approach could actually be efficient on vector computers for spectral line data from Plateau de Bure interferometer, because the sin and cos functions needs to be evaluated only once for all channels. Moreover, the method is well suited to real-time display, since the dirty image can be easily updated for each new visibility.

15.1.2 Fast Fourier Transform

In practice, everybody uses the Fast Fourier Transform because of its definite speed advantage. The drawback of the methods is the need to regrid the visibilities (which are measured at arbitrary points in the (u, v) plane) on a regular grid to be able to perform a 2-D FFT. This gridding process will introduce some distortion in the dirty image and dirty beams, which should be corrected afterwards. Moreover, the gridded visibilities are sampled on a finite ensemble. As discussed in more details below, this sampling introduces aliasing of the dirty image (and beam) in the map plane.

15.1.3 Gridding Process

The goal of gridding is to resample the visibilities on a regular grid for subsequent use of the FFT. At each grid point, gridding involves some sort of interpolation from the values of the nearest visibilities. The visibilities being affected by noise, the interpolating function needs not fit exactly the original data points. Although any interpolation scheme could a priori be used, such as smoothing spline functions, it is customary to use a *convolution* technique to perform the gridding.

Using a convolution is justified by several arguments. First, from Eq.15.1, $V = \widehat{BI} = \hat{B} ** \hat{I}$. Hence V is already a convolution of a (nearly Gaussian) function \hat{B} with the Fourier Transform of I . Nearby visibilities are not independent. Second, as mentioned above, exact interpolation is not desirable, since original data points are *noisy samples of a smooth function*. Third, if the width of the convolution kernel used in gridding is small compared to \hat{B} , the convolution added in the gridding process will not significantly degrade the information. Last, but not least, it is actually possible to correct for the effects of the convolution gridding.

To demonstrate that, let G be the gridding convolution kernel. Eq.15.3 becomes

$$I_w^g \rightleftharpoons G ** (S \times W \times V) \quad (15.6)$$

We thus have for the image I the following relations

$$I_w^g = \hat{G} \times (\widehat{SW} ** \hat{V}) = \hat{G} \times I_w \quad (15.7)$$

and for the dirty beams

$$D_w^g \Leftrightarrow G ** (S \times W) \quad D_w^g = \hat{G} \times \widehat{SW} \quad (15.8)$$

from which we derive the relation

$$\frac{I_w^g}{\hat{G}} = \frac{D_w^g}{\hat{G}} ** (BI) \quad (15.9)$$

Thus the dirty image and dirty beams are obtained by dividing the Fourier Transform of the gridded data by the Fourier Transform of the gridding function.

15.2 Sampling & Aliasing

Sampling on a regular grid is equivalent to multiplying by a series of periodically spaced delta functions, i.e. the so-called *shah* function III:

$$\left[\frac{1}{\Delta u}\right] \text{III}\left(\frac{u}{\Delta u}\right) = \sum_{k=-\infty}^{\infty} \delta(u - k\Delta u) \quad (15.10)$$

The Fourier Transform of the *shah* function above is the *shah* function

$$\text{III}(x\Delta u) = \frac{1}{\Delta u} \sum_{m=-\infty}^{\infty} \delta\left(x - \frac{m}{\Delta u}\right) \quad (15.11)$$

Hence, sampling the visibilities V results in convolving its Fourier Transform \hat{V} by a periodic *shah* function. This convolution reproduces in a periodic way the Fourier Transform of the visibilities \hat{V} .

If the Fourier Transform of the visibilities \hat{V} , i.e. the brightness distribution BI , has finite support ΔX , the replication poses no problem provided the support is smaller than the periodicity of the *shah* function, i.e.

$$(\Delta u)^{-1} \geq (\Delta X) \quad \Delta u \leq (\Delta X)^{-1} \quad (15.12)$$

If not, data outside $(\Delta u)^{-1}$ are *aliased* in the *imaged area* $(\Delta u)^{-1}$.

In aperture synthesis, finite support is ensured to first order by the finite width of the antenna primary beam B . However, strong sources in the antenna sidelobes may be aliased if the imaged area is too small. Moreover, the **noise** does not have finite support. White noise in the uv plane would result in white noise in the map plane. In practice, the noise in the uv plane is not completely white. However, its support is limited (since only a finite region of the uv plane is sampled in any experiment). Accordingly, its Fourier Transform in the map plane is not support limited. Noise aliasing thus occurs, and produces an increased noise level at the map edges.

15.3 Convolution and Aliasing

The combination of Gridding and Sampling produces the uv data set

$$V_m = \frac{1}{\Delta u \Delta v} \text{III}\left(\frac{u}{\Delta u}, \frac{v}{\Delta v}\right) \times (G ** (S \times W \times V))(u, v) \quad (15.13)$$

$$= \text{III} \times (G ** (S \times W \times V)) / (\Delta u \Delta v) \quad (15.14)$$

which analogous with Eq.15.6

The Fourier Transform of this uv data set is

$$\widehat{V}_m = \text{III}(x\Delta u, y\Delta v) ** (\hat{G} \times (\widehat{SW} ** \hat{V})) \quad (15.15)$$

$$= \text{III} ** (\hat{G} \times (\widehat{SW} ** (BI))) \quad (15.16)$$

\widehat{V}_m is thus the sky brightness multiplied by the primary beam (BI), convolved by the the dirty beam \widehat{SW} , then multiplied by the Fourier transform of the gridding function \hat{G} and periodically replicated (by the convolution with the Shah function).

Accordingly, aliasing of \hat{G} in the map domain will thus occur. Note at this stage that, providing aliasing of \hat{G} remains negligible, an exact convolution equation is preserved

$$\frac{\widehat{V}_m}{\hat{G}} = \widehat{SW} ** BI \quad (15.17)$$

The gridding function will thus have to be selected to minimize aliasing of \hat{G} . This criterion will depend on the image fidelity required. Obviously, if the data is very noisy, aliasing of the \hat{G} can be completely negligible.

Furthermore, the weighting function W is usually smooth, while the gridding function G is a relatively sharp function (since it ensures the re-gridding by convolution from *nearby* data points). Thus, to first order $G ** W = W$, and we could rewrite Eq.15.14 as

$$V_m = \text{III} \times W \times (G ** (S \times V)) / (\Delta u \Delta v) \quad (15.18)$$

Hence, the weighting can be performed *after* the gridding. The choice of weighting before or after gridding is essentially based on computational speed or algorithmic simplicity.

Let us focus on the choice of the gridding function. The gridding function will be selected according to the following principles:

1. small support, typically one or two cells wide (Δu).
2. small aliasing.
3. fast computation.

Points 1 and 2 are contradictory, since a small support for G implies a large extent of \hat{G} . Some compromise is required. For simplicity, gridding functions are usually selected among those with separable variables:

$$G(u, v) = G_1(u)G_1(v)$$

although this could break the rotation invariance.

The simplest gridding function is the **Rectangular function**

$$G(u) = \frac{1}{\Delta u} \Pi\left(\frac{u}{\Delta u}\right) \quad (15.19)$$

$$\hat{G}(x) = \frac{\sin(\pi \Delta u x)}{\pi \Delta u x} \quad (15.20)$$

where Π is the unit rectangle function. Obviously, aliasing will be important, since the **sinc** function falls off very slowly.

A better choice could be the **Gaussian function**

$$G(u) = \frac{1}{\alpha \Delta u \sqrt{\pi}} e^{-(u/\alpha \Delta u)^2} \quad (15.21)$$

$$\hat{G}(x) = e^{-(\pi \alpha x \Delta u)^2} \quad (15.22)$$

By proper selection of α (not too small, not too large), a compromise between computation speed (better for small α) and aliasing (better for large α) can be found. $\alpha = 2\sqrt{\ln(4)} \simeq 0.750$ is a standard choice.

However, a Gaussian still has fairly significant wings. \hat{G} should ideally be a rectangular function (1 inside the map, 0 outside). G would be a **sinc** function, but this falls off too slowly, and would require a

lot of computations in the gridding. Moreover, the (unavoidable) truncation of G would destroy the sharp edges of \hat{G} anyhow. Hence the idea to use an apodized version of the sinc function, the **Gaussian-Sinc function**

$$G(u) = \frac{\sin \pi u / (\alpha \Delta u)}{\pi u} e^{-(u / (\beta \Delta u))^2} \quad (15.23)$$

$$\hat{G}(x) = \Pi(\alpha x \Delta u) * (\sqrt{\pi} \beta \Delta u e^{-(\pi \beta x \Delta u)^2}) \quad (15.24)$$

It provides good performance for $\alpha = 1.55$ and $\beta = 2.52$.

The empirical approaches mentioned above do not guarantee any optimal choice of the gridding function. A completely different approach is based on the desired properties of the gridding function. We actually want \hat{G} to fall off as quickly as possible, but G to be support limited. Mathematically, this defines a class of functions known as **Spheroidal functions**. Spheroidal functions are solutions of differential equations, and cannot be expressed analytically. In practice, this is not a severe limitation since numerical representations can be obtained by tabulating the gridding function values. Given the limited numerical accuracy of the computations, the tabulation does not require a prohibitively fine sampling of the gridding function, and is quite practical both in term of memory usage and computation speed. Tabulated values are used in the task UV_MAP.

Note that the finite accuracy of the computation may ultimately limit the image dynamic range.

15.4 Error Analysis

We thus succeeded to preserve a convolution equation, with the slight restrictions due to the aliasing and gridding correction. Let us explore now what *errors* or *systematic* effects may appear in the image plane.

First, consider the **noise**. Aliasing increases the noise level at the map edges (by noise aliasing and then by the gridding correction since this amounts to divide by the Fourier Transform of the gridding function, which is unity at the map center, but smaller at the map edges). For example, the noise increases by a factor $(\pi/2)^2$ at map corners for the Gaussian-Sinc function. Near the map center, the effect is negligible. Note that for a given field of view, the noise increase can be arbitrarily limited by making a sufficiently large image, but this has a high computational price.

Concerning errors, it is important to separate two main classes of errors.

Additive errors

The Fourier transform being linear, additive errors result in artificial structure *added* to the true map, e.g.

- A single spurious visibility will produce fringes in the map
- An additive real term (correlator offset), will produce a point source at the phase tracking center.

Multiplicative errors

A multiplicative term on the visibility distorts the image, since

$$V(u, v) \times \epsilon(u, v) \longleftrightarrow \hat{V}(x, y) ** \hat{\epsilon}(x, y)$$

i.e. the map is convolved by the Fourier transform of the error. Calibration errors (in phase or amplitude) are of this type. Among these, the **seeing** should not be neglected.

Phase calibration errors result in antisymmetric patterns.

15.5 Weighing and Tapering

There is still a free parameter in the image construction process: the weighting function. At uv table creation, the sampling function is defined as

$$S(u, v) = \frac{1}{\sigma^2(u, v)} \quad (15.25)$$

where the noise σ is computed from system temperature, bandwidth, integration time, and system efficiency (including quantization and decorrelation).

$$\sigma(u, v) = \frac{\mathcal{J}_I T_{\text{sys}}}{\eta_Q \sqrt{2 \Delta \nu t_{\text{int}}}} \quad (15.26)$$

\mathcal{J}_I being the antenna temperature to flux density conversion factor:

$$\mathcal{J}_I = \frac{2k}{\eta_A A} \quad (15.27)$$

The weights $W(u, v)$ can be freely chosen. The selecting of weights is usually decomposed in two slightly different processes, called Weighting and Tapering.

Weighting deals with the local variations of weights for each grid cell after the gridding process. Since the original uv coverage is an ensemble of ellipses, the gridding may leave a weight distribution with very large dispersion. Weighting can be applied to uniformize this distribution.

On the other hand, **Tapering** consists in apodizing the uv coverage by $T(u, v) = \exp(-(u^2 + v^2)/t^2)$ where t is a tapering distance. This corresponds to smoothing the data in the map plane (by convolution with a gaussian).

The simplest possibility, called **Natural Weighting, without taper** is to keep the original spectral sensitivity function by setting $W(u, v) = 1$. This can be demonstrated to maximize sensitivity to *point sources* (i.e. sources smaller than the synthesized beam). Proper design (and use) of the array can ensure that the resulting synthesized beam is appropriate, in terms of size (angular resolution matched to the scientific goal) and shape (lowest possible sidelobes).

If the sources of interest are somewhat extended, tapering can be used to increase **brightness** sensitivity. Tapering may also have the advantage of lowering the sidelobes. This is usually true for limited tapering, which reduces the effect of the discontinuity at the outer edge of the uv plane, but is not the case for strong tapering, where the result becomes critically dependent on the actual sampling of the inner part of the uv plane. However, tapering is always throwing out some information, namely the long baselines part of the data set. Hence, it should be used either with moderate tapers, or as a complementary view on a data set. To increase brightness sensitivity, one should use preferentially compact arrays rather than tapering.

Uniform Weighting consists in selecting the weights $W(u, v)$ so that the sum of weights $\sum W \times S$ over a uv cell is a constant function (or zero if no uv data exists in that cell). The size (radius) of the uv cell is an arbitrary parameter. It can be the cell size resulting from the gridding process, i.e. the inverse of the field of view, but any other choice is possible. Using half of the dish diameter is well justified, since the visibilities are convolution of Fourier transform of the sky brightness by the Fourier transform of the primary beam. **Uniform Weighting** gives more weight to long baselines than natural weighting (because you spend less time per uv cell on long baselines than on short baselines for earth synthesis). **Uniform Weighting** produces smaller beam. Because it fills the uv plane more regularly, Uniform weighting could be thought also to produce lower sidelobes. However, because of the discontinuity of the weights at the edge of the sampled portion of the uv plane, the inner sidelobes tend to be increased, unless some tapering is combined with Uniform weighting.

Robust Weighting is a variant of uniform weighting which avoids to give too much weight to a uv cell with low natural weight. There are several ways to implement such a scheme. Roughly speaking, if the sum of natural weights in a cell is less than a threshold, the weighting is unchanged, if it is more, the weight is set to this threshold. Let S_n be the natural weight of a cell, and S_t a threshold for such weight. Robust weighting could be implemented by selecting the weight W as

$$\begin{aligned} S_n < S_t &\Leftrightarrow W = 1 \\ S_n > S_t &\Leftrightarrow W = S_t/S_n \end{aligned} \quad (15.28)$$

or a more continuous formula like

$$W = \frac{1}{\sqrt{1 + S_n^2/S_t^2}} \quad (15.29)$$

Robust weighting combines the advantages of **Natural** and **Uniform** weighting, by increasing the resolution and lowering the sidelobes without degrading too much the sensitivity. By adjusting the threshold, it approaches either case (large threshold \longleftrightarrow Natural, small threshold \longleftrightarrow Uniform).

Weighting and Tapering reduce point source sensitivity by

$$\sqrt{\sum T^2 W^2 / (\sum T W)} \quad (15.30)$$

15.6 The GILDAS implementation

We have now introduced the basic parameters of the imaging process: gridding, weighting and tapering. The main imaging task in the GILDAS software is UV_MAP. Before using UV_MAP, it is also recommended to use the associated task UV_STAT which evaluates the beam sizes, point source and brightness sensitivity as function of taper or robust weighting parameter.

Although the choice of configurations for the Plateau de Bure interferometer has been performed in order to optimize the uv coverage for most observing conditions, robust weighting can often offer a better compromise, unless signal to noise is insufficient. Task UV_STAT also suggests appropriate pixel sizes for UV_MAP

The imaging task UV_MAP is controlled by the following parameters:

- **MAP_SIZE**
The number of pixels in each direction. This should be powers of 2.
- **MAP_CELL**
The pixel size, in arcsecond, in each direction. It should respect proper sampling compared to the synthesized beam width. In practice, 3 – 4 pixels per beam width are required. Task UV_STAT can compute the optimum value for this parameter. Note that the imaged area is $\text{MAP_SIZE} \times \text{MAP_CELL}$
- **MCOL**
For spectral line data, the first and last channel to be imaged. (0,0) means all data.
- **WCOL**
The channel from which the natural weights S are taken. UV_MAP produces only one beam for all channels (by default, there is an alternate option for experts). $\text{WCOL} = 0$ is equivalent to $\text{WCOL} = (\text{MCOL}[1] + \text{MCOL}[2]) / 2$.
- **WEIGHT_MODE**
UN for **Uniform** or NA for **Natural** weighting. UNiform weighting is actually a **Robust** weighting in UV_MAP.
- **UV_CELL**
When UNiform weighting is used, UV_CELL[1] is the UV cell diameter (in meters), and UV_CELL[2] is the threshold for robust weighting: 1 corresponds to the mean natural weight of all cells. UV_CELL[1] should normally be 7.5 m for Plateau de Bure data.
- **CONVOLUTION**
This is the convolution type for gridding. Choices are offered for test purposes, but CONVOLUTION = 5 (Spheroidal) gives best results.

The other parameters are used to re-center the map (by phase shifting the uv data before imaging) when needed. This is convenient for **Mosaics**. UV_MAP performs all the imaging steps presented before: gridding, weighting, tapering, correction for gridding function, and computes the dirty beam and dirty image.

Both UV_STAT and UV_MAP are implemented as commands in the MAPPING program, or as tasks available from the GRAPHIC program. Using one or the other is a matter of personal preference.

15.7 Deconvolution

The first imaging step presented before leads to a convolution equation whose solution is the convolution product of the sky brightness distribution (apodized by the interferometer primary beam) by the dirty beam.

To derive the astronomically meaningful result, i.e. ideally the sky brightness, a deconvolution is required. Deconvolution is always a non linear process, and requires (in one way or another) to impose some constraints on the solution, or in other words to add some information, to better select plausible solutions. Such additional constraints can be explicit (e.g. positivity, or user specified finite support) or qualitative.

15.7.1 The CLEAN method

The standard deconvolution technique, CLEAN relies on such a qualitative constraint: it assumes that the sky brightness is essentially an ensemble of point sources (the sky is dark, but full of stars). The algorithm which derives from such an assumption is straightforward. It is a simple “matching pursuit”

1. Initialize a *Residual* map to the *Dirty* map
2. Initialize a *Clean component list* to zero.
3. Assume strongest feature in *Residual* map originates from a point source
4. Add a fraction γ (the *Loop Gain*) of this point source to the *Clean component list*, remove the same fraction, convolved with the dirty beam, from the *Residual* map.
5. If the strongest feature in the *Residual* map is larger than some threshold, go back to point 3 (each such step is called an iteration).
6. If the strongest feature is below threshold, or if the number of iterations N_{iter} is too large, go to point 7.
7. Convolve the *Clean component list* by a properly chosen *Clean Beam* (this is called the restoration step).
8. add to the result the *Residual* map to obtain the *Clean Map*.

The CLEAN algorithm has a number of free parameters. The loop gain controls the convergence of the method. In theory, $0 < \gamma < 2$, but in practice one should use $\gamma \simeq 0.1 - 0.2$, depending on sidelobe levels, source structure and dynamic range. While high values of γ would in principle give faster convergence, since the remaining flux is $\propto (1 - \gamma)^{N_{\text{iter}}}$ if the object is made of a single point source, deviations from an ideal convolution equation force to use significantly lower values in order to avoid non linear amplifications of errors. Such deviations from the ideal convolution equation are unavoidable because of thermal noise, and also of phase and amplitude errors which distort the dirty beam.

The threshold for convergence and number of iterations define to which accuracy the deconvolution proceeds. It is common practice to CLEAN down to about the noise level or slightly below. However, in case of strong sources, the residuals may be dominated by dynamic range limitations rather than by noise.

The clean beam used in the restoration step plays an important role. It is usually selected as a 2-D Gaussian, which allows the convolution to be computed by a simple Fourier transform, although other choices could be possible. The size of the clean beam is a key parameter. It should be selected to match the (inner part of) the dirty beam, otherwise the flux density estimates may be incorrect. To understand this problem, let us note first that the units of the dirty image are undefined. Simply, a 1 Jy isolated point source appears with a peak value of 1 in the dirty map. This is no longer true (because of sidelobes) if there is more than one point source, or a fortiori, an extended source. The unit of the clean image is well defined: it is Jy per beam, which can easily be converted to brightness temperature from the effective clean beam solid angle and the observing wavelength. Now, assume the source being observed is just composed of 2 separate point sources of equal flux, and that the dirty beam is essentially a Gaussian. Let us clean the dirty image in such a way that only 1 of the 2 point sources is actually included in the clean component list. If we restore the clean image with a clean beam which is, e.g. twice smaller than the original dirty beam, the final result will undoubtedly be odd. The second source would appear extended and have a larger flux than the first one. No such problem appears if the clean beam matches the dirty beam. Admittedly, the above example shows a problem which results from a combination of two effects: an inappropriate choice for the clean beam, and an insufficient deconvolution. However, the second problem always exists to some extent, because of noise in the original data set. Hence, to minimize errors, it is important to match the clean and dirty beams.

Note that in some circumstances, there may be no proper choice. An example is a dirty beam with narrow central peak on top of a broad “shoulder”. Small scale structures will be properly reconstructed, but larger ones not.

The last step in the CLEAN method plays a double role. On one hand, it protects against insufficient deconvolution. Furthermore, since the residual image should be essentially noise if the deconvolution has converged, it allows noise estimate on the cleaned image.

15.7.2 Interpretation of CLEAN

If CLEAN converged, the *Clean component list* is a plausible solution of the measurement equation (within the noise), but it is not unique... Hence, because of convolution by the clean beam, the clean image is **not** a solution. However, besides allowing a reasonable definition of the image unit in case of incomplete convergence, there are two reasons to convolve by a clean beam. First, convolution by the clean beam smears out artifacts due to extrapolation beyond the measured area of the uv plane. This is an **a posteriori regularization**. Second, the clean components are forced to reside on the grid defined by the image. This discrete representation has a number of limitations (e.g. necessity of negative clean components, limited accuracy due to the finite size of the component list), which are reduced by convolution by the clean beam, because the clean image then has finite resolution and can be properly represented on a discrete grid provided the Nyquist sampling is preserved.

An important property of CLEAN is that (to first order) only the inner quarter of the dirty image can be properly cleaned. This is easily understood when dirty beam and dirty images are computed on the same grid size, since a source at one edge of the inner quarter requires knowledge of the dirty beam sidelobes beyond the map size to be deconvolved from the opposite edge. However, this also remains true if one computes the dirty beam on a twice larger grid than the dirty image: more than the inner quarter can be deconvolved, but because of aliasing, the map edges can never be.

Finally, CLEAN offers a very simple way to impose further constraints on the class of solution which is acceptable, by allowing definition of a *support*. This can be the standard (simple or multiple) *Clean Box* available in many non interactive implementations, or a user defined mask in interactive implementations. The search region can even be modified from iteration to iteration to help clean convergence. Such a flexible support is available inside the MAPPING program. Note however that the Clean Box or support should not be too limited: cleaning the noise is necessary too (as well as incorporating negative Clean component).

15.7.3 The CLEAN variants

The original CLEAN method is due to [Hogbom 1974]. Several variants exist.

One of the most popular (CLARK) is due to [Clark 1980], and involves minor and major cycles. In **Minor** cycles, an Hogbom CLEAN is performed, but with a truncated dirty beam, and only on the list of brightest pixels. This search is fast, because of the dirty beam truncation and because of the limited support. The Clean components identified during the minor cycles are removed at once by a FFT during a **Major** cycle. Because removal is done by FFT, slightly more than the inner map quarter can be cleaned.

A second variant, called MX, due to [Cotton & Schwab 1984], is similar to the CLARK method, except that the Clean components are removed from the uv table at the **Major** cycle stage (and thus the imaging process is repeated at each major cycle). This avoid aliasing of sidelobes, allows to clean more than the inner quarter, but is relatively slow because of the re-imaging at major cycles. Unless disk storage is a real problem, a faster result of equal quality is obtained by standard Clean with a twice larger map.

The next variant, called SDI (from [Steer et al. 1984]), is again like the CLARK method, but in **Minor** cycles, no deconvolution is performed, but only a selection of the strongest components down to some threshold. **Major** cycles are identical to those of the CLARK method. Although the principle is simple, the implementation is not easy because of normalization subtleties in the minor cycle stage. This method is reasonably well suited for more extended structures, but could become unstable if the threshold is inappropriate.

The Multi Resolution Clean (MRC, [Wakker & Schwartz 1988]) separates the problem in a smooth map and a difference map. Since the measurement equation is linear, both maps can be Cleaned (with Hogbom or Clark method) independently. This is faster than the standard CLEAN because the smooth map can be compressed by pixel averaging, and only fine structure left in difference map, so fewer Clean components are required.

15.7.4 The GILDAS implementation

All the above variants are implemented in the GILDAS software. All of them, except MX, are implemented both as tasks and as interactive commands in the MAPPING program. The later implementation allows definition of a flexible support constraint. The default method is CLARK. SDI & MRC are usually not necessary for Plateau de Bure, because of the small ratio between the field of view (primary beam) and the resolution (< 30).

MX is implemented only as a task, and not recommended because of its relatively slow speed. Since Plateau de Bure images are relatively small (128×128), it is easier to use a standard clean on larger images.

The GILDAS software does not include any implementation of the Maximum Entropy Method, MEM. The main reason is that MEM is not suited for limited uv coverage. But MEM also has some undesirable properties, among which its attempt to give a unique solution, with no physical justification, the noise dependent resolution, and the definition of a global criterium for adjustment to data. Furthermore, no noise estimate is possible on MEM deconvolved images.

Chapter 16

Advanced Imaging Methods: WIPE

Eric Anterrieu

Eric.Anterrieu@obs-mip.fr

Observatoire Midi-Pyrénées – UMR5572, 14, avenue Edouard Belin, F-31400 Toulouse, France

16.1 Introduction

This lecture is the second part of a series describing how the visibility samples provided by an interferometric device can be used to produce a high quality image of the sky.

WIPE is a regularized Fourier synthesis method recently developed in radio imaging and optical interferometry. The name of WIPE is associated with that of CLEAN, the well-known deconvolution method presented in the previous lecture, and intensively used by astronomers at IRAM as well as in many institutes, worldwide.

The regularization principle of WIPE refers to the Shannon sampling formula and to theoretical considerations related to multiresolution analysis. The notions of field and resolution appear via the definition of two key spaces: the *object space* and the *object representation space* (a subspace of the first). The complex visibilities define a function in another space: the *data space*. The functions lying in this space take their values on a frequency list which is the concatenation of the *experimental frequency list* and a *regularization frequency list*. The latter defines a virtual frequency coverage beyond the *frequency coverage to be synthesized*, up to the highest frequencies of the *scaling functions* generating the *object space*. This virtual sampling is performed at the Shannon rate corresponding to the synthesized field. The reconstructed image, also called the *neat map*, is defined as the function minimizing a regularized objective functional in which the data are damped appropriately. To describe WIPE we adopt a terminology derived from that of CLEAN.

In this lecture, we present the basic foundations of WIPE, and its implementation in the IRAM data processing software. The reader interested in the theoretical aspects and developments of WIPE is invited to consult the articles [Lannes et al. 1994], [Lannes et al. 1996], [Lannes et al. 1997].

16.2 Object space

In the problems of Fourier synthesis encountered in astronomy, the *object function* of interest, Φ_o , is a real-valued function of an angular position variable $\boldsymbol{\sigma} \equiv \boldsymbol{x} = (x, y)$. The geometrical elements under consideration are presented in Fig. 16.1.

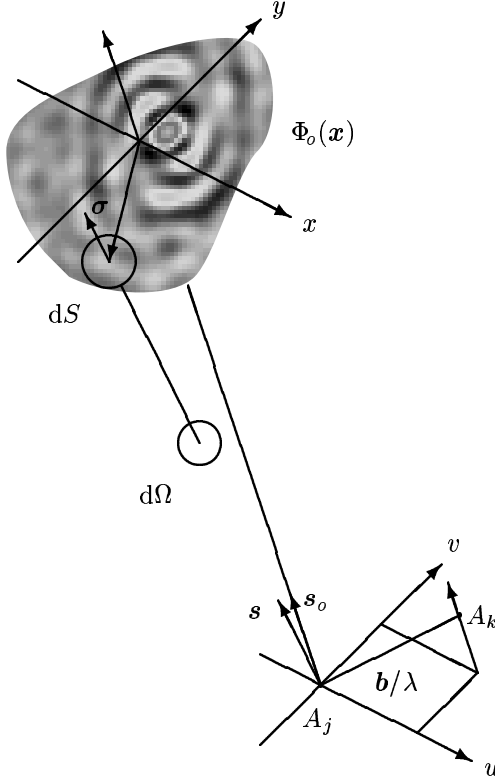


Figure 16.1: Traditional coordinate systems used to express the relation between the complex visibilities and the brightness distribution of a source under observation. Here, the two antennas A_j and A_k point toward a distant radio source in a direction indicated by the unit vector \boldsymbol{s} , and \boldsymbol{b} is the interferometer baseline vector. The position pointed by the unit vector \boldsymbol{s}_o is commonly referred to as the *phase tracking center* or *phase reference position*: $\boldsymbol{s} - \boldsymbol{s}_o = \boldsymbol{\sigma}$.

The *object model variable* ϕ lies in some *object space* H_o whose vectors, the functions ϕ , are defined at a high level of resolution. This space is characterized by two key parameters: the extension $\Delta \boldsymbol{x}$ of its field, and its resolution scale $\delta \boldsymbol{x}$. To define this *object space* more explicitly, we first introduce the finite grid (see Fig. 16.2):

$$\boldsymbol{G} = \boldsymbol{L} \times \boldsymbol{L}, \quad \boldsymbol{L} = \left\{ \boldsymbol{p} \in \boldsymbol{Z} : -\frac{N}{2} \leq \boldsymbol{p} \leq \frac{N}{2} - 1 \right\}, \quad (16.1)$$

where N is some power of 2.

On each *pixel* $\boldsymbol{p} \delta \boldsymbol{x} (\boldsymbol{p} \in \boldsymbol{G})$, we then center a *scaling function* of the form

$$e_{\boldsymbol{p}}(\boldsymbol{x}) = e_{\mathbf{0}}(\boldsymbol{x} - \boldsymbol{p} \delta \boldsymbol{x}) \quad \text{with} \quad e_{\mathbf{0}}(\boldsymbol{x}) = \text{sinc}\left(\frac{x}{\delta x}\right) \text{sinc}\left(\frac{y}{\delta x}\right). \quad (16.2)$$

It is easy to verify that these functions form an orthogonal set. In this presentation of WIPE, the *object space* H_o is the Euclidian space generated by the basis vectors $e_{\boldsymbol{p}}$, \boldsymbol{p} spanning \boldsymbol{G} (see Fig. 16.2).

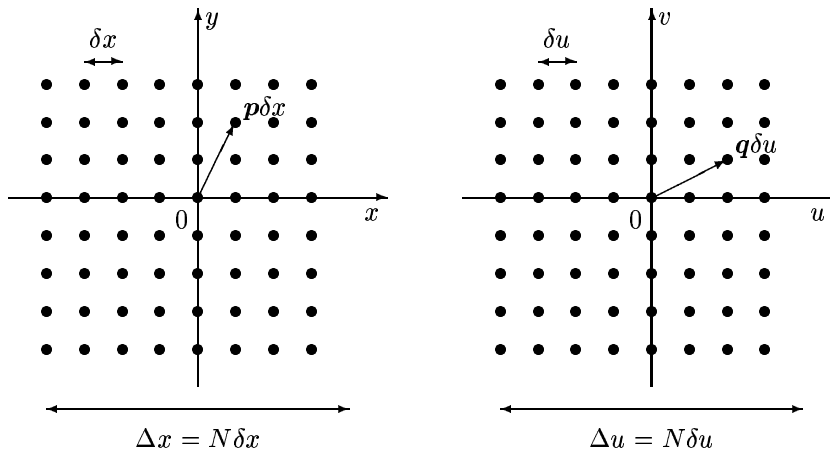


Figure 16.2: Object grid $\mathbf{G} \delta x$ (left hand) and Fourier grid $\mathbf{G} \delta u$ (right hand) for $N = 8$. The object domain is characterized by its resolution scale δx and the extension of its field $\Delta x = N \delta x$, where N is some power of 2 (the larger is N , the more oversampled is the object field). The basic Fourier sampling interval is $\delta u = 1/\Delta x$, the extension of the Fourier domain is $\Delta u = 1/\delta x$.

The dimension of this space is equal to N^2 : the number of *pixels* in the grid \mathbf{G} . The functions ϕ lying in H_o can therefore be expanded in the form

$$\phi(\mathbf{x}) = \sum_{\mathbf{p} \in \mathbf{G}} a_{\mathbf{p}} e_{\mathbf{p}}(\mathbf{x}), \quad (16.3)$$

where the $a_{\mathbf{p}}$'s are the components of ϕ in the interpolation basis of H_o .

The Fourier transform of ϕ is defined by the relationship

$$\hat{\phi}(\mathbf{u}) = \int \phi(\mathbf{x}) e^{-2i\pi \mathbf{u} \cdot \mathbf{x}} d\mathbf{x},$$

where \mathbf{u} is a two-dimensional angular spatial frequency: $\mathbf{u} = (u, v)$. According to the expansion of ϕ we therefore have:

$$\hat{\phi}(\mathbf{u}) = \sum_{\mathbf{p} \in \mathbf{G}} a_{\mathbf{p}} \hat{e}_{\mathbf{p}}(\mathbf{u}), \quad (16.4)$$

where

$$\hat{e}_{\mathbf{p}}(\mathbf{u}) = \hat{e}_0(\mathbf{u}) e^{-2i\pi \mathbf{p} \cdot \frac{\mathbf{u}}{\Delta u}} \quad \text{with} \quad \hat{e}_0(\mathbf{u}) = \frac{1}{(\Delta u)^2} \text{rect}\left(\frac{u}{\Delta u}\right) \text{rect}\left(\frac{v}{\Delta u}\right) \quad (16.5)$$

and $\Delta u = 1/\delta x$.

The dual space of the *object space*, \hat{H}_o , is the image of H_o by the Fourier transform operator: \hat{H}_o is the space of the Fourier transforms of the functions ϕ lying in H_o . This space is characterized by two key parameters: its extension $\Delta u = 1/\delta x$, and the basic Fourier sampling interval $\delta u = 1/\Delta x$ (see Fig. 16.2).

16.3 Experimental data space

The *experimental data* $\Psi_e(\mathbf{u})$ are blurred values of $\hat{\Phi}_o(\mathbf{u})$ on a finite list of frequencies in the Fourier domain:

$$\mathcal{L}_e = \{\mathbf{u}_e(1), \mathbf{u}_e(2), \dots, \mathbf{u}_e(N_e)\}. \quad (16.6)$$

As the *object function* of interest Φ_o is a real-valued function, it is natural to define $\Psi_e(-\mathbf{u})$ as the complex conjugate of $\Psi_e(\mathbf{u})$. The *experimental frequency list* \mathcal{L}_e is defined consequently: if $\mathbf{u} \in \mathcal{L}_e$, then $-\mathbf{u} \in \mathcal{L}_e$ (except for the null frequency $\mathbf{u} = \mathbf{0}$: in the convention adopted here, either it does not lie in \mathcal{L}_e , or there exists only one occurrence of this point). The *experimental frequency coverage* generated by \mathcal{L}_e is therefore centrosymmetric (see Fig. 16.3).

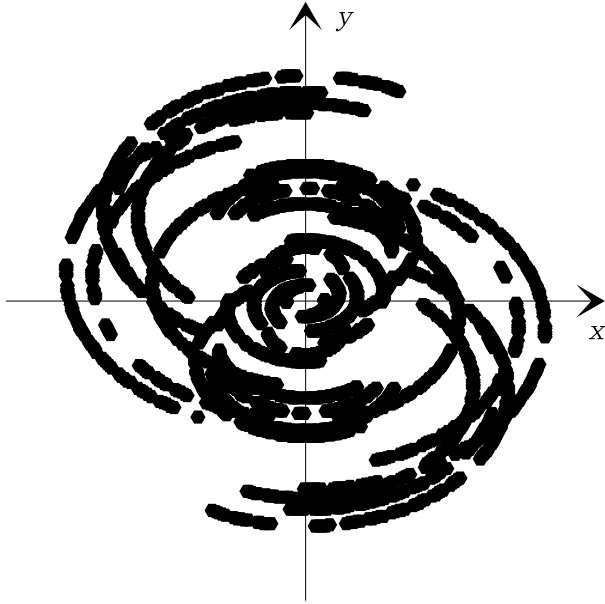


Figure 16.3: An example of an *experimental frequency coverage* provided by the IRAM interferometer. Here, the number of points N_e in the *experimental frequency list* \mathcal{L}_e is equal to 2862.

The *experimental data vector* Ψ_e lies in the *experimental data space* K_e , the real Euclidian space underlying the space of complex-valued functions ψ on \mathcal{L}_e , such that $\psi(-\mathbf{u}) = \bar{\psi}(\mathbf{u})$. The dimension of this space is equal to N_e : the number of points in the *experimental frequency list* \mathcal{L}_e .

16.4 Image reconstruction process

As the *experimental frequency list* is finite, and in addition the *experimental data* blurred, the object representation that can be obtained from these data is of course incomplete. This simple remark shows that the inverse problems of Fourier synthesis must be regularized: the high-frequency components of the *image to be reconstructed* must be negligible.

The central problem is to specify in which conditions it is possible to extrapolate or interpolate, in some region of the Fourier domain, the Fourier transform of a function ϕ whose support is contained in some finite region of H_o . It is now well established that extrapolation is forbidden, and interpolation allowed to a certain extent. The corresponding regularization principle is then intimately related to the concept of resolution: the interpolation is performed in the frequency gaps of the *frequency coverage to be synthesized*.

16.4.1 Synthesized aperture

Let \mathcal{H} be the Fourier domain: $\mathcal{H} = (-\Delta u/2, \Delta u/2)^2$. In Fourier synthesis, the *frequency coverage to be synthesized* is a centro-symmetric region $\mathcal{H}_s \subset \mathcal{H}$ (see Fig. 16.4).

CLEAN and WIPE share a common objective, that of the *image to be reconstructed*. This image, Φ_s , is defined so that its Fourier transform is quadratically negligible outside \mathcal{H}_s . More explicitly, Φ_s is defined by the convolution relation:

$$\Phi_s = \Theta_s \star \Phi_o. \quad (16.7)$$

The “synthetic beam” Θ_s is a function resulting from the choice of \mathcal{H}_s : the well-known *clean beam* in CLEAN, the *neat beam* in WIPE.

16.4.2 Synthetic beam

The *neat beam* can be regarded as a sort of optimal *clean beam*: the optimal apodized point-spread function that can be designed within the limits of the Heisenberg principle. More precisely, the *neat beam* Θ_s is a centro-symmetric function lying in the *object space* H_o , and satisfying the following properties:

- The energy of $\hat{\Theta}_s$ is concentrated in \mathcal{H}_s . In other words, $\hat{\Theta}_s$ has to be small outside \mathcal{H}_s in the mean-square sense: we impose the fraction χ^2 of this energy in \mathcal{H}_s to be close to 1 (say $\chi^2 = 0.98$).
- The effective support \mathcal{D}_s of Θ_s in H_o is as small as possible with respect to the choice of \mathcal{H}_s and χ^2 . The idea is of course to have the best possible resolution.

This apodized point-spread function is thus computed on the grounds of a trade-off between resolution and efficiency, with the aid of the *power method*.

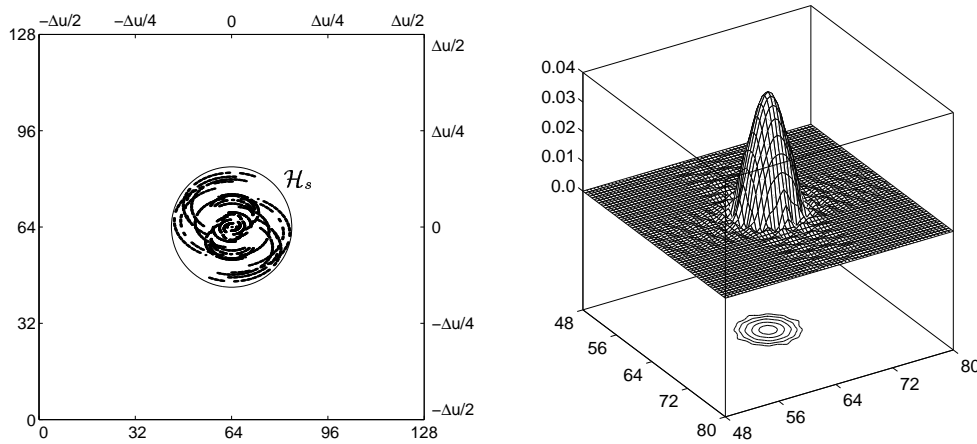


Figure 16.4: *Experimental frequency coverage and frequency coverage to be synthesized \mathcal{H}_s (left hand).* The *experimental frequency list* \mathcal{L}_e includes $N_e = 2862$ frequency points. The *frequency coverage to be synthesized \mathcal{H}_s* is centred in the Fourier grid $\mathbf{G} \delta u$, where $\delta u = \Delta u / N$ with $N = 128$ (here, the diameter of the circle is equal to $40 \delta u$). The *neat beam* Θ_s (right hand) represented here corresponds to the *frequency coverage to be synthesized \mathcal{H}_s* for a given value of $\chi^2 = 0.97$. It is centred in the object grid $\mathbf{G} \delta x$ where $\delta x = 1 / \Delta u$ (here, the full width of Θ_s at half maximum is equal to $5 \delta x$).

16.4.3 Regularization frequency list

As extrapolation is forbidden, and interpolation only allowed to a certain extent in the frequency gaps of the *frequency coverage to be synthesized*, the *experimental frequency list* \mathcal{L}_e should be completed by high-frequency points. These points, located outside the *frequency coverage to be synthesized \mathcal{H}_s* , are those for which the high-frequency components of the *image to be reconstructed* are practically negligible.

The elements of the *regularization frequency list* \mathcal{L}_r are the frequency points \mathbf{u}_r located outside the *frequency coverage to be synthesized \mathcal{H}_s* at the nodes of the Fourier grid $\mathbf{G} \delta u$:

$$\mathcal{L}_r = \{\mathbf{u}_r = \mathbf{q} \delta u, \mathbf{q} \in \mathbf{G} : \mathbf{q} \delta u \notin \mathcal{H}_s\}. \quad (16.8)$$

The *global frequency list* \mathcal{L} is then the concatenation of \mathcal{L}_e with \mathcal{L}_r .

16.4.4 Data space

According to the definition of the *image to be reconstructed*, the Fourier data corresponding to Φ_s are defined by the relationship:

$$\Psi_s(\mathbf{u}) = \widehat{\Theta}_s(\mathbf{u})\Psi_e(\mathbf{u}) \quad \forall \mathbf{u} \in \mathcal{L}_e. \quad (16.9)$$

Clearly, Ψ_s lies in the *experimental data space* K_e .

Let us now introduce the *data vector*:

$$\Psi_d(\mathbf{u}) = \begin{cases} \Psi_s(\mathbf{u}) & \text{on } \mathcal{L}_e; \\ 0 & \text{on } \mathcal{L}_r. \end{cases} \quad (16.10)$$

This vector lies in the *data space* K_d , the real Euclidian space underlying the space of complex-valued functions ψ on \mathcal{L} , such that $\psi(-\mathbf{u}) = \bar{\psi}(\mathbf{u})$. This space is equipped with the scalar product:

$$(\psi_1 | \psi_2)_d = \sum_{\mathbf{u} \in \mathcal{L}_e} \bar{\psi}_1(\mathbf{u})\psi_2(\mathbf{u})W(\mathbf{u})(\delta u)^2 + \sum_{\mathbf{u} \in \mathcal{L}_r} \bar{\psi}_1(\mathbf{u})\psi_2(\mathbf{u})(\delta u)^2; \quad (16.11)$$

$W(\mathbf{u})$ is a given *weighting function* that takes into account the reliability of the data via the standard deviation $\sigma_e(\mathbf{u})$ of $\Psi_e(\mathbf{u})$, as well as the local redundancy $\rho(\mathbf{u})$ of \mathbf{u} up to the sampling interval δu .

The *Fourier sampling operator* A is the operator from the *object space* H_o into the *data space* K_d :

$$A : H_o \longrightarrow K_d, \quad (A\phi)(\mathbf{u}) = \begin{cases} \widehat{\phi}(\mathbf{u}) & \text{on } \mathcal{L}_e; \\ \widehat{\phi}(\mathbf{u}) & \text{on } \mathcal{L}_r. \end{cases} \quad (16.12)$$

As the *experimental data* $\Psi_e(\mathbf{u})$ are blurred values of $\widehat{\Phi}_o(\mathbf{u})$ on \mathcal{L}_e , this operator will play a key role in the image reconstruction process. The definition of this *Fourier sampling operator* suggests that the action of A should be decomposed into two components: A_e on the *experimental frequency list* \mathcal{L}_e , and A_r on the *regularization frequency list* \mathcal{L}_r .

16.4.5 Object representation space

The *reconstructed image* is defined as the function Φ_E of the *object space* H_o minimizing some objective functional. The definition of this functional takes into account the nature of the data, as well as other constraints. For example, the *image to be reconstructed* may be confined to a subspace, or more generally to a convex set, of the *object space* H_o : this convex set is the *object representation space* E . It may be defined from the outset (in an interactive manner, for example), or step by step throughout the image reconstruction procedure (this is the case of the current implementation of WIPE). In both cases, the projection operator onto this space, the projector P_E , will play an essential role in the image reconstruction process.

REMARK 1: positivity constraint.

In most cases encountered in practice, the scalar components of Φ_E in the interpolation basis of H_o must be non-negative (cf. Eq.??). In the current implementation of WIPE this constraint is taken into account. The *object representation space* E is then built, step by step, accordingly.

16.4.6 Objective functional

The *reconstructed image* is defined as the function Φ_E minimizing on E the objective functional:

$$q(\phi) = \|\Psi_d - A\phi\|_d^2. \quad (16.13)$$

According to the definition of the *data vector* Ψ_d and to that of the *Fourier sampling operator* A , this quantity can be written in the form:

$$q(\phi) = q_e(\phi) + q_r(\phi) \quad \text{with} \quad \begin{cases} q_e(\phi) = \sum_{\mathbf{u} \in \mathcal{L}_e} |\Psi_s(\mathbf{u}) - \widehat{\phi}(\mathbf{u})|^2 W(\mathbf{u})(\delta u)^2; \\ q_r(\phi) = \sum_{\mathbf{u} \in \mathcal{L}_r} |\widehat{\phi}(\mathbf{u})|^2 (\delta u)^2. \end{cases} \quad (16.14)$$

The experimental criterion q_e constrains the *object model* ϕ to be consistent with the damped Fourier data Ψ_s , while the regularization criterion q_r penalizes the high-frequency components of ϕ .

Let now F be the image of E by A (the space of the $A\phi$'s, ϕ spanning E), A_E be the operator from E into F induced by A , and Ψ_F the projection of Ψ_d onto F (see Fig. 16.7). The vectors ϕ minimizing q on E , the solutions of the problem, are such that $A_E\phi = \Psi_F$. They are identical up to a vector lying in the kernel of A_E (by definition, the kernel of A_E is the space of vectors ϕ such that $A_E\phi = 0$).

As $\Psi_d - \Psi_F$ is orthogonal to F , the solutions ϕ of the problem are characterized by the property: $\forall \varphi \in E, (A\varphi | \Psi_d - A\phi)_d = 0$. On denoting by A^* the adjoint of A , this property can also be written in the form:

$$\forall \varphi \in E, (\varphi | r)_o = 0, \text{ with } r = A^*(\Psi_d - A\phi). \quad (16.15)$$

where r is regarded as a residue. This condition is of course equivalent to $P_E r = 0$, where P_E is the projector onto the *object representation space* E . The solutions of the problem are therefore the solutions of the *normal equation* on E :

$$A_E^* A_E \phi = A_E^* \Psi_d, \quad (16.16)$$

where $A_E^* = P_E A^*$.

Many different techniques can be used for solving the *normal equation* (or minimizing q on E). Some of these are certainly more efficient than others, but this is not a crucial choice.

REMARK 2: beams and maps.

The action of A^*A involved in $A_E^*A_E$ is that of a convolutor. As the two lists \mathcal{L}_e and \mathcal{L}_r are disjoint, we have: $A^*A = A_e^*A_e + A_r^*A_r$. Thus, the corresponding point-spread function, called the *dusty beam*, has two components: the traditional *dirty beam* Θ_d and the *regularization beam*. The latter corresponds to the action of $A_r^*A_r$, the former to that of $A_e^*A_e$ (see Fig. 16.5). Likewise, according to the definition of the *data vector*, $A^*\Psi_d = A_e^*\Psi_s$ is called the *dusty map* (as opposed to the traditional *dirty map* $A_e^*\Psi_d$ because it is damped by the *neat beam*).

REMARK 3: construction of the *object representation space*.

With regard to the construction of the *object representation space* E , CLEAN and WIPE are very similar: it is defined through the choice of the (discrete) object support. It is important to note that this space may be constructed, in a global manner or step by step, interactively or automatically. In the last version of WIPE implemented at IRAM, the image reconstruction process is initialized with a few iterations of CLEAN. The support selected by CLEAN is refined throughout the iterations of WIPE by conducting a matching pursuit process at the level of the components of r in the interpolation basis of H_o : the current support is extended by adding the nodes of the object grid $G\delta x$ for which these coefficients are the largest above a given threshold (half of the maximum value, for example). The objective functional is then minimized on that new support, and the global residue r updated accordingly. The *object representation space* of the *reconstructed image* is thus obtained step by step in a natural manner.

The simulation presented on Fig.16.5-16.6 corresponds to the conditions of Fig. 16.4. The Fourier data Ψ_e were blurred by adding a Gaussian noise: for all $\mathbf{u} \in \mathcal{L}_e$, the standard deviation of $\Psi_e(\mathbf{u})$ was set equal to 5% of the total flux of the object ($\hat{\Phi}_o(\mathbf{0})/20$). The image reconstruction process was initialized with a few iterations of CLEAN, and the construction of the final support of the *reconstructed image* was made as indicated in Remark 3. At the end of the reconstruction process, a final smoothing of the current object support was performed. In this classical operation of mathematical morphology, the effective support of Θ_s, \mathcal{D}_s , is of course used as a structuring element. The boundaries of the effective support of the reconstructed *neat map* are thus defined at the appropriate resolution. In particular, the connected entities of size smaller than that of \mathcal{D}_s are eliminated.

16.4.7 Uniqueness and robustness

When the problem is well-posed, A_E is a one-to-one map ($\ker A_E = \{0\}$) from E onto F ; the solution is then unique: there exists only one vector $\phi \in E$ such that $A_E\phi = \Psi_F$. This vector, Φ_E , is said to be the least-squares solution of the equation $A_E\phi = \Psi_d$.

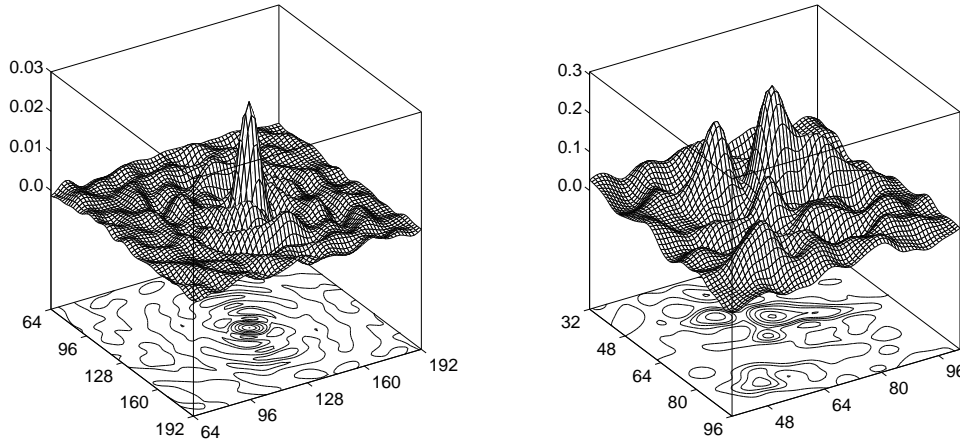


Figure 16.5: *Dirty beam* (left hand) corresponding to the *experimental frequency list* \mathcal{L}_e of Fig. 16.4, and *dusty map* (right hand) of a simulated data set (the simulated Fourier data Ψ_e were blurred by adding a Gaussian noise with a standard deviation σ_e equal to 5% of the total flux of the object Φ_o).

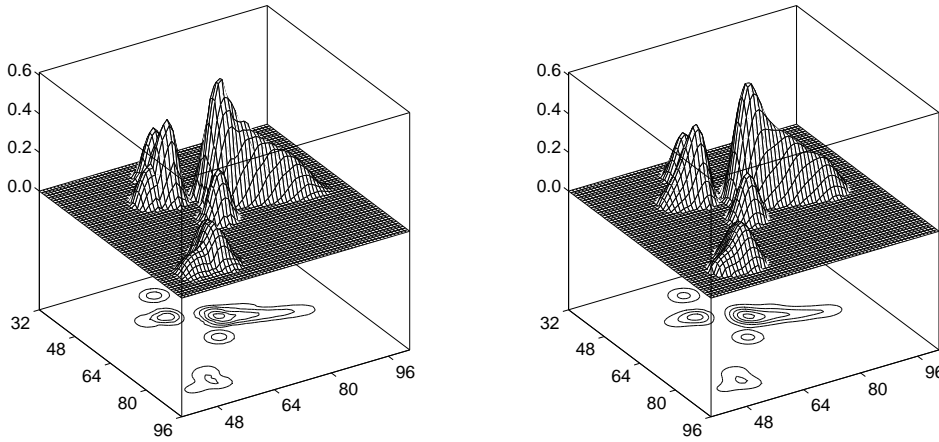


Figure 16.6: *Image to be reconstructed* Φ_s (left hand) at the resolution level defined in Fig. 16.4, and *reconstructed neat map* Φ_E (right hand) at the same resolution: the final *condition number* κ_E is equal to 2.46 (cf. Eq. 16.17 and 16.18).

In this case, let $\delta\Psi_F$ be a variation of Ψ_F in F , and $\delta\Phi_E$ be the corresponding variation of Φ_E in E (see Fig. 16.7). It is easy to show that the robustness of the reconstruction process is governed by the inequality:

$$\frac{\|\delta\Phi_E\|_o}{\|\Phi_E\|_o} \leq \kappa_E \frac{\|\delta\Psi_F\|_d}{\|\Psi_F\|_d}. \quad (16.17)$$

The error amplifier factor κ_E is the condition number of A_E :

$$\kappa_E = \frac{\sqrt{\lambda'}}{\sqrt{\lambda}}; \quad (16.18)$$

here λ and λ' respectively denote the smallest and the largest eigenvalues of $A_E^* A_E$. The closer to 1 is the condition number, the easier and the more robust is the reconstruction process (see Fig. 16.8 and 16.9).

The part played by inequality 16.17 in the development of the corresponding error analysis shows that a good reconstruction procedure must also provide, in particular, the condition number κ_E . This is the

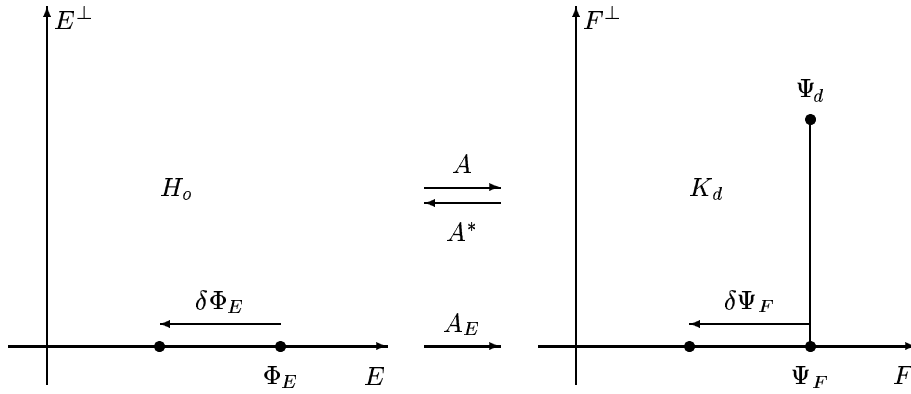


Figure 16.7: Uniqueness of the solution and robustness of the reconstruction process. Operator A is an operator from the *object space* H_o into the *data space* K_d . The *object representation space* E is a particular subspace of H_o . The image of E by A , the range of A_E , is denoted by F . In this representation, Ψ_F is the projection of the data vector Ψ_d onto F . The inverse problem must be stated so that A_E is a one-to-one map from E onto F , the condition number κ_E having a reasonable value.

case of the current implementation of WIPE which uses the *conjugate gradient* method for solving the *normal equation* 16.16.

To conduct the final error analysis, one is led to consider the eigenvalue decomposition of $A_E^* A_E$. This is done, once again, with the aid of the *conjugate gradient* method associated with the *QR* algorithm. At the cost of some memory overhead (that of the M successive residues), the latter also yields approximations of the eigenvalues λ_k of $A_E^* A_E$. It is thus possible to obtain the scalar components of the associated eigenmodes Φ_k in the interpolation basis of H_o . The purpose of this analysis is to check whether some of them (in particular those corresponding to the smallest eigenvalues) are excited or not in Φ_E . If so, the corresponding details may be artefacts of the reconstruction.

The reconstructed map is then decomposed in the form:

$$\Phi_E = \sum_{k=1}^M w_k \Phi_k, \quad w_k = (\Phi_k | \Phi_E). \quad (16.19)$$

The separation angle θ_k between Φ_E and Φ_k is explicitly given by the relationship:

$$\cos \theta_k = \frac{w_k}{\sqrt{\sum_{k=1}^M w_k^2}} \quad (0 \leq \theta_k \leq \pi/2). \quad (16.20)$$

The closer to $\pi/2$ is θ_k , the less excited is the corresponding eigenmode Φ_k in the reconstructed *neat map* Φ_E .

To illustrate in a concrete manner the interest of equations 16.19 and 16.20, let us consider the simulations presented in Fig. 16.4 and 16.9. Whatever the value of the final condition number is, the error analysis allows the astronomer to check if there exists a certain similitude between some details in the *neat map* and some features of the critical eigenmodes. This information is very attractive, in particular when the resolution of the reconstruction process is greater than a reasonable value (the larger is the *aperture to be synthesized* \mathcal{H}_s , the smaller is the full width at half-maximum of Θ_s). In such situations of “super resolution,” the error analysis will suggest the astronomer to redefine the problem at a lower level of resolution, or to keep in mind that some details in the reconstructed *neat map* may be artefacts of the reconstruction process.

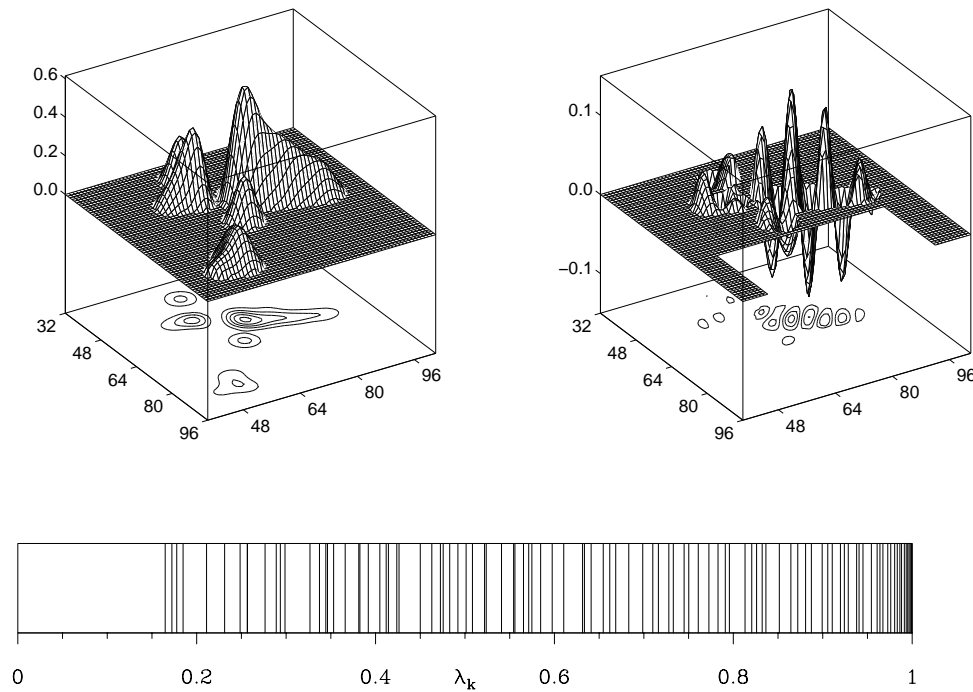


Figure 16.8: Reconstructed *neat map* Φ_E (left hand) and eigenmode Φ_1 (right hand) corresponding to the smallest eigenvalue $\lambda_1 = 0.165$ of $A_E^* A_E$. The conditions of the simulations are those of Fig. 16.4 and 16.5: in particular, the diameter of \mathcal{H}_s is equal to $40 \delta u$. The final condition number is $\kappa_E = 2.46$ (the eigenvalues of $A_E^* A_E$ are plotted on the bar code below). This eigenmode is not excited in Φ_E : the separation angle θ_1 between Φ_E and Φ_1 is greater than 89° . In other situations, when the final condition number is greater, this mode may be at the origin of some artefacts in the *neat map* (see Fig. 16.9).

16.5 Implementation of WIPE at IRAM

In this section we describe the successive steps of the image reconstruction process as it is implemented now in the MAPPING program included in the IRAM software. For more information on this program, the reader is invited to read the last version of the *Mapping Cookbook*.

The first step of the image reconstruction process is to define the *object space* H_o . This space is characterized by two key parameters: the extension Δx of its field, and its resolution scale $\delta x = \Delta x/N$ (see Fig. 16.2). The procedure `wipe_init` is used to set these parameters properly.

The *frequency coverage to be synthesized* \mathcal{H}_s is defined with the aid of the procedure `wipe_aper`. This tool provides an interactive way of fitting an ellipse over the *experimental frequency coverage* generated by the *experimental frequency list* \mathcal{L}_e (see Fig. 16.4).

Once \mathcal{H}_s has been defined, the procedure `wipe_beam` is ready for computing the *neat beam* Θ_s , as well as the *dirty beam* Θ_d . The latter plays a key role in the action of the convolutor $A_E^* A_E$, while the Fourier transform of the former is involved in the definition of the *data vector* Ψ_d (cf. Eq. 16.9 and 16.10).

The last step in the image reconstruction process concerns the *neat map*. It is implemented in the `wipe_solve` command. Before the initialization of the reconstruction, the *dusty map* $A^* \Psi_d$ is computed, and an optional support can be selected (this support plays the role of the *clean box* of CLEAN). As WIPE can be slow when reconstructing large images, it can be initialized with a few CLEAN iterations to quickly build a first *object representation space* E . When switching to WIPE, the program starts by optimizing the solution provided by CLEAN with the corresponding support. Then, at each iteration of WIPE, the support grows, and for a given and fixed *object representation space* E , the *normal equation* 16.16 is solved by using the *conjugate gradient* method, which also provides the condition number κ_E of A_E . When leaving WIPE, a final smoothing of the current object support is performed, removing (through an appropriate morphological analysis) the details of the *reconstructed image* smaller than the resolution limit

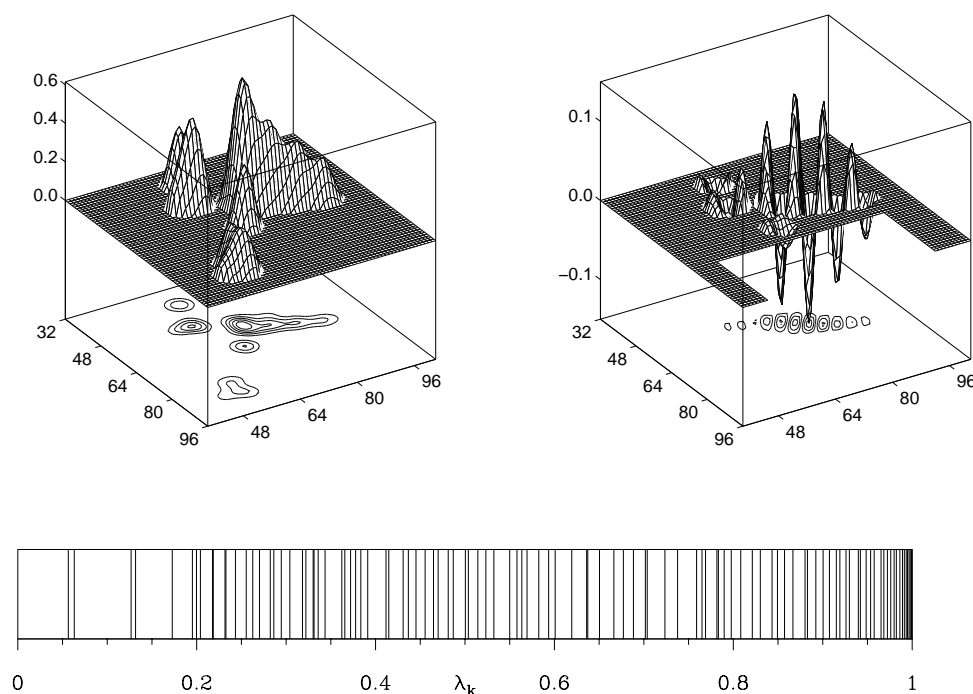


Figure 16.9: Reconstructed *neat map* Φ_E (*left hand*) and related critical eigenmode Φ_1 (*right hand*). The latter corresponds to the smallest eigenvalue $\lambda_1 = 0.057$ of $A_E^* A_E$. The conditions of the simulations are those of Fig. 16.5, but here the diameter of \mathcal{H}_s is taken equal to $48 \delta u$: the final condition number is $\kappa_E = 4.19$ (the eigenvalues of $A_E^* A_E$ are plotted on the bar code below). The critical eigenmode Φ_1 is at the origin of the oscillations along the main structuring entity of Φ_E . This mode is slightly excited (the separation angle θ_1 between Φ_E and Φ_1 is less than 86°), thus the corresponding details may be artefacts. In this case of “super-resolution” the error analysis provided by WIPE suggests that the procedure should be restarted at a lower level of resolution (see Fig. 16.8), so that the final solution be more stable and reliable.

of the reconstruction process. The final *reconstructed image* Φ_E is the function minimizing the objective functional 16.13 on that support.

The control of the robustness of the reconstruction process is performed through an additional step with the `wipe_error` command. This procedure computes with a fine accuracy the final *condition number* κ_E , as well as the eigenvalues and the critical eigenmodes of $A_E^* A_E$. One of the aims of this last step is to check that the features present in the *reconstructed image* are not artefacts. This can be done by comparing these features with those of the critical eigenmodes. When there exists a certain similitude (between these features), it is then recommended to restart the process with a lower resolution, so that the final solution be more stable and reliable.

Glossary

L, N	One-dimensional grid, number of elements in L
$G = L \times L$	Two-dimensional grid
$\mathbf{p} = (p, q)$	Two-dimensional integer vector
$\mathbf{x} = (x, y)$	Two-dimensional angular position variable
$\mathbf{u} = (u, v)$	Two-dimensional angular spatial frequency
Δx	Extension of the synthesized field
δx	Resolution scale of the synthesized field
Δu	Extension of the Fourier domain
δu	Basic Fourier sampling interval
$G \delta x, G \delta u$	Object grid, Fourier grid
\mathcal{L}	Global frequency list
$\mathcal{L}_e, \mathcal{L}_r$	Experimental frequency list, regularization frequency list
\mathcal{H}	Fourier domain $[-\Delta u/2, \Delta u/2]$
\mathcal{H}_s	Frequency coverage to be synthesized
\mathcal{D}_s	Support of the neat beam Θ_s
χ^2	Energy confinement parameter
Θ_s	Apodized point-spread function (neat beam)
Θ_d	Instrumental point-spread function (dirty beam)
$H_o, e_p(\mathbf{x})$	Object space, basis functions of H_o
E, F	Object representation space, image of E by A
K_e, K_d	Experimental data space, data space
$W(\mathbf{u})$	Weighting function
$\rho(\mathbf{u}), \sigma_e(\mathbf{u})$	Redundancy of \mathbf{u} , standard deviation of $\Psi_e(\mathbf{u})$
A	Regularized Fourier sampling operator
A_e, A_r	Fourier sampling operator on \mathcal{L}_e , on \mathcal{L}_r
P_E, A_E	Projection operator onto E , restriction of A to E
Φ_o, Φ_s	Original object function, image to be reconstructed
$\Phi_E, \delta\Phi_E$	Reconstructed image, reconstruction error on Φ_E
Ψ_e, Ψ_s	Experimental data, damped experimental data
Ψ_d	Regularized data vector
$\Psi_F, \delta\Psi_F$	Projection of Ψ_d onto F , effective error on Ψ_F
λ_k, Φ_k	Eigenvalue of $A_E^* A_E$ and related eigenmode
θ_k	Separation angle between Φ_E and Φ_k
λ, λ'	Smallest and largest eigenvalues of $A_E^* A_E$
κ_E	Condition number of A_E
$q(\phi)$	Regularized criterion
$q_e(\phi), q_r(\phi)$	Experimental criterion, regularization criterion

Chapter 17

Mosaicing

Frédéric Gueth^{1,2}

gueth@iram.fr

¹ Max Planck Institute für Radioastronomie, Auf dem Hügel 69, D-5300 Bonn, Germany

² IRAM, 300 rue de la piscine, F-38406 Saint-Martin-d'Hères, France

17.1 Introduction

For a single-field interferometric observation, the dirty map F is obtained by Fourier Transform of the observed visibilities. It is related to the actual sky brightness distribution I by:

$$F = D * (B \times I) + N \quad (17.1)$$

where D is the dirty beam, B the antenna primary beam, and N a noise distribution¹. Hence, an interferometer only measures the product $B \times I$. B is a rapidly decreasing function, and it therefore limits the size of the region it is possible to map. Correcting for the primary beam attenuation (i.e. dividing the map by B) is possible, and necessary for a proper estimate of the flux densities, but it does not enlarge the field of view, because of the noise distribution strongly increasing with the distance to the map center after such a correction.

Due to the coupling between the receiver horn and the primary mirror of the antennas (see Chapter 1 by A. Greve), the primary beam B is, to a good approximation, a Gaussian. Its FWHM, proportional to the ratio of the wavelength λ to the antenna diameter \mathcal{D} , can therefore be used to quantify the field of view. Note that this size does not correspond to a clear cut of the map, but to the 50% attenuation level. Table 17.1 gives the resulting values for the Plateau de Bure interferometer, for different frequencies. To map regions more extended than the primary beam width, it is necessary to observe a *mosaic* of several

¹In the following, we will assume an uniform noise rms, i.e. we do not take into account variation of the noise introduced by the imaging process (see Chapter 15 by S. Guilloteau).

Frequency (GHz)	Wavelength (mm)	Field of View ($''$)	Largest structure ($''$)
85	3.5	58	36
100	3.0	50	31
115	2.6	43	27
215	1.4	23	14
230	1.3	21.5	13
245	1.2	20	12

Table 17.1: Field of view of the Plateau de Bure interferometer (15 m dishes). The two groups of frequencies correspond to the two receivers that are currently available. The last column gives *rough estimates* of the size of the largest structure which can be observed.

adjacent fields. Clearly, due to the gaussian-shape of the primary beam attenuation, these fields have to strongly overlap to ensure a roughly uniform sensitivity over the whole mapped region.

A further complication arises from the lack of the short-spacings information in the interferometer data set. Due to their diameter, the antennas cannot be put too close to each other, which results in a minimal measured baseline (24 m at the Plateau de Bure). Even if projection effects reduce the effective baselines, a central “hole” in the data distribution in the uv plane cannot be avoided. As a consequence, the extended structures (whose visibilities are confined in a small region in the uv plane) are filtered out. The largest structure it is possible to map with a single-field interferometric observation is thus even smaller than the field of view, and can be very roughly estimated by the ratio of the wavelength to the minimal baseline (Table 17.1).

17.2 Image formation in a mosaic

Some important mosaic properties can be understood by analyzing the combination of the data directly in the uv plane. This analysis was first proposed by [Ekers & Rots 1979]. The reader is also referred to [Cornwell 1989]. We consider a source with a brightness distribution $I(x, y)$, where x and y are two angular coordinates. The “true” visibility, i.e. the Fourier Transform of I , is noted $V(u, v)$. An interferometer baseline, with two identical antennas whose primary beam is $B(x, y)$, measures a visibility at a point (u, v) which may be written as:

$$V_{\text{mes}}(u, v) = \iint_{-\infty}^{+\infty} B(x, y) I(x, y) e^{-2i\pi(ux + vy)} dx dy \quad (17.2)$$

If the observation is performed with a phase center in $(x = 0, y = 0)$ but with a pointing center in (x_p, y_p) , the measured visibility (whose dependence on (x_p, y_p) is here explicitly indicated) is:

$$V_{\text{mes}}(u, v, x_p, y_p) = \iint_{-\infty}^{+\infty} B(x - x_p, y - y_p) I(x, y) e^{-2i\pi(ux + vy)} dx dy \quad (17.3)$$

Using the symmetry properties of the primary beam B , this last relation can be rewritten:

$$V_{\text{mes}}(u, v, x_p, y_p) = B(x_p, y_p) * \mathcal{F}(u, v, x_p, y_p) \quad (17.4)$$

where $*$ denotes a convolution product and the function \mathcal{F} is defined as:

$$\mathcal{F}(u, v, x_p, y_p) = I(x_p, y_p) e^{-2i\pi(ux_p + vy_p)} \quad (17.5)$$

Now, let’s imagine an ideal “on-the-fly” mosaic experiment: for a given, fixed, (u, v) point, the pointing direction is continuously modified, and the variation of the visibility V_{mes} with (x_p, y_p) can thus be monitored. The Fourier Transform of these data with respect to (x_p, y_p) would give (from Eq. 17.4):

$$[\text{FT}_p(V_{\text{mes}})](u_p, v_p) = T(u_p, v_p) V(u + u_p, v + v_p) \quad (17.6)$$

where:

- FT_p denotes the Fourier Transform with respect to (x_p, y_p) .
- (u_p, v_p) are the conjugate variables to (x_p, y_p) .
- $[\text{FT}_p(V_{\text{mes}})](u_p, v_p)$ is the Fourier Transform of the observations.
- $T(u_p, v_p)$ is the Fourier Transform of the primary beam $B(x_p, y_p)$. T is thus the transfer function of each antenna. For a dish of diameter \mathcal{D} , $T(u_p, v_p) = 0$ if $(u_p^2 + v_p^2)^{1/2} > \mathcal{D}/\lambda$.
- $V(u + u_p, v + v_p)$ is the Fourier Transform of $\mathcal{F}(u, v, x_p, y_p)$ with respect to (x_p, y_p) . Indeed, \mathcal{F} is the product of the sky brightness distribution (whose Fourier Transform is V) by a phase term (see Eq. 17.5). Hence, its Fourier Transform is V taken at a shifted point.

For $\sqrt{u_p^2 + v_p^2} < \mathcal{D}/\lambda$, we can thus derive:

$$V(u + u_p, v + v_p) = \frac{[\text{FT}_p(V_{\text{mes}})](u_p, v_p)}{T(u_p, v_p)} \quad (17.7)$$

This relation illustrates an important property of the experiment we have considered. The observations were performed at a given (u, v) point but with a varying pointing direction. Eq. 17.7 shows that is possible to derive from this data set the visibility $V(u + u_p, v + v_p)$ at all (u_p, v_p) which verify $(u_p^2 + v_p^2)^{1/2} < \mathcal{D}/\lambda$. In other terms, the measurements have been done at (u, v) but the redundancy of the observations allows to compute (through a Fourier Transform and a division by the antenna transfer function) the source visibility at all the points of a disk of radius \mathcal{D}/λ , centered in (u, v) .

Interpretation

In very pictorial terms, one can say that the adjacent pointings reinforce each other and thereby yield an estimate of the source visibility at unmeasured points. Note however that the resulting image quality is not going to be drastically increased: more information can be extracted from the data, but a much more extended region has now to be mapped². The redundancy of the observations has only allowed to rearrange the information in the uv -plane. This is nevertheless extremely important, as e.g. it allows to estimate part of the missing short-spacings (see below).

How is it possible to recover unmeasured spacings in the uv -plane? It is actually obvious that two antennas of diameter \mathcal{D} , separated by a distance \mathcal{B} , are sensitive to all the baselines ranging from $\mathcal{B} - \mathcal{D}$ to $\mathcal{B} + \mathcal{D}$. The measured visibility is therefore an average of all these baselines: V_{mes} is actually the convolution of the “true” visibility by the transfer function of the antennas. This is shown by the Fourier Transform of Eq. 17.2, which gives: $V_{\text{mes}} = T * V$. Now, if the pointing center and the phase center differ, a phase gradient is introduced across the antenna apertures, which means that the transfer function is affected by a phase term. Indeed, the Fourier Transform of Eq. 17.3 yields:

$$V_{\text{mes}}(u, v) = \left[T(u, v) e^{-2i\pi(ux_p + vy_p)} \right] * V(u, v) \quad (17.8)$$

Hence, the measured visibilities are (still) a linear combination of the “true” visibilities. Measurements performed in various directions (x_p, y_p) give many such linear combinations. One can thus expect to derive from this linear system the initial visibilities, in the baseline range from $\mathcal{B} - \mathcal{D}$ to $\mathcal{B} + \mathcal{D}$. Eq. 17.7 just shows that a Fourier Transform allows to do that operation.

Field spacing in a mosaic

In the above analysis, a continuous drift of the pointing direction was considered. However, the same results can be reached in the case of a limited number of pointings, provided that classical sampling theorems are fulfilled. We want to compute the visibility in a finite domain, which extends up to $\pm\mathcal{D}/\lambda$ around the nominal (u, v) point, and therefore the pointing centers have to be separated by an angle of

²We have considered observations in different directions, performed with the same uv -coverage. The analysis presented here shows that such an experiment is somehow equivalent to a single observation of the whole source, but with a denser uv -coverage.

$\lambda/2\mathcal{D}$ radians (see [Cornwell 1988]). In practice, the (gaussian) transfer function of the millimeter dishes drops so fast that one can use without consequences a slightly broader, more convenient, sampling, equal to half the primary beam width (i.e. $1.2\lambda/2\mathcal{D}$).

Mosaics and short-spacings

As with any other measured point in the uv plane, it is possible to derive visibilities in a small region (a disk of diameter \mathcal{D}/λ) around the shortest measured baseline. This is the meaning of the statement that mosaics can recover part of the short-spacings information: a mosaic will include (u, v) points corresponding to the shortest baseline minus \mathcal{D}/λ .

In practice, however, things are more complex. First, we have to deal with noisy data. As a consequence, it is not possible to expect a gain of \mathcal{D}/λ : the transfer function T which is used in Eq. 17.7 is strongly decreasing, and thus signal-to-noise ratio limits the gain in the uv plane to a smaller value, typically $\mathcal{D}/2\lambda$ ([Cornwell 1988]). This is still a very useful gain: for the Plateau de Bure interferometer, this corresponds to a distance in the uv plane of $7.5\text{ m}/\lambda$, while the shortest (unprojected) baseline is $24\text{ m}/\lambda$. Secondly, the analysis described above would be rather difficult to implement with real observations, which have a limited number of pointing centers and different uv -coverages. Instead, one prefers to combine the observed fields to directly reconstruct the sky brightness distribution. The resulting image should include the information arising from the redundancy of the adjacent fields, among them part of the short-spacings. However, the complexity of the reconstruction and deconvolution algorithms that have to be used precludes any detailed mathematical analysis of the structures in the maps. For instance, the (unavoidable) deconvolution of the image can also be interpreted as an interpolation process in the uv plane (see [Schwarz 1978] for the case of the CLEAN algorithm) and its effects can thus hardly be distinguish from the intrinsic determination of unmeasured visibilities that occur when mosaicing.

17.3 Mosaicing in practice

Observation and calibration

The observation of a mosaic with the Plateau de Bure interferometer and the calibration of the data do not present any specific difficulties. We just mention here a few practical remarks:

- As shown in the previous paragraph, the optimal spacing between adjacent fields is half the half-power primary beam width. Larger separations can be used (e.g. to map larger field of view in the same amount of time) but the image reconstruction is not optimal in that case. Since observations are performed with dual-channel receivers (operating at 1.3 and 3 mm), the field spacing has to be chosen for one of the frequencies. Consequently, the mosaic observed at the other frequency is either under- or oversampled.
- Even if this is not formally required by the reconstruction and deconvolution algorithm described in the following section, it seems quite important to ensure similar observing conditions for all the pointing centers. Ideally, one wants the same noise level in each field – so that the noise in the final image is uniform – and the same uv -coverage – to avoid strong discrepancies (in terms of angular resolution and image artifacts) between the different parts of the mosaic. In practice, the fields are observed in a track-sharing mode, i.e. in a loop with a few minutes integration time per pointing direction: hence, atmospheric conditions and uv -coverage are similar for all the fields.
- In most cases, a mosaic is not observed during an amount of time significantly larger than normal projects. As the observing time is shared between the different pointing centers, the sensitivity of each individual field is thus smaller than what would have been achieved with normal single-field observations. Note however that the sensitivity is further increased in the mosaic, thanks to the strong overlap between the adjacent fields (see below, Fig. 17.1).
- The number of fields, and therefore the size of the mosaic, is limited by the requirement to get good enough sensitivity and uv -coverage for all the fields in a reasonable amount of observing time. The

current observing mode used at the Plateau de Bure limits the maximum number of fields to about 20. Observing more fields is in principle possible, but would require (much) more observing time and/or an other approach (e.g. mosaic of several mosaics). Note that in any case, the uv -coverage obtained for each field is sparse as compared to normal synthesis observations. Finally, a potential practical limitation is the disk and memory sizes of the computers, as mosaicing requires to handle very large data cubes.

- The calibration of the data, including the atmospheric phase correction, is strictly identical with any other observation performed with the Plateau de Bure interferometer, as only the observations of the calibrators (quasars) are used. At the end of the calibration process, a uv table and then a dirty map are computed for each pointing center.

Mosaic reconstruction

The point is now to reconstruct a mosaic from the observations of each field, in an optimal way in terms of signal-to-noise ratio. For the time being, let's forget the effects of the convolution by the dirty beam. Each field i can then be written: $F_i = B_i \times I + N_i$, where B_i is the primary beam of the interferometer, centered in a different direction for each observation i , and N_i is the corresponding noise distribution. In practice, the same phase center (i.e. the same coordinate system) is used for all the fields.

Hence, the mosaic observations can be described as several measurements of the same unknown quantity I , each one being affected by a weighting factor B_i . This is a classical mathematical problem: the best estimate J of I , in the least-square sense, is given by:

$$J = \frac{\sum_i \frac{B_i}{\sigma_i^2} F_i}{\sum_i \frac{B_i^2}{\sigma_i^2}} \quad (17.9)$$

where the sum includes all the observed fields and σ_i is the rms of the noise distribution N_i . (Note that in Eq. 17.9 as well as in the following equations, σ_i is a number while other letters denote two-dimensional distributions).

Linear vs. non-linear mosaicing

The problem which remains to be address is the deconvolution of the mosaic. This is actually the main difficulty of mosaic interferometric observations. Two different approaches have been proposed (e.g. [Cornwell 1993]):

- *Linear mosaicing*: each field is deconvolved using classical techniques, and a mosaic is reconstructed afterwards with the clean images, using Eq. 17.9.
- *Non-linear mosaicing*: a joint deconvolution of all the fields is performed, i.e. the deconvolution is performed after the mosaic reconstruction.

The deconvolution algorithms are highly non-linear, and the two methods are therefore not equivalent. The first one is straightforward to implement, but the non-linear mosaicing algorithms give much better results. Indeed, the combination of the adjacent fields in a mosaic allows to estimate visibilities which were not observed (see previous paragraph), it allows to remove sidelobes in the whole mapped area, and it increases the sensitivity in the (large) overlapping regions: these effects make the deconvolution much more efficient.

Non-linear deconvolution methods based on the Maximum Entropy Method (MEM) have been proposed by [Cornwell 1988] and [Sault et al 1996]. As CLEAN deconvolutions are usually applied on Plateau de Bure data, a CLEAN-based method adapted to the case of the mosaics has been developed. The initial idea was proposed by F. Viallefond (DEMIRM, Paris) and S. Guilloteau (IRAM), and the algorithm is now implemented in the MAPPING software.

17.4 A CLEAN-based algorithm for mosaic deconvolution

The dirty mosaic

The dirty maps of each field i are computed with the same phase center (i.e. the same coordinate system) and can thus be written:

$$F_i = D_i * (B_i \times I) + N_i \quad (17.10)$$

Note that the dirty beams D_i are *a priori* different for each pointing center, because the uv -coverages, even if similar, are slightly different. The dirty mosaic J can then be constructed according to Eq. 17.9:

$$J = \frac{\sum_i \frac{B_i}{\sigma_i^2} F_i}{\sum_i \frac{B_i^2}{\sigma_i^2}} = \frac{\sum_i B_i \sigma_i^{-2} [D_i * (B_i \times I) + N_i]}{\sum_i B_i^2 \sigma_i^{-2}} \quad (17.11)$$

This relation is homogeneous to the sky brightness distribution I : the mosaic is corrected for the primary beams attenuation. In practice, a slightly modified mosaic is computed, in order to avoid noise propagation (it makes no sense to add to the center of a field noise coming from the external, attenuated regions of an adjacent field). For that purpose, the primary beams used to construct the mosaic are truncated to some value, typically 10 to 30% of the maximum. The mosaic is thus defined by:

$$J = \frac{\sum_i \frac{B_i^t}{\sigma_i^2} F_i}{\sum_i \frac{B_i^{t2}}{\sigma_i^2}} = \frac{\sum_i B_i^t \sigma_i^{-2} [D_i * (B_i \times I) + N_i]}{\sum_i B_i^{t2} \sigma_i^{-2}} \quad (17.12)$$

where B_i^t denotes the truncated primary beam of the field i . This relation is the “measurement equation” of a mosaic, connecting the observed quantity J to the sky brightness distribution I (Eq. 17.1 was the measurement equation of a single-field observation).

Noise distribution

Due to the correction for the primary beams attenuation, the noise distribution in a mosaic is not uniform. From Eq. 17.12, it can be written:

$$N = \frac{\sum_i B_i^t \sigma_i^{-2} N_i}{\sum_i B_i^{t2} \sigma_i^{-2}} \quad (17.13)$$

Accordingly, the noise rms σ_J depends on the position and is given by:

$$\sigma_J = \frac{\sqrt{\sum_i B_i^{t2} \sigma_i^{-2}}}{\sum_i B_i^{t2} \sigma_i^{-2}} = \frac{1}{\sqrt{\sum_i B_i^{t2} \sigma_i^{-2}}} \quad (17.14)$$

Hence, the noise strongly increases at the edges of the mosaic, and the resulting image has thus to be truncated (see Fig. 17.1). The non-uniformity of the noise level with the position makes it impossible to use classical CLEAN methods to deconvolve the mosaic: the risk to identify a noise peak as a CLEAN component would be too important. It is thus necessary to identify the CLEAN components on another distribution. For that purpose, the “signal-to-noise” distribution is computed:

$$H = \frac{J}{\sigma_J} = \frac{\sum_i B_i^t \sigma_i^{-2} F_i}{\sqrt{\sum_i B_i^{t2} \sigma_i^{-2}}}$$

i.e. :

$$H = \frac{\sum_i B_i^t \sigma_i^{-2} [D_i * (B_i \times I) + N_i]}{\sqrt{\sum_i B_i^{t2} \sigma_i^{-2}}} \quad (17.15)$$

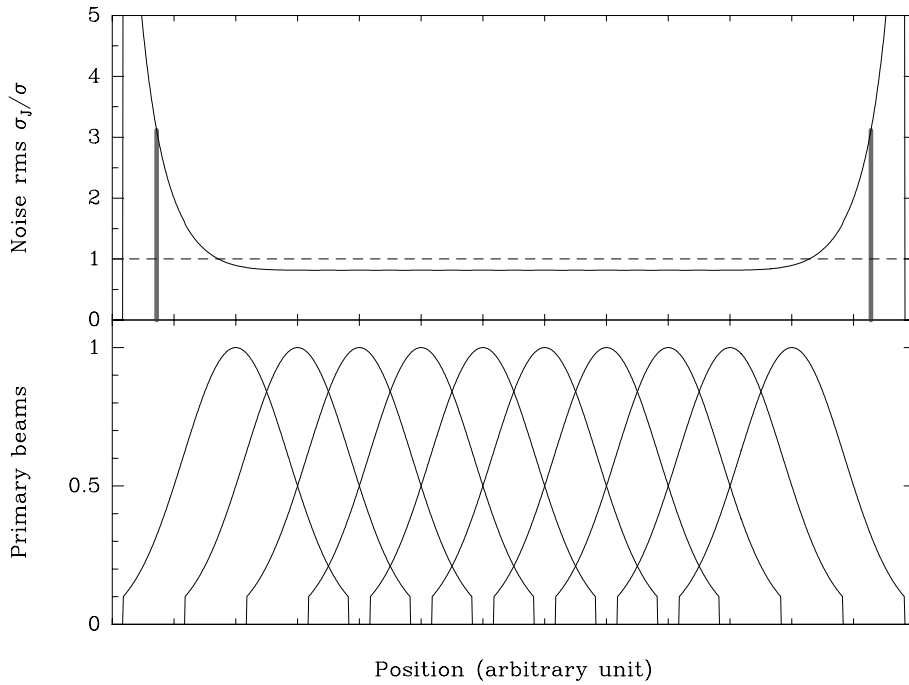


Figure 17.1: One-dimensional mosaic of 10 half-power overlapping fields, with identical noise level σ . Lower panel: Normalized primary beams, truncated to $B_{\min} = 0.1$. Upper panel: Resulting noise distribution (Eq. 17.14). The noise rms in the mosaic is roughly constant, about 20% lower than the noise of each individual field, but strongly increases at the edges. The two thick vertical lines indicate the truncation of the mosaic done by the algorithm at $\sigma_J = \sigma/\sqrt{B_{\min}}$.

Deconvolution algorithm

The main idea of the algorithm is to iteratively find the *positions* of the CLEAN components on H , and then to correct the mosaic J . The initial distributions J_0 and H_0 are computed from the observations and the truncated primary beams, using Eqs. 17.12 and 17.15. The following operations have then to be performed at each iteration k :

1. Find the position (x_k, y_k) of the maximum of H .
2. Find the value j_k of J at the position (x_k, y_k) , whether it is the maximum of J or not.
3. Remove from J the contribution of a point-like source of intensity γj_k , located at (x_k, y_k) (γ is the loop gain, as in the normal CLEAN algorithm):

$$J_k = J_{k-1} - \frac{\sum_i B_i^t \sigma_i^{-2} \left[D_i * \left[\gamma j_k B_i(x_k, y_k) \delta(x_k, y_k) \right] \right]}{\sum_i B_i^{t^2} \sigma_i^{-2}} \quad (17.16)$$

$\delta(x_k, y_k)$ denotes a Dirac peak located at (x_k, y_k) .

4. Do the same for H : remove the contribution of a point-like source of intensity γj_k , located at (x_k, y_k) :

$$H_k = H_{k-1} - \frac{\sum_i B_i^t \sigma_i^{-2} \left[D_i * \left[\gamma j_k B_i(x_k, y_k) \delta(x_k, y_k) \right] \right]}{\sqrt{\sum_i B_i^{t^2} \sigma_i^{-2}}} \quad (17.17)$$

Note that in the two last relations, the CLEAN component is multiplied by the true, not truncated, primary beam (taken at the (x_k, y_k) position).

After k_{\max} iterations, the mosaic J can thus be written:

$$J = \frac{\sum_i B_i^t \sigma_i^{-2} \left[D_i * \left(B_i * \left[\sum_{k=1}^{k_{\max}} \gamma j_k \delta(x_k, y_k) \right] \right) \right]}{\sum_i B_i^t \sigma_i^{-2}} + J_{k_{\max}} \quad (17.18)$$

Enough iterations have to be performed to ensure that the residual $H_{k_{\max}}$ is smaller than some user-specified threshold (typically 1 to 3). The comparison between Eqs. 17.12 and 17.18 shows that, within the noise, the sum of the CLEAN components can be identified with the sky brightness distribution I . As with the normal CLEAN algorithm, the final clean image is then reconstructed as:

$$M = C * \left[\sum_{k=1}^{k_{\max}} \gamma j_k \delta(x_k, y_k) \right] + J_{k_{\max}} \quad (17.19)$$

where C is the chosen clean beam. Note that the algorithm takes into account the dirty beams being different for each field, but the restoration is done using a single clean beam, which implicitly assumes that the dirty beams have similar widths. In practice, the observing mode of mosaics with the Plateau de Bure interferometer yields similar uv -coverages, and therefore similar dirty beams, for all the fields.

The modified CLEAN algorithms proposed e.g. by [Clark 1980] or [Steer et al. 1984] can be similarly adapted to handle mosaics, the main idea being to identify CLEAN components on H and to correct J . Note however that the multi-resolution CLEAN [Wakker & Schwartz 1988] cannot be directly adapted, as it relies on a linear measurement equation, which is not the case for a mosaic.

The MAPPING software

MAPPING is a superset of the GRAPHIC software, which has been developed to allow more sophisticated deconvolutions to be performed. For instance, it allows to choose a support for the deconvolution (clean window) or to monitor the results of the deconvolution after each iteration. Several enhancements of CLEAN (e.g. multi-resolution CLEAN) as well as the WIPE algorithm (see [Lannes et al. 1997]) are also available. The deconvolution of a mosaic has to be done with MAPPING. The implemented algorithm assumes that the noise levels in each field are similar (i.e. $\forall i \sigma_i = \sigma$), which is a reasonable hypothesis for Plateau de Bure observations. In that case, the equations of the previous paragraphs are slightly simplified: J is independent from σ , and H can be written as the ratio H'/σ , where H' is independent from σ and is used in practice to localize the CLEAN components.

We refer to the *Mapping Cookbook* for a description of the MAPPING software. To deconvolve mosaics, the following steps are performed:

- Create a uv table for each observed field. Then, run the UV_MAP task to compute a dirty map and a dirty beam for each field, with the *same* phase center (variable UV_SHIFT = YES).
- The task MAKE_MOSAIC is used to combine the fields to construct a dirty mosaic. Two parameters have to be supplied: the width and the truncation level B_{\min} of the primary beams. Three images are produced: the dirty mosaic³ (yourfile.lmv), all the dirty beams written in the same file (yourfile.beam), and a file describing the positions and sizes of the primary beams (yourfile.lobe). The dirty maps and beams of each individual field are no longer used after this step and can thus be removed if necessary.
- The data have to be loaded into the MAPPING buffers. This is done by the READ DIRTY yourfile.lmv, READ BEAM yourfile.beam, and READ PRIMARY yourfile.lobe commands. The latter automatically switches on the mosaic mode of MAPPING (the prompt is now MOSAIC>). From now, the deconvolution commands H0GB0M, CLARK and SDI (for Steer-Dewdney-Ito) can be used and will apply the algorithm described above. Use the command MOSAIC to switch on or off the mosaic mode if necessary.

³More precisely, this file contains the non normalized mosaic $\Sigma B_i^t \times F_i$. The proper normalization (see Eq. 17.12) is further done by the deconvolution procedures.

- The clean beam of the final image can be specified by the user (variables MAJOR and MINOR). Otherwise, the clean beam computed from the first field is used. To check if there are differences between the various dirty beams, just use the FIT i command, which computes the clean beam for the i th field.
- The deconvolution uses the same parameters as a classical CLEAN: support, loop gain, maximal number of iterations, maximal value of the final residual, etc.
- In addition, two other parameters, SEARCH_W and RESTORE_W, can be supplied. Due to the strong increase of the noise at its edges, the mosaic has to be truncated above some value of σ_J , and these two variables are used to define this truncation level, in terms of $(\sigma_J/\sigma)^{-2}$. More precisely, SEARCH_W indicates the limit above which CLEAN components have not to be searched, while RESTORE_W indicates the limit above which the clean image is not reconstructed. Default values of these two parameters (both equal to B_{\min}) are strongly recommended. The corresponding truncation is shown in Fig. 17.1.

Tests of the method

Several tests of the method described in this paragraph have been performed, either with observations (including the comparison of independent mosaics from the same source) or with simulations. They show that very satisfactory results can be achieved with typical Plateau de Bure observations. Interestingly, deconvolution of the same data set using MEM (e.g. the task VTESS in AIPS) seems to give worse results: this is most probably related to the limited uv -coverage obtained with the Plateau de Bure interferometer, as compared to typical VLA observations (MEM is known to be vulnerable when there is a relatively small number of visibilities).

17.5 Artifacts and instrumental effects

The behaviour of the mosaicing algorithm towards deconvolution artifacts and/or instrumental effects can be studied by the means of simulations of the whole mosaicing process. The simulations presented below were computed with several models of sky brightness distributions. uv -coverages of real observations were used (4-antennas CD configuration of a source of declination $\delta = 68^\circ$). No noise has been added to the simulations shown in the figures, so that pure instrumental effects can directly be seen.

Stripes

A well-known instability of the CLEAN algorithm is the formation of stripes during the deconvolution of extended structures. After the dirty beam has been subtracted from the peak of a broad feature, the negative sidelobes of the beam are showing up as positive peaks. The next iterations of the algorithm will then identify these artificial peaks as CLEAN components. A regular separation between the CLEAN components is thereby introduced and the resulting map shows ripples or stripes. [Steer et al. 1984] proposed an enhancement of CLEAN (implemented as the command SDI in MAPPING) which prevents such coherent errors: the CLEAN components are identified and removed in groups. As mosaics are precisely observed to map extended sources, the formation of stripes can *a priori* be expected. Indeed, the algorithm described in the previous paragraph presents this instability. Fig. 17.2 shows an example of the formation of such ripples. To make them appear so clearly, an unrealistic loop gain ($\gamma = 1$) was used. Interestingly, the algorithm of [Steer et al. 1984], adapted to the mosaics, does not result in these stripes, even with the same loop gain. It seems thus to be a very efficient solution to get rid of this problem, if it should occur. Note however that more realistic simulations, including noise and deconvolved with normal loop gain, do not show stripes formation. This kind of artifacts seems thus not to play a significant role in the image quality, for the noise and contrast range of typical Plateau de Bure observations. In practice, they are never observed.

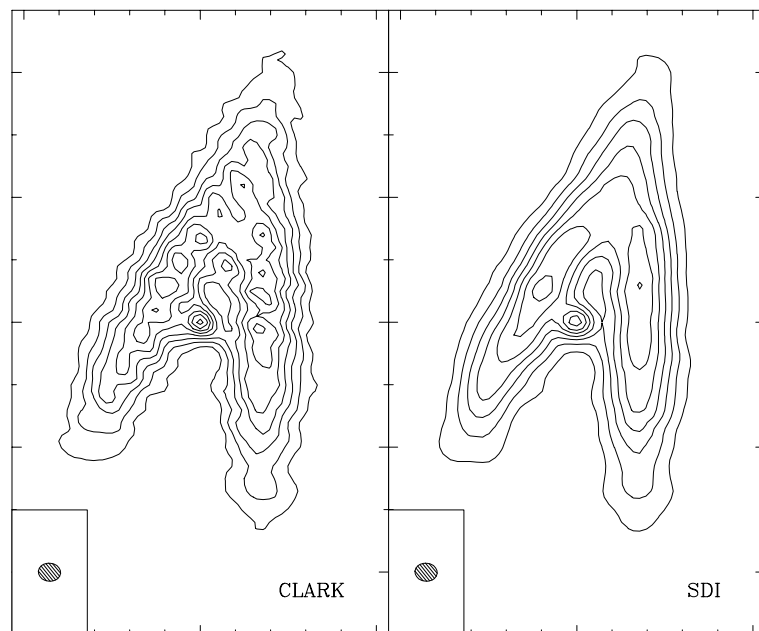


Figure 17.2: Mosaic deconvolved with the CLARK or SDI algorithms. Deconvolution parameters were identical (with a loop gain = 1) and contours are the same in the two images. The formation of stripes does not occur when using the SDI algorithm.

Short-spacings

The mosaicing technique allows, at least in theory, to recover part of the short-spacings information (see Section 17.2). In practice, however, the lack of the short-spacings cannot be fully compensated, and thus still introduces severe artifacts in the reconstructed images. The mosaic case is actually more complex than the single-field case, because the most extended structures are filtered out in each field, thus introducing a lack of information on an *intermediate* scale as compared to the size of the mosaic. As a consequence, a very extended emission can be split into several pieces, each one having roughly the size of the primary beam. This effect can be very well seen on the simulation presented in Fig. 17.3. To correct for this problem, it is necessary to add the short-spacings informations (deduced typically from single-dish observations) to the interferometric data set. Note however that the effects of the missing short-spacings on the reconstructed mosaic strongly depend on the actual uv -coverage of the observations, as well as on the size and morphology of the source: the artifacts can be small or negligible if the observed emission is confined into reasonably small regions. From this point of view, the example shown in Fig. 17.3 represents the worst case.

In any case, CLEAN is known to be not optimal to deconvolve smooth, extended structures. In order to partially alleviate this problem and the effects of the missing short-spacings, [Wakker & Schwartz 1988] proposed an enhanced algorithm, the so-called multi-resolution CLEAN: deconvolutions are performed at low- and high-resolution, and the results are combined to reconstruct an image which then accounts for the extended structures much better than in the case of a classical CLEAN deconvolution. As already quoted before, this algorithm cannot be applied to a mosaic, because it relies on a linear measurement equation. A multi-resolution CLEAN adapted to mosaics has however been developed ([Gueth 1997]) and is implemented in MAPPING. This method will not be described here.

Pointing errors

Pointing errors during the observations can of course strongly affect the images obtained by mosaicing. The rms of the pointing errors of the antennas of the Plateau de Bure interferometer is about $3''$. By comparison, the primary beam size at 230 GHz is $\sim 22''$ (Table 17.1). The pointing errors are difficult to model precisely: they are different for each antenna, random errors as well as slow drifts occur, the

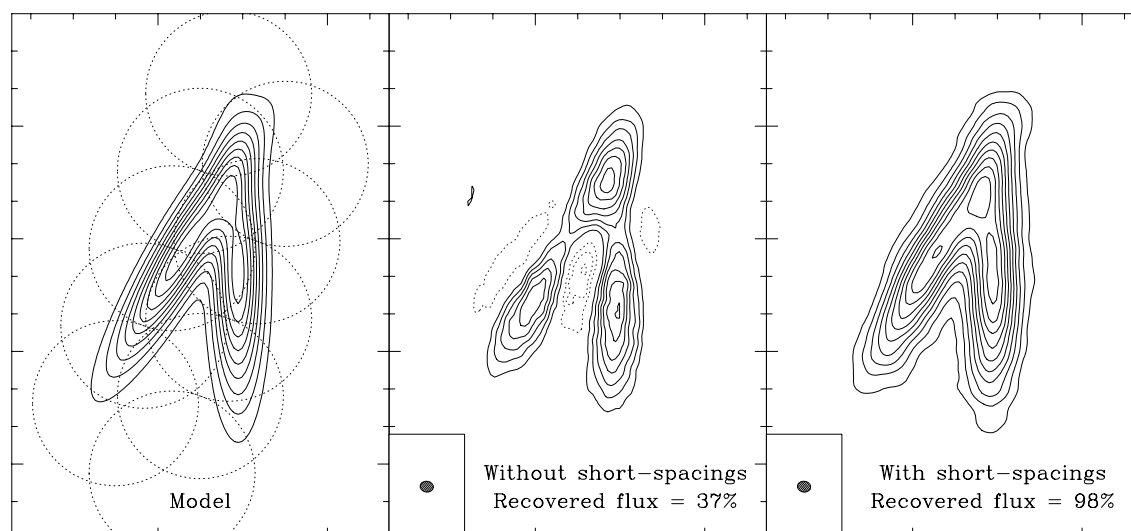


Figure 17.3: Left: Initial model of a very extended sky brightness distribution. Dotted circles indicate the primary beams of the simulated observation. Middle: Reconstructed mosaic, without the short-spacings information. Right: Reconstructed mosaic, with the short-spacings information. The contours are the same in the two simulated observations.

amplitude calibration partially corrects them, etc. A complete simulation should therefore introduce pointing errors during the calculation of each visibility. For typical Plateau de Bure observations, such a detailed modeling is probably not necessary, as the final image quality is dominated by deconvolution artifacts. To get a first guess of the influence of pointing errors, less realistic simulations were thus performed, in which each field is shifted as a whole by a (random) quantity. Such a systematic effect most probably maximizes the distortions introduced in the images. (Note that for a single field, the source would simply be observed at a shifted position in such a simulation. For a mosaic, the artifacts are different, because each individual field has a different, random pointing error. See [Cornwell 1987] for a simplified analysis in terms of visibilities. Figure 17.4 presents typical reconstructed mosaics for different rms of the pointing errors of the Plateau de Bure antennas. Obviously, the larger the pointing error, the worse the image quality. With a pointing error rms of $3''$, reasonably correct mosaics can be reconstructed even at 230 GHz. Clearly, care to the pointing accuracy has however to be exercised when mosaicing at the highest frequencies.

17.6 Concluding remarks

Mosaic observations are now routinely performed with the Plateau de Bure interferometer, at both λ 3 mm and λ 1.3 mm. It has proven to be a very efficient method to map extended sources, including using the most extended configuration of the array. The number of fields are usually ≤ 6 , but can be more important in some cases: as of the date of writing, the largest observed mosaic has 20 fields. Data processing requires a few more operations than normal observations, but does not present any specific difficulties. Reconstruction and deconvolution algorithms are available in the MAPPING software.

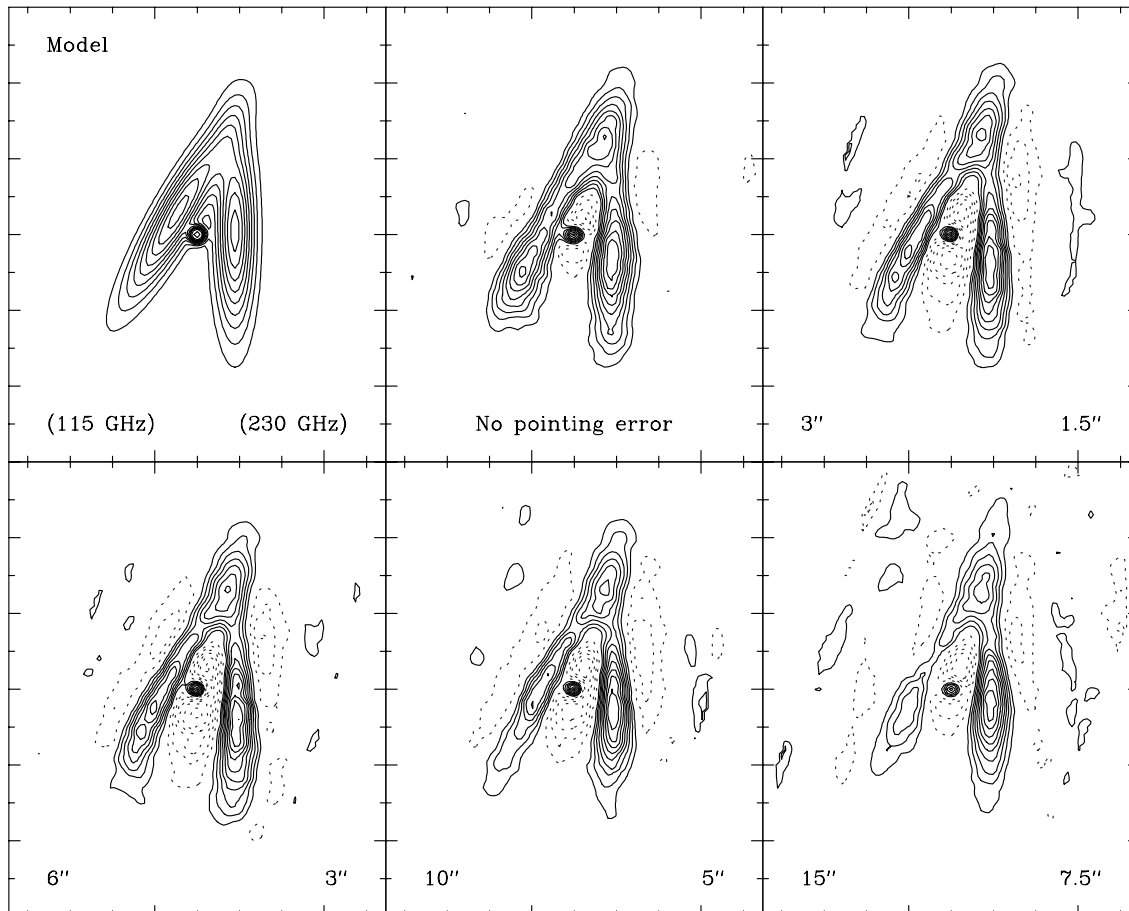


Figure 17.4: Simulations of a 10-fields mosaic observed with the Plateau de Bure interferometer. Each field is affected by a pointing error (see text). The corresponding rms are indicated in the lower left (observations performed at 115 GHz) and lower right (230 GHz) corners of each panel.

Chapter 18

Imaging in Practice

Stéphane Guilloteau

guillote@iram.fr

IRAM, 300 rue de la Piscine, F-38406 Saint Martin d'Hères, France

18.1 Visualisation

Contrary to the lower frequencies where continuum emission processes are dominant, mm interferometry most frequently deals with spectral lines, and hence involves handling and display of *data cubes*. Only a few astronomy packages have been designed for this: GIPSY, GILDAS, MIRIAD. Although the presentation which follows is general enough about the principles (e.g. for the noise analysis or flux density measurements), I will only present the tools which are currently available in GILDAS. Within GILDAS, two display tools are available:

- The GRAPHIC program
- The MVIEW task

In GRAPHIC, easy display is available using the following commands

- GO MAP, for simple channel contour maps
- GO BIT, same with overlaid color bit map
- GO NICE, with clean beam in addition
- GO POS, for Position-Velocity plots
- GO SPECTRE, for maps of spectra.

Easy access to the parameters of these procedures is available through the Windowing interface. GRAPHIC also provides access to all image processing tasks such as UV_MAP, UV_STAT, CLEAN, etc..., and flexible controls for publication quality plots.

Task MVIEW provides a different approach. It is a Window based application which provides simple, intuitive, and fast interactive 3-D data cube display. It provides spectrum display at cursor position, slices, moments, movie features, color manipulation, etc... It also has a direct interface to some important tasks (e.g. moments evaluation, subset extraction) for which interactively selecting parameters using mouse

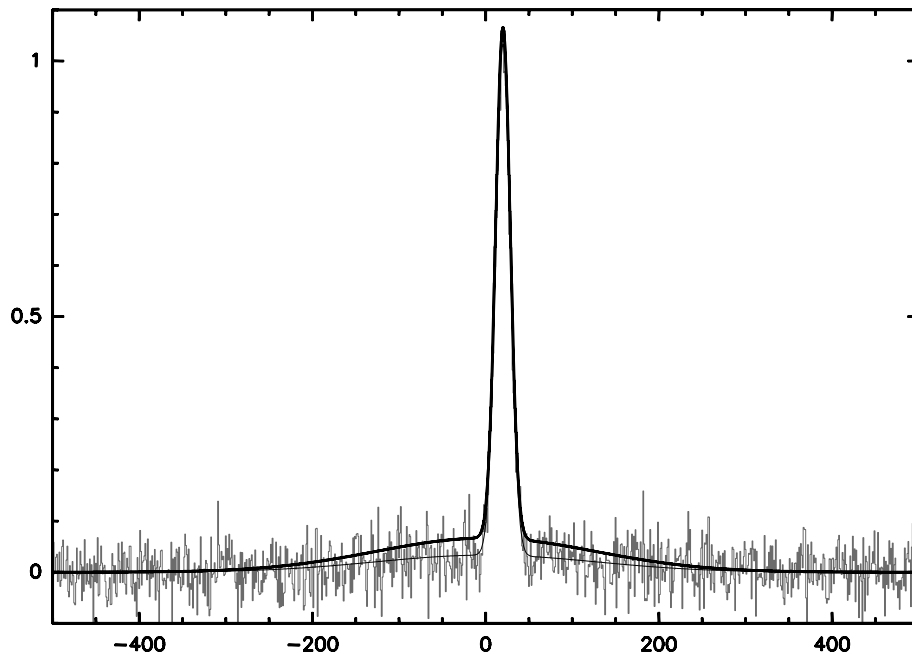


Figure 18.1: Illustration of the difficulty to deconvolve a weak, extended structure. In this 1-D example, half of the flux is in the extended structure, and cannot be recovered properly by deconvolution because of low signal to noise.

motion is convenient. However, contrary to GRAPHIC, it cannot be customized to produce publication quality images.

18.2 Photometry

18.2.1 From Flux density to Brightness temperature

The unit of the dirty map is ill defined. A single point source of 1 Jy appears with peak intensity of 1. But if more than 1 point source is in the field of view, the combination of positive or negative sidelobes from the other source modifies this result. It is thus necessary to deconvolve. After deconvolution, the beam area is well defined: the CLEAN map unit is Jy per beam area.

The conversion to brightness temperature can then be done using the standard equation

$$S_\nu = \frac{2k\Omega_s}{\lambda^2} T_B \quad (18.1)$$

$$= \frac{2k\pi\theta_s^2}{4\log 2\lambda^2} T_B \quad (18.2)$$

for Gaussian beams. GO MAP and its variants automatically display the Jy/K conversion factor mentioned above. The integrated flux density in a user defined area can then be computed on the clean map using command GO FLUX.

18.2.2 Accuracy of Flux density estimates

The accuracy of flux measurements is limited by several factors.

Deconvolution Errors and Missing Flux

Deconvolution limits are among the most important. Deconvolution is required (see Chapter 15), but it is impossible to deconvolve weak structures near the noise level. Nevertheless, these structures,

when sufficiently extended, can contribute to a significant flux. The relevance of the missing flux to the astronomical interpretation is to be decided by the astronomer. In most cases, however, the missing flux does not correspond to any significant brightness, and its absence may not modify the astronomical interpretation. A schematic illustration is given in Fig.18.1: half of the flux is buried in the noise, but the brightness is measured properly (within the statistical error). Note also that WIPE ([Lannes et al. 1997]) offers an upper limit to the noise amplification factor due to the non linear deconvolution process. This upper limit is often discouragingly large for the rather poor dirty beams provided by current mm arrays (4 or 5 is not unusual).

Comparing the recovered flux to a single dish measurement can help you in estimating the corresponding brightness level and evaluate whether this is important in your astronomical case. To convert from flux to brightness, the characteristic size of the missed flux should be used. This is in between several synthesized beam widths and about half of the primary beam. Although in general the problem is not as severe as one would think (because, unfortunately, one is often signal to noise limited), this is an important information, specially in the case of mosaics.

Seeing

A second important effect which affects flux density measurements is the seeing. Seeing result in an underestimation of Point source flux. On the other hand, the total flux is spread over the seeing disk, and is in principle conserved. Insufficient seeing conditions limit the deconvolution process, since the effective synthesized beam (which should include atmospheric phase errors) is significantly different from the theoretical synthesized beam (computed from uv coverage and weights). A good check is to make an image of the two calibrators, and measure the corresponding point source flux and apparent size.

Noise estimate

Finally, the noise should be estimated. `G0 RMS` gives the sigma of the image flux density distribution. This is an improper estimate, since it includes any possible signal, all spectral channels, and map edges where the noise level increases due to aliasing and gridding. A better estimate, derived from effective weights, is in principle given by task `UV_STAT`. However, this estimate does not take into account possible deconvolution problems or dynamic range limitations due to atmospheric phase noise. The optimal procedure is to use command `G0 FLUX` on an empty area of the image to find out the point source rms noise. The precision of the estimate is limited by statistical uncertainties linked to the number of beams in the area. Then, another `G0 FLUX` command on the emission area will give the total flux and number of independent beams, n ; the rms on the total flux is \sqrt{n} times the point source rms determined by the `G0 FLUX` command applied to an empty region. Another good method to determine the noise level (yet to be implemented as a `G0 NOISE` procedure...) would be to build the histogram of the pixel values and fit a Gaussian to it; if source structure only covers a small fraction of the image, this method provides a good estimate.

Primary beam

One should emphasize that primary beam correction is essential in any correct flux density estimate. All image plane analysis should be carried out on a primary beam corrected image. This introduces a slight complication, since the noise level is then not uniform. The `G0 FLUX` commands discussed before should be applied in regions of similar extent and location vis-a-vis the primary beam(s).

uv plane analysis is also extremely useful both in measuring integrated flux densities and rms noise level, at least for simple, relatively compact, source models. Task `UV_FIT` provides statistical errors for all parameters of the fit. Primary beam correction should be applied a posteriori, based on the location of the region of interest.

Dynamic Range

As mentioned above, the dynamic range may be a limitation. The dynamic range D_r is defined as the ratio of the peak intensity to the lowest "believable" contour. D_r is obviously lower than the signal to noise ratio. It can be estimated as the absolute value of the peak to maximum negative contour ratio. As usual,

map edges should not be included in this evaluation. Dynamic range is related to seeing and calibration errors. It is typically 10 to 40 at Plateau de Bure (if signal to noise ratio allows). Errors should include dynamic range effects.

Flux density scale

Finally, remember that the flux scale is determined by bootstrapping flux of (variable) quasars from that of reference sources. Any errors accumulated in this process must be transferred to the source flux estimate.

In summary, flux density estimates should quote errors which include

- Effective thermal noise
- Dynamic range problems
- Relative (calibrator) flux uncertainty
- Absolute flux scale uncertainty **OR** reference flux scale.
- Primary beam correction

18.3 Short Spacings

Extended structure are missed, attenuated or distorted in interferometric maps by lack of short uv spacing information. While this effect may be negligible for some astronomical problems, it could also be essential in a proper analysis. Deconvolution recovers some of them, but under-estimate the total flux because the integral of the dirty beam is zero (the integral of the dirty beam is the weight of the (0,0) uv cell in the uv data set).

Constructing a beam with a non zero integral can help deconvolution. This can be done by incorporating the **Zero spacing** flux or spectrum.

Short spacings provides even more information, because they give information on the spatial distribution of this flux on scales between half the primary beam and the primary beam itself. Short spacings can be provided by a smaller interferometer (e.g. BIMA) or a large single dish (e.g. 30-m). In theory, short spacings can also be provided by the interferometer antennas used in single-dish mode. However, because most interferometer have not been designed with total power stability as a goal, this has not been practiced so far.

Incorporating short spacings into interferometer data is a two step process. Task `UV_SINGLE` extracts short spacing information from single dish data (spectra) and creates a uv table. Task `UV_MERGE` merges the single-dish and interferometer tables. Coordinates system should be consistent and checked before (coordinates are always J2000.0 at Plateau de Bure, often B1950.0 at the other observatories...).

18.3.1 UV_SINGLE

Incorporating short spacings from the 30-m into Plateau de Bure data is a 3 step process for the user.

- Creation of a table of spectra

First, one should resample (in frequency) all spectra to same frequency grid than interferometer data, using command `RESAMPLE` in `CLASS`. Then a table of spectra is produced using command `GRID` (with no options) in `CLASS`.
- Image creation

The next step is the creation of “well behaved” map from the table of spectra. It starts with resampling (in space) on a regular grid by a convolution kernel (interpolation techniques such as the `GREG` command `RANDOM_MAP` are inappropriate). Weights are also resampled. Then, we follow by extrapolation to zero outside the convex hull of the mapped region, using a kernel twice broader than the single-dish beam, to avoid introducing spurious structure.

Because of noise, the map still contains spurious high spatial frequencies. These are removed during the uv table creation. The algorithm steps are

- Fourier transform of map and weight images
- Division by Fourier Transform of the single-dish beam
- Gridding correction (division by Fourier Transform of the gridding function)
- Truncation to some maximum uv distance ($<$ dish diameter)
- Inverse Fourier Transform back to image plane
- Multiplication by primary beam of the interferometer
- Fourier Transform to uv plane
- Normalization of the weights so that the sum of weights is the weight of the total flux (derived from integration time, bandwidth and system temperature).
- Optional application of an amplitude scaling factor.
- Optional application of a weight scaling factor.

This produces a uv table with optimal weights in terms of signal to noise ratio for the total flux, and with effective tapering following the single-dish illumination pattern, except for the truncation at some uv distance.

- Merging with interferometer data

The final step is to merge the resulting uv table with the interferometer uv table. Re-weighting and re-scaling is again possible at this stage. Note that the choice of weighting function is arbitrary. It may result in poorly behaved synthesized beams when combined with the interferometer uv data. Weights can be lowered by any arbitrary factor (increasing the weights is only allowed if signal to noise is not an issue). A good choice is to adjust the weights so that there is almost no negative sidelobe.

18.4 Dirty Tricks

Besides flux density estimate, which, as discussed before, is a non trivial task, analyzing spectral line images may force the astronomer to face some really tricky problems. The two most obvious are moment evaluation and continuum subtraction.

18.4.1 MOMENTS

The lowest order moment of a spectral line data cubes offer very convenient ways of interpreting images. The zeroth order moment is the integrated intensity, the first order moment the velocity, the second order moment the line width. While these moments are linear combination of the channel maps, the deconvolution process is non linear. Accordingly, the two operations do not commute.

Hence, it is impossible to recommend deconvolving before computing the mean intensity, or summing up the individual cleaned channel maps. In the latter, limited signal to noise can prevent proper deconvolution. In the former, velocity gradients can spread emission over an extended area which is difficult to handle in the deconvolution. Choice can be a matter of trial (and errors).

To avoid introducing noise, a *window* in velocity is important. While noise on the integrated intensity only increases as the square root of the window width, the effect on the higher order moments is much more dramatic, and results in non-gaussian noise distribution on these variables. A *threshold* in intensity is useful to prevent spurious noisy features. The window should in principle be pixel dependent to allow for velocity gradients. Smoothing both in the spatial and spectral domains may help in obtaining better results in moment extraction. A line fitting procedure (e.g. a Gaussian line fit at each pixel) may sometimes be the best solution (under construction, check later...).

Moments can be computed using task `MOMENTS` and displayed using the `GO VELOCITY` command in `GRAPHIC`.

18.4.2 Continuum Subtraction

Continuum subtraction is a related problem. It is in principle needed to compute properly moment maps. However, it may be completely impossible, for example in the case of an optically thick line partially covering a continuum source. Continuum subtraction can be done in the image plane or in the uv plane. uv plane subtraction avoid the non linearity in the deconvolution, and thereby any amplification of errors induced in this process. Task `UV_SUBTRACT` performs this operation. Although signal to noise on the continuum is often much better than on the spectral line, it may be advantageous to subtract a source model rather than the measured visibilities; this is only true when thermal noise is more important than phase noise. Task `UV_MODEL` compute visibilities from an input image.

Chapter 19

Low Signal-to-noise Analysis

Stéphane Guilloteau

guillote@iram.fr

IRAM, 300 rue de la Piscine, F-38406 Saint Martin d'Hères, France

Low Signal to Noise (S/N) is unfortunately a frequent situation in mm astronomy. Since S/N increases only as the square root of the integration time, it may not be feasible at all to go from a case of low S/N to a case of even “decent” S/N. Thus the astronomer has to worry about interpreting properly low S/N data. The risk of over-interpretation in such cases is to be considered seriously. This lecture will give you some hints, as well as point out some traps which must be avoided.

19.1 Continuum Source

Let us start with a continuum source to simplify. The basic source parameters are position (x,y) , flux density S_ν , and size. To determine the first 3 parameters, the best strategy is to avoid resolving the source. Since the position errors are proportional to the beam size, one should thus try to match the source size to the beam size. Having *a priori* information on the source position (by other observations, e.g. an optical image) will help to get a better accuracy on the source flux.

19.1.1 Flux measurement

- **Accurate Position:** If the position is known to better than $1/10^{\text{th}}$ of the beam, you should then use UV_FIT with the position fixed to determine the flux and the noise. In doing so, you should use an appropriate fixed source size, based on any *a priori* information you have (as you are following the “best strategy”, this source size should be smaller than the beam size). In such a case, you only have one free parameter, the flux, and a 3σ signal is sufficient to claim a detection.
- **Rough Position** If the source position accuracy is not sufficient, you need to measure the position

Rule 1	Do not resolve the source		
Rule 2	Get the best absolute position before		
Rule 3	Use UV_FIT to get the parameters and their errors		
	<i>a priori</i> position accuracy		
	< 0.1 Beam	\simeq Beam	Any
Minimum signal	3σ	4σ	5σ
Position	fixed	free	free, (make an image)
Source size	fixed	fixed	fixed

Table 19.1: Recipes to use UV_FIT to measure the flux of a weak source

also. As you now have more parameters to derive, a higher S/N will be required to do so. When the position uncertainty is about the beam size, a 4σ signal will be required to get a firm detection. Use UV_FIT to measure the flux and source position, with the same fixed source size as before.

- **Unknown Position** When the source position is really unknown, a 5σ signal may become necessary to claim a detection. To locate the source position, make an image first. Cleaning is usually not required at that level, unless the sidelobe level is higher than the noise to signal ratio. Then, use UV_FIT to measure the source flux, position and their associated errors, always using the same fixed source size as before.

Note that in all cases, the source size being used should be at least equal to the effective seeing of the observations, even if the source is actually a point source.

Table 19.1 summarizes the procedure to be followed. Once you have done your best in determining the source parameters, they remain to be properly interpreted. As a rule of thumb, remember that **All fluxes for detected weak sources are biased by 1 to 2 σ** . The only exception is when the source position and size is known *a priori*. The reason for the bias is very intuitive. Assume you have observed just enough to get a 3σ detection. A positive noise peak will bring that up to a 4σ value, a negative noise peak down to 2σ , which you will consider as a non-detection.

19.1.2 Other parameters

The other source parameters (position & size) require higher signal to noise to be determined. The position accuracy is the synthesized beam size divided by the S/N ratio. Hence, to get a position accuracy to 25 % of the beam size, at least a 4σ detection is required.

The above limitations are valid for a point source. If the source is not expected to be small enough, additional complications occur. If you have performed the experiment according to the guidelines given before (i.e. avoiding resolving the source), the source size may be just about the beam size. In such circumstances, no source size at all can be estimated with current mm interferometers if the detection is less than 6σ . To convince yourself, let us perform a simple thought experiment. Assume we have detected a source at the 6σ level. Take this 6σ signal, and divide the observations in two equal (in sensitivity) data sets, one containing only the shortest baselines, the other ones only the longest baselines. Each subset has a $\sqrt{2}$ times higher noise level, and the error on the flux difference between these two data sets is 2 times the original noise level. Assume that the shortest baselines give us twice more flux than the longest one. In such a case, we would in fact have a better detection (6.4σ) with the short baselines only, but the difference flux is only measured with 3σ . Such an experiment is not optimal from the detection point of view, since we would have obtained a better result (6.4σ) by observing only half of the time... Table 19.2 summarizes the corresponding numbers, and indicates that the minimum detection level to resolve a source at the 4σ level is 7.1σ .

The interpretation of such data is made even more difficult by the fact that if the size is unknown, the error on the total flux increases **quite** significantly. Fig.19.1 shows the detection of a weak high-redshift object in the Hubble Deep Field area [Downes et al 1999] Although the detection is at the 7σ level, the source size is not constrained by these observations, and the total flux becomes uncertain by as much as 40 % when the uncertainty on the source size is included.

		Point Source			Beam Size Source			Minimum Size Resolved		
		Flux	Noise	S/N	Flux	Noise	S/N	Flux	Noise	S/N
(1)	Short baselines	6	1.4	4.2	9	1.4	6.4	10	1.4	7.1
(2)	Long baselines	6	1.4	4.2	3	1.4	2.1	2	1.4	1.4
(3)	Difference	0	2	0	6	2	3	8	2	4
(4)	Mean	6	1	6	6	1	6	6	1	6

Table 19.2: Signal to Noise example for source size measurement. Line (1) indicate the flux measured on short baselines, line (2) on long baselines, line (3) the difference between (1) and (2), and line (4) the average. Three cases are shown: a point source, a source with size similar to the beam, and the smallest source which can be resolved at the 4σ level.

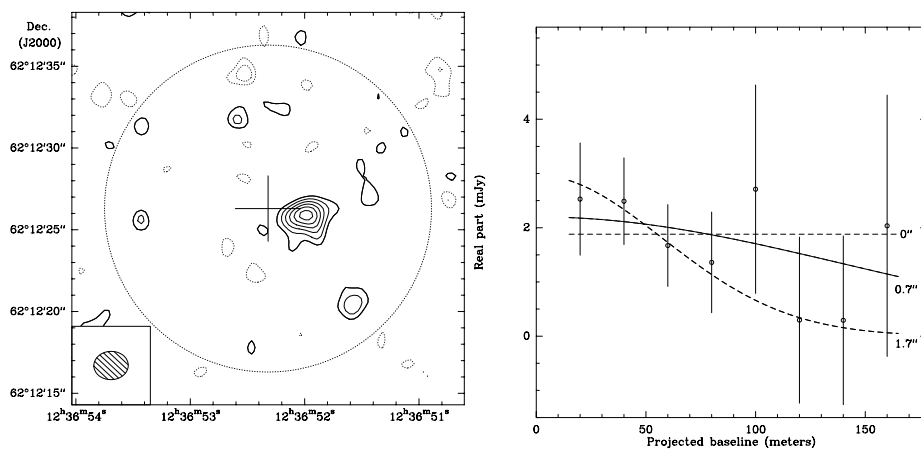


Figure 19.1: Left: 7σ detection of the strongest source in the Hubble Deep Field. Note that the contours are visually misleading (they start at 2σ but with 1σ steps, given the impression of a much better detection). Right: Attempt to derive a size. Size can be as large as the synthesized beam... Note that the integrated flux increases with the source size.

19.2 Spectral Line Sources

Unfortunately, things get even worse for spectral lines, because the uncertainties on the line width and source velocity add up to the position and size problem. If the source velocity is unknown, the observer will tend to select the brightest part of the spectrum to define the integrated flux. This results in a positive bias on the flux. Furthermore, if the line width is not known, the observer may limit the line to the brightest part of the spectrum, resulting in another bias. This bias is in general positive, since positive noise peaks will be included in the line region, but could be negative for specific line shapes.

If the source position was *a priori* unknown, it is common practice to determine it from the integrated line flux map made using the tailored line window specified by the astronomer. Such a procedure results in a positively biased total flux. Any speculated extension will also increase the total flux, by enlarging the selected image region by selection of positive noise peaks. The net effect is a 1 to 2 σ positive bias on the integrated line flux. Things get really messy if a continuum is superposed to the weak line...

A good strategy is required to minimize these biases. The correct approach to point sources (or sources less than about $1/3^{\text{rd}}$ of the synthesized beam), is to first determine the position (e.g. from continuum data is available, or from the integrated line map if not, or ideally from other data). Once the position is fixed, the line profile can be derived by fitting a point (or small fixed size) source, at fixed position into the UV data. Using this line profile, the total line flux, as well as source velocity and line width, can be derived by fitting an appropriate lineshape, e.g. a Gaussian if no other information is available. In this last step, a constant baseline offset should be added if there is a continuum contribution.

For extended sources, which may be affected by velocity gradient, one has to fit a multi-parameter (6 for an elliptical gaussian) source model for each spectral channel into the UV data. As a consequence, the signal in each channel should be at least 6σ to derive any meaningful information. The strict minimum is 4σ (per line channel...) to get flux and position for a fixed size source. Velocity gradients are not believable unless even better signal to noise is obtained per line channel!... Moreover, for narrow lines, most correlators produce spectral channels which are not independent; the correlation between adjacent channels should be taken into account when analyzing velocity gradients.

To sum up the weak spectral line problems:

- Do not believe velocity gradient unless proven at a 5σ level. This requires a S/N larger than 6 in each channel. Remember that position accuracy per channel is the beamwidth divided by the signal-to-noise ratio...
- Do not believe source size unless $S/N > 10$ (or better)
- Expect line widths to be very inaccurate
- Expect integrated line intensity to be positively biased by 1 to 2 σ
- or even more biased if the source is extended

These biases are the analogous of the Malmquist bias.

Unfortunately, examples for such problems are numerous, especially for high redshift CO lines. The $z = 2.8$ galaxy 53 W 002 was detected in CO with the OVRO interferometer by [Scoville et al 1997], who claim an extended source, with velocity gradient. The published images (contour maps) look convincing, but this is biased by the chosen visual representation, with contours starting at 2σ but spaced by 1σ . This creates the visual impression of higher S/N ratio. The published spectra also look convincing, but are presented as a fully sampled spectra (i.e. channel width equal to twice the channel separation). Although this is the proper way to present a complete information, the astronomer's eye is not accustomed to such a presentation, and the astronomer tends to interpret the data as if the channels were independent, thereby underestimating the noise. Yet the total line flux is 1.5 ± 0.2 Jy.km/s i.e. (at best) only 7σ , and thus, according to the discussion presented above, no extension/gradient should be measurable. Indeed, using the IRAM interferometer, [Alloin et al 2000] find a line flux of 1.20 ± 0.15 Jy.km/s, no source extension, no velocity gradient, different line width and redshift. Note that the line fluxes agree within the errors, with the second determination just 1σ below the first one, as expected for an initially biased result...

Another example of visually misleading result is shown in Fig.19.2. Although the two spectra appear different, there is a weak continuum (which was measured independently) on the Northern source. Once the continuum offset and a scale factor have been applied, the lack of visible structure in the difference

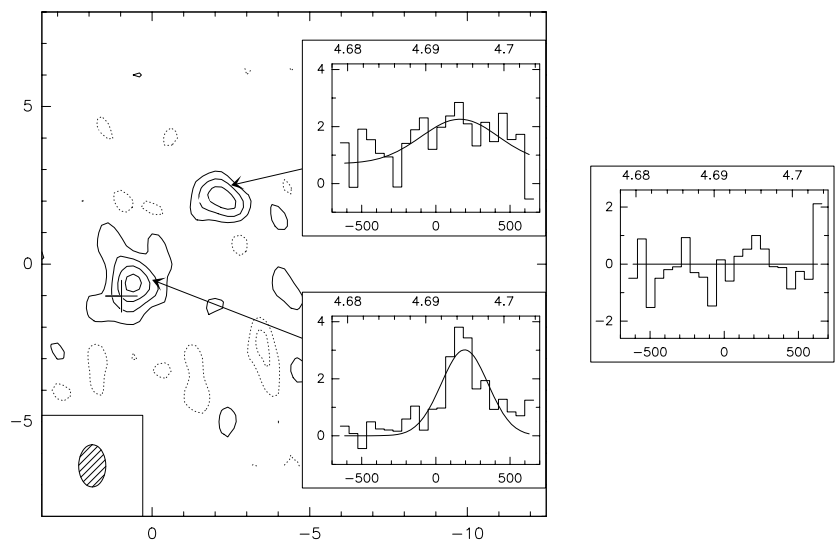


Figure 19.2: Example of search for a Velocity Gradient: BR 1202-0725. The image is a contour map of dust emission at 1.3 mm, with 2σ contours. The inserts are redshifted CO(5-4) spectra from the indicated directions. A weak continuum (measured *independently*) exist on the Northern source. The rightmost insert is a difference spectrum (with a scale factor applied, and continuum offset removed) (Cox, Guélin, Guilloteau & Omont, in preparation).

spectrum shows that both line profiles are indistinguishable, i.e. that there is no measurable velocity gradient. These two sources could be lensed images of the same galaxy...

Chapter 20

Basic Principles of Radio Astrometry

Alain Baudry¹ & Roberto Neri²

baudry@observ.u-bordeaux.fr & neri@iram.fr

¹ Observatoire de Bordeaux, BP 89, F-33270 Floirac, France

² IRAM, 300 rue de la piscine, F-38406 Saint-Martin-d'Hères, France

20.1 Introduction and Basic Formalism

Modern astrometry aims at improving our knowledge of celestial body positions, motions and distances to a high accuracy. The quest for accuracy began in the early days of astronomy and is still continuing in the optical domain with most sophisticated instruments (automated meridian circles, the Hipparcos satellite or future astrometric space missions) as well as in the radio domain (connected-element interferometers and VLBI). New instrumental concepts or calibration procedures and increased sensitivity are essential to measure highly accurate positions of stars and radio sources. Positions accurate to about one thousandth to one tenth of an arcsecond have now been obtained for hundreds of radio sources and for about 100 000 to one million stars in the Hipparcos and Tycho catalogues respectively.

In this lecture we are concerned with some basic principles of position measurements made with synthesis radio telescopes and with the IRAM interferometer in particular. More details on interferometer techniques can be found in the fundamental book of [Thompson et al. 1986]. The impact of VLBI in astrometry and geodesy is not discussed here. (For VLBI techniques see [Sovers et al. 1998].)

We first recall that measuring a position is a minimum prerequisite to the understanding of the physics of many objects. One example may be given for illustration. To valuably discuss the excitation of compact or masing molecular line sources observed in the direction of late-type stars and HII regions sub-arcsecond position measurements are required. This is because the inner layers of circumstellar envelopes around late-type stars have sizes of order one arcsecond or less and because several compact HII regions have sizes of one to a few arcseconds only. Position information is crucial to discuss not only the respective

importance of radiative and collisional pumping in these line sources but also the physical association with the underlying central object.

The output of an interferometer per unit bandwidth at the observing wavelength λ is proportional to the quantity

$$R = \int A(\vec{k})I(\vec{k}) \cos(2\pi\vec{B}\cdot\vec{k}/\lambda) d\Omega \quad (20.1)$$

where \vec{k} is the unit vector toward the observed source, A is the effective antenna aperture, I the source brightness, and \vec{B} the baseline vector of the interferometer. For an extended source one refers the observations to the reference direction \vec{k}_0 and supposing that the radiation comes from a small portion of the sky we have $\vec{k} = \vec{k}_0 + \vec{\sigma}$ where $\vec{\sigma}$ is the position vector describing the source coordinates. (Since both \vec{k}_0 and \vec{k} are unit vectors we obtain $\vec{k}_0\cdot\vec{\sigma} = 0$.) The interferometer output is given by

$$R = V \cos(2\pi\vec{B}\cdot\vec{k}_0/\lambda + \Psi) \quad (20.2)$$

where

$$V \exp(i\Psi) = \int A(\vec{\sigma})I(\vec{\sigma}) \exp(i2\pi\vec{b}\cdot\vec{\sigma}) d\Omega \quad (20.3)$$

is the complex source visibility and $\vec{b}(u, v)$ is the baseline vector projected on a plane normal to the tracked direction. The exact definition of the baseline coordinates u and v is given in Section 20.3.

The astrometry domain corresponds to those cases where the source visibility amplitude is equal to 1 (point-like sources) and the phase provides the source position information.

20.2 The Phase Equation

The most important measurement for radio astrometry is that of the actual fringe phase of a connected-element interferometer (or similarly the group delay in VLBI). Let θ be the angle between the reference direction and the meridian plane of a given interferometer baseline. The phase is then defined by

$$\phi_r = 2\pi\mathcal{B} \sin(\theta)/\lambda \quad (20.4)$$

If the point-like source of interest is offset by $\Delta\theta$ from the reference direction the total phase is

$$\phi = 2\pi\mathcal{B} \sin(\theta + \Delta\theta)/\lambda \simeq \phi_r + 2\pi\mathcal{B} \cos(\theta)\Delta\theta/\lambda \quad (20.5)$$

It is thus clear that measuring an angle or an offset position on the celestial sphere becomes possible only when all phase calibration problems have been understood and solved.

Accounting for uncertainties in the baseline and source position vectors the actual phase is

$$\phi = 2\pi(\vec{B} + \delta\vec{B})\cdot(\vec{k}_0 + \delta\vec{k})/\lambda \quad (20.6)$$

where \vec{B} is a first approximation of the baseline, \vec{k}_0 the tracking direction; $\vec{B} + \delta\vec{B}$ and $\vec{k}_0 + \delta\vec{k}$ are the true baseline and source position vectors, respectively. The reference phase is given by

$$\phi_r = 2\pi\vec{B}\cdot\vec{k}_0/\lambda \quad (20.7)$$

and, neglecting the term involving $\delta\vec{B}\cdot\delta\vec{k}$, we obtain

$$\phi - \phi_r = 2\pi(\vec{B}\cdot\delta\vec{k} + \delta\vec{B}\cdot\vec{k}_0)/\lambda \quad (20.8)$$

We consider all vector projections in the right-handed equatorial system defined by the unit vectors a_1 ($H = 6$ h, $\delta = 0$), a_2 ($H = 0$ h, $\delta = 0$), a_3 ($\delta = 90^\circ$). (Note that this system is not the Cartesian coordinate system used in [Thompson et al. 1986].) H and δ are the hour angle and declination, respectively. In the

equatorial system the baseline vector \vec{B} has components $(B_\infty, B_\epsilon, B_\ominus)$ and the components of the reference position \vec{k}_0 are given by $(\cos(\delta) \sin(H), \cos(\delta) \cos(H), \sin(\delta))$

The two limiting cases $\delta\vec{k} = 0$, and $\delta\vec{B} = 0$ correspond to those where we either calibrate the baseline or determine the exact source position.

In the first case the source coordinates are perfectly known and by comparing the observed phase ϕ with the reference phase ϕ_r one determines $\delta\vec{B}$ and hence the true baseline $\vec{B} + \delta\vec{B}$. The reference sources observed for baseline calibration are bright quasars or galactic nuclei whose absolute coordinates are accurately known. The most highly accurate source coordinates are those of the radio sources used to realize by VLBI the International Celestial Reference Frame (ICRF); distribution of coordinate errors are below one milliarcsecond. However, the ICRF catalogue is insufficient for phase and baseline calibrations of millimeter-wave arrays because most sources are not bright enough in the millimeter-wave domain. The IRAM calibration source list is thus a combination of several catalogues of compact radio sources. Today, the Plateau de Bure Interferometer catalogue of calibration sources is based mostly on compact radio sources from the Jodrell Bank – VLA Astrometric Survey (JVAS – [Patnaik et al 1992], [Browne et al. 1998], [Wilkinson et al. 1998]).

20.3 Determination of Source Coordinates and Errors

Once the baseline is fully calibrated ($\delta\vec{B} = 0$) the exact source coordinates are known from the $\delta\vec{k}$ vector components. These components are formally deduced from the differential of \vec{k}_0 . In the right-handed equatorial system defined in Section 20.2 we obtain

$$\begin{aligned} \delta\vec{k} = & \begin{pmatrix} -\sin(\delta) \sin(H) \Delta\delta - \cos(\delta) \cos(H) \Delta\alpha, \\ -\sin(\delta) \cos(H) \Delta\delta + \cos(\delta) \sin(H) \Delta\alpha, \\ \cos(\delta) \Delta\delta \end{pmatrix} \end{aligned} \quad (20.9)$$

where $\Delta\alpha$ and $\Delta\delta$ are the right ascension and declination offsets in the equatorial system ($\Delta\alpha = -\Delta H$). The phase difference is then a sinusoid in H

$$\frac{(\phi - \phi_r)\lambda}{2\pi} = \vec{B} \cdot \delta\vec{k} = C_1 \sin(H) + C_2 \cos(H) + C_3 \quad (20.10)$$

where

$$C_1 = -B_1 \sin(\delta) \Delta\delta + B_2 \cos(\delta) \Delta\alpha \quad (20.11)$$

$$C_2 = -B_2 \sin(\delta) \Delta\delta - B_1 \cos(\delta) \Delta\alpha \quad (20.12)$$

$$C_3 = B_3 \cos(\delta) \Delta\delta + \phi_{\text{ins}} \quad (20.13)$$

and C_3 contains the instrumental phase ϕ_{ins} .

Measurement of the phase at time intervals spanning a broad hour angle interval allows us to determine the three unknowns C_1 , C_2 , and C_3 , and hence $\Delta\alpha$ and $\Delta\delta$ and the exact source position. Note that for sources close to the equator, C_1 and C_2 alone cannot accurately give $\Delta\delta$. In the latter case, C_3 must be determined in order to obtain $\Delta\delta$; this requires to accurately know the instrumental phase and that the baseline is not strictly oriented along the E-W direction (in which case there is no polar baseline component).

A synthesis array with several, well calibrated, baseline orientations is thus a powerful instrument to determine $\delta\vec{k}$. In practice, a least-squares analysis is used to derive the unknowns $\Delta\alpha$ and $\Delta\delta$ from the measurements of many observed phases ϕ_i (at hour angle H_i) relative to the expected phase ϕ_r . This is obtained by minimizing the quantity $\Sigma(\Delta\phi'_i - (C_1 \sin(H_i) + C_2 \cos(H_i) + C_3))^2$ with respect to C_1 , C_2 , and C_3 where $\Delta\phi'_i = (\phi_i - \phi_r)\lambda/2\pi$. A complete analysis should give the variance of the derived quantities $\Delta\alpha$ and $\Delta\delta$ as well as the correlation coefficient.

Of course we could solve for the exact source coordinates and baseline components simultaneously. However, measuring the baseline components requires to observe several quasars widely separated on the sky. At mm wavelengths where atmospheric phase noise is dominant this is best done in a rather short

observing session whereas the source position measurements of often weak sources are better determined with long hour angle coverage. This is why baseline calibration is usually made in separate sessions with mm-wave connected-element arrays.

The equation giving the source coordinates can be reformulated in a more compact manner by using the components u and v of the baseline projected in a plane normal to the reference direction. With v directed toward the north and u toward the east, the phase difference is given by

$$(\phi - \phi_r) = 2\pi(u \cos(\delta)\Delta\alpha + v\Delta\delta) \quad (20.14)$$

Comparing this formulation to the sinusoidal form of the phase difference we obtain

$$u = (-\mathcal{B}_1 \cos(H) + \mathcal{B}_2 \sin(H))/\lambda \quad (20.15)$$

$$v = (\mathcal{B}_3 \cos(\delta) - \sin(\delta)(\mathcal{B}_1 \sin(H) + \mathcal{B}_2 \cos(H)))/\lambda \quad (20.16)$$

Transforming the $\mathcal{B}_{1,2,3}$ into a system where the baseline is defined by its length $\mathcal{B} = (\mathcal{B}_1^2 + \mathcal{B}_2^2 + \mathcal{B}_3^2)^{0.5}$ and the declination d and hour angle h of the baseline vector (defined as intersecting the northern hemisphere) we obtain

$$\mathcal{B}_1 = \mathcal{B} \cos(d) \sin(h), \mathcal{B}_2 = \mathcal{B} \cos(d) \cos(h), \mathcal{B}_3 = \mathcal{B} \sin(d) \quad (20.17)$$

and

$$u = (\cos(d) \sin(H - h))\mathcal{B}/\lambda \quad (20.18)$$

$$v = (\cos(\delta) \sin(d) - \sin(\delta) \cos(d) \cos(H - h))\mathcal{B}/\lambda$$

which shows that the locus of the projected baseline vector is an ellipse.

In order to derive the unknowns $\Delta\alpha$ and $\Delta\delta$ the least-squares analysis of the phase data is now performed using the components u_i, v_i derived at hour angle H_i . In the interesting case where the phase noise of each phase sample is constant (this occurs when the thermal noise dominates and when the atmospheric phase noise is “frozen”) one can show that the error in the coordinates takes a simple form. For a single baseline and for relatively high declination sources the position error is approximated by the equation

$$\sigma_{\alpha,\delta} = \Delta\theta \simeq \sigma_\phi / (2\pi\sqrt{n_p}(\mathcal{B}/\lambda)) \quad (20.19)$$

where σ_ϕ is the phase noise and n_p the number of individual phase measurements. This result implies (as expected a priori) that lower formal uncertainties are obtained with longer observing times and narrower synthesized beams. Of course the position measurements are improved with several independent interferometer baselines; the precision improves as the inverse of the square root of $n(n-1)/2$ for n antennas in the array.

We have shown that for a well calibrated interferometer the least-squares fit analysis of the phase in the (u, v) plane can give accurate source coordinates. However, the exact source position could also be obtained in the Fourier transform plane by searching for the coordinates of the maximum brightness temperature in the source map. The results given by this method should of course be identical to those obtained in the (u, v) plane although the sensitivity to the data noise can be different.

Finally, it is interesting to remind that the polar component of the baseline does not appear in the equation of the fringe frequency which is deduced from the time derivative of the phase. There is thus less information in the fringe frequency than in the phase.

20.4 Accurate Position Measurements with the IRAM Interferometer

Let us start with two general and simple remarks. First, the phase equation in Section 20.2 or the least-square analysis of the uv data in Section 20.3 show that higher position accuracy is achieved for smaller values of the fringe spacing λ/\mathcal{B} . Thus, for astrometry it is desirable to use long baselines and/or to go to

short wavelengths. However, the latter case implies that the phases are more difficult to calibrate especially at mm wavelengths where the atmospheric phase fluctuations increase with long baselines. Second, sensitivity is always important in radio astrometry. For a point-like or compact source the sensitivity of the array varies directly as $D^2(n(n-1))^{0.5}$ where D is the antenna diameter and n the number of antennas. Thus, the detection speed varies as $D^4n(n-1)$ and big antennas are clearly advantageous [Baudry 1996].

Comparison of the IRAM 5-element array with one of its competitors, the Owens Valley Radio Observatory array (OVRO) with 6×10.4 m, gives a ratio of detection speed of 1 over 0.36 at 3 mm and 1 over 0.65 at 1.3 mm in favour of the Plateau de Bure array (see Table 1 below where the two entries correspond to 3 mm and 1 mm; system temperatures have been adopted according to advertised array specifications [June 2000]; sensitivity and speed are defined in Table 1). (Note also that the sixth antenna in the Bure array will increase its detection speed by 50%.) For comparison we include in Table 1 the BIMA array located in California and the Nobeyama array in Japan (NMA). In addition, it is interesting to note that the large dishes of the IRAM array are well adapted to quick baseline and phase calibrations; this is another clear advantage of the IRAM interferometer in astrometric observations.

Table 1. Comparison of Sensitivity and Speed of mm-wave Interferometers

	BIMA		IRAM		NMA		OVRO	
Antennas	9		5		6		6	
Baseline (m)	2000		400		400		480	
Sensitivity	0.31	0.26	1.00	1.00	0.42	0.06	0.36	0.65
Speed	0.10	0.07	1.00	1.00	0.18	—	0.13	0.42

$$\text{Sensitivity} = \frac{\eta_A D^2 \sqrt{n(n-1)}}{T_{\text{sys}}}, \quad \text{Speed} = \left[\frac{\eta_A D^2 \sqrt{n(n-1)}}{T_{\text{sys}}} \right]^2$$

20.4.1 Absolute positions

To illustrate the potential of the IRAM array for astrometry we consider here observations of the SiO maser emission associated with evolved late-type stars. Strong maser line sources are excited in the $v = 1, J = 2 - 1$ transition of SiO at 86 GHz and easily observed with the sensitive IRAM array. Because of molecular energetic requirements (the vibrational state $v = 1$ lies some 2000 K above the ground-state) the SiO molecules must not be located too much above the stellar photosphere. In addition, we know that the inner layers of the shell expanding around the central star have sizes of order one arcsecond or less. Therefore, sub-arcsecond position accuracy is required to locate the SiO sources with respect to the underlying star whose apparent diameter is of order 20-50 milliarcseconds. For absolute position measurements one must primarily:

- select long baselines to synthesize small beamwidths,
- make a highly accurate baseline calibration observing several quasars selected for their small position errors,
- observe at regular intervals two or more quasars (phase calibrators) in the field of each program star in order to determine the instrumental phase and to correct for atmospheric phase fluctuations,
- observe the program star over a long hour angle interval, and use the best estimate of the stellar coordinates (corrected for proper motion).

Our first accurate radio position measurements of SiO masers in stars and Orion were performed with the IRAM array in 1991/1992. We outline below some important features of these observations [Baudry et al. 1994]. We used the longest E-W baseline available at that time, about 300 m, thus achieving beams of order 1.5 to 2 arcseconds. The RF bandpass calibrations were made accurately using strong quasars only. To monitor the variable atmosphere above the array and to test the overall phase stability, we observed a minimum of 2 to 3 nearby phase calibrators. Prior to the source position analysis we determined accurate baseline components; for the longest baselines the r.m.s. uncertainties were in the range 0.1 to 0.3 mm. The positions were obtained from least-square fits to the imaginary part of the

calibrated visibilities. (Note that the SiO sources being strong, working in the (u, v) or image planes is equivalent.)

The final position measurement accuracy must include all known sources of uncertainties. We begin with the formal errors related to the data noise. This is due to finite signal to noise ratio (depending of course on the source strength, the total observing time and the general quality of the data); poorly calibrated instrumental phases may also play a role. In our observations of 1991/1992 the formal errors were around 10 to 30 milliarcseconds. Secondly, phase errors arise in proportion with the baseline error $\delta\vec{B}$ and the offset between the unit vectors pointing toward the stellar source and the nearby phase calibrator. This phase error is $\delta(\phi - \phi_r) = (\delta\vec{B} \cdot (\vec{k}_{\text{quasar}} - \vec{k}_0))2\pi/\lambda$. Typical values are $\delta B \simeq 0.2$ mm and $\delta k \sim 10^\circ - 20^\circ$ corresponding to phase errors of 3° to 7° , that is to say less than the typical baseline residual phases. A third type of error is introduced by the position uncertainties of the calibrators. This is not important here because the accuracy of the quasar coordinates used during the observations were at the level of one milliarcsecond.

The quadratic addition of all known or measured errors is estimated to be around $0.07''$ to $0.10''$. In fact, to be conservative in our estimate of the position accuracy we measured the positions of nearby quasars using another quasar in the stellar field as the phase calibrator. The position offsets were around $0.1''$ to $0.2''$ depending on the observed stellar fields; we adopted $0.1''$ to $0.2''$ as our final position accuracy of SiO sources. The SiO source coordinates are derived with respect to baseline vectors calibrated against distant quasars. They are thus determined in the quasi-inertial reference frame formed by these quasars.

Finally, it is interesting to remind a useful rule of thumb which one can use for astrometry-type projects with any connected-element array provided that the baselines are well calibrated and the instrumental phase is stable. The position accuracy we may expect from a radio interferometer is of the order of 1/10th of the synthesized beam (1/20th if we are optimistic). This applies to millimeter-wave arrays when the atmospheric fluctuations are well monitored and understood. With baseline lengths around 400 m the IRAM array cannot provide position uncertainties much better than about $0.05 - 0.1''$ at 86 GHz. Extensions to one kilometer would be necessary to obtain a significant progress; the absolute position measurements could then be at the level of 50 milliarcseconds which is the accuracy reached by the best optical meridian circles.

20.4.2 Relative Positions and Self-calibration Techniques

We have measured with the IRAM array the absolute position of the SiO emission sources associated with each spectral channel across the entire SiO emission profile. Any spatial structure related to the profile implies different position offsets in the direction of the star. Such a structure with total extent of about 50 milliarcseconds is observed in several late-type stars. This is confirmed by recent VLBI observations of SiO emission in a few stars. VLBI offers very high spatial resolution but poor absolute position measurements in line observations.

The best way to map the relative spatial structure of the SiO emission is to use the phase of one reference feature to map all other features. This spectral self-calibration technique is accurate because all frequency-independent terms are cancelled out. The terms related to the baseline or instrumental phase uncertainties as well as uncalibrated atmospheric effects are similar for all spectral channels and cancel out in channel to channel phase differences. By making the difference

$$(\phi(\nu) - \phi(\nu_{\text{ref}}))(\lambda/2\pi) = \vec{B} \cdot \delta\vec{k}(\nu) - \vec{B} \cdot \delta\vec{k}(\nu_{\text{ref}}) \quad (20.20)$$

where the SiO reference channel is at frequency ν_{ref} we obtain a phase difference equation whose solution gives the coordinate offsets $\Delta\alpha(\nu)$ and $\Delta\delta(\nu)$ relative to channel ν_{ref} . The main limitation in such self-calibration techniques comes from the thermal noise and the achieved signal to noise ratio SNR. In this case [Reid et al. 1988] showed that the one sigma position uncertainty or angular uncertainty $\Delta\theta$ is approximately given by the equation

$$\Delta\theta = 0.5(\lambda/B)/\text{SNR} \quad (20.21)$$

Common practice with connected-element arrays shows that selection of a reference channel is not critical; it must be strong in general. Self-calibration proved to be successful with the IRAM array in several stars

and Orion where we have obtained accurate relative maps of SiO emission. Detailed and accurate relative maps were also obtained for the rare isotope ^{29}SiO emission which is nearly 2 orders of magnitude weaker than that of the main isotope [Baudry et al. 1998]. A relative position accuracy of 2 to 5 milliarcsec was obtained in the Orion spot map of ^{28}SiO emission (Fig. 20.1).

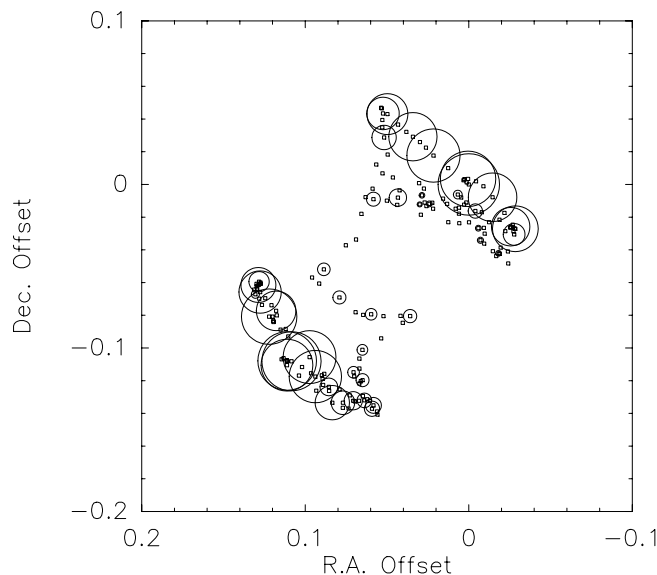


Figure 20.1: Spot map of $^{28}\text{SiO } v = 1, J = 2 \rightarrow 1$ emission observed on August 1995 in the direction of Orion IRc2 [Baudry et al. 1998]. The right ascension and declination offsets are in arcsec. Each small open square marks the center of an individual channel. The diameter of each circle, given every 3 channels, is proportional to the line intensity. The two main ridge of ^{28}SiO emission cover $-1 \rightarrow -10$ (southern ridge) and $12 \rightarrow 20 \text{ km s}^{-1}$.

The relative spot maps obtained with connected-element arrays do not give the detailed spatial extent of each individual channel. This would require a spatial resolution of about one milliarcsecond which can only be achieved with VLBI techniques. Note however that VLBI is sensitive to strong emission features while the IRAM array allows detection of very weak emission; thus the two techniques appear to be complementary.

With SiO spatial extents of about 50 milliarcseconds and absolute positions at the level of 0.1 arcsecond it is still difficult to locate the underlying star. We have thus attempted to obtain simultaneously the position of one strong SiO feature relative to the stellar photosphere and the relative positions of the SiO sources using the 1 and 3 mm receivers of the IRAM array. This new dual frequency self-calibration technique is still experimental but seems promising.

20.5 Sources of Position Uncertainty

We have given evidence that extended baselines are best for accurate position measurements. In addition, as long as sensitivity is not an issue and that observed sources are not resolved by the array, the outermost stations should always be preferred (Section 20.4). The great asset of the IRAM array is clearly sensitivity coupled with resolving power, although atmospheric fluctuations and instrumental limitations may limit the accuracy of position measurements.

We further discuss below the boundary conditions or requirements in astrometric observations. Table 2 at the end of this section summarizes the limitations with respect to the IRAM array.

20.5.1 Known Limitations

Among several practical limitations it is worth mentioning: wind effects, thermal effects in the antenna structure (including de-icing instabilities), the influence of refraction effects, imperfections in subreflector displacements, imperfections in the azimuth and elevation bearings of the antennas and, not least, uncertainties in the “crossing point” of the azimuth and elevation axes. These imperfections, and in fact the resulting differential effects of each antenna pair in the array, have adverse effects on the visibility phase measurements; however, many of them can be removed to a large extent by phase calibration (a posteriori), and thus will not be discussed further.

In order to make the reader more aware of these questions, we just mention that the large-scale unevenness of the azimuth bearings gives rise, in places, to optical path deviations of about $40\ \mu\text{m}$ which translate into position offsets of $0.04''$ with 200 m baselines. Likewise, position uncertainties result from imperfections in the “crossing point” of the azimuth and elevation (nodal point) of each antenna in the array (see Chapter 6). Slow drifts in the focal position are also corrected to first order by the calibration procedure. Only large and rapid focal drifts are problematic if not recognized as such in the phase of a reference calibrator.

20.5.2 Practical Details

We elaborate here on some properties of the IRAM array related to inaccuracies in the determination of baseline lengths, and we briefly discuss how atmospheric phase noise and source strength can limit the accuracy of position measurements.

- **Baselines:** are easily measured with the IRAM interferometer on Plateau de Bure with a precision of a few degrees or a small fraction of one millimetre. As a reference, good winter conditions allow us to measure baselines at 86 GHz, using a number of quasars well-distributed in hour-angle and declination, with uncertainties of $5^\circ - 8^\circ$ in the D configuration (the most compact one at IRAM) and $10^\circ - 20^\circ$ in the A configuration. But even the most accurate baseline measurement will be limited in precision. Residual uncertainties in the baselines will finally produce phase errors that scale with $\Delta\vec{k} = \vec{k}_{\text{quasar}} - \vec{k}_{\text{source}}$, the distance between a calibration quasar and the source. Combining the different forms of the phase equation defined in Section 20.2, we can then derive a rough estimate of the mean uncertainty in the absolute position of a source from

$$\Delta\theta \simeq (\delta\vec{B} \cdot \Delta\vec{k})/B \simeq (\delta\phi/2\pi) (\lambda/B) \simeq (\delta\phi/2\pi) \theta_B \quad (20.22)$$

where $\delta\phi$ is the phase error due to inaccuracies in the baselines. This formula is convenient, as it associates uncertainties in the knowledge of the baseline length at a given frequency with θ_B , the synthesized beam. For instance, observations at 86 GHz in the D configuration with baseline phase residuals $\delta\phi$ between 2° and 5° (i.e. assuming baseline errors, $\delta\vec{B} = 0.2\ \text{mm}$, and typical phase calibrator distances, $\Delta\vec{k} = 5^\circ - 15^\circ$) appear to have position uncertainties smaller than $0.20''$. See Subsection 20.4.2 for suggestions to improve these uncertainties.

- **Atmospheric phase fluctuations** are among the most important limitations that affect the accuracy of position measurements. Poor seeing conditions imply phase decorrelation which in turn implies reduced flux density sensitivity and larger apparent source sizes (see Chapters 9 and 10). When the atmospheric phase noise dominates, phase decorrelation can be estimated by least-square fitting in time the phase profile of a reference calibrator. Under the assumptions made at the end of Section 20.3 or assuming here that the atmospheric phase fluctuations remain unchanged, namely σ_ϕ is similar for each phase sample, we can estimate the mean angular uncertainty from

$$\Delta\theta \simeq \sigma_\phi / (2\pi\sqrt{n_p}(B/\lambda)) = \sigma_\phi \theta_B / (2\pi\sqrt{n_p}) \quad (20.23)$$

where n_p is the number of phase samples. The size of the associated “seeing disk” is defined as $(\sigma_\phi/2\pi)\sqrt{8\ln 2}\theta_B$. For instance, measuring mean atmospheric phase fluctuations $\sigma_\phi \simeq 10^\circ$ at 86 GHz on a 60 m baseline is equivalent to observe in $\simeq 0.78''$ seeing conditions (which is small since $\theta_B \sim \lambda/B \sim 12''$ and corresponds to a small fraction of the synthesized beam). Observations at the same

frequency, on the same baseline and with similar atmospheric conditions will then provide a position accuracy of order $\Delta\theta \simeq 0.33''/\sqrt{n_p}$ (or 3% of $\theta_B \sim 12''$).

- **Source strength** and finite signal to noise ratio is another important limitation to astrometric accuracy. While reference calibrators have to provide enough sensitivity for rapid detection, detection of program sources may require hours of integration. In addition, observed sources are sometimes resolved out with extended configurations. Therefore, the interesting astrometric case described in Section 20.4 where spectral sources are rather easily detected may not be common in mm-wave astronomy. As mentioned in Section 20.4.2 we can use the result of [Reid et al. 1988] to estimate the one sigma position uncertainty

$$\Delta\theta = \sigma_\theta \simeq (\theta_B/2)(\sigma_S/S) = \theta_B/(2 \cdot \text{SNR}) \quad (20.24)$$

where σ_S is the noise in the map and S the source flux density. With the IRAM array in the D configuration, a source at mean declination (e.g. $30^\circ - 40^\circ$) detected with a signal-to-noise $\text{SNR} \simeq 5$, cannot be located with a precision better than 10% of θ_B (e.g. $0.25''$ at 230 GHz). Uncertainties in declination measurements will obviously be larger for southern sources owing to the elongation of the synthesized beam.

On the other hand, astrometric observations of bright sources such as the SiO line sources presented in Section 20.4 are not limited by SNR issues in general, but by the accuracy of the bandpass calibration. While delay calibration (see Chapter 5) already removes the bulk of the phase gradient across the band selected for observations, residual variations can only be removed by observing strong calibrators. Using the classical radiometric equation, bandpass calibration requires the following:

$$\Delta t^C = (S \cdot \sigma_S)^2 / (C \cdot \sigma_C)^2 \Delta t^S \quad (20.25)$$

In this expression, S and C are the flux densities of the source and calibrator, σ_S and σ_C the respective r.m.s. noise levels, and Δt^S and Δt^C the integration times on the source and calibrator. For instance, a 1 sec integration on a 15 Jy calibrator like 3C273 (at the time of writing, the strongest calibrator at 86 GHz available in the northern sky) is sufficient for bandpass calibration in the case of a 5σ -detection of a 2 mJy source. (In practice, however, several seconds integration would be better.) On the other hand, a 10 min integration on the same calibrator would just be sufficient to meet the minimum requirement ($\sigma_S = \sigma_C$) to calibrate 1 min observations of a 50 Jy strong source.

There are a few other issues which we list below. They are worth mentioning although there is little implication for observations with the IRAM array. (For other effects such as bandwidth smearing and visibility averaging, we recommend reading the book of [Thompson et al. 1986]; see Chapter 6.)

- **Pointing offsets** is a potential source of position errors. Ideally, the phase of the incoming wavefront does not depend on pointing offsets across the Airy (or diffraction) pattern. However, imperfections in the optical system may result in differences in the Airy pattern from an antenna to another in the array (although all antennas are of comparable quality). Experience at 86 GHz shows, that rather strong phase differences (up to 10°) may appear when antennas are individually offset from the target position by a distance equal to half the primary beamwidth (HPBW).
- **Primary beam attenuation** produces a radial displacement for off-axis targets. It needs to be corrected for targets at large angular distances ($\simeq \text{HPBW}/2$) from the phase tracking center of the interferometer.
- **Gravitational Lensing** by the Sun introduces positional offsets $\sim M_\odot/D_E(\sqrt{1 + \cos\theta}/\sqrt{1 - \cos\theta})$ which are negligible for targets outside the Sun avoidance region of the IRAM antennas ($\theta \geq 45^\circ$). For instance $\Delta\theta \simeq 0.1''$ at $\sim 5^\circ$ from the Sun limb.

A summary of the main practical position uncertainties for the IRAM array is given in Table 2 in arc second or in terms of the synthesized beam θ_B ; \mathcal{B} is the baseline length in meter. Only instrumental errors are removed to first order by calibration.

Table 2. Plateau de Bure Interferometer – Main Sources of Position Uncertainty

TELESCOPE*	$\Delta\theta$	Calibration
Focus Offset	$\leq 0.20'' \cdot (100/\mathcal{B})$	Yes
Axes Non-Intersection	$\leq 0.10'' \cdot (100/\mathcal{B})$	Yes
AzEl Bearings	$\leq 0.08'' \cdot (100/\mathcal{B})$	Yes
OBSERVATION		
Atmospheric Seeing [†]	$\leq 0.06 \cdot \theta_B$	No
Calibrator Distance [†]	$\leq 0.02 \cdot \theta_B$	No
Pointing Offset	$\leq 0.02 \cdot \theta_B$	Partially
Source Intensity	$\leq (0.5/\text{SNR}) \cdot \theta_B$	No

[†] Upper limits are illustrative for astrometric observations in limiting conditions. See text for more details.

* Instrumental values are all calibrated out to first order.

Chapter 21

Mm versus Optical Interferometry: a qualitative comparison

A Panel Discussion by

Anne Dutrey^{1,2}, Fabien Malbet², Stéphane Guilloteau¹
Robert Lucas¹, Dennis Downes¹ and Roberto Neri¹

¹ IRAM, 300 rue de la Piscine, F-38406 Saint Martin d'Hères, France

² LAOG, BP 53, F-38041 Grenoble cedex 9, France

This chapter is a brief summary of the panel discussion. The goal was to present the main differences concerning not only the instrumentation itself but also the language which is used by both community.

The summary does not appear as a standard panel discussion where several people interact because we have chosen to compare both techniques through three fundamental aspects:

- The expression of the interferometric equation
- The instrumental differences
- The atmospheric behaviour and the noise properties

21.1 The basic equation of interferometry

In a two element interferometer, the signal coming on the detectors from telescopes 1 and 2 is the sum of contributions from the background $B_{1,2}$ (either the atmosphere or the instrumentation itself) and from the astronomical source $I_{1,2}$.

21.1.1 Additive interferometry

For **direct detection (or additive) interferometry**, as in the optical domain, an interferometer measures *on-source* on the baseline B_{12} :

$$I_{12} = I_1 + I_2 + 2\sqrt{I_1 I_2} V_o + B_1 + B_2 |\mathcal{V}_{12}| \cos \Phi_{12} \quad (21.1)$$

The term $I_1 + I_2 + B_1 + B_2$ is the continuum term while $2\sqrt{I_1 I_2} V_o |\mathcal{V}_{12}| \cos \Phi_{12}$ is the interferometric term. After doing an *on-off* (also called the “sky calibration”), Eq.21.1 becomes:

$$I_{12} = I_1 + I_2 + 2\sqrt{I_1 I_2} V_o |\mathcal{V}_{12}| \cos \Phi_{12} \quad (21.2)$$

Where \mathcal{V}_{12} is the visibility of the astronomical source measured on baseline B_{12} of amplitude $|\mathcal{V}_{12}|$ and phase Φ_{12} .

The visibility to calibrate can be expressed by:

$$V_{corr} = \frac{2\sqrt{I_1 I_2}}{I_1 + I_2} V_o |\mathcal{V}_{12}| \cos \Phi_{12} \quad (21.3)$$

V_o is the contrast which takes into account the calibration of all the system (instrumentation + atmosphere). The photometric term is given by $\frac{2\sqrt{I_1 I_2}}{I_1 + I_2}$ (note that I_1 and I_2 are relatively easily measured).

The visibility $\mathcal{V}_{12} = |\mathcal{V}_{12}| \cos \Phi_{12}$ appears as a fringe contrast (which is flux calibrated), therefore it is normalized to unity. Note finally that in the optical case $B_{1,2} \ll I_{1,2}$.

21.1.2 Multiplicative interferometry

For **heterodyne or multiplicative detection**, the output of the interferometer (correlator) gives a correlation rate r_{12} which is a dimensionless number (this uses a simple correlation between two antennas, not a “bi-spectrum”).

The correlation corresponding to $\sqrt{I_1 I_2} V_o \mathcal{V}_{12}$ is the term of astronomical interest, and is related to r_{12} by:

$$\sqrt{I_1 I_2} V_o |\mathcal{V}_{12}| e^{i\Phi_{12}} = r_{12} \sqrt{(B_1 + I_1)(B_2 + I_2)} \quad (21.4)$$

Where $(B_1 + I_1)$ and $(B_2 + I_2)$ are the autocorrelations measured on telescopes 1 and 2, respectively.

At mm waves, $B_{1,2} \gg I_{1,2}$ because the atmospheric thermal emission strongly dominates with typically $I_{1,2}/B_{1,2} \sim 10^{-3} - 10^{-4}$ (except for the Sun and bright planets). Therefore, Eq.21.3 simplifies as:

$$\sqrt{I_1 I_2} V_o |\mathcal{V}_{12}| e^{i\Phi_{12}} = r_{12} \sqrt{B_1 B_2} \quad (21.5)$$

The heterodyne technique does not allow to measure the continuum term but preserves the phase (thanks to the use of a complex correlator, see Chapter 2). V_o can be seen as the correlation efficiency of the interferometer (instrumental + atmospheric). The calibrated visibilities (as defined in previous chapters) $V_{12} = \sqrt{I_1 I_2} \mathcal{V}_{12}$ are expressed in unit of flux density (Jy) while $\sqrt{B_1 B_2}$ can be considered as the photometric term (including the photometric calibration of the atmosphere).

21.2 Getting the fringes

For details about both techniques, we invite the reader to read Chapters 2 and 4. We only focus here on some basic points.

Additive detection versus Heterodyne technique

An heterodyne system preserves the phase information, therefore one major interest of the heterodyne detection is to allow high resolution spectroscopy. Some interferometers working at $10\mu\text{m}$ such as ISI use heterodyne technique. However they have a low efficiency and can only observe very bright sources.

Electronic compensating delay versus delay lines

Direct detection at optical wavelengths uses delay lines which are well suited to the wavelengths and baseline lengths. In the mm range, due to the low wavelengths and the long baselines, the size of the mirrors would be prohibitive. To avoid losses due to diffraction in the delay lines, the mirror size must be larger than about $\sqrt{B} \times \lambda$. For example, at $\lambda = 3$ mm and assuming a baseline of $B = 400$ meters (which is of medium size), the mirror should be larger than 1.1 meters. For ALMA, assuming baselines of 14 km and a wavelength 3 mm, the required diameter goes up to 6 m. Using electronic compensating delay is definitely easier for the purpose of mm interferometry.

Note finally that the term *white fringe* in the optical is similar to the *fringe stopping*, at mm waves.

Phase calibration

Since t_o is typically of order several 10 minutes at $\lambda \sim 1.3$ mm, the atmospheric phase can be regularly calibrated by reference to a nearby source close to the astronomical source. This allows phase retrieval.

This is not possible in the optical because t_o is of order a few 10-100 milli seconds, and also because the angular scale over which the atmospheric phase is coherent (the isoplanetic patch) is too small. Instead as soon as optical arrays have three telescopes (or more), opticians use the phase closure relations in order to retrieve the astronomical phase.

Phase closure relations

In this sense, the phase closure relations *are not applied* in mm interferometry because individual visibilities are very noisy (dominated by the atmospheric noise, as explained above). Hence applying such a method does not really bring new constraints on the phase.

However a careful reader of Chapters 7, 9 and 12 should have noticed that mm interferometric data are mostly calibrated *per antenna* and not *per baseline*, the interest being to reduce the number of unknowns and therefore increase the SNR. This calibration technique implicitly assumes that the closure relations in phase and in amplitude are applied on the calibrators. This remains possible because the closure relations are indeed respected by the instrumentation.

21.3 Atmospheric behaviour and noise properties

Table 21.3 summarises the properties of the atmosphere and the resulting noise (including also the instrumentation) at both wavelengths.

Mm versus optical interferometry: Atmosphere & Noise properties

Item	Radio mm	Optical
λ	0.6mm to 1cm	0.4 to 30 μm
ν	30 to 450 GHz	10 to 600 THz
Comparison given for	$\lambda \sim 1.3\text{mm}$	$\lambda \sim 1\mu\text{m}$
Noise sources Main instrumental noise Signal Detection	background limited (gaussian) Receiver (thermal) thermal sky emission $T_{\text{signal}}/T_{\text{sys}} \sim 10^{-2} \cdot 10^{-4}$	photon limited (poisson)* Detector (read-out) photon limited
Seeing origin Fried Parameter r_o (size of the coherence cell) Coherence Time t_o (time to reach $\Delta\Phi \approx 180^\circ$) Equivalent to	Variation of W(H₂O) > antenna several 10 minutes Single-speckle	Variation of T_{atm} \leq telescope ~ 10 milli-seconds Multi-speckle
Atmospheric correction Photometry Seeing Phase Calibration	 monitoring of T_{sys} radiometric phase correction phase referenced on nearby sources	 “standard” photometry technics tip tilt adaptive optics t_o too short closure phase on dual interferometer
Measurements Information on	complex correlator rates: r_i, r_r complex visibility V $ V $ & Φ_V	$V_{12}^{raw} = \frac{I_{max} - I_{min}}{I_{max} + I_{min}}$ fringe contrast $ V $, amplitude
Imaging Algorithms	Complex visibilities all standard imaging	Phase retrieval by closure relations + amplitude model fitting in the UV plane

* Note that for $\lambda \geq 2.5\mu\text{m}$, the atmosphere and the telescope are starting to contribute as main sources of noise (thermal emission), therefore the noise becomes background limited.

Bibliography

- [Alloin et al 2000] Alloin, D., Barvainis, R., Guilloteau, S., 2000, *Ap J* **528**, L81
New CO and Millimeter Continuum Observations of the $Z = 2.394$ Radio Galaxy 53W002
- [Altenhoff et al. 1994] Altenhoff, W., Thum, C., Wendker, H.J., 1994, *A&A* **281**, 161-183
Radio emission from stars: a survey at 250 GHz.
- [Baudry et al. 1994] Baudry A., Lucas R., Guilloteau S., 1995, *A&A* **293**, 594
Accurate position of SiO masers.
- [Baudry 1996] in *Science with Large Millimetre Arrays*, ed. P.A.Shaver, p. 353
ESO Astrophysics Symposia, Springer
- [Baudry et al. 1998] Baudry A., Herpin F., Lucas R. 1998, *A&A* **335**, 654
 ^{29}SiO ($v=0$) and ^{28}SiO ($v=1$) $J=2-1$ maser emission from Orion IRC2
- [Beasley et al. 1995] Beasley et al. 1995, in *First mm-VLBI Workshop*, Boston, 53
- [Berger et al. 2001] Berger J.-P., Haguenaer P., Kern P., Rousselet-Perraut K., Malbet F., Schanen-Duport I., Séveri M., Millan-Gabet R., Traub W. 2001, in preparation
- [Born & Wolf 1975] Born, M., and Wolf, E., 1975 *Pergamon Press*
Principles of Optics, New Physical Optics Notebook
- [Bracewell 1978] Bracewell R.N. 1978, *Nature* 274, 780
- [Bremer 1994] Bremer, M. 1994, IRAM internal report
The Phase Project: First Results
- [Bremer 1995] Bremer, M., 1995, IRAM report **238**
The Phase Project: Observations on Quasars
- [Bremer et al. 1995] Bremer, M., Guilloteau, S., Lucas, R. 1995, IRAM Newsletter **24** (Nov. 1995)
Atmospheric Phase Correction: from random phase down to 20 degree r.m.s. at 230 GHz.
- [Browne et al. 1998] Browne, I.W.A., et al. 1998 *MNRAS* **293**, 257
Interferometer phase calibration sources – II
- [Cernicharo 1988] Cernicharo, J., 1998, PhD Thesis Paris, and IRAM report 52
ATM: A Program to compute Theoretical Atmospheric Opacity for Frequencies below 1 THz
- [Cernicharo & Pardo 1999] Private communication.
- [Christiansen and Hogbom 1969] Christiansen, W.N., and Hogbom, J.A., 1969, *Cambridge University Press*
Radiotelescopes

- [Clark 1980] Clark, B.G., 1980, *A&A*, **89**, 377
An efficient implementation of the algorithm "CLEAN"
- [Cooper 1970] Cooper, B.F.C., 1970, *Aust. J. Phys.* **23**, 521
- [Cornwell 1987] Cornwell, T.J., 1987, MMA Memo. 42
- [Cornwell 1988] Cornwell, T.J., 1988, *A&A*, **202**, 316
Radio interferometric imaging of very large objects.
- [Cornwell 1989] Cornwell, T.J., 1989
in *Synthesis Imaging in Radio Astronomy*,
Perley R.A., Schwab F.R., Bridle A.H. (eds),
ASP Conferences Series Volume 6, p. 277
- [Cornwell 1993] Cornwell, T.J., 1993
in *Astronomy with Millimeter and Sub-millimeter Wave Interferometry*,
Ishiguro M., Welch W.J. (eds),
ASP Conference Series Volume 59, p. 96
- [Cotton & Schwab 1984] Schwab, F.R., 1984, *Astron. J.* **89**, 1076
Relaxing the isoplanetism assumption in self-calibration: applications to low
frequency radio interferometry. (see top of p.1078)
- [Coudé Du Foresto, Mazé, & Ridgway 1993] Coudé du Foresto V., Mazé G., Ridgway S. 1993, ASP Conf.
Ser. 37: Fiber Optics in Astronomy II, 285
- [Coudé Du Foresto, Ridgway, & Mariotti 1997] Coudé Du Foresto V., Ridgway S., & Mariotti J.-M. 1997,
A&AS, **121**, 379
- [D'Addario 1989] D'Addario, L., 1989, in
Synthesis Imaging in Radio Astronomy,
Perley R.A., Schwab F.R., Bridle A.H. (eds),
ASP Conferences Series Volume 6, p. 59
- [Danchi et al. 1988] Danchi W.C., Bester M., Townes C.H. 1988, in ESO Conf. Workshop Proc.,
29, 867
- [Downes & Altenhoff 1989] Downes, D., Altenhoff, W.J., 1989
Anomalous refraction at radio wavelengths
URSI/IAU Colloquium on Radio Astronomical Seeing, Beijing (China)
J.E.Baldwin, Wang Shouguan, eds., International Academic Publisher &
Pergamon Press, p. 31
- [Downes et al 1999] Downes, D., Neri, R., Greve, A. et al, 1999 *A&A* **347**, 809
Proposed identification of Hubble Deep Field submillimeter source HDF 850.1
- [Ekers & Rots 1979] Ekers, R.D., Rots, A.H., 1979, in
Images formation from coherence function in astronomy, C. van Schooneveld
(ed.),
Proc. IAU Symp. 49, p. 61
- [Evans & Stephens 1995] Evans, K. F., and Stephens, G.L., 1995 *Journal of the Atmospheric Sciences*,
52, 2058-2072.
- [Felli & Spencer 1989] Felli, M., and spencer R.E., 1989 *NATO ASI Series*, **283**
Very Long Baseline Interferometry

- [Feynman et al. 1964] Feynman R.P., Leighton R.B. and Sands M. 1964, *Addison- Wesley Publishing Company*
The Feynman Lectures on Physics
- [Fizeau 1868] Fizeau H. 1868, C. R. Acad. Sci. 66, 932
- [Froehly 1981] Froehly C. 1981, Coherence and Interferometry through Optical Fibers. In: Ulrich M.-H., Kjær K. (eds) Proc. ESO Conf., Science Importance of High Angular Resolution at Infrared and Optical Wavelengths. ESO, Garching, p. 285.
- [Gay & Journet 1973] Gay J., Journet A. 1973, Nature Phys. Sci. 241, 32
- [Goldsmith 1988] Goldsmith P.F., 1988, *IEEE press*
Instrumentation and Technique for Radio Astronomy
- [Goodman 1985] Goodman J.W. 1985, Statistical Optics (New York: John Wiley & Sons)
- [Greve & Hooghoudt 1981] Greve A., Hooghoudt, B. 1981, *A&A* **93**, 76
Quality evaluation of radio reflector surface.
- [Greve et al. 1995] Greve et al., 1995, *A&A* **299**, L 33
- [Greve et al. 1998] Greve A., Kramer, C., & Wild, W., 1998, *A&A Supp* **133**, 271
The beam pattern of the IRAM 30-m telescope (a reflector with several surface error distributions).
- [Gueth 1997] Gueth, F., 1997, PhD thesis, University of Grenoble
- [Gundlach 1989] Gundlach, K.H., 1989 (NATO ASI series, F 59, p. 259)
- [Guilloteau 1990] Guilloteau, S., 1990, IRAM Documentation
Amplitude Calibration
- [Guilloteau et al. 1993] Guilloteau, S., Dutrey, A., Marten, A., & Gautier, D., 1993, *A&A* **279**, 661
CO in the troposphere of Neptune: Detection of the J=1-0 line in absorption
- [Guilloteau et al. 1999] Guilloteau, S., Dutrey, A., Simon, M., 1999, *A&A* **348**, 570.
GG Tauri: the ring world.
- [Hanbury Brown & Twiss 1956] Hanbury Brown R., Twiss R.Q. 1956, Nature 177, 27
- [Hogbom 1974] Högbom, J.A., 1974, *A&A Supp.*, **15**, 417.
Aperture synthesis with a non regular distribution of interferometer baselines.
- [Hagen et al. 1973] Hagen, J.B., Farley, D.T., 1973, *Radio Science* **8**, 775
- [Hill & Cliffort 1981] Hill, R.J., and Cliffort, S.F., 1981, *Radio Science* **16** No. 1, 77
- [Johnson et al. 1974] Johnson M.A., Betz A.L., Townes C.H. 1974, Phys. Rev. Lett. 33, 1617
- [Karpov 1999] Karpov A., 1999, C.R.Acad.Sci.Paris, t.327, IIb, p.539
- [Kellerman & Thompson 1985] Kellerman & Thompson 1985, *Science* **228**, 123
- [Kemball et al. 1995] Kemball et al. 1995, *AAS* **110**, 383
- [Kolmogorov 1941] Kolmogorov, A.N. (1941), in
Dissipation of energy in a locally isotropic turbulence, Doklady Akad. Nauk SSSR, **32**, 141
(English translation in: American Mathematical Society Translations 1958, Series 2, Vol 8, p. 87, Providence R.I)

- [Kraus 1982] Kraus, J.D., 1982 *McGraw Hill*
Radio Astronomy
- [Krichbaum et al. 1994] Krichbaum et al. 1994, *Proc. 2nd EVN/JIVE Symp.*, Torun, 47
- [Krichbaum et al. 1998] Krichbaum et al. 1998, *A&A* **335**, L 106
- [Labeyrie 1975] Labeyrie A. 1975, *ApJ* 196, L71
- [Labeyrie 1978] Labeyrie, A. 1978, *ARA&A*, 16, 77
- [Landau & Lifshitz 1959] Landau L.D. & Lifshitz E.M. 1959 *Pergamon Press*, p.49 // Fluid Mechanics
- [Lannes et al. 1994] Lannes, A., Anterrieu, E., and Bouyoucef, K., *J. mod. Optics*, 1994, **41**, 1537-1574.
"Fourier Interpolation and Reconstruction via Shannon-type Techniques.
Part I: Regularization principle."
- [Lannes et al. 1996] Lannes, A., Anterrieu, E., and Bouyoucef, K., *J. mod. Optics*, 1996, **43**, 105-138.
"Fourier Interpolation and Reconstruction via Shannon-type Techniques.
Part II: Technical developments and applications"
- [Lannes et al. 1997] Lannes, A., Anterrieu, E., and Maréchal, P., *A&A Supp.*, 1997, **123**, 183-198.
CLEAN and WIPE
- [Lay 1997] Lay, O., 1997, *A&A Supp* **122**, 547
Phase calibration and water vapor radiometry for millimeter wave arrays.
- [Lo and Lee] Lo, S.W., & Lee
Antenna Handbook theory, applications and design
- [Love 1978] Love, A.W., 1978, *IEEE press*
Reflector Antennas
- [Lucas 1995] Lucas, R. 1995, IRAM internal report
Practical Implementation of phase correction.
- [Malbet et al. 1999] Malbet F., Kern P., Schanen-Duport I., Berger J.-P., Rousselet-Perraut K., Benech P. 1999, *A&AS* 138, 135
- [Mariotti et al. 1992] Mariotti J.-M. et al. 1992, Coherent Combined Instrumentation for the VLT Interferometer. VLT Report No. 65. ESO, Garching.
- [Martin-Pintado et al. 1988] Martin-Pintado, J., et al 1988 *A&A* **197**, L15-L18.
Radiocontinuum and recombination lines towards CRL618 - Evidence for an ionized stellar wind ?
- [Mauersberger et al. 1989] Mauersberger, R. et al 1989, *A&A Suppl* **79**, 217
Line calibrators at λ 1.3, 2 and 3 mm
- [Matsushita et al. 1999] Matsushita S, Matsuo H, Pardo J.R., Radford S., 1999 *Publ. Astron. Soc. Japan*, **51**, 603-610.
- [Michelson & Pease 1921] Michelson A.A., Pease F.G. 1921, *ApJ* 53, 249
- [Minnet & Thomas 1968] Minnet & Thomas 1968, *Proc. IEE* **115**, 1419.
- [Mishchenko 2000] Mishchenko, M.I., 2000, *Applied Optics*, **39**, 1026-1031.

- [Padin et al. 1990] Padin et al. 1990, *ApJ* **360**, L 11
- [Paine et al. 2000] Paine S, Blundell R, Papa D.C., Barrett J.W., Radford S.J.E., 2000 *PASP*, **767**, 108-118.
- [Pardo et al. 2001a] Pardo, J.R., E. Serabyn, and J. Cernicharo, 2001, *J. Quant. Spectrosc. Radiat. Transfer*, **68**, 419-433.
- [Pardo et al. 2001] Pardo, J.R., Cernicharo J., and Serabyn E., 2001, *IEEE trans. Antennas and Propagation*, accepted (10 Feb., 2001).
- [Patnaik et al 1992] Patnaik, A., et al 1992 *MNRAS* **254**, 655
Interferometer phase calibration sources – I
- [Pedretti et al. 2000] Pedretti E., Labeyrie A., Arnold L., Thureau N., Lardiere O., Boccaletti A., Riaud P. 2000, **147**, 285
- [Penzias & Burrus 1973] Penzias A.A., & Burrus C.A., 1973, *ARA&A* **11**, 51
- [Perrin et al. 2000] Perrin G., Lai O. Léna P.J. 2000, SPIE 4006, 708
- [Queney 1974] Elements de Météorologie, P. Queney, 1974,
Collection de l'Ecole Nationale de Techniques Avancées, Masson & Cie Pub. Paris
- [Reid et al. 1988] Reid, M. et al. 1988, *ApJ* **330**, 809
The distance to the center of the Galaxy – H₂O maser proper motions in Sagittarius B2(N)
- [Reynolds et al. 1989] Reynolds, G.O., DeVelis, J.B., Parrent, G.B.Jr., & Thompson, B.J., 1989, *SPIE Optical Engineering Press*
Physical optics notebook: Tutorial in Fourier optics.
- [Rogers et al. 1984] Rogers et al. 1984, *Radio Science* **19**, 1552
- [Rodier 1981] Rodier F. 1981, Progress in optics. Volume 19. Amsterdam, North-Holland Publishing Co., 1981, p. 281-376., **19**, 281
- [Ruze 1966] Ruze 1966, *Proc. IEEE* **54**, 633
- [Sault et al 1996] Sault R.J., Staveley-Smith L., Brouw W.N., 1996, *A&A Supp.*, **120**, 375
An approach to interferometric mosaicing
- [Schwarz 1978] Schwarz U.J., 1978, *A&A*, **65**, 345
Mathematical-statistical description of the iterative beam removing technique (method CLEAN).
- [Scoville et al 1997] Scoville, N.Z., Yun, M.S., Windhorst, R.A., Keel, W.C., Armus, L., 1997. *Ap J* **485** L21
CO J=3-2 Emission in the Radio Galaxy 53W002 at $z = 2.394$
- [Serabyn & Weisstein 1996] Serabyn E, Weisstein EW., 1996 *Applied Optics*, **35**, 2752-2763.
- [Shannon 1949] Shannon, C.E., 1949, *Proc. IRE*, **37**, 10-21
- [Shao & Colavita 1992] Shao M., Colavita M.M. 1992, *A&A* **262**, 353
- [Sovers et al. 1998] Sovers O.J., Fanselow J.L., Jacobs C.S., in *Reviews of Modern Physics*, Vol. **70**, No. 4, October 1998, p.1393.
- [Steer et al. 1984] Steer D.G., Dewdney P.E., Ito M.R., 1984, *A&A*, **137**, 159
Enhancement to the deconvolution algorithm “CLEAN”.

- [Stéphan.1873] Stéphan E. 1874, C. R. Acad. Sci. 78, 1008
- [Tatarski 1961] Tatarski V.I. 1961
Wave Propagation in a turbulent Medium, McGraw-Hill
- [Tatarski 1971] Tatarski V.I. 1971
The Effects of the turbulent Atmosphere on Wave Propagation
(translated from Russian by the Israel Program for Scientific Translations
Ltd, ISBN 0 7065 0680 4)
reproduced by National Technical Information Service, U.S. Department of
Commerce, Springfield, Va. 22151
- [Thayer 1974] Thayer G.D. 1974, *Radio Science* **9** No 10, p. 803
- [Thompson et al. 1986] Thompson, A.R., Moran, J.M., Swenson, G.W., 1986
Interferometry and Synthesis in Radio Astronomy (Wiley : New York)
- [Townes & Schawlow 1975] C.H. Townes, A.L. Schawlow, 1975
Microwave Spectroscopy, Dover Pub. New York
- [Van Vleck 1966] Van Vleck, J.H., Middleton, D., 1966, *Proc. IEEE* **54**, 2
- [Waters 1976] Absorption and Emission by atmospheric gases, J.W. Waters 1976,
in *Methods of experimental physics*, **12**, ed. M.L. Meeks p. 147 Academic
Press, New York
- [Wakker & Schwartz 1988] Wakker B., Schwarz U.J., 1988, *A&A*, **200**, 312
The multi-resolution CLEAN and its application to the short-spacing prob-
lem in interferometry.
- [Weigelt et al. 2000] Weigelt G. et al. 2000, SPIE 4006, 617
- [Wilkinson et al. 1998] Wilkinson, P.N., et al. 1998 *MNRAS* **300**, 790
Interferometer phase calibration sources – III
- [Zensus et al. 1995] Zensus A.J., Diamond P.J, Napier P.J, 1995, *ASP Conf. Series* **82**
Very Long Baseline Interferometry and the VLBA